Experimental Investigation of the Filling Process in Evacuated Spacecraft Propulsion System Feedlines

Experimentelle Untersuchung des Füllprozesses evakuierter Treibstoffleitungen von Raumfahrtantrieben

Von der Fakultät für Maschinenwesen der Rheinisch-Westfälischen Technischen Hochschule Aachen zur Erlangung des akademischen Grades eines Doktors der Ingenieurwissenschaften genehmigte Dissertation

vorgelegt von

Cristiano Bombardieri

Berichter: Univ.-Prof. Dr. rer. nat. Michael Oschwald
Associate Prof. Dr. ir. Johan Steelant

Tag der mündlichen Prüfung: 13 April 2018

Abstract

During the start-up of the propulsion system of a satellite or spacecraft, the opening of the tank isolation valve will cause the propellant to flow into an evacuated feedline and slam against a closed thruster valve. This filling process, called priming, can cause severe pressure peaks that could lead to structural failure. In the case of monopropellants such as hydrazine also the risk of adiabatic compression detonation must be taken into account in the design of the feedline subsystem. The phenomenon of priming involves complex two-phase flow aspects: the liquid entering the evacuated pipe undergoes flash evaporation creating a vapor cushion in front of the liquid that mixes with the residual inert gas in the pipeline. In addition, the desorption of the dissolved pressurizing gas strongly affects the pressure wave characteristics, such as peak, frequency and attenuation.

In this research work an extensive experimental campaign is carried out in a dedicated test facility which allows to test in the same conditions as the operating space system. The influence of several parameters such as pressurizing condition, material and geometry is intensively investigated, as well as the effect of different operating conditions such as tank pressure, line pressure and test fluid (water and ethanol). The most important fluid properties are identified and their influence on the different physical processes involved in priming are evaluated. The differences in the pressure wave between water and ethanol is also analyzed with respect to their fluid properties. Among the key-parameters used to describe the flow, the speed of sound is found to play a crucial role since its value affects both the pressure peak and the wave frequency. However its assessment is not an easy task due to rapidly changing flow conditions. Phenomena such as cavitation and gas desorption create strong gradients in the fluid which make the speed of sound, as well as other quantities, both time and space dependent. Flow visualizations is a valuable support for the correct interpretation of the flow behavior. Image analysis allows to characterize the flow pattern and to examine the evolution of the two-phase/two component flow.

Understanding the flow evolution in the feedline system during the start-up is important not only for a safe design of the system but also to improve the numerical modeling. The obtained experimental data are used to validate numerical simulations performed with EcosimPro/ESPSS. The validation focuses in particular on the gas desorption model and on the unsteady friction model. Including these sub-models in the equations leads to a significant improvement in the wave prediction.

Further possible development of sensitive parameters is proposed and others important effects to be considered, such as the bubble dynamics, are suggested.

Kurzfassung

Während des Starts des Antriebssystems eines Satelliten oder eines Raumfahrzeugs wird durch das Öffnen des Tankabsperrventils der Treibstoff in eine evakuierte Leitung strömen und gegen ein geschlossenes Ventil schlagen. Dieser Füllprozess, auch Priming genannt, kann zu starken Druckspitzen führen, die zu einem strukturellen Versagen führen können. Bei einem Monergol wie Hydrazin muss auch die Gefahr einer adiabatischen Kompressionsdetonation berücksichtigt werden. Das Phänomen des Primings beinhaltet komplexe Aspekte von Zweiphasenströmungen: Flashverdampfung, Kavitation, Kondensation und Mischung der Treibstoffe mit dem restlichen Inertgas in der Leitung. Darüber hinaus hat die Desorption des gelösten Bedrückungsgases einen starken Einfluss auf die Druckwellencharakteristiken wie Druckspitze, Frequenz und Dämpfung.

In dieser Forschungsarbeit wurde eine umfangreiche experimentelle Kampagne in einer Testanlage durchgeführt, die es erlaubt, unter den gleichen Bedingungen wie im Antriebssystem zu testen. Der Einfluss verschiedener Parameter wie Bedrückungsbedingungen, Material und Geometrie der Leitung wird ebenso intensiv untersucht wie der Einfluss unterschiedlicher Betriebsbedingungen wie Tankdruck, Leitungsdruck und Testmedien (Wasser und Ethanol). Die wichtigsten Fluideigenschaften wurden identifiziert und ihr Einfluss auf die verschiedenen physikalischen Prozesse des Primings bewertet. Unter den Schlüsselparametern, die zur Beschreibung der Strömung verwendet werden, spielt die Schallgeschwindigkeit eine entscheidende Rolle. Die Bewertung ist aber keine leichte Aufgabe: Phänomene wie Kavitation und Gasdesorption erzeugen starke Gradienten in der Flüssigkeit, die die Schallgeschwindigkeit, sowie andere Größen, zeit- und raumabhängig machen. Für eine bessere Interpretation des Strömungsverhaltens wurden Strömungsvisualisierungen realisiert. Die Analyse der optischen Aufnahmen erlaubt es, das Strömungsmuster zu charakterisieren und die Entwicklung der Zweiphasen-Zweikomponentenströmung zu untersuchen.

Das Verständnis der Strömungsentwicklung in Treibstoffleitungen während der Inbetriebnahme ist nicht nur für eine sichere Auslegung des Systems wichtig, sondern auch für die Verbesserung der numerischen Modellierung. Die gewonnenen experimentellen Daten wurden zur Validierung von numerischen Simulationen, die mit EcosimPro/ESPSS durchgeführt wurden, verwendet. Die Validierung konzentriert sich insbesondere auf das Gasdesorptionsmodell und auf das instationäre Reibungsmodell. Die Einbeziehung dieser Teilmodelle in die Gleichungen führt zu einer signifikanten Verbesserung der Vorhersage der Druckwelle. Mögliche Weiterentwicklungen von relevanten Parametern werden formuliert und zusätzliche zukünftig zu berücksichtigende physikalische Effekte, wie die Blasendynamik, werden vorgeschlagen.

Acknowledgments

Just like in football, no achievement is solely personal, but it is the result of a combined effort of all the team players. This PhD work is no exception: although the pain and suffering have been personal, I could have not crossed the finishing line without the help of many people along the journey.

First, rather than a mere acknowledgment for their technical support, I would like to thank all my colleagues and friends at DLR Lampoldshausen for the wonderful experience and the fantastic group we have built together. Just like in football, talented people alone are not enough to achieve something, it is the team spirit that makes the difference.

An excellent team needs an excellent trainer, therefore I would like to thank first my *Doktorvater* Prof. Dr. rer. nat. Michael Oschwald for his guidance and his continuous support. As head of the rocket propulsion department at DLR Lampoldshausen, he always made sure I had the best conditions to perform my research work. His suggestions have been valuable to improve my manuscript. My gratitude to Johan Steelant from ESA-ESTEC for reviewing the manuscript and the corrections proposed, and for the pleasant technical exchanges we have had during many conferences. I would also like to extend my gratitude to Prof. Dr. Ing. Dieter Moormann as committee chairman of my oral defense at RWTH AAchen.

A successful team needs a good captain, and I had the fortune to have a great captain, Chiara Manfletti, as my mentor. Chiara was the first person who mentioned this research opportunity to me and she has shown faith in my work since the beginning. Her curiosity and attention to the details made me consider every single aspect of my research work. Above all I wish to thank Chiara for her never-ending support, her precious advises and, equally important, her heat shield protection, which allowed me to focus on my work.

If the Sunday match is successful, a great deal of merit go the assistant coaches as well, whose work behind the scene during the week is equally fundamental. In fact, no experimental work is successful without skilled technicians. Therefore, I would also like to express my deep gratitude to Markus Dengler, Artur Waltz-Steinbach, Johann Fröse, Michael Zepmeisel and Manuel Hofmann, for their support in the construction of the test-bench and for fixing the not rare hardware problems. I extend my thanks to Bernard Knapp for his coordination of the technicians team and for ensuring me a prompt support during the test campaign preparation.

Among the many team players, I have to mention first my office mate Tobias Traudt: thank you for helping me in my first steps in the research world and the many scientific discussions we had. I enjoyed our amazing team work at the test-bench and the outstanding papers we published together. As an added value, I now know everything about car engine turbines, I'd like to think you know a little more

about football as well. To complete our M3 gang were Michael Börner and Andreas Rees. Our countless coffee breaks (aka KK break) and the non-scientific discussion have been essential to preserve our mental health in the long and dark days where nothing seemed to work. Not to mention our many unauthorized research projects, like the LN2 frozen fruit experiments, the rocket car, the lab laser games and more: I will miss that! And speaking of mood improvement measures, I will also miss the colorful anecdotes of Dr. Dmitry Suslov and his cheers to the weekend vodka.

Playing in the first team comes with the responsibility to train the youth team as well. During this PhD work I have supervised several students and I wish to acknowledge their contribution: my thanks to Gianluigi Somma, Johanne Batut, Tatjana Rösner, Dominik Meller, Nicolo' Cattaneo and Francesco Sacco .

What I really treasure at the end of this journey is not the mere personal satisfaction of accomplishing a PhD, but the great people I have met during this experience. I have had, and still have, the honor and privilege to share a special bond with many of my colleagues, a bond forged in the legendary Wohnheim, where generations of rocket scientists have passed through. Among them, the best ever, featuring Dr. Michele Negri, my best Italian buddy or *compagno di merende*; Dr. Justin Hardi, Dr. Samuel Webster and Dr. Scott Beinke, the proud Aussie gang; Dr. Stefan "Matty" Gröning, my first German teacher; Dr. Jan Deeken, the only German I can drink wine with; Enrico Behler and Mike Ziemßen, the buddies I can always count on for football and for a *Feierabendbierchen*; and the not yet Dr. but soon to join the club: Michael Börner, Dirkino Schneider, Michael Wohlhüter, Christian Hendrich and Wolfgang Armbruster. Thank you guys, it was a fantastic time together, a real band of brothers!

Not only brothers of course, how can I not mention my wonderful Kolleginnen and dear friends Anna Petrarolo, Janine Herdel and Sarah Dommers, in strict alphabetical order for obvious reasons. The team spirit would have been incomplete without you.

So many football metaphors, but finally comes the real one. Ein großes Dankeschön geht natürlich an meine Mannschaft: Spvgg Möckmühl, meine Stadt, mein Verein! Nicht nur für das wöchentliche Training und die unvergesslichen Sonntagsschlachten, sondern auch dafür, dass ich mich seit dem ersten Tag in einer neuen Stadt wie zu Hause fühle. Ich konnte mir keine bessere Mannschaft mit wunderbaren Teamkollegen wünschen, um meine professionelle Fußballkarriere zu beenden.

Infine, un grazie particolare alla mia famiglia, a mio papa' Michele, a mia mamma Giulia e a mia sorella Lara. Un pensiero speciale a mia nonna Michelina e a mio nonno Aldo.

Contents

List of Figures

List of Tables

Nomenclature

Symbols

A	cross-section area [m^2]
C_P	specific heat capacity [J/kg/K]
$C^\star$	Vardy's shear stress coefficient [-]
c	speed of sound [m/s]
c_k	coefficient for gas desorption
D	diameter [m]
E	Young's modulus [Pa]
e	wall thickness [m]
f	friction factor [-]
f	frequency [1/s]
G	gas properties coefficient
g	gravity acceleration [m/s^2]
H_{vap}	enthalpy of vaporization [J/kg]
K	compressibility modulus [Pa]
K_Γ	correction coefficient for gas desorption
k	gas polytropic index [-]
k_H	solubility coefficient in Henry's law
k_3	Brunone's friction coefficient [-]
k_4	correction coefficient [-]
L	length [m]
M	gas molecular weight [g/mol]
m	mass [kg]
OD	outer diameter [m]
P	pressure [Pa or bar]
R	ideal gas constant [J/mol/K]
R_p	dimensionless parameter for injection
r	bubble radius [m]
T	temperature [K]
t	time [s]
t	time coordinate [s]
V	flow velocity [m/s]
x	gas/vapor mass fraction [-]
x	spatial coordinate [m]

Greek Symbols

α	void fraction [-]
γ	gas adiabatic index
Δ	difference, increase
ϵ	wall roughness [m]
λ	thermal conductivity [W/m/K]
μ	fluid viscosity [Pa·s]
ν	Poisson ratio [-]
ρ	density [kg/m^3]
σ	surface tension [N·m]
τ	time constant [s]
Φ	two-phase friction multiplier [-]
ψ	coefficient for pipe anchoring [-]
Ω	source term [kg/s]

Dimensionless numbers

Ca	$\frac{P-P_{vap}}{\frac{1}{2}\rho V^2}$	Cavitation number
Fr	$\frac{V}{\sqrt{gD}}$	Froude number
Ja	$\frac{C_P \Delta T}{\Delta H_{vap}}$	Jakob number
Ma	$\frac{V}{c}$	Mach number
Oh	$\frac{\mu}{\sqrt{\rho \sigma D}}$	Ohnesorge number
Pr	$\frac{\mu C_P}{k}$	Prandtl number
Re	$\frac{\rho V D}{\mu}$	Reynolds number
We	$\frac{\rho V^2 D}{\sigma}$	Weber number

Subscripts

b	bubble
d	dissolved
$dear$	deareated
eq	equilibrium
eth	ethanol
f	fluid
g	gas

L	liquid
$line$	line (test section)
mat	material
max	maximum
mix	mixture
ncg	non-condensable gas
ref	reference conditions
sat	saturated
$tank$	tank
u	unsteady
vap	vapor
w	water

Acronyms

ATV	Automatic Transfer Vehicle (spacecraft)
CNES	Centre National d'Etudes Spatiales
DLR	Deutsche Zentrum für Luft und Raumfahrt
ESA	European Space Agency
ESPSS	European Space Propulsion System Simulation
FFT	Fast Fourier Transform
FOV	Fast Opening Valve
FSI	Fluid-Structure Interaction
GHe	Gaseous Helium
GN2	Gaseous Nitrogen
HEM	Homogeneous Equilibrium Model
HSI	High Speed Imaging
HWHM	Half Width at Half Maximum
LRE	Liquid Rocket Engine
MMH	Monomethylhydrazine
MV	Manual Valve
NASA	National Aeronautics and Space Administration
NCG	Non Condensable Gas
NTO	Dinitrogen Tetroxide (N_2O_4)
ONERA	Office National d'Etudes et de Recherches Aérospatiales
PMQ	Propulsion Qualification Model
UFM	Unsteady Friction Model(s)
UDMH	Unsymmetrical Dimethylhydrazine

Chapter 1

Introduction

1.1 Work motivations

Among chemical propulsion systems for space applications, the best performances are offered by liquid propellants which provide the highest specific impulse and allow thrust modulation and multiple restarts compared to their solid rocket system counterparts. The cryogenic propellants combination oxygen-hydrogen is widely used in main and upper stages thanks to its highest specific impulse and non-toxicity. Storable hypergolic propellants, either as a bipropellant or as a monopropellant system, are instead preferred for satellites and spacecrafts propulsion. They ensure a reliable ignition and offer advantages in terms of propellant thermal management, but are toxic and chemically aggressive. The requirement of a reliable ignition is mandatory to enable multiple restarts, increasing the mission flexibility. A reliable and safe start-up and shut-down procedure of a liquid rocket engine is of vital importance for the correct functioning of the engine itself. The definition of the valve opening and closing sequence is a delicate task since it involves complex fluid dynamic phenomena, among them the water hammer is one of the most important.

During the start-up of the propulsion system of a satellite or spacecraft, the opening of the tank isolation valve will cause the propellant to flow into an evacuated feedline and slam against a closed thruster valve inducing a pressure surge. This filling process, called priming, can cause severe pressure peaks that could lead to structural failure. In this respect, priming is a water hammer-like event, where the pressure wave characteristics such as peak, frequency and damping must be predicted for a proper design of the feedline subsystem. In addition to the classical well-known water hammer aspects however, the phenomenon of priming occurring in a spacecraft feedline presents some peculiarities. When a satellite or spacecraft is launched to space, for safety reasons, its propellant feedlines are evacuated or filled with a small amount of inert gas. Once in orbit, the tank isolation valve opens (usually a pyrotechnic valve, as sketched in Fig. 1.1) and the propellant entering the evacuated pipe undergoes flash evaporation creating a vapor cushion in front of the liquid that mixes with the residual inert gas in the line. In addition, during the storage in the tank the pressurizing gas is absorbed in the liquid and it will consequently desorb as the pressure drops from the equilibrium value, resulting in a time-dependent gas content. All these aspects make the priming process much

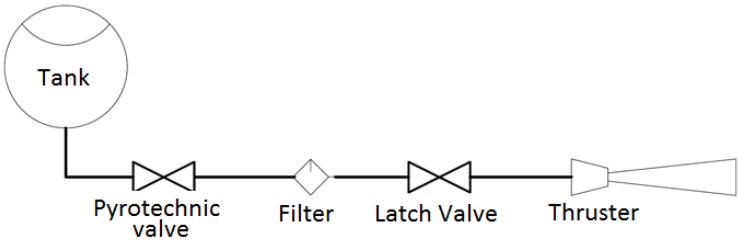

Figure 1.1: Simplified schematics of a satellite/spacecraft propulsion system

more complex than the classic water hammer and difficult to model numerically.

Another peculiarity is given by the fluids used in satellite and spacecraft propulsion systems. Storable hypergolic propellant combinations used typically are $N_2O_4 - MMH$ and $N_2O_4 - UDMH$, but their toxicity makes them difficult and costly to handle. In the case of monopropellants such as hydrazine, the risk of adiabatic compression detonation due to the high pressure surge during the priming is a hazard that must be taken into account.

Very few experiments are available in literature that match the specifications of a real spacecraft system, and most of them are not designed to properly investigate the physical phenomena of interest. Because of the complex two-phase flow aspects, numerical modeling is not a reliable tool yet. Therefore, in order to gain insight into the priming process with a focus on the aforementioned physical phenomena, in this research work it has been decided to undertake the problem experimentally by building a dedicated test facility which allows fluid transient experiments in the same conditions as the operating space system with a measurement technique specifically designed to achieve the research objectives.

1.2 Research objectives

The main objective of this research work is to investigate the physical behavior of the priming process, focusing in particular on the related two-phase flow aspects. Phenomena such as cavitation, flash boiling, gas desorption occur simultaneously and can lead to a very complex pressure profile as shown in Fig. 1.2. The effect of the operating conditions (tank pressure, line pressure, fluid) and the influence of different parameters (geometry, material, pressurizing gas) are also addressed in detail and evaluated. Flow visualizations by means of a quartz pipe with the support of high speed camera are performed to gain further insight into the two-phase flow pattern. Another aspect of interest is the fluid-structure interaction. Due to

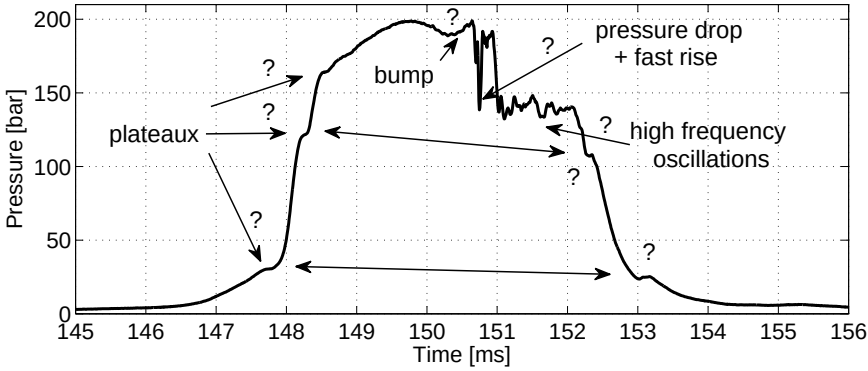

Figure 1.2: Detail of the first pressure peak at the dead-end during a typical priming test in vacuum: the pressure rise presents a surprising shape, the explanation of which is part of this work

the high pressure surge, the elasticity of the pipeline can not be neglected since it interacts with the fluid dynamic behavior, an effect known as Poisson coupling. To this purpose, strain gages and accelerometers are therefore included in the instrumentation. To carry out the experimental investigation, a new test facility is designed and built at DLR Lampoldshausen to reproduce as closely as possible the real operating space system. Water and ethanol are the test fluids, being the latter the best test replacement fluid for toxic MMH, in terms of fluid properties. A detailed analysis of which fluid properties are of importance and how to assess the behavior of a real propellant (NTO, MMH and hydrazine) based on the obtained tests results is also a goal of this work.

A second objective is to improve the numerical modeling of the design tools by developing dedicated sub-models of two important physical aspects: a) unsteady friction; b) gas desorption. In fact, the classical friction model are known to give not satisfactory results when applied to transient conditions, therefore an unsteady friction model is implemented in the code of the program used. A model for the gas desorption is also evaluated by calibrating empirical coefficients based on the test results. The software used to model the system is *EcosimPro* in conjunction with ESPSS library.

Finally, as an added value, the third objective is to provide an extensive experimental database of the priming phenomenon to be used both to validate numerical tools and to give the designer of the spacecraft feedline subsystem real data to be used as guidelines.

1.3 Structure of the thesis

The thesis is structured as follows:

Chapter 2 The priming phenomenon is briefly described, underlining similarities and differences with the classic water hammer upon valve closing. Physical aspects such as cavitation, flash boiling, gas absorption/desorption, fluid-structure interaction are presented and their related literature is provided. Previous works dedicated to priming in spacecraft feedlines are reviewed.

Chapter 3 The experimental facility is presented with a detailed description of the measurement techniques. In particular the design drivers are explained with respect to the scientific goals. The numerical model of the test bench and its set-up are also given.

Chapter 4, 5, 6 The experimental results obtained are analyzed with respect to the main distinguishing characteristics of a water hammer wave: peak (chap. 4), frequency (chap. 5) and attenuation (chap. 6). In the analysis, the effect of the boundary conditions such as tank pressure and line pressure, the effect of the pressurizing conditions and the effect of different geometries are evaluated. In particular, the differences between deareated and saturated liquid are underlined with the valuable support of high speed imaging. These findings are key-results of this thesis. The analysis includes numerical simulations, which are compared to the experimental data obtained. An unsteady friction model is implemented (chap. 6) and validated against test results.

Chapter 7 The flow evolution during the filling is investigated numerically. The flow pattern is described including a qualitatively comparison with the images obtained by the flow visualization.

Chapter 8 The results are summarized with respect to their implications and application to spacecraft feedline system design taking into account the start-up transient. This chapter provides some practical guidelines to help designers of feedline subsystems. An analysis of the importance of specific fluid properties is also presented.

Chapter 9 Conclusions are summarized and possible future work is suggested.

The use of high speed imaging will support the description wherever necessary to help the understanding, rather than to be used as a stand-alone chapter. In the same way, numerical simulations will be compared against test results throughout the chapters with particular focus on the gas desorption process and the modeling of unsteady friction.

Chapter 2

Physical Background and Literature Survey

2.1 Introduction

In this chapter, the relevant literature used to support this research work is presented. An introductory description of the priming process is given in order to underline the complex physics involved in this process. The similarities and differences with the classical water hammer upon valve closing are also highlighted. A necessary overview of the classical water hammer phenomenon is then given, together with the most important aspects on which today's researchers focus. Finally, a more detailed review of past studies focusing on priming in spacecraft feedline systems is provided, distinguishing the common engineering qualification tests from the more scientific investigations.

2.2 Description of the priming process in feedlines

In the feedline system of a satellite of spacecraft using toxic propellants such as hydrazine or MMH, three barriers are required for safety reasons. The configuration (Fig. 1.1) foresees three valves, more precisely a pyrotechnic valve, a latch valve and a thruster valve are installed to protect the personnel against potential leakage during ground operations. In addition the propellant feedlines are usually evacuated prior to launch. Once in orbit, the start-up of the propulsion system of the satellite involves the opening of the pyrotechnic valve, causing the propellant to flow into the evacuated feedline and slam against the closed latch valve. This filling process, called priming, can cause severe pressure peaks that could lead to structural failure. In this respect, priming is a water hammer-like event, where the pressure wave characteristics such as peak, frequency and damping must be predicted for a proper design of the feedline subsystem. In addition to the classical well-known water hammer aspects however, the phenomenon of priming occurring in a spacecraft feedline presents some peculiarities. The propellant entering the evacuated pipe undergoes flash evaporation creating a vapor cushion in front of the liquid that mixes with the residual inert gas in the line. In particular conditions cavitation may also occur and bubble dynamics can not be neglected. Moreover, the pressurizing gas dissolved in the liquid during the storage in the tank will des-

orb making the flow not only two-phase but also two-component. All these aspects make the priming process rather complex and difficult to model numerically. Some of these physical phenomena are well-known problems in water hammer literature and will be presented in the next section.

2.3 Water hammer overview

Water hammer[1] is a pressure surge occurring in a fluid system as a result of a change in the flow velocity. This is commonly experienced upon a sudden valve closing, usually accompanied by a loud banging resembling a hammering noise. The overpressure increase ΔP due to a change in flow velocity ΔV is given by the well-known Joukowsky equation [110]:

$$\Delta P = -\rho c \Delta V \tag{2.1}$$

where ρ is the fluid density and c is the speed of sound in the liquid. Changes in flow velocity can be due to the rapid closing or opening of valves, to the stopping or starting of pumps, or to a change in the boundary conditions of the system, e.g. caused by the ignition pressure peak in LRE combustion chamber. Water hammer is one of the most important fluid transient phenomena. The prediction of the pressure peak and wave shape is a fundamental task for the safe design of a fluid system in many technical situations, e.g. nuclear power plants, chemical and petroleum industries, and generally any fluid network system. In the space propulsion industry it is a major issue during the operation of a liquid rocket engine, where the multiple valve opening and closing induce transient conditions. Pressure peaks generated upon water hammer can be one order of magnitude greater than the initial fluid pressure in steady conditions, and must be considered in the design of the pipeline. Water hammer not only causes high pressure peaks, but also low pressure regions. If the pressure drops below the vapor pressure of the liquid, vapor bubbles form, a phenomenon known as cavitation.

The frequency of the water hammer pressure wave is also an important parameter. In case of single phase flow, the frequency can be easily estimated by:

$$f = n\frac{c}{4L} \tag{2.2}$$

where L is the length of the pipeline and the index $n = 1, 3, 5, 7...$ gives the fundamental frequency ($n = 1$) and its overtones. In the acoustic theory, Eq. (2.2) represents the eigenfrequencies of an open-closed pipe. From a mathematical point

[1] in literature the more general term "fluid hammer" is also used

of view, this corresponds to the boundary conditions of constant pressure (at the tank) and zero flow velocity (at the closed valve).

A detailed description of the pressure evolution during the transient is usually done by numerically solving the water hammer partial differential equations [110]:

$$\frac{\partial P}{\partial t} = -\rho c^2 \frac{\partial V}{\partial x} \tag{2.3}$$

$$\frac{\partial V}{\partial t} = -\frac{1}{\rho}\frac{\partial P}{\partial x} - \frac{f}{2D} V\,|V| \tag{2.4}$$

where f is the steady friction factor and D is the pipe internal diameter. Equation (2.3) is another form of the continuity equation while Eq. (2.4) is the momentum equation. This set of hyperbolic partial differential equations is usually solved by the method of characteristics. The basic concepts of water hammer and general fluid transient problems can be found in the classical textbook of Wylie and Streeter [110]. A good review on water hammer with an historical background is given by Bergant et al. [10], while the state of the art of the current challenges is well presented by Ghidaoui et al. [35].

Single-phase water hammer is well understood and numerical models have reached a sufficient reliability. Two-phase flow is more complex. When cavitation and/or gas release occur, the formation of bubbles inside the liquid has the primary effect to dramatically change the speed of sound of the liquid. The presence of vapor and/or gas in the liquid can lead to several different flow patterns, each of them has a different behavior in terms of flow dynamics, mass and heat transfer and acoustics [103]. The modeling of cavitation and gas release during flow transient are two of the current challenges for a reliable prediction of water hammer [35].

In this section, the most important flow characteristics and physical processes involved in priming, but investigated so far only in water hammer events, will be presented with their relevant references in order to provide the necessary physical background. They are grouped as follows:

1. vaporous cavitation
2. gaseous cavitation
3. bubble dynamics
4. two-phase flow patterns
5. speed of sound in two-phase flow
6. fluid-structure interactions (FSI)
7. unsteady friction models (UFM)

2.3.1 Vaporous cavitation

When the fluid static pressure drops below the vapor pressure value, a vapor bubble forms in the liquid. This process is known as vaporous cavitation or simply cavitation. In a water hammer, two type of cavitation can be observed:

1. distributed cavitation, when tiny vapor bubbles appear in the fluid over an extended length of the pipe;

2. column separation, when the vapor cavities coalesce into a larger bubble occupying a large section of the pipe, usually at the valve.

As described by Kranenburg [50], these two conditions can be identified by the value of the local void fraction α: in case of distributed cavitation, values of α are very small ($\alpha \ll 1$), while in case of column separation α is close to 1. An excellent review of water hammer with column separation is provided by Bergant et al. [8].

An important feature of cavitation is that it could lead to a pressure peak higher than the Joukowsky pressure. It usually occurs on the second peak, upon cavity collapse. The collapse of a cavity induces a short-duration pressure pulse which is superimposed on the main pressure wave trace. The pressure directly caused by the cavity collapse might be less than the water hammer pressure generated at the valve closing, but the resulting (superimposed) pressure peak can exceed the Joukowsky pressure. The mechanism is explained in detail by Simpson [82] and it is sketched in Fig. 2.1.

Based on this effect, Bergant and Simpson [6] added a further distinction of cavitation scenario according to the maximum pipeline pressure: a) active column separation flow regime, where the maximum pressure at the valve is governed by the intensity of the short-duration pressure pulse (Joukowsky pressure exceeded); b) passive column separation flow regime, where the maximum pressure is the water hammer pressure before intense cavitation occurs. (i.e. Joukowsky pressure). The authors also underline that column-separation collapse is probably the most important source of very steep wave fronts.

Cavitation significantly affects the water hammer wave and the equations developed for pure liquid flow (Eq. 2.3, 2.4) are not valid in such scenario. The problem arises because the vapor cavities dramatically change the way the pressure waves propagate (i.e. the speed of sound is not constant nor uniform in the pipe) and localized vapor cavities may form at a boundary. For a proper modeling of cavitation during flow transient additional set of equations must be taken into account to describe the physical state of the fluid: two-phase flow equations for a liquid-vapour mixture, shock equations for condensation of liquid-vapour mixture and equations for a discrete vapor cavity. A good description of the mathematical models can be found e.g. in the works of Bergant and Simpson [6, 81]. Among them, it is worth

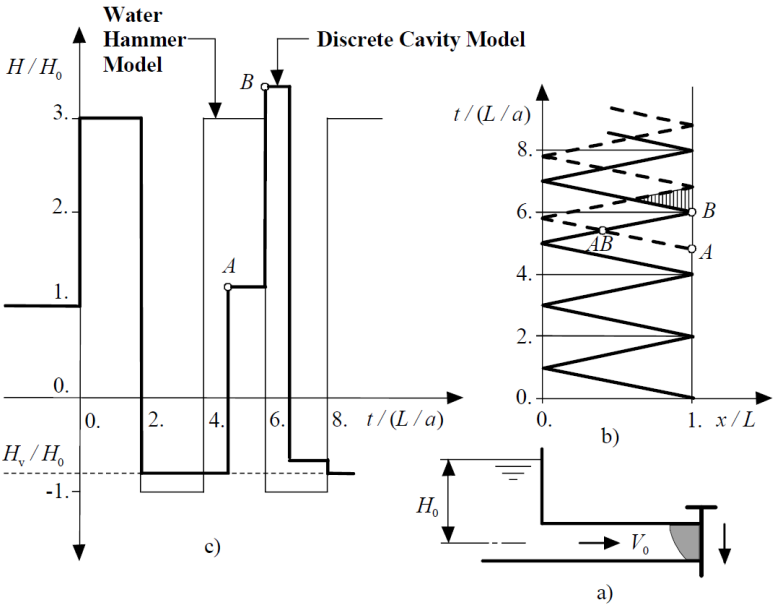

Figure 2.1: A short-duration pressure pulse due to cavity collapse can lead to pressure peak higher than Joukowski (point B) as a consequence of the superposition of the cavity-collapse pressure and the pressure wave reflected from the reservoir. The diagram is adapted by Bergant [8], originally from Simpson [82].

citing the discrete vapor cavity model (DVCM), which is the most commonly used model for column separation implemented in water hammer commercial software. The model allows vapor cavities to form at any computational node in the method of characteristics when the pressure drops to the liquid vapor pressure. A modified version of DVCM has been recently proposed by Adamkowski and Lewandowski [2].

An important consideration in cavitation events is to predict how the microscopic vapor cavities form. To this purpose the concept of nuclei was introduced [92]. Basically, a nucleus is a “hole" of molecular dimension in the liquid which may grow into macroscopic bubbles under moderate liquid tensions. Nuclei might be tiny gas bubbles, solid particles in the stream (e.g. dust, contaminants or impurities in general) or gas-filled pockets in the crevices of the pipe wall or the vessel.

Concerning LRE applications, very few studies are available dealing with water hammer upon downstream valve closing (not priming). Among them only one reference investigates the cavitation event. The work of Traudt et al. [91] analyzes

the cavitation scenario in a LRE feedline system mock-up. In the tests, the authors measured a second pressure peak 25% higher than the first peak, confirming that the maximum pressure is not necessary the Joukowsky pressure in case of cavitation.

An interesting example of how cavitation can be extremely costly if not taken into account occurred during the inaugural launch of Delta 4-Heavy rocket on the 21 December 2005. The RS-68 engines suffered a premature shutdown caused by fluid cavitation in the liquid-oxygen feed system. Cavitation originated at the entrance to the propellant feedline, where a filtration screen and elbow turn restricted the flow as it accelerated leaving the tank. As the tank drained, conditions at the inlet worsened, causing the cavitation to extend down the feedline until it reached and triggered the liquid depletion sensors, initiating engine shutdown. As a result, the payload was released in a lower than intended orbit [41].

Flash evaporation

During priming, the pipe downstream of the fast opening valve is under vacuum condition. As the valve opens, the liquid will undergo intense boiling, since the downstream pressure is lower than the fluid vapor pressure. This physical process is referred to as flash evaporation or flash boiling or simply flashing. It is a fundamental process in many practical applications, such as spray atomization and fuel injection system. Because of its importance it is widely investigated and the related literature is vast. Flash boiling is a common event of cryogenic propellants when injected in a LRE combustion chamber during the engine start-up, since cryogenic fluids are stored near their saturation point and/or the the combustion chamber is in vacuum condition as in the case of upper stage engines. For application in LRE injection systems, a good overview is given e.g. by Lamanna et al. [52]. Although the physics is of course the same, the flash boiling occurring during priming presents some characteristics that would not allow a straightforward comparison with the results available in literature. First, in flash evaporation for injection applications, the injectors (or nozzles) have typical diameters of < 1 mm, and the superheated fluid is sprayed in a chamber with a much larger diameter, so that the chamber wall does not affect the flashing behavior[2]. This condition is totally different in the priming process, where the valve seat has a similar diameter as the pipe. Consequently, the spray angle, which is an important parameter in characterizing the injection behavior, can not be defined in the priming process. Another key-parameter is the injection velocity, whereas in priming the fluid has an initial null velocity and accelerate progressively, therefore a proper Reynolds number can not be defined. For all these differences, the results available in literature concerning flashing can not be directly applied to priming.

[2] in a real injector head, there is also a mutual interaction of the injectors close to each others

A major difference between flash evaporation and cavitation is that in flashing the temperature change is higher and can not be neglected. Brusiani et al. [21] underlined that cavitation is pressure-driven, and flashing is in addition also temperature-driven. In a subcooled fluid, bubble formation is usually faster in cavitation, while in flashing the thermal transport effect will cause a delay [73]. From a physical point of view, a further distinction can be pointed out. In cavitation events, the cavitation number is usually introduced to characterize the flow:

$$Ca = \frac{P - P_{vap}}{\frac{1}{2}\rho V^2} \tag{2.5}$$

When flashing occurs, the fluid temperature also changes because the high energy required for boiling is taken from the fluid internal energy (its temperature). To describe the phase change during flashing the Jakob number is used:

$$Ja = \frac{C_{P,L}(T_L - T_{vap})}{\Delta H_{vap}} \tag{2.6}$$

which involves the two fluid properties heat capacity C_P and latent heat of vaporization ΔH_{vap}.

2.3.2 Gaseous cavitation (gas desorption)

The solubility of a gas into a liquid is described by Henry's law, which states that the amount of dissolved gas is proportional to its partial pressure P_g:

$$x_d = P_g / k_H \tag{2.7}$$

where the concentration x_d is usually measured in mg/kg or mol/mol. The proportionality factor k_H is called the solubility coefficient and depends on the temperature and also slightly on the pressure, so that the concentration of a gas is not rigorously linear with the pressure. The amount of dissolved gas in a liquid usually decreases with increasing temperature of the solution. Tables 2.1,2.2 list the solubility values of nitrogen and helium in water and ethanol, as found in several references.

The values found in literature present a small scatter. In this work the following values of dissolved gas amount are used for the analysis:

- nitrogen:
  - in water, x_d: 20 mg/kg and 380 mg/kg respectively at 1 and 20 bar
  - in ethanol, x_d 220 mg/kg and 4200 mg/kg respectively at 1 and 20 bar
- helium in water, ethanol: as from Table 2.2 (reference [112]), at 20 bar the values are assumed as 20 times higher

Nitrogen solubility

water		ethanol	
1 bar	20 bar	1 bar	20 bar
19.6 mg/kg [84]	380 mg/kg [84]	152 mg/kg at 298 K [32]	4200 mg/kg at 298 K [32]
21.5 mg/kg at 288 K [5]		220 mg/kg [5]	
20.8 mg/kg [90]		223 mg/kg [90]	
19 mg/kg [47]			

Table 2.1: Solubility of GN2 in water and ethanol. Reference temperature is 293 K (20 °C) if not specified differently.

Helium solubility

water		ethanol	
1 bar	20 bar	1 bar	20 bar
1.7 mg/kg (±2%) at 298 K [112]	not found	6.8 mg/kg [112]	not found

Table 2.2: Solubility of GHe in water and ethanol

In terms of kinetics, the solution of a gas into a liquid (dissolution or absorption) is a slow process. It can take several hours, depending on the surface contact area and the tank size [57]. Much faster is the opposite process, the desorption or gas release, also named gaseous cavitation. When the liquid pressure drops below the gas saturation equilibrium pressure ($P_{g,sat}$), the dissolved gas is released out of the liquid. It is the same effect when opening a soda bottle. The desorption rate describes how fast this process is, i.e. the amount of gas released out of the liquid per unit time. The desorption rate depends on several parameters, such as the degree of agitation of the fluid (i.e. the turbulence of the flow), the solubility coefficient k_H, the degree of supersaturation, the void fraction and the molecular bounds of the two components. Since the precise equation is rather complex, a more practical expression was proposed by Street and Wiley [110]:

$$\dot{m}_d = c_k(P_{g,sat} - P) \tag{2.8}$$

where the parameter c_k is an empirical coefficient which includes the aforementioned parameters. Equation (2.8) is valid for $P_{g,sat} < P$. When the instantaneous fluid pressure P exceeds $P_{g,sat}$, gas release ceases and theoretically the gas starts dissolving back into the liquid until the new gas saturation equilibrium pressure is reached. In practical fluid transient situations, the process of dissolution is neglected due to

its longer time scale, so that a one-way process can be assumed [107, 110]. This is also referred to as rectified diffusion.

The value of c_k is rather difficult to assess and it is usually estimated by experimental trial and error since a proper theoretical formulation is still lacking. No data are available for the typical storable propellants used in rocket engines, such as MMH, hydrazine, NTO and ethanol. Lema [55], based on his experimental results, assumed that the desorption rate of GN2 in ethanol is faster than in water.

Plesset [70] analytically calculated the rate of rectified diffusion under the assumption that the diffusion coefficient D can be related to the liquid viscosity μ. By means of a dimensional analysis, Plesset assumed that the rate of diffusion is proportional to:

$$\dot{m}_d \propto D x_c \rho_L / \rho_g \tag{2.9}$$

where x_c is the concentration of the dissolved gas in the liquid (dimensionless by mass, kg/kg). Plesset applied the Stokes–Einstein equation for diffusion in a solution at low Reynolds number to show that $D \propto T/\mu$. Considering the same temperature and pressure, the ratio between the diffusion in two different liquids is:

$$\frac{c_{k,2}}{c_{k,1}} = \frac{D_2 x_{c,2} \rho_{L,2}}{D_1 x_{c,1} \rho_{L,1}} = \frac{\mu_1 x_{c,2} \rho_{L,2}}{\mu_2 x_{c,1} \rho_{L,1}} \tag{2.10}$$

Substituting the values of ethanol and water, the diffusion rate in ethanol with respect to the rate in water is about 7 times higher.

The effect of gas release during fast transients has been investigated both experimentally and numerically. Wiggert and Sundquist [107] run a series of water hammer tests with air and CO2 dissolved in water. They concluded that the released gas clearly increases the wave attenuation and also lowers the wave frequency. This was also correctly simulated numerically by adopting in their model a gas release equation of the type of Eq. (2.8). They expressed $c_k = K_\Gamma k_H$, but nevertheless K_Γ was calculated by a trial and error procedure to fit the experimental data. Wiggert and Sundquist also pointed out that the dynamics of the gas mass transfer across the large cavity-liquid interface occurring upon column separation might be different from the diffusion process of small bubbles at dispersed sites in the fluid.

This very difference was numerically considered in the model implemented by Kranenburg [50], by adopting two different coefficients according to the type of cavitation. Kranenburg drew the same conclusion concerning the effect of gas release on the general pressure wave, but he remarked that in case of column separation the gas release has a greater effect than in case of dispersed cavitation. Perko [67] used an optical device to analyze the number and size of formed bubbles, showing that the release of gas is much higher at the wall due to the wall nuclei.

Lema [55] experimentally investigated the effects of gas desorption during priming in evacuated pipes. As for the previous researchers, the released gas adds damping and lower the pressure peak. The occurrence of the first pressure peak is slightly delayed and Lema justified this delay assuming that the released gas increases the flow friction, and thus slows down the liquid front.

2.3.3 Bubble dynamics

Cavitation, either vaporous or gaseous, causes the formation of bubbles in a liquid. These bubbles can grow, collapse and oscillate, affecting the general evolution of the flow. Such behavior is usually described by assuming the bubble radius $r(t)$ as the dynamic variable in the analysis, under the assumption of spherical bubble. The evolution of the bubble radius in the absence of mass transport across the interface bubble/liquid (i.e evaporation or condensation) is described by the Rayleigh-Plesset equation (e.g. Brennen [16, page 48-54]):

$$\frac{P_{vap} - P_\infty(t)}{\rho_L} + \frac{P_g}{\rho_L}\left(\frac{r_0}{r}\right)^{3k} = r\frac{d^2r}{dt^2} + \frac{3}{2}\left(\frac{dr}{dt}\right)^2 + \frac{4\mu_L}{r\rho_L}\frac{dr}{dt} + \frac{2\sigma}{r\rho_L} \tag{2.11}$$

where $P_\infty(t)$ is the external pressure acting on the bubble (liquid pressure infinitely far from the bubble which is assumed as a boundary condition) and P_g is the partial pressure of the gas inside the bubble assumed to be known. As initial condition, the bubble radius r_0 corresponds to the equilibrium state at a pressure $P_\infty(0)$, which is the balance of forces between the internal pressure and the surface tension: $P_{vap} + P_g - P_\infty(0) = 2\sigma/r_0$. If the external liquid pressure decreases, the bubble will grow, while in the opposite case collapse will occur. The behavior of the gas is modeled by the exponent k, so that $k = 1$ implies a isothermal bubble dynamics and $k = \gamma$ would model adiabatic behavior. Equation (2.11) can be integrated numerically and typical solutions for different initial/boundary conditions can be found e.g. in the textbook of Brennen [16]. For a step function change of the pressure, an analytic solution of the Rayleigh-Plesset equation exists and some interesting characteristics of the bubble behavior can be described. This is of particular interest for this work, as the water hammer is indeed a step pressure change in the flow. Expressions for the minimum radius, the corresponding maximum pressure and temperature of the gas in the bubble, the bubble collapse velocity and collapse time, the frequency of the oscillations, etc. can be analytically derived (see again Brennen [16]). Among them, it is useful for the later discussions to report the bubble collapse time t_b:

$$t_b = 0.915\sqrt{\frac{\rho_L r_0^2}{P - P_{vap}}} \tag{2.12}$$

This collapse time was first calculated by Rayleigh [74], assuming absence of both surface tension and gas content. Bubble collapse is a particularly important subject because of the noise and material damage that can be caused by the high velocities, pressures and temperatures resulting from that collapse.

The Rayleigh-Plesset equation allows to describe the response of a bubble to oscillations in the external pressure. When bubbles are disturbed, they pulsate (that is, they oscillate in size) at their natural frequency, which can be calculated by the following equation [16, page 198]:

$$f_b = \frac{1}{2\pi r_0}\sqrt{\frac{3\gamma\left(P_0 - P_{vap}\right)}{\rho_L} + \frac{2(3\gamma - 1)\sigma}{\rho_L r_0} - \frac{8\mu_L^2}{\rho_L^2 r_0^2}} \tag{2.13}$$

For large bubbles, surface tension and thermal conductivity can be neglected so that adiabatic pulsation can be considered, which means that no heat is transferred either from the liquid to the gas or vice versa. In literature, typical values of bubble natural frequencies are given in the range of 5-25 kHz [16, page 200].

Bubble cloud When the concentration of bubbles in a flow exceeds some small value, the bubbles will begin to have a substantial effect on the fluid dynamics [108]. In these conditions, rather than analyzing the dynamic of a single bubble, the whole bubble population is considered. It is usually referred to as bubble cloud. Among the earliest investigations of the dynamics of bubble clouds are the works of van Wijngaarden [108, 109]. Because of the strong non-linear effects, the subsequent dynamic behavior of the bubble cloud is quite different from that of a single bubble. For example, the natural frequencies of the cloud are smaller than the individual bubble frequencies [108] :

$$f_{cloud} = f_b\left(1 + \frac{4}{3\pi^2}\frac{r_{cloud}^2}{r_0^2}\frac{\alpha}{1-\alpha}\right)^{-0.5} \tag{2.14}$$

where α is the void fraction of the liquid-gas mixture. Equation (2.14) was derived under the assumption of homogeneous bubbly mixture.

An important effect of bubble cloud dynamics on the behavior of a homogeneous bubbly flow is the formation of shock waves. The collapse of a cloud of bubbles induces the formation and propagation of a shock wave and this is usually accompanied by an enhancement of the noise and damage potential since the collapse can be more violent than that of individual bubbles [16, 109]. This effect might be of importance for priming, since the presence of gas, due to the desorption of the dissolved gas and the initial residual one, is quite relevant and would make the flow tend to the bubbly pattern.

2.3.4 Two-phase flow patterns

While a single-phase flow is characterized by its Reynolds number which determines e.g. laminar or turbulent regime, a two-phase flow is classified according to the liquid/gas distribution. Different flow structures or patterns can occur depending on the size and orientation of the pipe, on the magnitudes of the gas and liquid flow parameters and on the fluid properties of the two phases. Several flow patterns have been defined by various researchers and the corresponding literature is vast. A good overview can be found in the classical handbook of Hewitt [40]. Horizontal two-phase flow exhibits flow patterns different from those in vertical two-phase flow because the distribution of the liquid is influenced by gravity which acts perpendicularly to the flow direction. In general, most flow patterns in horizontal tubes show a non-symmetrical structure, which is due to the effect of gravity on the different densities of the phases. This generates a tendency toward stratification in the vertical direction, with the liquid having a tendency to occupy the lower part of the channel and the gas, the upper part. Figure 2.2 shows the most commonly observed flow patterns for gas-liquid flow in a horizontal tube.

Important flow characteristics such as heat transfer and pressure drop are depending on the flow regime, therefore various approaches have been developed to predict two-phase flow patterns. Theoretical, numerical and empirical models have been produced over the decades by various investigators and operators. The models based on experimental data have resulted in empirical correlations that have some degree of success in predicting the two-phase flow regime [23]. For a more practi-

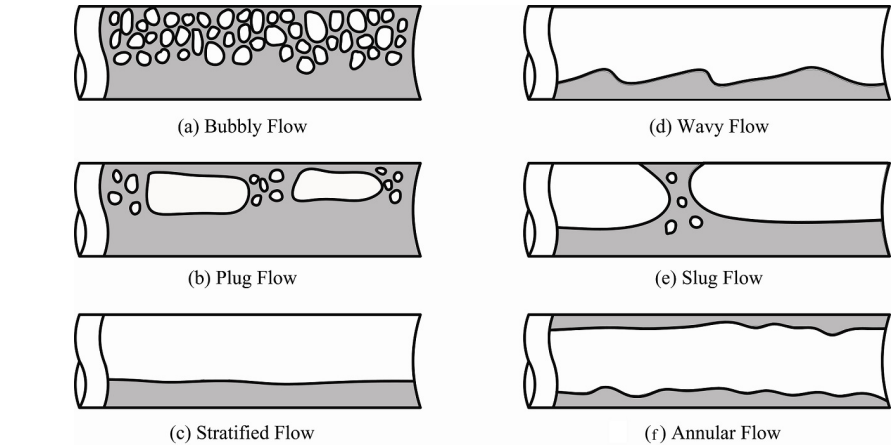

Figure 2.2: Two-phase flow patterns in horizontal pipe flow, from Hewitt [40]

cal use, a number of graphic diagrams referred to as flow maps have been created. These diagrams allows to determine the actual flow regime based on flow dimensionless parameters. The most widely used flow pattern map for horizontal two-phase flow is Taitel and Dukler's map [85], shown in Figure 2.3. The axis coordinates are defined as follows:

$$X = \sqrt{\frac{(dP/dx)_L}{(dP/dx)_g}} \tag{2.15}$$

$$K = Fr \cdot Re_L^{0.5} \tag{2.16}$$

where X is the Martinelli parameter with (dP/dx) the frictional pressure gradient as if the liquid or gas in the two-phase flow were flowing alone in the tube; Fr is the Froude number modified by the density ratio $Fr = \sqrt{\frac{\rho_g}{\rho_L - \rho_g}} * \frac{u_g}{\sqrt{Dg}}$ and Re_L is the Reynolds number of the liquid. The determination of the actual two-phase flow pattern is also a crucial information to calculate the speed of sound of the mixture.

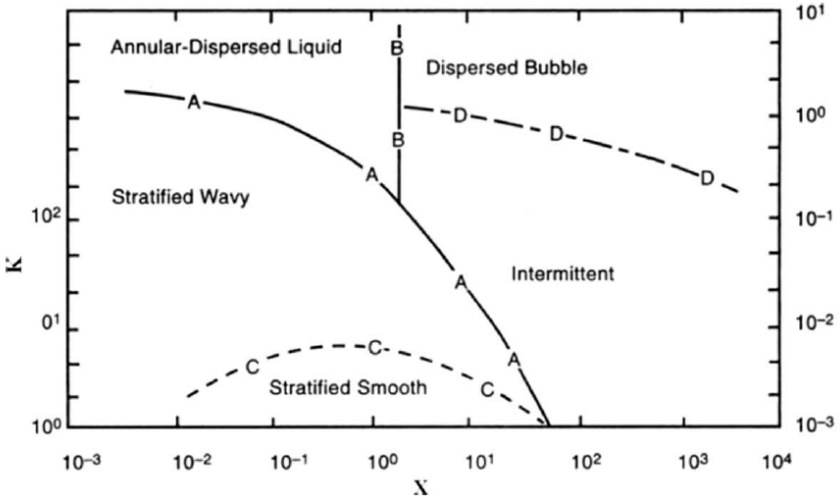

Figure 2.3: The Taitel and Dukler [85] flow pattern map for horizontal two-phase flows

2.3.5 Speed of sound in liquid-gas mixture

The presence of gas bubbles in a liquid can dramatically change some of the fluid physical properties which may become very different from the properties of either of the constituent phases. Among them, the speed of sound is strongly affected. For an incompressible fluid, the propagation velocity[3] of a small disturbance is given by the well-known Newton–Laplace formula:

$$c = \sqrt{\frac{K_L}{\rho}} \tag{2.17}$$

where K_L is the bulk modulus of elasticity of the liquid and ρ is the liquid density. Both these properties are slightly pressure-dependent, and therefore also the speed of sound is not constant with pressure as shown in Fig. 2.4.

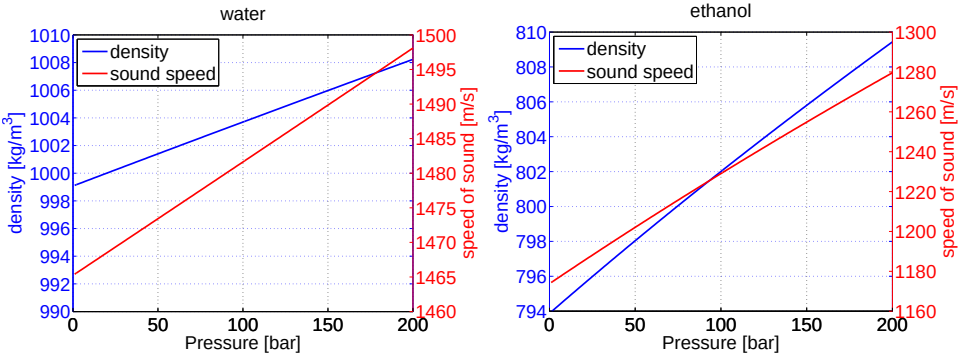

Figure 2.4: Variation of density and speed of sound with pressure, for water (left) and ethanol (right)

In a more general sense, for any fluid including liquid-gas mixture, the speed of sound is calculated as:

$$c = \sqrt{\frac{\partial P}{\partial \rho}} \tag{2.18}$$

Using a barotropic equation for water and gas of the form $P = P(\rho)$ and under some basic assumptions, a straightforward application of Eq. (2.18) allows to derive the speed of sound for a liquid-gas mixture (e.g. Brennen [16], Kieffer [48]):

[3] An interesting mathematical-physical analysis on the nature of the wave speed is discussed by Tijseeling and Vardy in "What is wave speed?" [87]

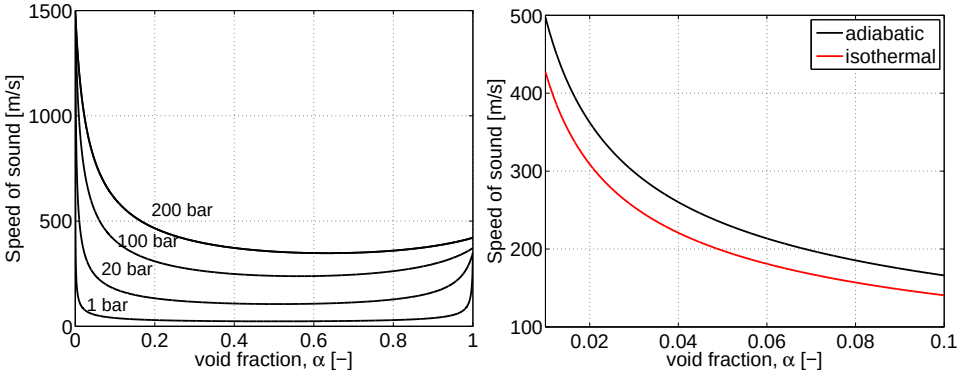

Figure 2.5: Speed of sound in water-nitrogen mixture as a function of the gas content at different pressure level (left). The difference in the speed of sound assuming isothermal vs adiabatic gas behaviour is plotted on the right, at P = 20 bar.

$$c = x\rho_L \left(\frac{G}{P}\right)^{1/\gamma} + \frac{\exp(\frac{P-P_0}{K_L})}{\left[(1+x)\,\rho_L \left(\frac{x\rho_L G^{1/\gamma}}{\gamma P^{(\frac{\gamma+1}{\gamma})}} + \frac{1}{E}\exp(\frac{P-P_0}{K_L})\right)\right]^{1/2}} \tag{2.19}$$

where x is the mass fraction of gas ($x = 0$ pure liquid, $x = 1$ pure gas), γ is the gas polytropic index and $G = T_0 R/M\rho_0^{\gamma-1}$, with R the ideal gas constant and M the gas molecular weight. A graphical representation of Eq. (2.19) is shown on the left of Fig. 2.5, where the more common void fraction α is used instead of the mass fraction, because void fraction is the natural variable of mixing theory. The first striking characteristic is that the speed of sound in a mixture is lower than the corresponding speed of sound in either the liquid or the gas alone. This non-intuitive characteristic can be understood by considering that the mixture is relatively easily compressed thanks to the presence of gas bubbles, whereas it remains relatively dense due to the dominant mass of liquid.

In a water-nitrogen mixture the speed of sound can reach values as low as 24 m/s for a void fraction $\alpha = 0.5$. A second important characteristic is that a very tiny amount of non-dissolved gas in the liquid can considerably lower the speed of sound. For example, for water at 1 bar, a GN2 presence of $\alpha = 6 \cdot 10^{-3}$ is enough to drop the value of the speed of sound to 150 m/s, one order of magnitude smaller than the one in pure liquid.

The speed of sound in a mixture depends also on the behavior of the gas, i.e.

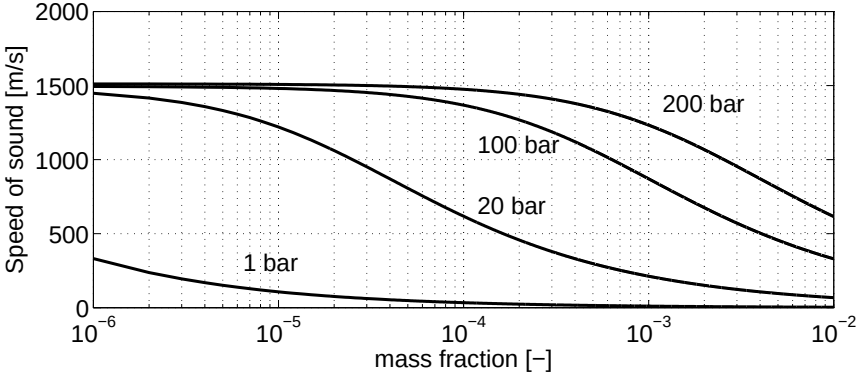

Figure 2.6: Speed of sound in liquid-gas mixture at different pressure levels as a function of the gas content expressed in mass fraction

the polytropic exponent γ. If the period of the compressions and rarefactions of the gas bubbles following the passage of the sound wave is smaller (faster) than time in which heat can be conducted from the gas to the liquid, the gas behaves adiabatically ($\gamma = 1.4$ for GN2, $\gamma = 1.66$ for GHe), whereas the process will be isothermal ($\gamma = 1$) in the opposite case. A comparison between the isothermal and the adiabatic sound speed is depicted on the right of Fig. 2.5. The wave speed of the mixture assuming isothermal gas behavior is slightly lower than the adiabatic case. This implies that there is a small dependency of the speed of sound on the excitation frequency because it causes a shift towards the adiabatic conditions. This is true at high frequencies, in the order of 10 kHz [108], but it can be neglected in the usual condition of a LRE feedline sytem as its acoustic frequencies are around 100 Hz. Therefore, in the present investigation the speed of sound is calculated as in isothermal conditions.

In many engineering applications, the mass fraction is used as a measure of the gas content, rather than the void fraction, because the mass fraction is invariant with surface tension and pressure. This is the approach adopted here, as the calculations of non-dissolved gas is simpler in terms of mass. For sake of completeness, the dependency of the speed of sound on the mass fraction is shown in Fig. 2.6.

Wave speed in separated flows The wave speed in a mixture as given by Eq. (2.19) is derived under the assumption of a homogeneous distribution of the gas bubbles in the liquid. Another typical two-phase flow pattern is the separated flow, where the liquid and the gas occupy well-separated parts of the cross-section of a

pipe. This situation occur for instance in stratified flows and in annular flows. In such flows the wave speed is (e.g. Dijk [27]):

$$c^2 = c_L^2 \frac{\alpha + (1-\alpha)\frac{\rho_L}{\rho_g}}{\alpha + (1-\alpha)\frac{\rho_L c_L}{\rho_g c_g}} \tag{2.20}$$

where c_L and c_g are the speed of sound in water and gas respectively. As it can be seen in Fig. 2.7, in separated flows the wave speed of the mixture is always between the values of the two phases, unlike the homogeneous case.

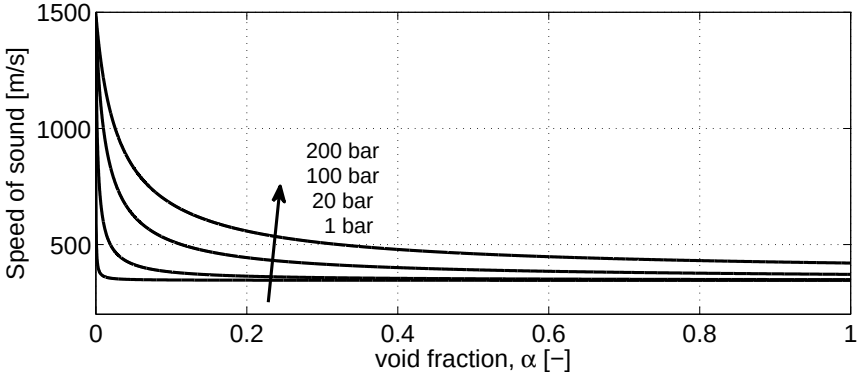

Figure 2.7: Speed of sound in separated flow of water-nitrogen as a function of the void fraction

Effect of the surface tension For small bubbles, the pressure in a gas bubble P_g is no longer equal to the pressure in the surrounding liquid P_L, but exceeds it by a margin depending on the magnitude of the bubble radius r, according to the expression:

$$P_g = P_L + \frac{2\sigma}{r} \tag{2.21}$$

where σ is the surface tension. McWilliam and Duggins [60] derived the speed of sound taking the surface tension into account:

$$c^2 = \frac{3A^2B - CD}{3A^2E - CF} \tag{2.22}$$

where:

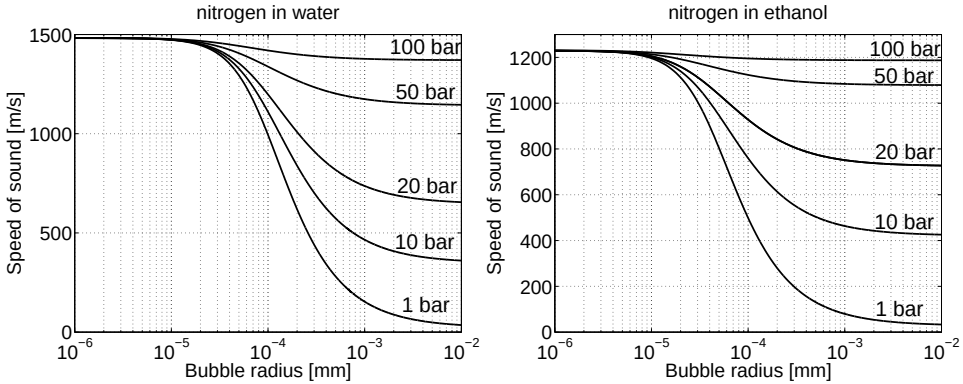

Figure 2.8: Effect of the surface tension on speed of sound. The non-dissolved GN2 amount is $\eta = 10^{-4}$.

$$\begin{cases} A = \frac{2\sigma}{R} \\ B = \frac{1+x}{\rho_L x G} \left(A + P\right)^2 \\ C = 32\pi x \sigma^3 / 3M \\ D = \gamma / xG \\ E = \exp\left(\frac{P_{ref} - P}{K_L}\right) \left(A + P\right)^2 / (K_L \rho_L x G) + 1 \\ F = \left(E - 1\right) / xG \end{cases}$$

Figure 2.8 shows the effect of the bubble radius when surface tension is taken into account, for the case $x = 10^{-4}$. Three regions can be distinguished: (1) if the bubble radius is smaller than 10^{-5} mm the speed of sound is independent of both bubble size and pressure, meaning that the surface effect cancels the two-phase nature of the flow in terms of wave speed; (2) if the bubble is higher than 10^{-2}mm the speed of sound is constant and equal to the value obtained neglecting surface tension effects, it depends only on the pressure; (3) an intermediate region where the speed of sound depends on both bubble size and pressure. The limits of these regions depend on the gas mass fraction x.

Wave speed in single-component, two-phase In comparison to a two-phase two-component system, such as water-air, the calculation of the wave speed in a single-component two-phase (e.g. water-steam) is more difficult because the pressure and temperature are not independent variables. The difficulty arises because mass transfer between the phases occurs (i.e. condensation or evaporation). The expression of the speed of sound in a single-component, two-phase system has been

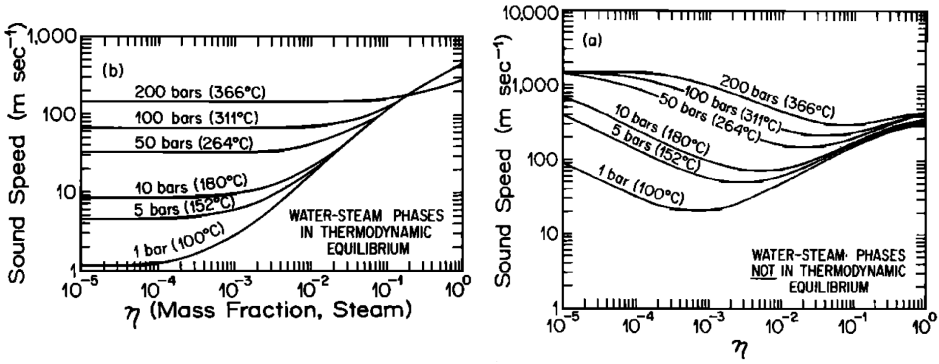

Figure 2.9: Speed of sound in water-steam, from Kieffer [48]

derived by Davies [25]. The equation is rather complex and it requires the knowledge of the thermodynamic derivatives. In addition, one must distinguish between equilibrium and non-equilibrium. The conditions of equilibrium exist if the mass transfer occurs faster than the acoustic wave period [48]. Figure 2.9 shows the speed of sound in water-steam mixture with the phases in thermodynamic equilibrium (left) or not (right). As an interesting note, in case of water at 1 bar, for a very small fraction of vapor (liquid containing few vapor bubbles) the speed of sound drops to ~ 1 m/s.

Wave speed in an elastic pipe The speed of sound of a fluid in a pipe must take the pipe elasticity into account. In fact, the more general expression of the wave speed in a compressible fluid within a elastic pipe is (e.g. [35, 49, 110]):

$$\frac{1}{c^2} = \frac{\partial \rho}{\partial P} + \frac{\rho}{A}\frac{\partial A}{\partial P} \tag{2.23}$$

Korteweg [49] used the elastic theory of continuum mechanics to evaluate $\partial A/\partial P$, which includes the pipe diameter D, the wall thickness e and the Young modulus of elasticity E. In his derivation, he neglected the axial stresses in the pipe and the inertia of the pipe itself. Considering instead the axial stress (Poisson's effect), the resulting wave speed in a elastic pipe is (e.g. [35, 110]):

$$c^2 = \frac{\frac{K_L}{\rho_L}}{1 + \psi \frac{K_L}{E}\frac{D}{e}} \tag{2.24}$$

where the coefficient ψ depends on the anchoring type as follows:

1. $\psi = 1 - \upsilon^2$: fully anchored against axial movement;
2. $\psi = 1 - \upsilon/2$: upstream anchored only;
3. $\psi = 1$: with expansion joints throughout the pipe length.

In case axial stresses are not important ($\psi = 1$), Eq. (2.24) becomes the original formulation derived by Korteweg [49].

2.3.6 Fluid Structure Interaction

Fluid-structure interaction (FSI) in piping systems refers to the transfer of momentum and forces between the pipe and the liquid during unsteady flow. The interaction is manifested in pipe vibrations which in turn induce perturbations in the liquid pressure. In case of thin-walled pipe or not rigidly anchored structure, significant FSI may occur so that the dynamic behavior of the liquid and pipe system cannot be treated separately: interaction mechanisms have to be taken into account [88]. Three mechanisms can be observed:

1. friction coupling
2. Poisson coupling
3. junction coupling

Friction coupling is the classic wall friction between liquid and pipe. Poisson coupling is due to a radial expansion of the pipe induced by pressure in the fluid, which in turn induces a pipe radial contraction downstream through a traveling axial stress. The pipe radial contraction itself causes an increase of pressure in the fluid. This axial stress travels at the sound velocity of the material, which is greater than the sound velocity of the fluid, and Poisson coupling leads to precursor waves in the fluid, which travel in front of the water hammer wave. Junction coupling acts at specific points in a pipe system, such as bends, T-junctions, etc. A more detailed description of FSI effects can be found e.g. in Tijseeling [88] or Wiggert and Tijseeling [106].

When FSI effects are not negligible, additional terms must be included in the water hammer equations as well as axial stress-strain relationships to take the pipe dynamics into account. The simplest FSI model is a four equations model, where the structure and fluid dynamics are coupled. More complex model considering the axial, lateral and torsional vibrations exist, which lead to a 14 equations system [106]. The implementation of a FSI model in the software code is not part of this research work. Nevertheless, experimental evidence of FSI effects will be highlighted throughout this work whenever necessary to better assess the results.

To this purpose, an important remark by Tijsseling [88] has to be mentioned. Since in practice pipe systems are never completely rigid, FSI will always occur and the problem is then to judge when FSI is of importance. Based on a time scale analysis, Tijsseling and Vardy [89] suggested that FSI is important when the time-scale of the structural behavior is: (1) smaller than the time-scale of the liquid behavior and (2) larger than the time-scale of the excitation. In liquid rocket engine feedlines, including the present priming set-up, both these conditions can occur.

To summarize, FSI involves a coupled dynamics between the structure and the liquid. Pipe vibrations affect the fluid motion and vice-versa.

2.3.7 Unsteady friction models

In the case of single phase water hammer, the pressure peak and the frequency of the pressure wave are well simulated, while the attenuation of the wave is usually underestimated compared to the experimental data. A well-known reason for this mismatching is the use of the steady friction factor despite the transient conditions. A proper modeling of friction stresses existing during the transient is therefore of importance to correctly simulate the wave attenuation. It has been proved that unsteady friction models work much better in this regard [1, 9, 35, 102]. Unlike other technical situations, e.g. hydroelectric power plants, piping systems for chemical and oil industries, liquid rocket engines are characterized by much shorter pipelines, in the order of few meters, a range usually not investigated in literature. At such short lengths, the unsteady friction is even more important than in typical geometries because the wave traveling time is smaller than the relaxation time of the boundary layer [15, 29].

Several unsteady friction models (UFM) have been proposed. Zielke [113] analytically derived a frequency-dependent friction related to the weighted past velocity changes. Although Zielke's model is derived for laminar flows, it can be also applied to low Reynolds turbulent flows [93]. Brunone et al. [19, 20] developed a model where the unsteady friction term is dependent on the instantaneous local acceleration $\partial V/\partial t$ and on the instantaneous convective acceleration $\partial V/\partial x$, as stated by Eq. (2.25):

$$f_u = \frac{2D}{V^2} k_3 \left(\frac{\partial V}{\partial t} - c \frac{\partial V}{\partial x} \right) \tag{2.25}$$

This is known in literature as Brunone's model and its main advantages is its implementation simplicity. The parameter k_3 in Eq. (2.25) is an empirical coefficient which is usually calibrated by a trial and error procedure.

Storli and Nielsen [83] implemented a modified version of Brunone's model introducing two coefficients, one for $\partial V/\partial t$ and one for $\partial V/\partial x$, which are position-dependent. With this assumption they were able to achieve a more accurate pre-

diction in the case of water hammer upon downstream valve closing. The model proposed by Vardy and Brown [96] assumes a two-layer turbulent viscosity distribution: a uniform value in the core and a linear variation in the annulus (at the wall). They analytically deduced the empirical coefficient used in the Brunone's model, correlating the limit unsteady friction $f_{u,lim}$ to Brunone's coefficient k_3. The same authors proposed a similar analysis for fully rough pipe flow [98], showing that $f_{u,lim}$ is independent of Re but it is strongly dependent on the relative roughness k_s/D. Pezzinga [68] created diagrams of k_3 as a function of Re and k_s/D by combining quasi-2D and 1D analysis. These sort of Moody diagram-like charts clearly illustrate the dependency of k_3 on both Re and roughness. Silva-Araya and Chaudhry [80] developed a method for unsteady friction losses that can be applied to smooth-to-rough transition and fully rough pipe flows. A more detailed overview of UFM can be found in Ghidaoui et al. [35].

In 2003 Vardy and Brown proposed an updated model [97] of their first work in 1996 [96]. They introduced a limiting unsteady friction coefficient $f_{u,lim}$ which can be analytically calculated under the assumption of flow with (a) uniform acceleration and (b) small velocity changes. The analytic expression, for smooth pipe flows, is:

$$f_{u,lim} = 2\sqrt{C^\star} \tag{2.26}$$

where $C^\star$ is the shear decay coefficient which depends on the flow regime:

$$\begin{cases} laminar & C^\star = 0.00476 \\ turbulent & C^\star = \frac{12.86}{Re^{log_{10}(15.29/Re^{0.0567})}} \end{cases}$$

In addition, in the particular case of uniform acceleration, they proved that the limiting unsteady friction coefficient matches the Brunone's coefficient k_3, so one can write $k_3 = f_{u,lim} = 2\sqrt{C^\star}$.

In subsequent work of Bergant et al. [9, 101], the authors used the relationship $k_3 = \frac{1}{4} \cdot 2\sqrt{C^\star}$, where the factor $1/4$ has been introduced to take the acceleration and deceleration cycle of the flow during water hammer into account, since Eq. (2.26) has been originally derived for accelerating flow only. Vitkovsky [102] proposed an updated formulation of Brunone's model by introducing sign correction in order to take into account all the possible flow directions and positions of the valve:

$$f_u = \frac{2D}{V\,|V|^2} k_3 \left(\frac{\partial V}{\partial t} - c \frac{V}{|V|} \left| \frac{\partial V}{\partial x} \right| \right) \tag{2.27}$$

Although UFM are implemented in many water hammer commercial codes, the implementation of UFM in software for space propulsion systems analysis is still lacking, to the knowledge of the author, and it is an objective of this work.

2.4 Water hammer in spacecraft feedlines: previous studies

The high pressure peak generated during priming can lead to structural failure or to adiabatic compression detonation in case of monopropellants such as hydrazine. Therefore, priming and water hammer tests are always part of the qualification campaign of the propulsion subsystem of a satellite or spacecraft that uses storable propellants. At this point it is useful to distinguish, among the several references, the engineering testing from the more scientific works. A special section is dedicated to hydrazine.

2.4.1 Propulsion Qualification Model

As part of the qualification process of a spacecraft system, a flight-like mock-up of the full system or the real hardware itself undergoes static and transient hydraulic testing. While the static testing aims to assess the system characteristics such as pressure drops and mass flows, the transient testing includes a more or less complex procedure with multiple and simultaneous opening/closing of several valves. Complex systems might include up to 24 valves of the Reaction Control System or the Attitude Control System. The validation of the transient behavior is part of Propulsion Qualification Model (PQM). The available literature dealing with priming and water hammer testing of spacecraft systems is vast. Limiting the survey to the recent years only, one can find PQM results for any engine thrust class:

- smaller spacecraft such as the Exomars propulsion subsystem [53, 66] and the Lunar Lander [75]
- upper stage such as AVUM of the Vega rocket [13]
- relative large spacecraft such as the ESA ATV [43] and the European Service Module for Orion [61]

The collected data are also used to validate fluid transient numerical models. Nevertheless, these works aim to ensure that the pressure peaks never exceed the maximum expected operation pressure of the system, without focusing on the scientific aspects of priming.

Another set of references that might be included in the engineering context, is the work dealing with the countermeasures taken to hinder unacceptable high pressure peaks. This includes the use of either a flow restriction device (venturi [79] or orifice [45][63]) or the gas cushion effect. However, the addition of flow restriction devices may significantly increase the system pressure loss. Cavitating venturis are effective in constraining the flow rate while minimizing the pressure

loss during normal operation, as experimentally showed by Scroggins [79]. A trade study was also undertaken by Hearn [39] in order to determine the best approach to reduce the priming impact. The solution involved incorporating cavitating venturis at selected locations to constrain the maximum fluid flow rate while minimizing the pressure losses during normal operation. For some missions, 10 psi (0.7 bar) of gaseous helium is loaded into the propulsion subsystem downstream of the closed latch valves. This added gas acts as a "cushion" to the liquid front and proves to be an effective way to decrease the surge pressure [39].

2.4.2 Analytic Model

A preliminary estimate of the pressure peak induced by priming can be obtained through the rigid liquid column theory. It considers the fluid in pipelines as an incompressible liquid slug and analyzes its unsteady motion. The analytic model based on the rigid liquid column theory has been successfully applied to the priming process of a satellite propulsion system in several works [14, 39, 56, 72, 111]. The first model was proposed by Yaggy [111], who performed parametric studies of storage tank pressure, upstream and downstream line lengths, propellant (NTO and MMH) and friction factor. The assumptions of the analytic model can be found in any of the cited works. The main advantages is that the model results in a second order non-linear ordinary differential equation, which can easily be numerically solved. An important point remarked by all the authors is the sensitivity of the pressure peak on the friction factor: an educated choice of the friction is crucial in order to not over-estimate the pressure peak. This is especially important for complex pipe networks where the presence of several junctions causes friction losses not easy to predict.

2.4.3 Hydrazine testing: adiabatic compression detonation

Due to the fact that hydrazine is a monopropellant, it undergoes exothermic decomposition. In particular conditions this might trigger a fast chain reaction and lead to explosive decomposition. This effect is referred to as adiabatic compression detonation and it is one of the major risks associated with hydrazine. A hydrazine hammer during priming on a NASA satellite [28] almost led to a mission failure. A higher than expected water hammer peak caused the primary subsystem to fail and to switch to the backup subsystem.

Because of the detonation risk, several experimental investigations using hydrazine as a test fluid exist in literature. Briles and Hollenbaugh [18] are among the first who attempted to assess the conditions under which hydrazine can detonate. Their work was motivated by the use of hydrazine in the auxiliary power units of the space shuttle. They focused on the effect of high compression rate (up to 3400

bar/s) and material compatibility. No hydrazine detonation occurred in the given test conditions.

In a subsequent work, Briles et al. [17] used a diaphragm to separate the driving pressurizing gas from the liquid hydrazine so that the adiabatic compression occurring in the liquid is not affected by the shock wave forming in the gas upon compression. They concluded that the detonation threshold is lowered when the membrane is not present (as in the real systems) because of the formation of hydrazine vapor which can undergo compression ignition.

Hutchinson and Schmitz [44] designed an adiabatic compression test setup. They systematically varied the test conditions in particular the content of the downstream line, which was filled with different gases including hydrazine vapor. A detonation occurred for a initial system temperature of 90 °C, which destroyed the test set-up. They then built a second test setup where they were now able to achieve a better temperature control of the line by means of a water bath. They concluded that a local hot spot caused hydrazine to detonate.

Bunker et al. [22] carried out further assessment on the explosive decomposition of hydrazine by rapid compression of a gas volume. In their experiments a transparent pipe was used and high speed imaging was performed. They observed a foam of nitrogen bubbles in liquid hydrazine and postulated that the compression wave generated by the water hammer adiabatically heats the bubbles. This heat is in turn transferred to the surrounded liquid hydrazine and triggers the thermal decomposition. Their results also indicated that a pressure surge of 170 bar can be taken as the threshold over which hydrazine decomposition starts.

The assessment of hydrazine detonability criteria is still the focus of on-going efforts [95]. Among the key-parameters, the pressurization rate and the compression ratio seem to play a major role. A detonation factor was proposed by ESA [95] based on the compression ratio of the initial gas and corrected by several semi-empirical correction factors. The detonation factor is to be compared to a given threshold in order to define a pass/fail criteria for hydrazine detonation. Adiabatic compression detonation is also an issue for the new generation of green propellants under development, which aim to replace the toxic hydrazine.

2.4.4 Scientific investigations of priming

Finally, a more circumscribed group of references dealing with the scientific aspects involved in priming is hereafter presented.

Gibec and Maisonneuve [37] performed water hammer experiments (Fig. 2.10) with real propellants, namely MMH, NTO and hydrazine. They also changed the geometry of the test element, using straight, bend, elbow and tee pipes. In the case of the bend pipe, the reproducibility was poor. The authors hypothesized that phenomena such as cavitation, pipe deformation and vapor pressure may interfere

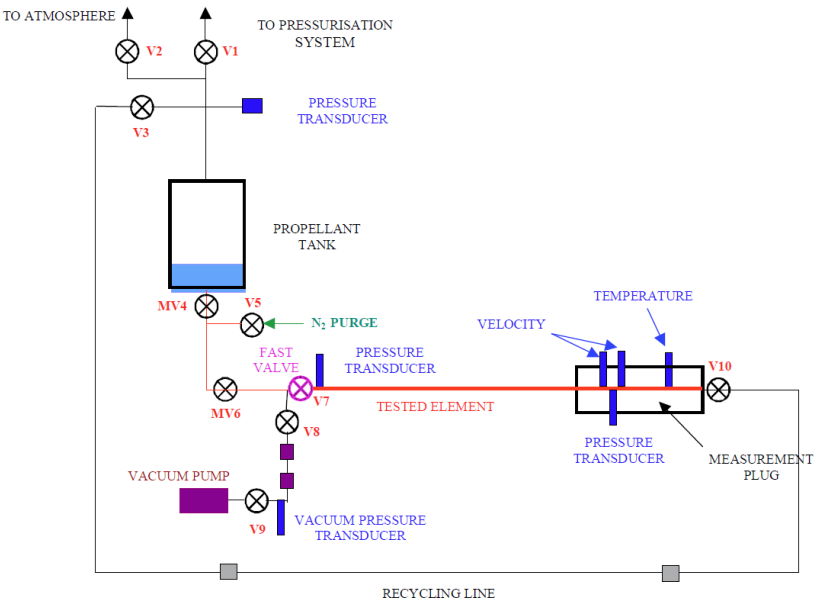

Figure 2.10: Experimental setup used by Gibec and Maisonneuve in 2005 [37] for priming test with MMH, NTO and hydrazine. The same setup was used by Lecourt and Steelant in 2007 [54] for ethanol, acetaldehyde and MMH.

with the water hammer process, but the instrumental apparatus did not allow to assess these hypothesis. In the case of hydrazine, the measured pressure peak was the highest for the highest initial line pressure, and a temperature increase of 23 °C was observed. The authors suspected that hydrazine decomposition had occurred and recommended further studies.

Using the same hardware with a minor improvement in the measurement module, Lecourt and Steelant [54] enlarged the experimental database by using ethanol, acetaldehyde and MMH for straight and bend pipes configuration. They observed a surprising multiple steps evolution of the first pressure peak, relating the rapid steps/plateaux to possible two-phase flow aspects such as cavitation and bubble collapse (Fig. 2.11). The speed of sound of the different liquids in the tank was also measured by means of an ultrasonic transducer. By comparing the pressure profile of the different fluids, they also demonstrated that ethanol can be used as a replacement fluid instead of toxic MMH. Among the physical parameters to be considered for the analysis, the authors suggested the vapor pressure, the latent

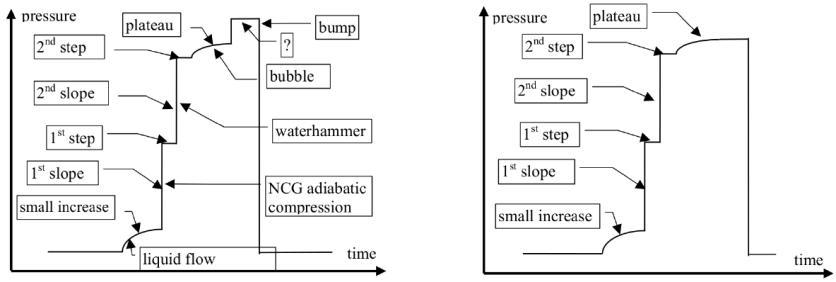

Figure 2.11: Schematics of the water hammer pressure evolution for straight (left) and bent pipe (right) as described by Lecourt and Steelant [54]

heat of vaporization and the surface tension, while the vapor pressure value was not deemed important for the pressure rise tendency.

In his doctoral work, Lema [55] performed several tests using water, ethanol and acetaldehyde for different geometries and different line pressures. Thanks to a specifically designed test-rig (Fig. 2.12), he was able to run tests with deareated and saturated liquids, so that the influence of the gas desorption effect could be evaluated. Test results showed that for the saturated liquid the pressure peak is slightly smaller due to the desorption of the dissolved gas which acts as a cushion in front of the liquid. In addition, the released gas increases the wave attenuation and causes a decrease in the wave frequency. The author remarked also that not only the amount of dissolved gas is important, but also the desorption rate plays a major role. Flow visualizations with high speed imaging was also conducted by means of a quartz pipe, which provided a remarkable insight of the multi-phase priming process and allowed to observe column separation under certain conditions.

Anthoine and Lestrade [4] used the same hardware of Lema, but mounted horizontally in the test facility of ONERA (Fig. 2.13). The experimental database was extended for real propellants such as MMH and NTO. They observed an unexpected behavior of NTO: the pressure peak is much lower than expected (by comparison with water and based on fluid properties) and the measured temperature at the dead-end was higher than 350 °C, unlike the other fluids that showed a temperature variation <1 °C. The authors had no explanation for that and recommended further refined temperature measurements together with flow visualizations. Minor differences with the experiments of Lema [55] were reported and assumed as due to the horizontal configuration.

The aforementioned scientific studies are listed in Table 2.3 with a short description of the test conditions.

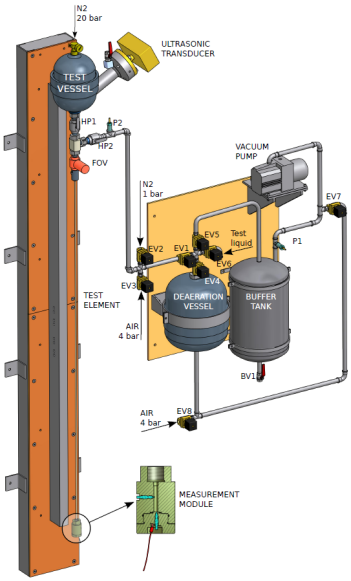

Figure 2.12: Experimental setup used by Lema [55]

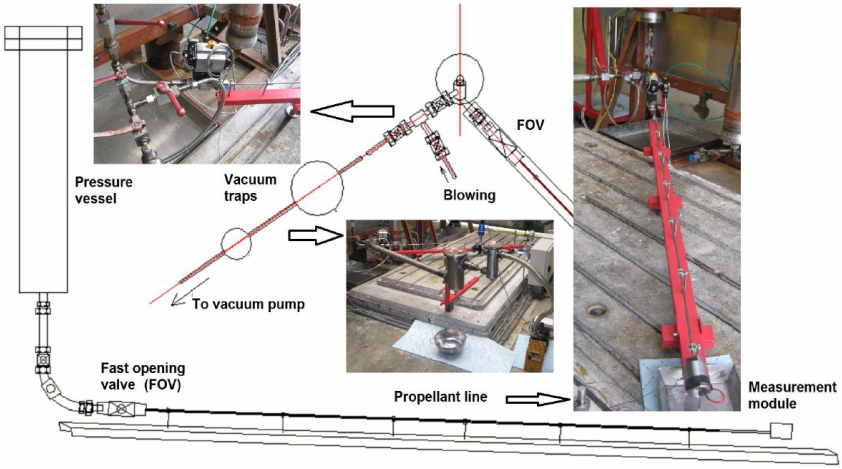

Figure 2.13: Experimental setup used by Anthoine and Lestrade [4]. The hardware is the same as used by Lema [55] but now mounted horizontally and with a different pressure vessel.

Author	**Fluids**	**Tank pressure**	**Line pressure**	**Line geometry: length L, OD x t**	**Goals, findings**
Gibec and Maisonneuve, [37] (at ONERA, 2005)	water, MMH, NTO, Hydrazine	10, 20 bar	10 mbar, 1 bar	straight, bend pipe and tee, L: 2000 mm, OD: 6.35x0.41 mm, titanium alloy	use of real propellants, observed an unexpected temperature increase for hydrazine
Lecourt and Steelant [54] (at ONERA, 2007)	ethanol, acetaldehyde, MMH	20 bar	10 mbar up to 5 bar	straight and bend pipe, L: 2000 mm, OD: 6.35x0.41 mm, titanium alloy	interesting evolution of the first peak; speculation of possible bubble dynamics and two-phase flow effects
Lema [55] (at VKI, 2014)	water, ethanol, acetaldehyde	10, 20 bar	10,50,100 mbar	straight, elbow, tee, L: 2100 mm, OD: 6.35x0.41 mm, titanium alloy	comparison deareated vs saturated fluid; use of flow visualizations
Anthoine and Lestrade [4] (at ONERA, 2014)	water, MMH, NTO	20 bar	10, 100 mbar, 1 bar	same as above, but mounted horizontally	use of real propellants, observed an unexpected low peak for NTO,
Present work (at DLR)	water, ethanol	10, 16, 20 bar	10, 40, 100, 300 mbar, 1 bar	straight, elbow, tee, L: 2083 mm, OD: 19x1.25 mm (see chap. 3)	described in the next paragraph

Table 2.3: Previous dedicated studies on priming in spacecraft feedline systems

Original contributions of this research work

After presenting the previous investigations of priming and the state of the art, it is useful at this point to give an overview of the original contributions of this research work, including improvements and extensions of already investigated aspects in literature. The original contributions of this work with respect to space propulsion system applications are:

1. detailed investigation of the effect of the pressurizing conditions. The importance of considering the desorption of a dissolved gas was underlined by Lema [55], who performed priming tests with deareated and completely saturated fluids. In this research work several pressurizing conditions will be compared to better assess the effect of gas desorption:
   (a) deareated fluid;
   (b) completely saturated fluid with GN2 and in addition with GHe as well;
   (c) partially saturated fluid, e.g. at 1 bar saturation level of GN2 and GHe
   (d) completely saturated fluid with the presence of a non-dissolved gas
2. analysis of fluid-structure interaction effects, by means of strain gages and accelerometers
3. analysis of the effect of material elasticity, by using different materials
4. detailed frequency analysis of the pressure wave
5. use of a relative large diameter of the test section (representative of ATV)
6. high quality flow visualizations performed at different locations. High speed imaging of priming was also performed by Bunker et al. [22] and successively by Lema [55]; in this work however the image resolution and the frame rate are definitely higher (see Section 3.1.5)
7. validation of gas desorption model (numerical)
8. implementation and validation of an UFM (numerical)

Chapter 3

Test facility and its numerical representation

3.1 Test bench description

The experimental data used for this work were obtained at the Fluid Transient Test Facility (FTTF) at DLR Lampoldshausen. A CAD model of the test bench is shown in Fig. 3.1. The test facility has been specifically designed to investigate the priming process as faithful as possible to real space operating systems. It features a 80 liters run tank which can be pressurized up to 50 bar, a flexible pressurization system (GN2 or GHe as a pressurizing gas) as well as a modular test section with its own conditioning system. This modularity ensures that the test bench is not limited to one test section. Conditioning of the test section includes purging with GN2 or GHe and evacuation by means of a vacuum pump. The latter is also used for the evacuation of the tank in order to remove dissolved gases out of the liquid. The test bench is equipped with a pneumatically actuated fast acting valve.

Before describing the test bench geometry in details and the measurement apparatus, the test procedure is illustrated first.

3.1.1 Test Procedure

With reference to the schematic shown in Fig. 3.1, the test procedure is as follows:

1. Before each test the downstream line is purged with GN2 flow by opening MV-4 and MV-2 and unscrewing the measurement module at the test-element end. The tank isolation valve MV-1 is kept closed.

2. The test section is evacuated by means of a vacuum pump to the desired vacuum level; the dead-end module is screwed back, MV-3 open, MV-5 and MV-4 close. The vacuum pump features a LN2 cold trap to condense vapor thus preventing it from entering the pump.

3. The fast opening valve FOV and MV-2 are then closed and MV-1 is opened to manually prime the upstream pipe. The FOV purge line is briefly open for 2-3 seconds to remove any residual gas.

4. Start of the automatic test-sequence: FOV opens and data are recorded for 4 seconds.

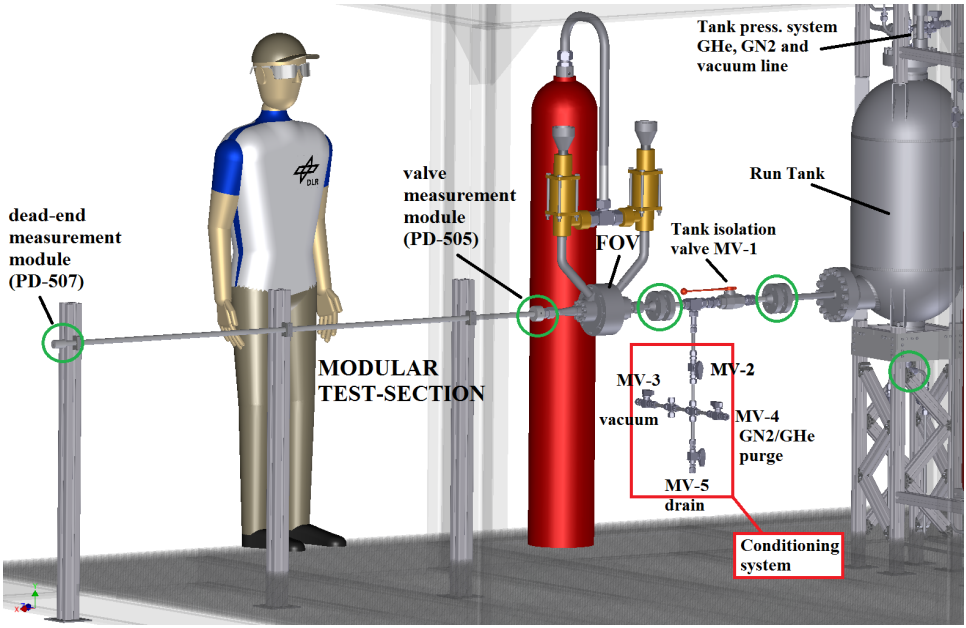

Figure 3.1: CAD mock-up of test-bench FTTF in priming configuration. The positions of the sensors are indicated by a green circle.

5. After the test, the liquid is drained from the line: MV-1 is closed, MV-5 is opened and the measurement module is unscrewed. The procedure is then repeated from step 1.

The condition of the liquid in the tank is carefully prepared according to the test objective and following specific procedures:

deareated fluid: the vacuum pump is connected to the tank pressurization line to remove any dissolved gas from the liquid, until the pressure drops to near the saturation value of the liquid. About 5 minutes rest time is allowed and then the procedure is repeated until the pressure in the tank is constant and slightly above the saturation pressure of the liquid. In order to ensure deareated conditions the fluid is then pressurized with GHe (which has a much lower solubility than GN2) and a maximum of six tests are performed in a row before evacuating the tank again. This usually takes 45 min and it is considered enough to ensure that the fluid is still deareated, since the dissolving of gas in liquid is a slow process.

This procedure is necessary because there is no membrane to separate the liquid from the gas.

saturated fluid: the liquid is left at least three days in the tank under pressure (20 bar) to allow GN2 or GHe to dissolve completely.

3.1.2 Geometry

The part of the test bench upstream the test section valve will be referred as the upstream line. This part is always kept the same without any modification over all the performed tests. It includes the 80 liters tank, a manual ball valve (tank isolation valve), a tee branch for the conditioning of the test section and the fast opening valve (FOV). The tank isolation valve is kept open during the test, while the conditioning system isolation valve is closed. For the analysis of the priming, two lengths are of importance:

- upstream line (tank to valve): 1023 mm (OD 22x1.5 mm)
- downstream line (valve to dead-end): 2083 mm (OD 19.05x1.24 mm)

The overall distance tank to dead-end is therefore 3106 mm, which is the length dictating the frequency of the water hammer. The main components are described as follows:

Tank: a 80 liters cylindrical stainless steel vessel of 406 mm internal diameter.

Tank isolation valve: a ball valve with an internal diameter of 20 mm. Since it is slightly bigger than the pipe internal diameter (19 mm) it should not cause perturbations in the flow. In fact diameter reductions are to be avoided as they restrict the flow passage and might induce cavitation.

Tee: a Swagelok tee connector of 22 mm used to divert the conditioning system of the test section. The internal diameter has been reworked to 19 mm to ensure a smooth passage of the flow.

Upstream pipe: the pipe segments connecting the components in the upstream line are made of stainless steel 1.4541, with OD 22 mm x1.5 mm.

FOV: the fast opening valve will be described more in details in the next paragraph.

Valve measurement module: it is mounted just downstream of the FOV and provides the interface for the pressure sensor at the test section inlet.

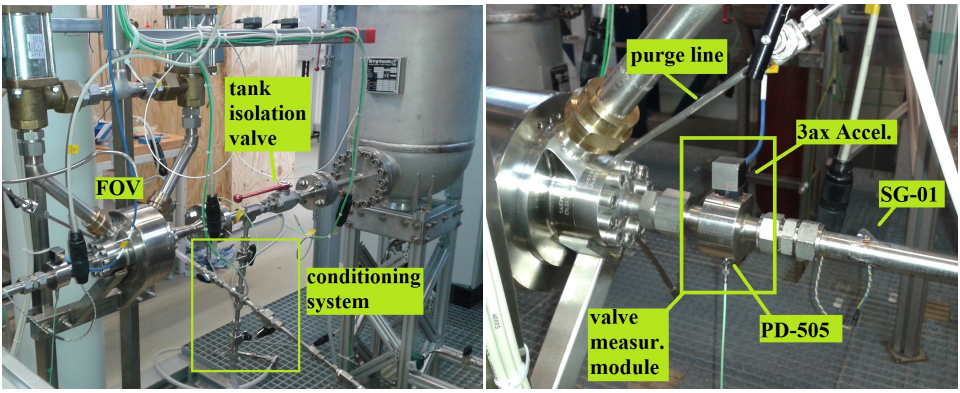

Figure 3.2: The actual upstream line with the conditioning system. Left: the mechanical connection of the valve to the test section, with the measurement module

Test section: different test sections are used. The straight configuration is a 1907 mm long pipe, OD 19.05 mm x 1.24 mm. This does not include the 176 mm downstream the main valve for the measurement module. More details will be given in a dedicated paragraph

3.1.3 Fast opening valve (FOV)

As reported in previous works [54, 56, 62], the valve opening should be faster than the impact time of the liquid front at the dead-end. In other words, the valve must be fully open before the liquid reaches the end of the downstream line. The impact time, as shown later, is in the range 130-150 ms, depending on the test conditions. As a fast opening valve (FOV), the co-axial model type Axius from company Stöhr was chosen, with an operating pressure up to 250 bar. It is pneumatic actuated (up to 40 bar actuation pressure) and its opening time is only 6 ms. This fast opening time is comparable with the characteristic one of the pyrotechnic valves used in satellite/spacecraft propulsion system, which open in 3-5 ms. The main characteristics of the valve are summarized in Table 3.1. The valve is mounted on a rigid support to limit vibrations during the opening, as can be seen in Fig. 3.2.

The knowledge of the valve opening transient is necessary for numerical validation. It is an important boundary condition although its value is not always available, as emerged in the review of most of the experiments in literature. A requirement for the experimental set-up is therefore to have a position measurement sensor, not only to provide the necessary opening profile but also to ensure the reproducibility of the same. The valve features a position encoder, and its opening

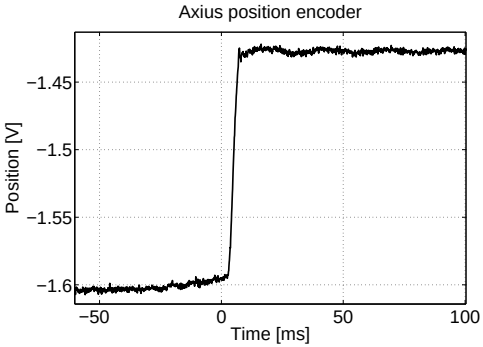

Figure 3.3: Example of the position measurement of the valve: complete opening is achieved in 6 ms

Technical data	
opening time	6 ms
valve seat	16 mm
seat sealing	copper
body material	st. steel
pressure loss coefficient (zeta)	12.5
max pressure	250 bar
operating fluid temperature	-196 C to +50 C
actuating pressure	40 bar

Table 3.1: Characteristics of the valve, model type Axius from company Stöhr

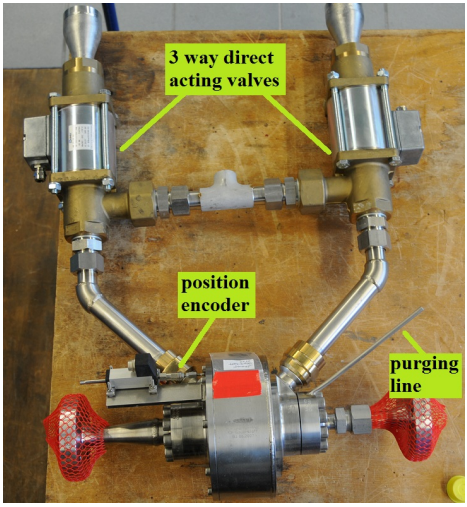

Figure 3.4: Layout of the valve with its pneumatic actuating system

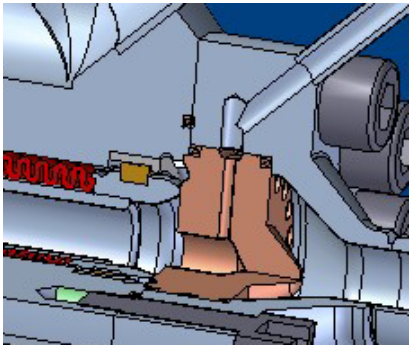

Figure 3.5: Detail of the valve purging line: it is diverted directly from the valve seat

profile has been perfectly reproducible over all the performed tests. An example of the position measurement of the valve opening is given in Fig. 3.3.

A second valuable feature of the valve is the possibility of purging the valve seat via a purge line. This is of utmost importance to ensure that no gas is present in the valve or in the upstream line after the conditioning of the test section. The sketch of the purging line is shown in Fig. 3.5

The mechanical interfaces of the valve consist of a flange for the upstream part and a DILO M2-16 for the downstream connection with the measurement module (see e.g. Fig. 3.2). The inner diameter of the DILO connector has been reworked to 16.56 mm to ensure a smooth flow in the test section.

3.1.4 Geometry of the test sections

Different line configurations are tested:

- three straight pipes, 1907 mm long
  - stainless steel 1.4541
  - titanium alloy Ti 3Al/2.5V
  - aluminum alloy 6061-T6
- elbow (L), 865 mm (upstr. branch)+ 1042 mm (downstr. branch)
- tee (T) in a left/right set-up, 865 mm + 521 mm/521 mm
- tee (T2) in a left/right set-up, with different branch lengths, 865 mm + 1042 mm /521 mm

The dimensions refer to the center line of the pipe and include also the inner length of the connectors L,T and the dead-end module (Fig. 3.6). In this way, the lengths represent the actual distances traveled by the liquid in the test section. To consider the overall path of the liquid once primed upon the valve opening (i.e the overall length of the evacuated pipe), the 176 mm of valve measurement module must be added to the test section geometry. The geometry of the L and T have the same equivalent inner volume of the straight pipe to allow a comparison of the filling process. The material of L, T, T2 is stainless steel, as well as the connectors.

The test sections, or also referred to as test elements, all feature the same diameter:

- outer diameter (OD): 19.05 mm (3/4 inch)saturation
- wall thickness : 1.24 mm (0.49 inch)

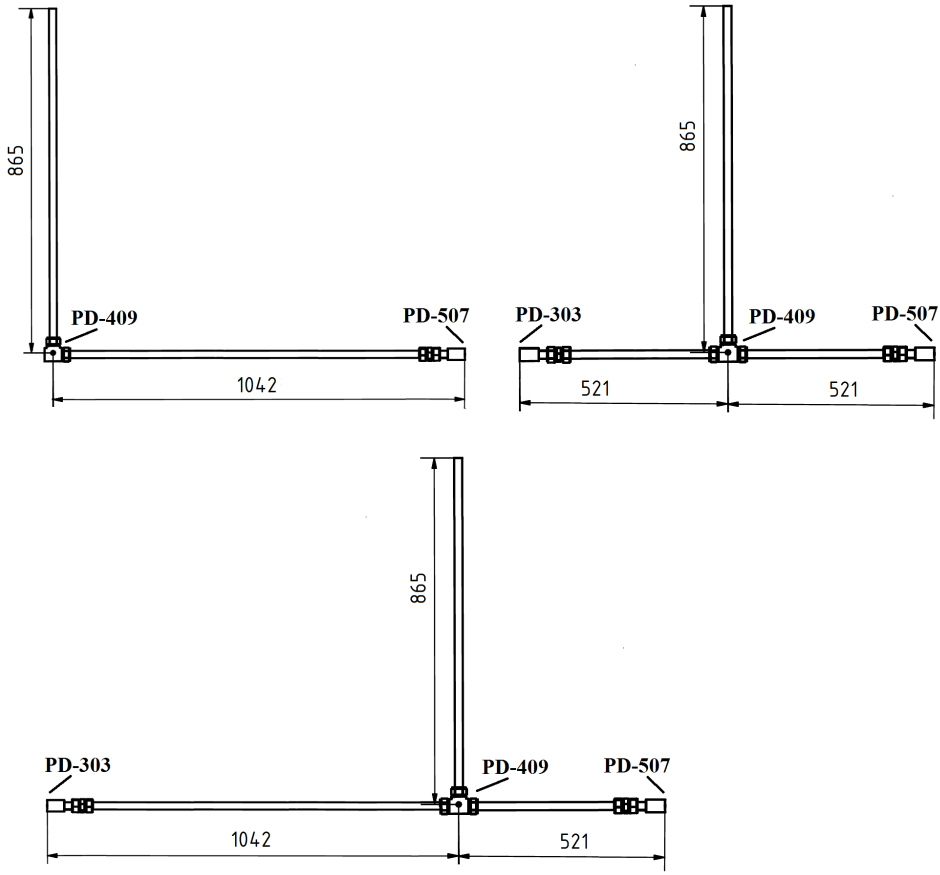

Figure 3.6: Sketches of the L, T, T2 configurations, dimensions in mm

This pipe dimension is the standard size used in the feedline system of spacecrafts or satellites requiring a high propellant mass flow, like the ESA automatic transfer vehicle ATV and the Orion-ESM. The actual material used for the feedlines is the titanium alloy Ti3Al2.5V (3% aluminum and 2.5 vanadium), which has a higher tensile strength than the pure titanium. The aluminum alloy 6061-T6 is widely used in aerospace applications, though not in propulsion system components. It is here investigated to enhance FSI effects due to its lower Young modulus.

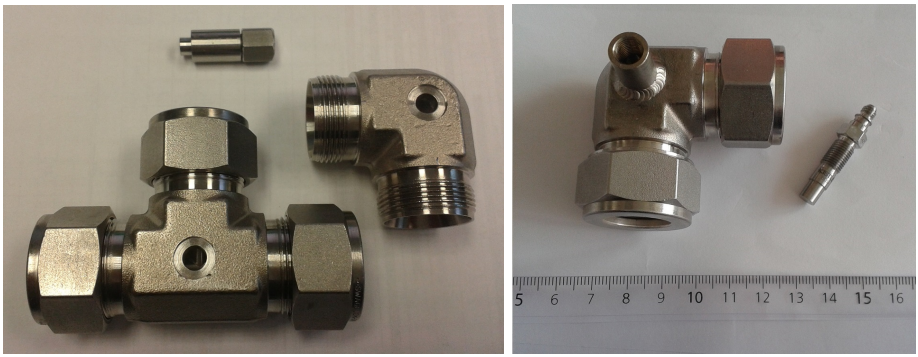

Figure 3.7: The tee and elbow Swagelok 3/4 inch connectors with the bore for the pressure sensor PD-409. In order to ensure the sensor to be flush mounted, a threaded insert is welded on it (left).

Mechanical interface All the connectors used in the test section are Swagelok tube fittings of 3/4 inch size. These include the straight union for the upstream connection with the valve measurement module (visible e.g. in Fig. 3.2), the junction elements elbow and tee (Fig. 3.7), and the weld-on fitting for the connection with the dead-end measurement module (Fig. 3.9). The inner diameter of the tested pipe is (ID) 16.56 mm. Therefore, in order to minimize any flow perturbation the inner diameter of the connectors has been reworked to this size. The test section is mounted at three points onto a rigid support structure to limit its movements. The support structure is made of aluminum profiles. The test section has a downward slope of about 1° to facilitate the purging procedure.

3.1.5 Sensors and Instrumentation

Several transducers are used in this experimental investigation. In addition to the most important pressure and temperature sensors, strain gauges and accelerometers are also used for the structural analysis and FSI effects. The electrical signal of each sensor is properly amplified and then filtered to avoid aliasing and high-frequency noise. The conditioned signals are sampled with National Instrument acquisition cards series NI-PXI with different resolution. Details of the sensors and their setting are summarized in Table 3.2.

Note on pressure measurements The dynamic pressure sensors 601A has a surface diameter of 5.5 mm, which is considered small enough not to perturb the flow when flush mounted, given the inner diameter of the pipe of 16.55 mm. The

Sensor	Model	Company	Sampling frequency [kHz]	Cut-off frequency [kHz]
pressure (P)	4043A200	Kistler	10	2
	4043A2 (for vacuum)	Kistler	10	none
dynamic pressure (PD)	601A	Kistler	150	30
temperature (T)	thermocouple type K 0.5 mm tip	Electronic Sensor	1	0.2
accelerometer (ACC)	3-axis; 8395A030	Kistler	50	20
strain gauge (SG)	CEA-06-125UN-350	VPG sensors	50	20

Table 3.2: Specification of the transducers used and their settings for the acquisition

piezoelectric sensors are not able to measure static pressure, displaying a zero value instead. The absolute pressure is measured by the static pressure sensors, which are mounted in the tank and in the upstream line, but they are not mounted in the test section to minimize the intrusive effects. The value of initial line pressure is provided by the pressure sensor in the vacuum line (4043A2) of the conditioning system and added to the PD signal to obtain the absolute pressure. The signal decay time of the PD is about of 5 s, longer than the actual attenuation of the pressure wave (<1 s).

Note on temperature measurements In a preliminary test campaign, measurements of the temperature at the dead-end have been performed with a different measurement module. A small increase in temperature of about 4 K has been observed with a line pressure >300 mbar, while in case of evacuated test section the increase is only 2.5 K. The measurement of fast temperature transients is limited by the size of the thermocouple and the actual 0.5 mm tip is too big to achieve a sufficient frequency response. Since no significant use of these temperature measurements could be drawn, the present measurement modules only feature the pressure sensor. This has the advantage to further minimize the intrusive effect and speeds up the purging procedure, since the thermocouple bore proved rather difficult to be removed from water. Thermocouples are installed in the upstream line, including the tank.

The temperature measurements at the dead-end obtained during the preliminary campaign as well as the description of the used measurement module are presented in Appendix C.1.

Measurement positions

Measurements of pressure and temperature are performed at different positions along the upstream line as well as in the test section, namely:

- pos. 1 : at the tank; P, T, PD-103
- pos. 2 : 235 mm downstream the tank; P, T, PD-403
- pos. 3 : 727 mm downstream the tank; P, T, PD-406
- pos. 4 : 127 mm downstream the FOV; PD-505 + ACC-A
- pos. 5 : at the dead-end; PD-507 + ACC-B

Additionally, for the L, T, T2 set-ups an additional sensor is placed at the junction and in case of T, T2 another one is placed at the dead-end of the second branch:

- pos. 6 : 1042 mm downstream the FOV; at the junction, PD-409
- pos. 7: at the second branch dead-end; PD-303

The position of the sensors in case of the straight test section can be seen in the schematic represented in Fig. 3.8, while Fig. 3.6 shows their position for L, T, T2. The measurement stations 1-2-3 consists of a 20 mm thick disk that is mechanically connected by means of a flange (it can be seen in Fig. 3.10). The dynamic pressure sensor and thermocouple are flush mounted, while the absolute pressure sensor is 2 mm beneath the surface through a 1mm bore. The valve measurement module

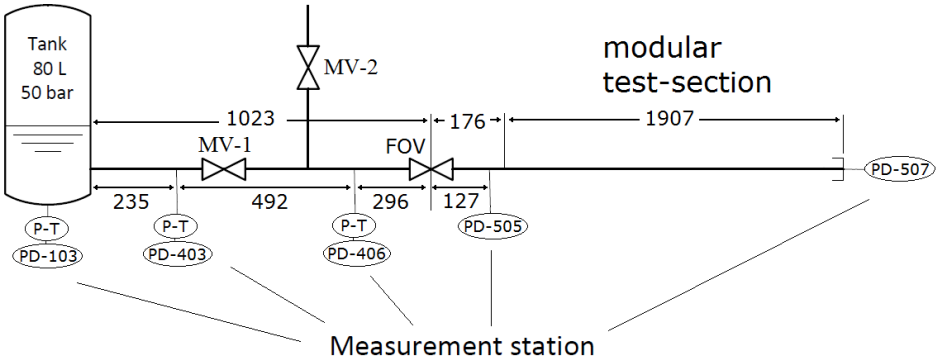

Figure 3.8: Schematic of the Fluid Transient Test Facility with the position of the measurement stations

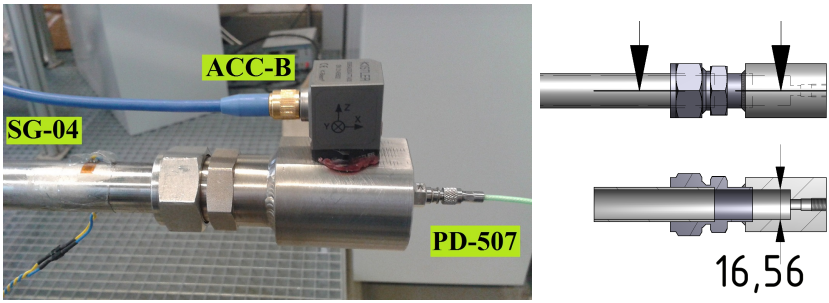

Figure 3.9: The measurement module at the dead-end. It is connected to the modular test section by means of a Swagelok weld-on fitting 3/4 inch. The inner diameter of the connector has been re-worked to have the same inner diameter of the test section, namely 16.56 mm.

(pos. 4) is also a thick disk where the dynamic pressure sensor is flush mounted. For simplicity, the sensor PD-505 in the valve measurement module will be referred to as the valve pressure sensor, although it is actually 176 mm downstream the valve itself. As for the pipe fittings, also the measurement module has been manufactured to ensure a constant inner diameter of 16.56 mm. Atop the measurement module, the accelerometer ACC-A is mounted. The measurement stations 1-4 are fixed for all the tested configurations. The dead-end measurement module (pos. 5) can be seen in the actual mounting in Fig. 3.9. The dynamic pressure sensor PD-507 is flush mounted to face the liquid front. The accelerometer ACC-B is placed atop.

Strain gauges (SG) Four strain gauges have been installed along the test section, for each set-up. The purpose of the strain gauges is not to measure the axial strain

	S and L	T	T2
		valve seat = 0	
SG-01	228 mm	228 mm	228 mm
SG-02	835 mm	835 mm	835 mm
SG-03	1405 mm	1470 mm, right branch (92 mm from dead-end)	1405 mm, right branch (678 mm from dead-end)
SG-04	1991 mm (92 mm from dead-end)	1470 mm, left branch (92 mm from dead-end)	1470 mm, left branch (92 mm from dead-end)

Table 3.3: Position of the strain gauges in the different geometries. The distance is relative to the valve seat

itself nor to act as a pressure transducers. They are used to detect the precursor wave in the pipe and to assess potential FSI effects. Therefore the SG are mounted in a 1/4 bridge configuration, with the main direction perpendicular to the pipe axial direction. The position of the SG is summarized in Table 3.3.

High Speed Imaging (HSI)

A Photron Fastcam SA-X is used for image acquisition. Flow visualizations are obtained by means of a 200 mm long quartz pipe, of 16.56 mm inner diameter and 31 mm outer diameter. Camera resolution is set to 1024x184 with a frame rate of 19200 fps. The quartz segment is mounted in-between two flanges and it is installed in two positions: a) at the beginning of the test section, just after the valve measurement module; b) at the dead-end. Figure 3.10 shows the set-up in both positions. In the installation at the dead-end, a blind flange is used at the bottom end, on which the liquid impacts. It features a threaded hole for the dynamic pressure sensor which is flush mounted to face the flow, in the same way as in the measurement module.

3.1.6 Structural natural frequencies

A particular frequency presents in the fluid pressure signal might be due to structural vibration rather than fluid dynamic effects, therefore the knowledge of the structural natural frequencies (eigenfrequencies) of the test section is necessary for the analysis of FSI effects. The impact hammer test is performed on the structure in order to determine its natural eigenfrequencies. The procedure is described in Appendix B as well as the resulting structural eigenfrequencies of different configurations.

3.1.7 Test matrix

In order to precisely assess the effect of the different physical processes involved during priming, the boundary conditions will by varied singularly to avoid a potential combined influence of the phenomena. The rule of analysis recommended by Descartes [26] is followed. The boundary conditions include the tank and line pressures, the pressurizing conditions of the liquid and the geometry of the test section. Additionally, the effect of the material is also investigated but only for the straight configuration.

The baseline configuration refers to a tank pressure of 20 bar and line pressure under vacuum conditions (<10 mbar) in the stainless steel straight test section. The variation range of the parameters is listed in Fig. 3.11, but deviations from these values are possible to investigated particular effect; e.g. the tank pressure is

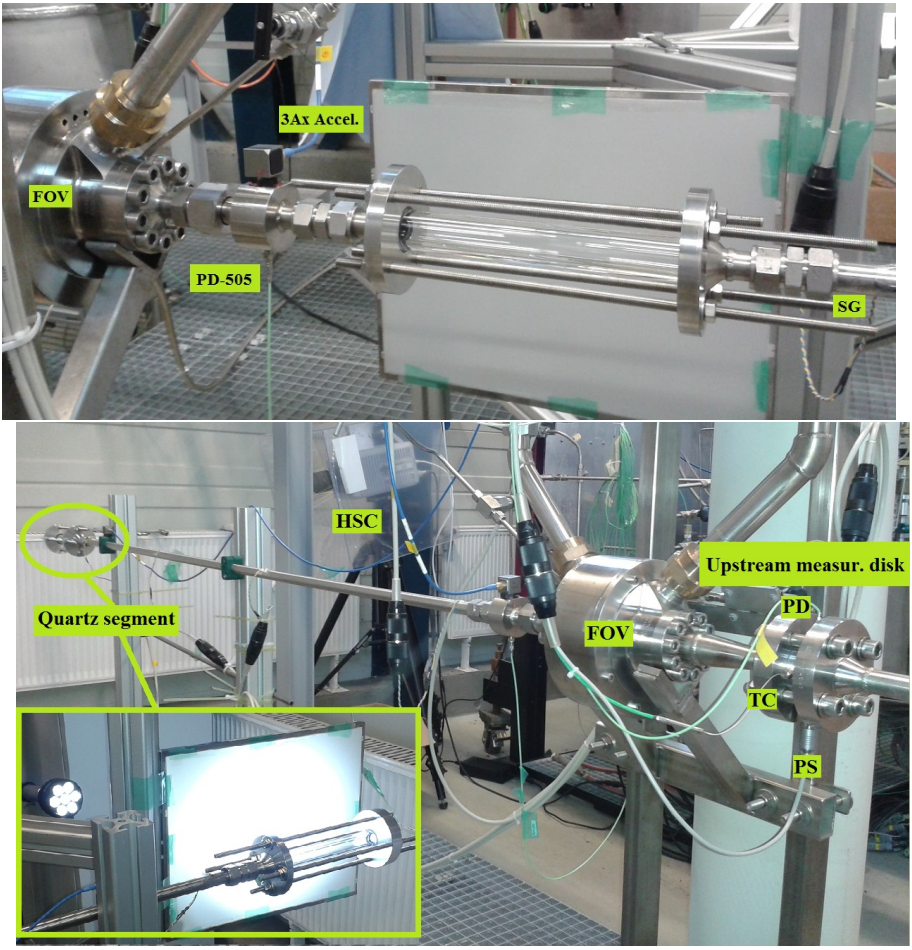

Figure 3.10: Set-up for upstream (top) and downstream (bottom) flow visualization with the quartz pipe and the high speed camera (HSC)

risen up to 26 bar in case of deareated water to force cavitation at the valve. The test fluids are water and ethanol.

Tests are repeated three times for each test conditions to examine reproducibility.

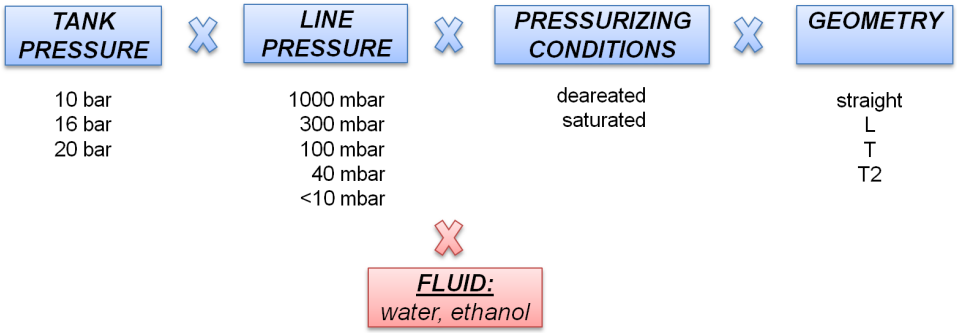

Figure 3.11: Test matrix

3.1.8 Physical properties of the test liquids

Ethanol is used as a replacement fluid instead of the toxic MMH. Ethanol has similar physical properties as MMH and it is considered its best inert replacement fluid [54]. The physical properties of the test liquids are reported in Table 3.4, including MMH as well to allow a comparison. The physical properties of the test liquids are based on the NIST database [65], while for MMH the data are taken from the ESPSS fluid database (release ESPSS 3.0.5).

Property, at 288 K, 1 bar	**water**	**ethanol**	**MMH**
density, ρ [kg/m^3]	999	794	880
viscosity, μ [mPa s]	1.14	1.33	1.04
vapor pressure, P_{vap} [Pa]	1689	4323	3415
specific heat, C_p [J/kg/K]	4188	2448	2849
enthalpy of vaporization, ΔH_{vap} [kJ/kg]	2460	1006	906
surface tension, σ [mN/m]	73.5	23.1	34.4
speed of sound, c [m/s]	1465	1174	1601

Table 3.4: Physical properties of the test liquids and propellant MMH

3.2 Numerical representation of the test-bench

3.2.1 Software description

The numerical model of the test-bench is built by using EcosimPro® software in conjunction with the ESPSS library. EcosimPro is an object-oriented programming language [30] and employs a set of libraries containing various types of components (mechanical, electrical, hydraulic, etc.) which can be interconnected for modeling complex dynamic systems that can be expressed in terms of differential algebraic equations or ordinary differential equations. Finite difference methods are used. The ESPSS (European Space Propulsion System Simulation) is a set of EcosimPro libraries developed in collaboration and financed by the European Space Agency to design and model space propulsion systems [31]. In particular for the present work the 1D fluid flow library of ESPSS has been used. It allows one dimensional transient simulation of two-fluid, two-phase flow systems. It is linked to the fluid properties library which provides the necessary real fluid properties.

Version EcosimPro 5.4.16 with ESPSS 3.0.5 is used in the present work.

3.2.1.1 Homogeneous Equilibrium Model (HEM)

The software EcosimPro can perform simulation of two-phase flows. The homogeneous equilibrium model (HEM) is adopted for the mixture liquid-gas. It assumes that the liquid and gas are perfectly mixed within a node and the velocity, temperature and pressure of the different phases or components are equal (thus the name equilibrium). The mixture properties are calculated simply by weighing the pure fluid properties z (e.g. viscosity, thermal conductivity or heat capacity) with the mass fractions:

$$z = x_{mix} z_{gas} + (1 - x_{mix}) z_L \tag{3.1}$$

where x_{mix} is the mixture quality, defined as the mass ratio of gas:

$$x_{mix} = \frac{\alpha \rho_{gas}}{\rho_L - \alpha(\rho_L - \rho_{gas})} \tag{3.2}$$

where α is the void fraction, i.e the gas volume divided by the total fluid volume.

The speed of sound c in the HEM is calculated assuming an equivalent two-phase mixture where the vapor phase is a mixture of a non-condensable fluid with 100% humidity (vapor):

$$\frac{1}{c^2} = (\alpha \rho_{gas} + (1 - \alpha)\rho_L) \left(\frac{\alpha}{\rho_{gas} c_{gas}^2} + \frac{1 - \alpha}{\rho_L c_L^2} \right) \tag{3.3}$$

Rapid accelerations or fast pressure changes in the flow can not be always accurately modeled with the HEM. In case of fast depressurization of vapor-liquid mixtures (flashing) or shock wave propagation through a multi-phase flow the HEM can give inaccurate predictions [46, chapter 17]. This is an important consideration to be kept in mind when evaluating the numerical simulations.

3.2.1.2 Gas desorption model

The library ESPSS includes a model for the gas absorption/desorption. In the governing conservation equations the following source term is added in order to take the gas release into account:

$$\Omega_d = \rho_{mix} \frac{P_{eq} - P}{P_{eq}} x_d / \tau_d \tag{3.4}$$

where P_{eq} is the equilibrium pressure at which the gas was dissolved, P is the instantaneous local pressure, x_d is the mass fraction of dissolved gas and τ_d is the desorption time constant. The values of P_{eq}, x_d and τ_d are user input data. The absorption of the gas is similarly considered. Further details can be found in the library manual [31].

3.2.1.3 Friction factor

The friction factor is calculated by means of Churchill's correlation [24], which is valid for laminar and turbulent flow:

$$f = 8 \left[\left(\frac{8}{Re} \right)^{12} + \frac{1}{(A+B)^{1.5}} \right]^{\frac{1}{12}} \tag{3.5}$$

with:

$$A = \left[-2.457 \ln \left(7/Re \right)^{0.9} + 0.27\varepsilon/D \right]^{16}$$

$$B = \left(37530/Re \right)^{16}$$

where ε is the pipe roughness. The friction factor so calculated is the steady part used in the general unsteady friction model.

For a two-phase flow, the Friedel correlation [33] is implemented, which uses a two-phase multiplier Φ to increase the pressure loss of the liquid phase ΔP_L:

$$\Delta P_{mix} = \Delta P_L \Phi^2 \tag{3.6}$$

The multiplier Φ is an empirical correlation depending on many parameters [31].

3.2.2 Model of the test-bench

Figure 3.12 shows the numerical model of the test-bench built with EcosimPro. Only the straight configuration is simulated. The working fluids are *Real Water* and *Real Ethanol* (*Real* to distinguish from the *Perfect Fluid* model), while the working gas is *Perfect Gas Nitrogen* and *Perfect Gas Helium* (no *Real Gas* is available).

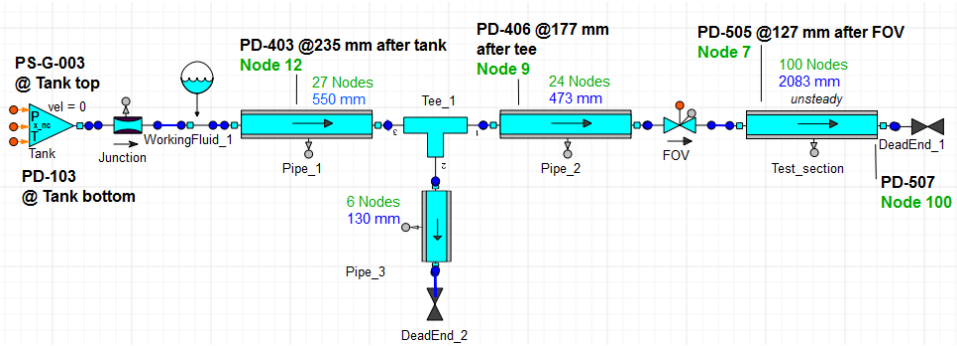

Figure 3.12: The EcosimPro model used for the numerical simulations

One of the most sensitive parameter to chose is the number of nodes. In a two-phase flow, the grid density strongly affects the frequency and damping characteristic of the wave, as it can be seen in Fig. 3.13. Increasing the number of nodes leads to a decrease of the frequency and of the attenuation. While the frequency increase shift towards the experimental value, the opposite occurs for the damping. However, a deeper physical analysis of the frequency and damping characteristic with respect to the numerical model implemented in the software will be described later, respectively in Chapter 5 and 6. This includes the gas desorption model and the unsteady friction model. A trade-off on the number of nodes led to a choice of 100 nodes as a good compromise between accuracy and CPU time.

The numerical pressure peak is not affected by the number of nodes. However the excellent matching of the pressure peak between simulation and experiment shown in Fig. 3.13 is the result of a parameter fitting. More precisely, the friction is the key-parameter that plays a decisive role in determining the magnitude of the first peak. In the numerical setting it is possible to chose a value of the friction multiplier *(k_f)*. As the name suggests, this parameter multiplies the friction coefficient obtained by the standard Darcy-Weisbach equation. Keeping the standard value $k\_f = 1$ leads to unrealistic pressure peak up to 200% higher than the experimental value. In order to match the first peak, the friction multiplier is set to 3 for water and 2.4 for ethanol. Similar values (2.5 and 1.9 respectively) have been also used by Lema [55] for the same reason.

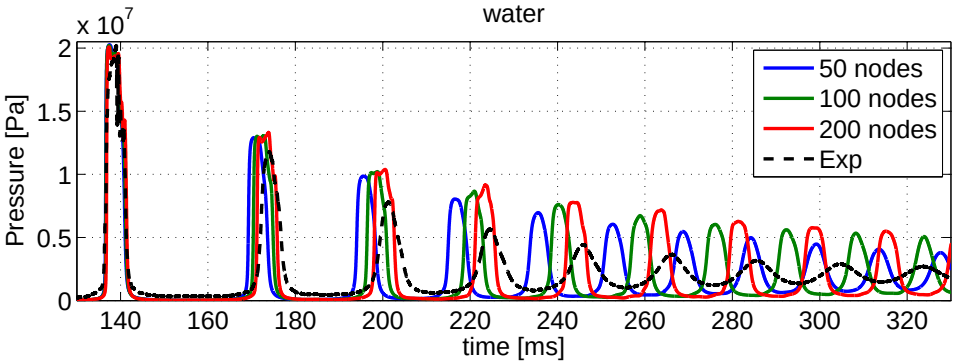

Figure 3.13: Grid sensitivity study

Numerical setting

Preliminary parametric and sensitivity studies have been performed in order to achieve a satisfactory level of accuracy with an acceptable CPU time. The numerical scheme proved to have an influence as well: the upwind scheme results in a slightly higher frequency and a slightly more damped pressure wave. In some particular conditions the upwind Roe scheme does not converge and the CPU time is three times higher than the centred scheme. The error tolerance recommended is at least 1e-5, while in some simulations (e.g. with gas desorption active and unsteady friction model implemented) 1e-6 might be necessary for stability reasons, but at the cost of considerably higher (6x) CPU time.

The final numerical settings used in the simulations are listed hereafter:

number of nodes	100
friction multiplier k_f	3 for water; 2.4 for ethanol
numerical scheme	centred
integration method	DASSL_SPARSE
numerical damping	1
absolute error	1e-5/1e-6
relative error	1e-5/1e-6

Chapter 4

Analysis of the Pressure Peaks

4.1 Introduction

This chapter analyzes the pressure peak characteristics, such as magnitude, shape and timing, and their dependency on the imposed boundary conditions, such as: the tank and the line pressure, the pressurizing conditions, the test section geometry and its material. High speed imaging (HSI) is used to support the description of the phenomena observed and numerical simulations are compared against test results to assess the merit of physical sub-models such as gas desorption, or to weigh the sensitivity of a particular parameter.

Reference boundary conditions are a tank pressure $P_{tank} = 20$ bar with a line pressure $P_{line} = vacuum$ (<10 mbar) in the 2000 mm straight pipe. This will be referred to as the baseline configuration, against which the effect of the aforementioned parameters are compared. The pressure peak profile of the baseline case is depicted in Fig. 4.1. The pressure rise has a complex shape, with multiple steps. Each is followed by a very fast plateau of <0.1 ms and similarly, also the down-slope presents a symmetrical profile with two plateaux almost at the same pressure level as the up-slope. This peculiar shape has also been noticed in previous experiments

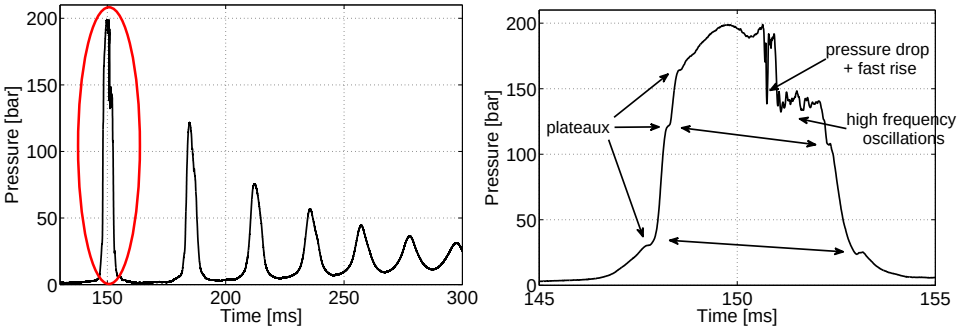

Figure 4.1: Pressure profile of a typical priming event, at $P_{tank} = 20$ bar and $P_{line} = 10$ mbar

performed by Lecourt and Steelant [54] (see Fig. 1.9) . The authors postulated that this multiple step increase is related to two-phase flow phenomena, such as cavitation, condensation and mixing of the liquid with the residual non condensable gas in the line. In addition to these, other possible effects to be considered are the gas desorption, the flash boiling and fluid-structure interaction. In order to precisely assess which process causes what, they will be singularly evaluated one at a time by carefully setting the boundary conditions of the tests.

4.2 Effect of tank and line pressure

4.2.1 Tank pressure

In Fig. 4.2 different tank pressures are compared whilst keeping the line pressure at vacuum (<10 mbar). The higher the tank pressure, the earlier the time occurrence of the first peak. At the same tank pressure, ethanol exhibits a faster impact time, due to its lower density compared to water which results in a higher velocity. As expected, the pressure peak increases with the tank pressure. A quantitatively analysis is presented in Chapter 8.

Cavitation In the case of water, it can be noted that the pressure peak profile becomes somewhat rougher for $P_{tank} \geq 20$ bar. A higher tank pressure leads to a higher velocity, thus to higher pressure losses at the valve, the limit being the occurrence of cavitation when the pressure loss decreases the static pressure below the vapor pressure. Once the fluid undergoes cavitation, the vapor bubble created

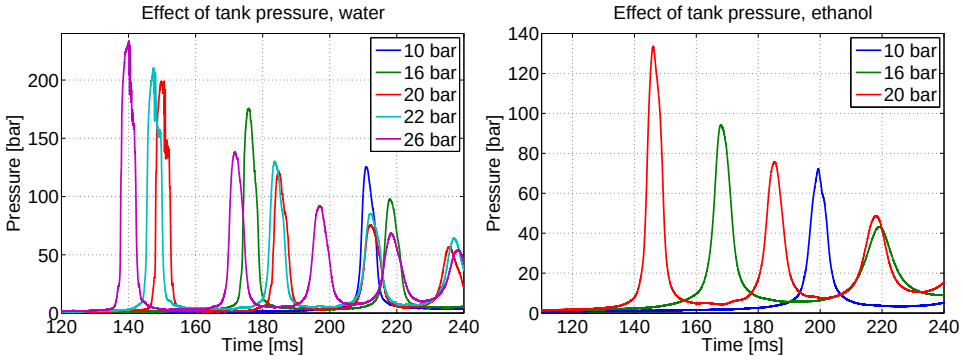

Figure 4.2: First pressure peak at different tank pressures for water (left) and ethanol (right)

at the valve does not collapse[1] immediately, since the downstream condition is still vacuum. When the pressure rises due to the water hammer wave starting from the dead-end, the bubble collapses inducing a strong perturbation in the fluid. Figure 4.3 shows a magnified profile of the pressure peak at the dead-end. The

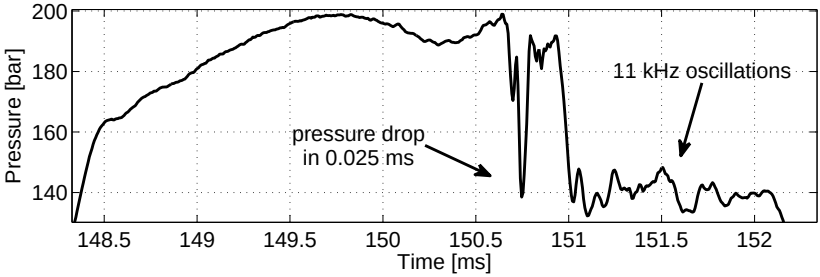

Figure 4.3: Zoom of the pressure peak highlighting the fast pressure drop and the high frequency oscillations caused by cavitation

sudden pressure drop takes place in only 25 μs and it is followed by a likewise fast pressure rise. Then high frequency oscillations appear in the pressure signal, with fluctuations of ±8 bar. The highest content of these frequency is 11 kHz. This value is exactly in the typical range of cavitation-induced bubble frequencies, which for water is between 5-25 kHz (see Section 2.3.3). Moreover, assuming 11 kHz as the bubble highest resonant frequency, it is possible to estimate the corresponding bubble radius as 3.5 mm (Eq. (2.13)). With this bubble radius, the bubble collapse time t_b can be analytically calculated by applying the results of the analytic solution of the Rayleigh-Plesset equation:

$$t_b = 0.915\sqrt{\frac{\rho_L r_0^2}{P - P_{vap}}} \tag{4.1}$$

Equation 4.1 neglects gas content and thermal effects, but it might be yet used to provide a rough estimation of the time scale involved. At the pressure conditions of 200 bar, the bubble collapse time is 22.6 μs, which can be assumed as the shortest

[1]When the valve opens, the fluid undergoes flash boiling due to the vacuum conditions downstream. However, flashing or macro-cavitation in pipelines is not to be confused with microscopic cavitation causing pitting corrosion on pump and turbine blades. The latter always strikes in the same place and is characterized by local high pressures of up to 1000 bar or more that develop when the microscopically small vapor bubbles collapse. With macro-cavitation, repetitive strain of this kind, or the bombarding of a sharply contoured area of the material surface, does not occur since the pressure rises are considerably lower

possible due to the approximation used to derive Eq. (4.1). The experimental value of 25 µs is surprisingly close to the analytic one, thus supporting the hypothesis of cavitation as the cause for the observed pressure spike in the profile.

The conditions at which cavitation takes place are intimately connected with the saturation conditions of the fluid, as it will be explained later in Section 5.3.

4.2.2 Line pressure

The effect of the line pressure is depicted in Fig. 4.4 for water and ethanol. The line pressure is decreased from ambient down to vacuum, keeping the tank pressure at 20 bar. As expected, the pressure peak increases with decreasing line pressure, and the occurrence of the pressure peak is also earlier. For line pressures higher than 100 mbar, no column separation takes place after the first peak as the amount of residual gas in the line is too high, thus preventing the pressure from dropping below the saturation value. When the line pressure level approaches the saturation pressure of the liquid (20 mbar for water and 42 mbar for ethanol), the difference between the pressure peaks is small: 194 vs 198 bar at P_{line} =40 and 100 mbar respectively for water; 121 and 129 bar at P_{line} =100 and 20 mbar respectively for ethanol. At these conditions the liquid undergoes flash boiling and the amount of the generated vapor outweigh the residual inert gas present in the line. Further tests performed with water with a line pressure lower than 20 mbar (i.e. 15-10-5 mbar) proved in fact that no difference in the pressure peak is visible.

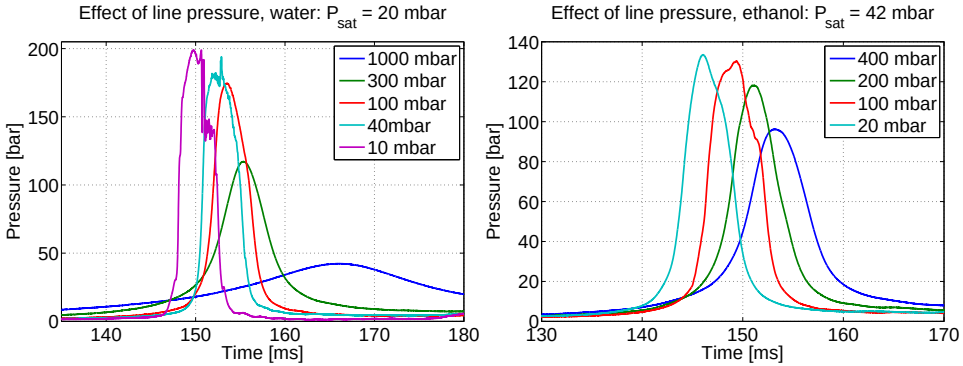

Figure 4.4: First pressure peak at different line pressures, water (left), ethanol (right)

High Speed Imaging

The study of the breakdown of a liquid injected into an environment with a pressure lower than P_{sat} is widely investigated[2] for its important applications in fuel injection and spray atomization. This is beyond the scope of this research, although some interesting remarks can be highlighted. Figure 4.5 depicts the flow pattern when the fluid is primed (or injected) in the test section at two different line pressures, respectively above and below the vapor pressure of the liquid. When $P_{line} > P_{sat}$ the liquid front appears compact and the liquid is homogeneous, without pockets. When $P_{line} < P_{sat}$, the liquid front is not well-defined anymore as it breaks down in ligaments and droplets.

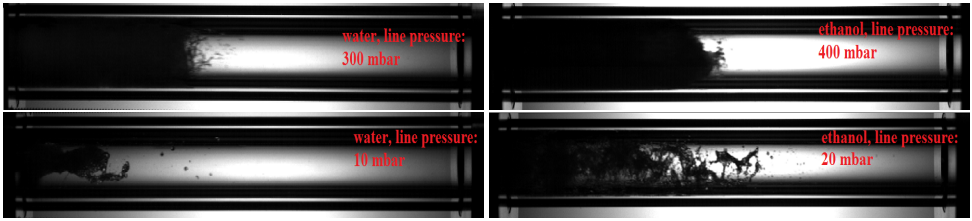

Figure 4.5: Images of the liquid front of water (left) and ethanol (right) entering the test section at different line pressures, respectively above (top) and below (bottom) the vapor pressure of the liquid. The position of the quartz segment is 200 mm downstream the valve; the fluid flows from left to right and appears as a dark slug.

Ethanol appears to break down into smaller bubbles. This is in line with its smaller surface tension compared to water. This would cause more gas pockets in the liquid and would lead to a more bubbly flow, which will smooth any sharp pressure gradient. In fact, the pressure rise of the first peak (Fig. 4.4) is not so steep as in the case of water. In addition, an important effect is that the different flow patterns will affect the speed of sound of the mixture as it does not depend on the gas content only but also on the flow regime.

4.3 Effect of pressurizing conditions

When the fluid is primed into the evacuated line, it will not only undergo flash boiling, but it will also release the dissolved pressurizing gas (desorption) at a given rate. In a similar way, when the pressure rises, some of the released gas will be

[2]Although the physics is the same, in the case of priming the boundary condition are quite different with respect to the classic flashing studies (see Section 2.3.1)

absorbed back into the fluid (absorption or dissolution). As proved by Lema [55] the gas desorption can not be neglected as it affects the pressure evolution. In order to evaluate the effect of the dissolved gas, four different pressurizing conditions are tested for water and ethanol:

- deareated
- partially GN2 saturated at 1 bar (= the amount of dissolved GN2 corresponds to the quantity at 1 bar, see Table 2.1, but P_{tank} is set to 20 bar)
- fully GN2 saturated 20 bar (= the amount of dissolved GN2 corresponds to the quantity at the same tank pressure, $P_{g,sat} = P_{tank}$)
- fully GHe saturated 20 bar (only water tested)

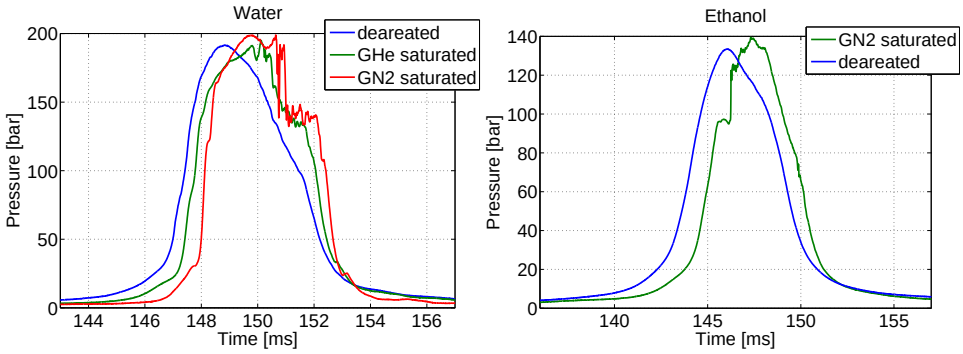

Figure 4.6: Comparison of the pressure peaks between deareated vs saturated liquid for water (left), ethanol (right)

Figure 4.6 compares the first pressure peak between deareated and saturated conditions. When the fluid is deareated the pressure profile is smoother than the saturated condition for both the liquids. The multiple steps/plateaux occuring in the saturated fluid are not observed when the fluid is deareated. The saturated pressure peak also occurs 2 ms later. This is explained by the release of the dissolved gas which acts as a cushion slowing down the liquid front. The same effect would also indicate a lower pressure peak. Experimentally however the pressure peak for the saturated case is slightly higher than the deareated one, being respectively 198 vs 192 bar for water and 139 vs 129 bar for ethanol. The reason for this is unclear, although an hypothesis can be formulated. As it will be described later with the support of high speed imaging, in the case of a saturated liquid, the gas desorption

will cause gas pockets in the fluid forming multiple liquid slugs. These slugs move ahead of the main flow and therefore the tank pressure acts on a smaller amount of liquid mass resulting in a slightly higher acceleration, thus a slightly higher impact velocity. It should be noted that the valve pressure losses also play an important role on the cavitation phenomenon.

In the case of water, additional tests with water saturated with GHe have resulted in a pressure profile with less pronounced steps, in between the profiles resulting from the GN2 saturated and deareated conditions (Fig. 4.6, left). This could have been expected as the solubility of GHe in water is much lower than the GN2 one.

Another way to change the amount of dissolved gas in the liquid is the pressurizing time. In order to achieve a complete dissolution of GN2, the tank must be left under pressure in contact with the pressurizing gas for several hours [57]; with the given tank size this minimum time results in at least 72 hours. Figure 4.7 shows the pressure peak profiles of water saturated with GN2 at 1 bar and 20 bar, the latter with two different pressurizing times, i.e. after one day and three days. Although the general profile is the same, small differences can be appreciated exactly in the position of the aforementioned step/plateaux in the pressure rise, labeled A and B. With a longer pressurizing time, which means more dissolved gas, the plateaux A and B become a sort of spikes with a very fast and small pressure drop. The higher dissolved gas is also responsible for the lack in reproducibility of the pressure peak, as it can be seen by comparing the red curve and the cyan curve in Fig. 4.7, left.

This experimental evidence is an additional clue that the steps/plateaux profile is due to the desorption process, as it does not appear in the deareated fluid.

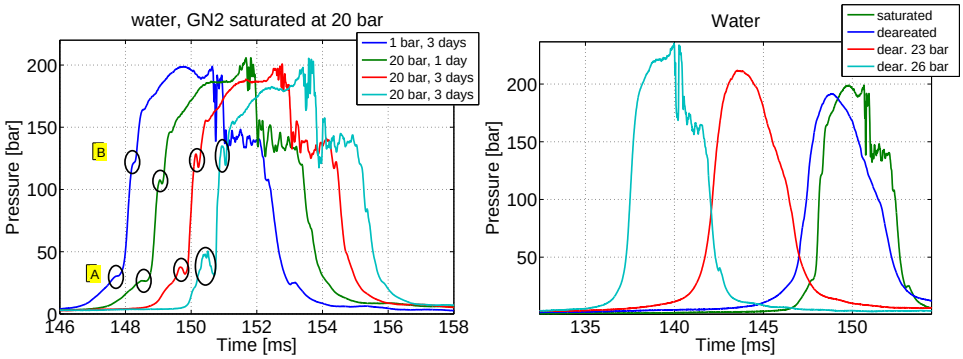

Figure 4.7: Comparison of the pressure peaks for different saturation conditions and different pressurizing times. In the figure at the right the pressure peaks are shifted to allow a comparison

4.3.1 Cavitation and dissolved gas

From the analysis of the test data, it was observed that cavitation takes place in water at the following pressurizing conditions:

- partially GN2 saturated 1 bar: $P_{tank} \geq 20$ bar
- fully GN2 saturated ($P_{g,sat} = P_{tank}$) : $P_{tank} \geq 16$ bar
- partially GHe saturated 20 bar: $P_{tank} \geq 24$ bar
- deareated: $P_{tank} \geq 26$ bar

The experimental results would suggest that the saturation conditions of the fluid can enhance the onset of cavitation. Indeed, there are both theoretical and experimental works in literature proving that the amount of dissolved gas in the liquid has an impact on the bubble nucleation rate [51, 59, 64, 76]. According to Mori et al.[64], when the amount of gas is increased, the nucleation rate also increases. This is due to the lowering of the surface tension of the liquid by solution of the gas, although many other possible explanations have been proposed [59]. The more soluble the gas, the more it reduces the surface tension, and the higher the nucleation rate. This is observed experimentally when comparing water saturated with GHe and with GN2: the threshold of cavitation is reduced in the case GN2 is dissolved, in line with its higher solubility in water compared to GHe.

Cavitation causes higher frequency and less damping of the wave as it will be described in Chapter 5 and 6. A detailed analysis of cavitation is beyond the purpose of this research work, although the effects of cavitation will be highlighted when necessary.

4.3.2 Effect of non-dissolved gas

To further investigate the effect of the dissolved gas, a different pressurizing technique is performed in the case of water. Instead of the usual pressurization from the top of the vessel, the GN2 is now injected from the bottom of the vessel so that it flows through the liquid and mix with it. GN2 is blown for one hour into the tank at 23 bar while the tank is kept at 20 bar by means of a pressure regulator valve. In this way not only the liquid will be saturated, but also free gas bubbles will be entrained in water. Tests are then run after different waiting times to evaluate the effect of the decreasing amount of non-dissolved GN2. With respect to the legend in Fig. 4.8, the waiting times of the tests are as follows:

1. test#1: just immediately after the GN2 injection
2. test#2: after 1 hour

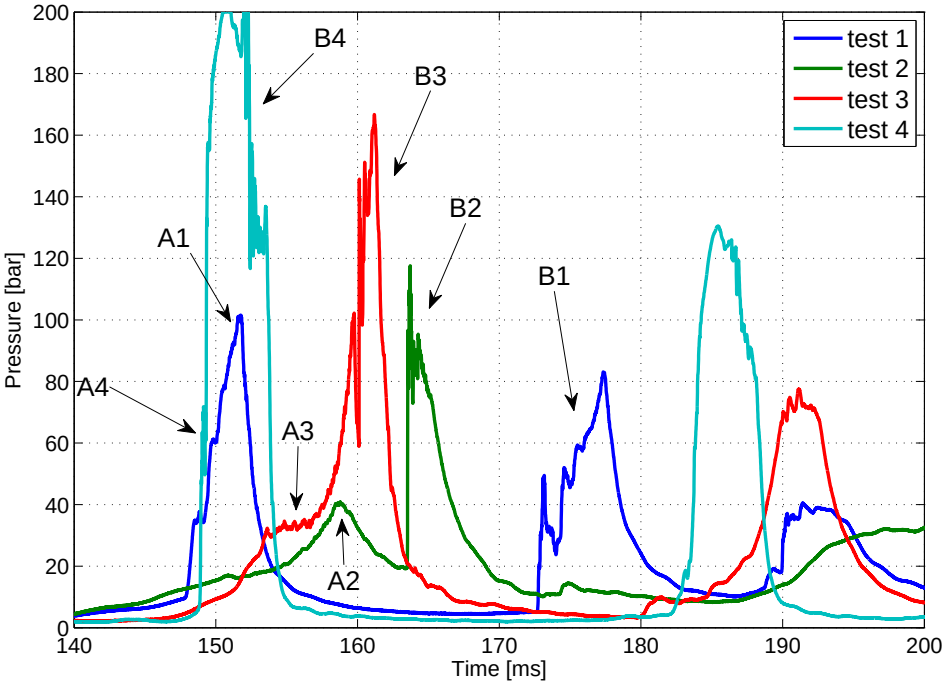

Figure 4.8: Evolution of the pressure profile for water with non-dissolved gas, achieved with a GN2 injection from the tank bottom. The different tests are run after a specified time to allow the amount of non-dissolved gas to decrease with time.

3. test#3: after 3 hours
4. test#4: after 24 hours

The initial line pressure is 10 mbar for all the tests. The tank pressure is kept at 20 bar over all the tests, so it can be assumed that the amount of dissolved GN2 in the liquid is constant and equal to the maximum value at this pressure. The amount of non-dissolved gas is instead decreasing with time, but it can not be measured. Free gas bubbles can be retained on the tank wall and in small surface imperfections (welding points, junctions, sensor surfaces). Part of them will move towards the ullage volume of the tank due to non-equilibrium conditions and pressure perturbations during the tests. In this respect, the forced injection of GN2

can be seen as a way to add extra GN2 beyond the maximum absorption quantity.

Results of the tests are shown in Fig. 4.8. To facilitate the description of the pressure evolution, A represents the first peak and B the second peak. Test#1 has a first peak A1 of quite a low pressure value (100 bar), while the second peak B1 is occurring rather sooner than it should (with respect to the standard case, at about 185 ms) and with a steep rise. That may indicate that A1 and B1 are not separated pressure peaks, i.e. two consecutive distinct peaks , but instead are both part of the same pressure rise. Test#2 shows in fact that peaks A1 and B1 moved closer, resulting in peak A2 and B2, where now B2 is higher than B1. In the next test#3 the two peaks have merged together, so that A2 becomes A3 and it is now a plateau, while peak B3 increases again in magnitude. Finally, after 24 hours, the pressure shape (test#4) tends to the standard case, where the plateau A3 becomes A4, now of shorter duration (<0.3 ms) and the pressure peak reaches 200 bar as the standard saturated case.

From the above description of the pressure evolution, the pressure step/plateaux profile is found as a two-phase flow effect due to the desorption of the dissolved pressurizing gas into the liquid rather than due to the residual gas in the line as hypothesized by Lecourt and Steelant [54]. They described the pressure evolution of the first peak as (possibly) due to different physical processes, assuming the adiabatic compression of the residual gas and the vapour bubble finite time to collapse to be responsible for the multiple steps. However, the adiabatic compression of the residual gas does not seem to play a role in causing the step profile being the amount of residual gas the same both in the deareated case and in the saturated case. In addition, Lecourt and Steelant speculated about the influence of the absorption/desorption of the pressurizing gas, a fact that is experimentally confirmed in this present work. In order to understand the mechanism that causes the step profile, a model is proposed in the next paragraph with the support of high speed imaging.

High Speed Imaging

To gain further insight of the priming process, a 200 mm quartz pipe is placed at the dead-end and high speed imaging (HSI) is performed at 19,200 fps. For safety reason, the tank pressure is reduced to 9.5 bar, whilst the line pressures is kept at vacuum (<10 mbar). Figure 4.9 displays some selected frames of the filling and Fig. 4.10 shows the pressure profile with the corresponding pressure point of the selected frames. Fluid is saturated water.

At around 100 ms after the valve opening, some pressure spikes occur: these are due to single droplets (image 1) that precede the main flow and hit the sensor surface. The flow is stratified due to gravity, the liquid wets the bottom of the pipe (2) and after slamming at the end turns back filling the top. At this stage

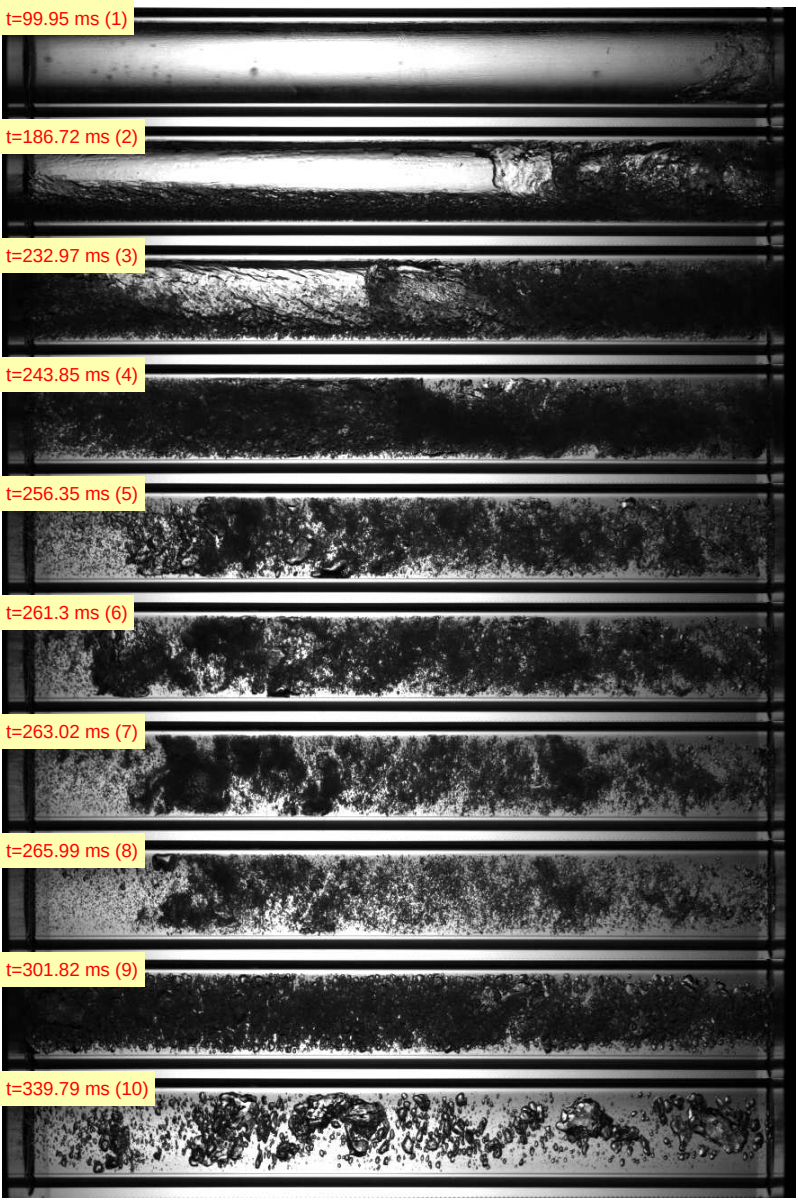

Figure 4.9: Video frames of the filling of the pipe at the dead-end. Fluid: saturated water, tank pressure: 9.5 bar, line pressure: < 10 mbar.

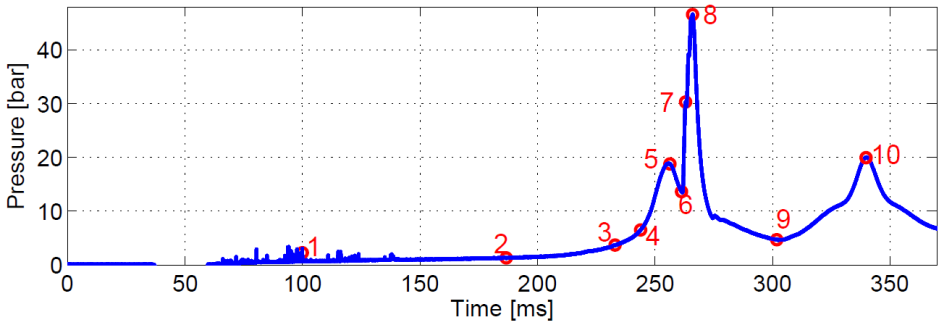

Figure 4.10: Pressure signal at the dead-end, the numbers indicate the selected frames depicted in the previous figure. Fluid: saturated water

the pressure is still low (1.3 bar) and not rising yet. The flow gradually increases until the whole diameter is wet (3) and the quartz segment is now completely filled with liquid-gas mixture (4). The pressure reaches a first local maximum (5) of 18 bar, drops to 15 bar (6) and then a second slug of liquid compress the existing liquid-gas mixture (7). The arrival of this liquid slug is clearly visible at the left side of the quartz segment, where the liquid comes in: the dense gas cloud moves rapidly towards right (6-7). The pressure reaches then the maximum value of 45 bar (8). This frame (8) is in fact the brightest indicating that the liquid amount by volume is the highest and the gas bubbles are tiny, still in a cloud form. As the wave moves upstream towards the tank, the pressure drops to 6 bar (9). Now the flow is fully bubbly. The pressure wave is then traveling from the tank and the pressure increases again (10). At the second pressure peak the bubbles have a bigger size and will move slowly upwards to the top of the pipe due to the gravity.

The crucial point of this analysis is the arrival of a second liquid slug (6-7) that provided an explanation for the pressure peak profile. The same mechanism shall occur at the high pressure case, causing the aforementioned step-plateau profile. At 20 bar, since the driving pressure is higher, the small and fast pressure drop (5-6) will evolve in the plateau previously described. The idea is that the desorption of the dissolved gas will create gas pockets inside the liquid, and the later could be modeled as multiple separated slugs that impinge one on the others resulting in the step-plateau profile.

4.3.3 Ethanol

The effect of the pressurizing conditions for ethanol is shown in Fig. 4.11. As in the case of water, the pressure peak is slightly higher in case of 1 bar GN2 saturated (dissolved GN2 amount is $2.2 \cdot 10^{-4}$ mg/g) and the profile rougher than the deareated case. At a gas saturation level of 20 bar (dissolved GN2 amount is $42 \cdot 10^{-4}$ mg/g) the effect of the higher desorbed gas is far more remarkable: the pressure peak is damped to half the value of the deareated case and the shape differs significantly, showing three distinct peaks. To ensure that this effect is not due to some wrong setting of the experiments, the same tests has been repeated in three different test days showing excellent reproducibility (Fig. 4.11, right). This significant attenuation of the pressure is undoubtedly due to the superior amount of released gas which acts as a cushion, however it might be questioned why this effect does not occur for water. The amount of dissolved GN2 in water at 20 bar is 11 times smaller than in ethanol, nevertheless it is still 20 times higher than the dissolved quantity at 1 bar; yet the pressure peaks are the same (see Fig. 4.7). The released amount of dissolved gas after 150 ms is therefore not considerable enough to damp the pressure peak. That means that the desorption process is not completed yet, or more precisely, the desorption rate for water is slower than for ethanol. The same conclusion was found by Lema [55], although in his experiments the pressure peak in case of saturated ethanol was only 13% attenuated compared to the deareated case.

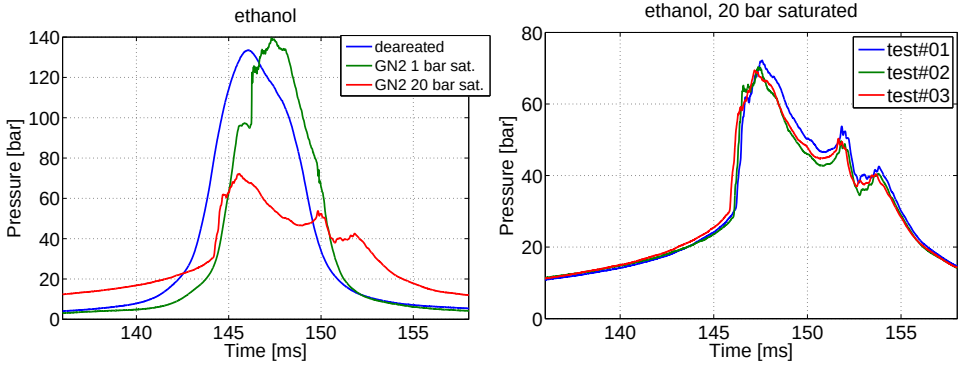

Figure 4.11: Right: comparison of the pressure peaks between deareated and two different saturation levels, fluid is ethanol. Left: reproducibility in case of ethanol saturated with 20 bar GN2.

High Speed Imaging

HSI allows a qualitative comparison between deareated and saturated conditions. Some significant images during the initial filling are shown in Fig. 4.12, including the pressure profile and the corresponding pressure points. These are chosen at the most meaningful pressure levels, such as at the first filling of the segment (1-4), at half point of the rise (6), at the peak (7) and at the valley (8). Deareated fluid is depicted on the left (L) in Fig. 4.12 while the saturated is depicted on the right (R). The tank pressure is set at 5.5 bar for safety reasons.

A first difference is noted in the conditions at which ethanol enters the dead-end: deareated fluid appears as a very tiny mist (1L), while the saturated one arrives instead as a mixture of bubbles and mist (1R). The more coarse pattern of saturated ethanol is visible in the following frames (2-3-4), whereas the deareated one appears not only finer but also more homogeneous. The pressure profile (R) at around 1-4 presents more spikes: this noise-like appearance in the signal is due to the individual bubbles that impact on the pressure sensor. The desorbed GN2 creates gas pockets and enhances the formation of bigger liquid droplets/slugs, the same mechanism described previously for saturated water.

The higher amount of desorbed gas can be seen by comparing frames 6-7-8. The gas bubbles are in fact somewhat bigger, in particular toward the end of the segment at its right. At its left (at the entrance of the quartz pipe) a dark cloud is present in both fluids (7-8): this is the initial residual gas that gets trapped as the main liquid front arrives. At the maximum pressure level (7) this cloud is bigger for the saturated case due again to the added gas coming from the desorption process. The dissolved gas causes the pressure peak to be smaller (21.0 bar vs 24.9 bar) as expected, although the curve is smooth without the steps or spikes observed previously for the saturated ethanol at 20 bar. The reason is the low driving tank pressure of 5.5 bar which lower the flow velocity and allows the fluid more time to assume a homogeneous pattern.

4.3.4 Numerical simulations of the gas desorption

In the software ESPSS it is possible to include a basic absorption/desorption model (see Section 3.2.1.2). The input requires to set a desorption time constant, a value that is typically unknown and not available in literature. A trial and error procedure is then undertaken to estimated the best fit value for the desorption time constant with respect to the experimental data.

Figure 4.13 shows the results of the numerical simulations for water and ethanol at 1 bar and 20 bar GN2 saturation. In the case of water saturated at ambient pressure, the pressure peak is practically the same for the three different time constants selected, namely 300, 100 and 10 ms, and the slope of the pressure rise is also not

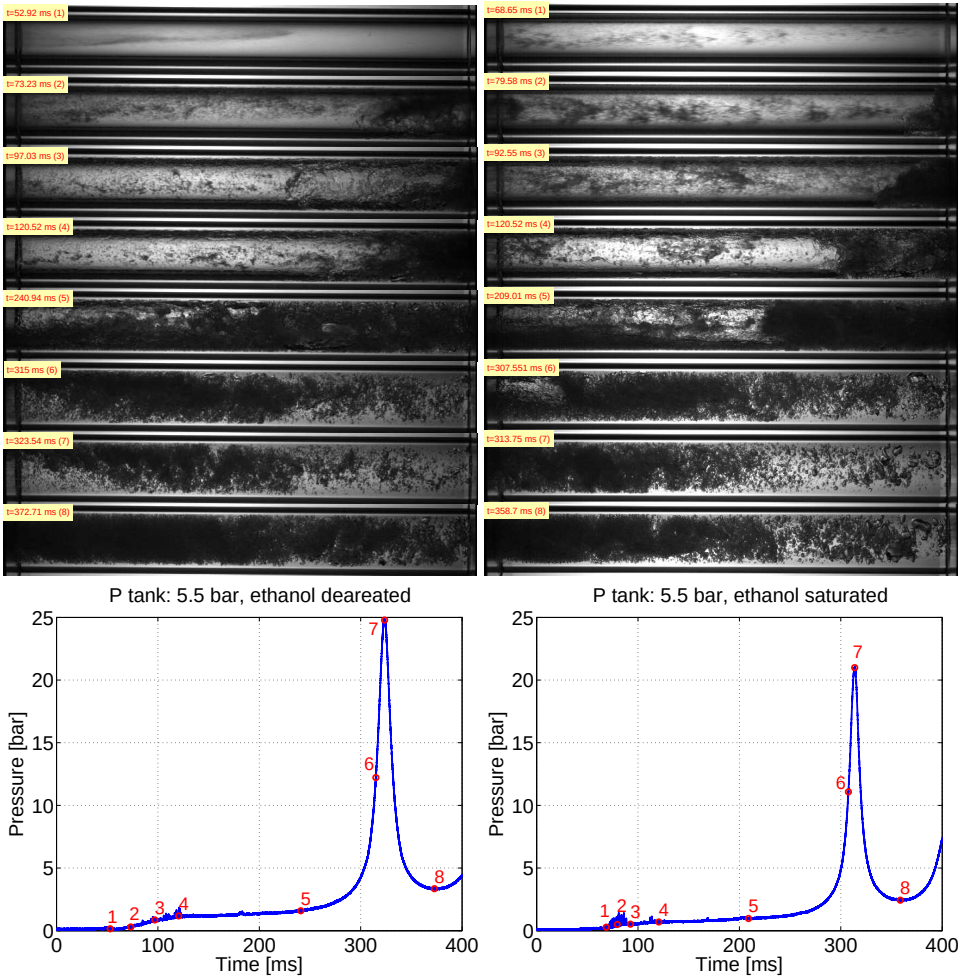

Figure 4.12: Video frames of the filling of the pipe at the dead-end and corresponding pressure points. Left: deareated ethanol, right: saturated ethanol; line pressure: 20 mbar for both cases

affected. Major differences can be noted with a higher amount of dissolved gas, that is the case of water saturated at 20 bar. The faster the desorption, the less steep the pressure slope is. Moreover, for the time constants of 500 and 300 ms, the pressure rise presents now a plateau at 137 ms, similar to the experimental one. This is an additional confirmation of the gas desorption as the cause for the peculiar step in the profile. The best fitting time constant is then somewhat between 500 and 300 ms, whereas 50 ms appears to be too short a time constant for desorption of GN2 in water.

Concerning ethanol, the dissolved amount of GN2 at ambient pressure has already an influence on the pressure profile, presenting a step at 122 ms as in the

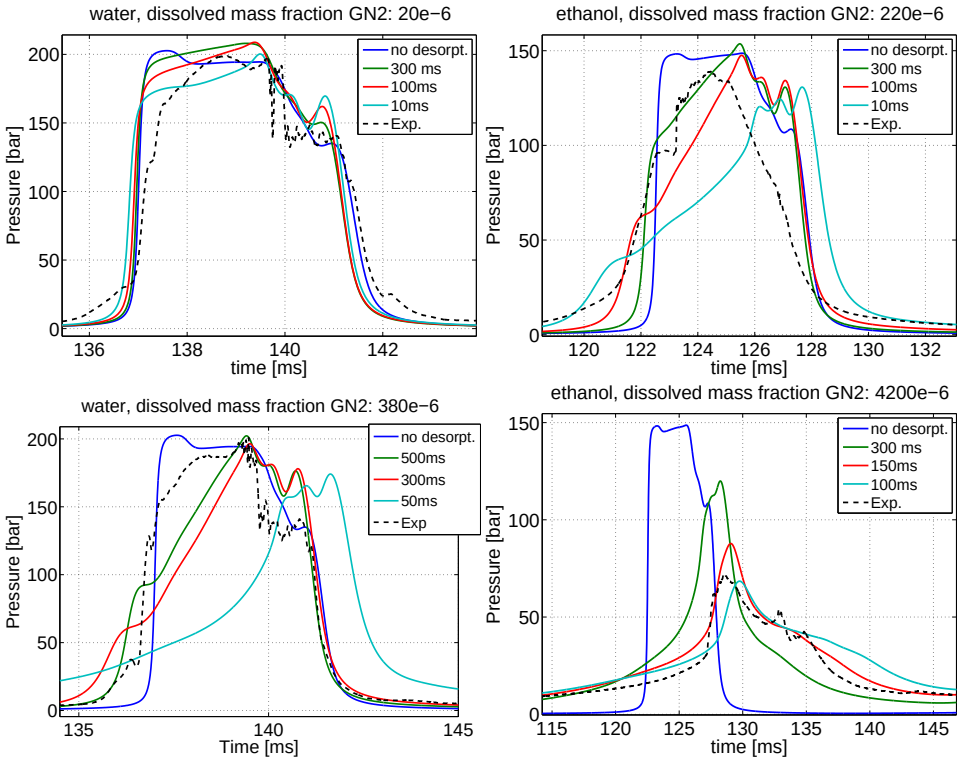

Figure 4.13: Numerical simulations including the desorption model with different time constants. Water (left) and ethanol (right) at 1 bar saturated (top) and at 20 bar saturated (bottom). The experimental curves have been shifted to allow a better comparison.

experiment, though at different pressure. The main difference is that, after the step, the slope is less steep compared to the experimental curve. This indicates a higher compressibility of the mixture, which means a higher gas content. In the experimental curve on the contrary, the slope is not only steeper, but the steepness after the plateau is even higher than the initial steepness before the plateau. This is however in line with the hypothesis of a separated slug impinging on the precedent one: at the impact the pulse of a slug will compress the precedent one causing a pressure rise with a gradient proportional to the speed of sound of the mixture near the sensor. In this position, as described in the HSI analysis, the gas content is less than in the previous 10 cm, therefore the speed of sound is higher. The numerical 1D code can not simulate such local (spatial) gradients in the fluid, resulting instead in a smoother spatial profile. The desorption model, although not matching the general peak profile, allows at least to justify the presence of the step in the slope. The effectiveness of adopting a gas release model can be better appreciated when comparing the results for ethanol saturated at 20 bar (Fig. 4.13, right bottom). Assuming 100 ms as the desorption time constant, a surprisingly excellent match with the experimental curve is achieved. Not only the numerical pressure peak now coincides with the (unexpectedly low) experimental value, but also the profile is well reproduced: the initial slope and its higher steepness at 127 ms are simulated, and so is the down-slope (left flank of the peak). The two small spikes observed in the experiment at 134 ms are not reproduced, as they are likely due to bubble dynamics effects which are not taken into account by the software.

The best fitting desorption time constant for ethanol can then be assumed somewhat between 150 and 100 ms, confirming the speculation that the desorption process in ethanol is faster than in water.

4.4 Effect of geometry

The pressure peak for the different tested geometries is shown in Fig. 4.14. As expected, the pressure peaks for T and L configurations are smaller than the straight pipe case due to the momentum loss introduced by the connector. The attenuation of the pressure peak is more pronounced in the case of the T configuration for both water and ethanol, being respectively 168.8 bar and 112.5 bar, while in the case of the L geometry the reduction is smaller, being 190.8 bar and 134.4 bar for water and ethanol respectively. The case of T2 geometry with asymmetrical branches exhibits a pressure peak of 225.4 bar. Details of the geometries and sensors are described in Chapter 3, L and T configurations have the same inner volume of the straight pipe to allow a fair comparison.

For all the configurations, a somewhat minor reproducibility has been noted, with the case of saturated fluid showing a higher dispersion of the pressure peak values.

4.4.1 Elbow (L)

In the case of water in the elbow configuration, the first pressure peak shows a double spike, with the first spike at 153 ms and the second spike at 160 ms. This characteristic is also observed in case of deareated water, but is not present in the case of deareated ethanol (Fig. 4.15). A comparison between deareated and saturated water shows an almost identical pressure profile, with the minor difference that the curve is smoother for the deareated case. Again, this indicates that the release of the dissolved gas introduces high frequency effects related to the gas bubble dynamics making the pressure signal look more noisy. The reason of the double spike is possibly related to two different slugs of liquid impinging at the dead-end. The first slug detaches from the main flow due to the elbow, inducing the first pressure peak of 80 bar; it is then followed by the main flow which generates the actual water hammer pressure peak.

The case of ethanol is more interesting, since it poses various questions. With deareated ethanol, the curve is smooth and regular, as in the straight pipe (Fig. 4.14, right). When ethanol is saturated instead, the curve exhibits the double spike as similarly described for water. The pressure loss at the elbow enhances the gas desorption from the liquid and induces the separation of a liquid slug that precedes the main flow and hits the dead-end, as explained for water. The argument against this explanation is why this occurs also for deareated water. Since no gas is released, the only physical fluid properties which might justify the generation of a slug flow regime are the fluid viscosity and the surface tension. The flow pattern of liquid-gas flow in horizontal pipes is widely investigated due to its important

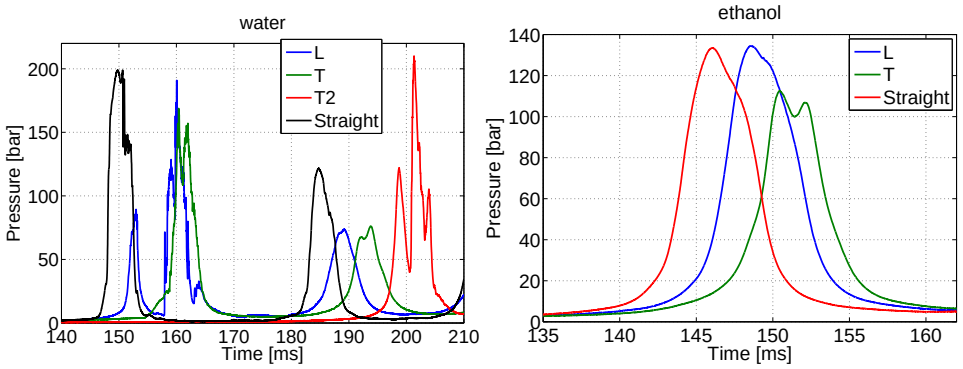

Figure 4.14: Pressure peak profile for different geometries for water (left) and ethanol (right). Water is at 1 bar GN2 saturated, while ethanol is deareated.

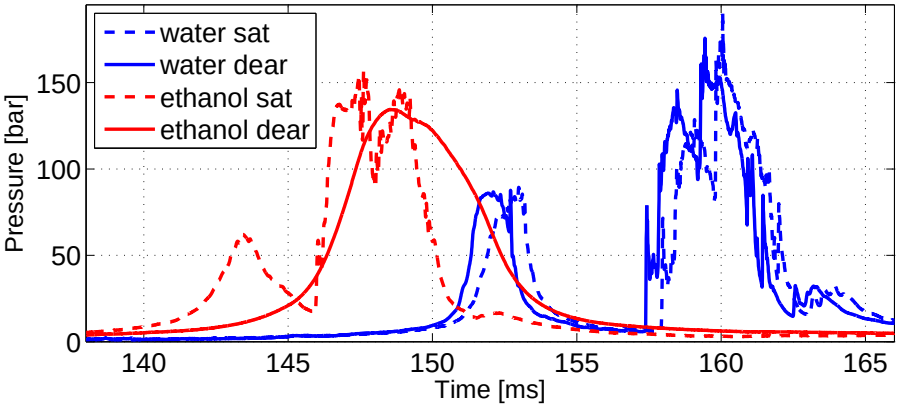

Figure 4.15: Comparison between deareated and saturated conditions in the elbow geometry, at $P_{tank} = 20$ bar P_{line} at vacuum

industrial applications. Unfortunately, all the proposed flow regime maps hold for stationary flow, with well-defined and constant liquid velocity and gas velocity. These conditions are far from the actual situation occurring during priming, where the fast transients and the flash boiling dominate the physics. As a general rule the flow regime depends mainly on the phase velocities[3] rather than fluid properties. Keeping in mind these limitations, some general remarks might nevertheless be of help in understanding the difference between ethanol and water. The effects of fluid properties on the two-phase flow pattern transition was investigated by Weisman et al. [105]. The transition from stratified flow to wave flow depends on the parameter $\sigma^{0.2}/\mu^{0.45}$, with higher values to shift toward slug regime. Ethanol has smaller surface tension than water (22 vs 72 mN/m) and higher viscosity (1.40 vs 1.14 mPa·s), thus this will hinder the transition towards wavy flow, which precedes the slug regime.

Sadatomi et al. [77] investigated the effect of the surface tension on the gas-liquid flow in a horizontal pipe, observing that the fluid with a lower surface tension generates smaller bubbles which easily coalesce and promote the transition from bubbly flow to slug flow. This is in contrast with the actual test results. Andritsos et al. [3] focus instead on the effect on viscosity, concluding that a fluid with higher viscosity will hinder the initiation of slug flow. That is in line with the test results,

[3]The use of phase velocity for gas and liquid allows to define Reynolds number and to introduce the Kelvin-Helmotz instability as the main mechanics for regime transition.

and would allow to affirm that the viscosity is more important than the surface tension, at least in the formation of this particular pressure profile.

A more classical approach based on the Reynolds number can also provide a plausible explanation. As known, in classical fluid dynamics the Reynolds number is often used to define flow patterns and flow transitions. The flow velocity is not known, but it can be approximated by $V \approx \sqrt{2P_{tank}/\rho}$, neglecting the friction losses. Therefore the Reynold number is:

$$Re = \frac{\rho V D}{\mu} = \frac{\sqrt{\rho}\sqrt{2P_{tank}}D}{\mu}$$

The actual Re is not calculated, nor it would be of some use in these fast transient conditions. What could be of help is the ratio between the Re of water and the Re of ethanol:

$$\frac{Re_{water}}{Re_{ethanol}} = \frac{(\sqrt{\rho}/\mu)_{water}}{(\sqrt{\rho}/\mu)_{ethanol}} = 1.4$$

In the same conditions, water has a 40% higher Reynolds number. This means that the transition to slug pattern is easier for water than for ethanol.

High Speed Imaging Some significant snapshots during the priming in the L geometry for deareated water are shown in Fig. 4.17, while the corresponding pressure points and the general pressure profile are plotted in Fig. 4.16. Tank pressure is 7 bar. Frame (1) is shown to allow comparison with frame (2), where the image gets blurry (it can be clearly seen at the dead-end, where the gasket is

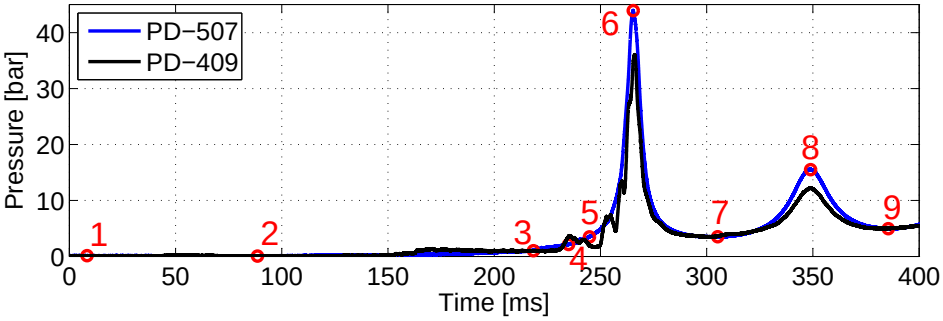

Figure 4.16: Pressure profile and the corresponding points of the selected snapshots. Sensor PD-507 is at the dead-end, while PD-409 is at the elbow.

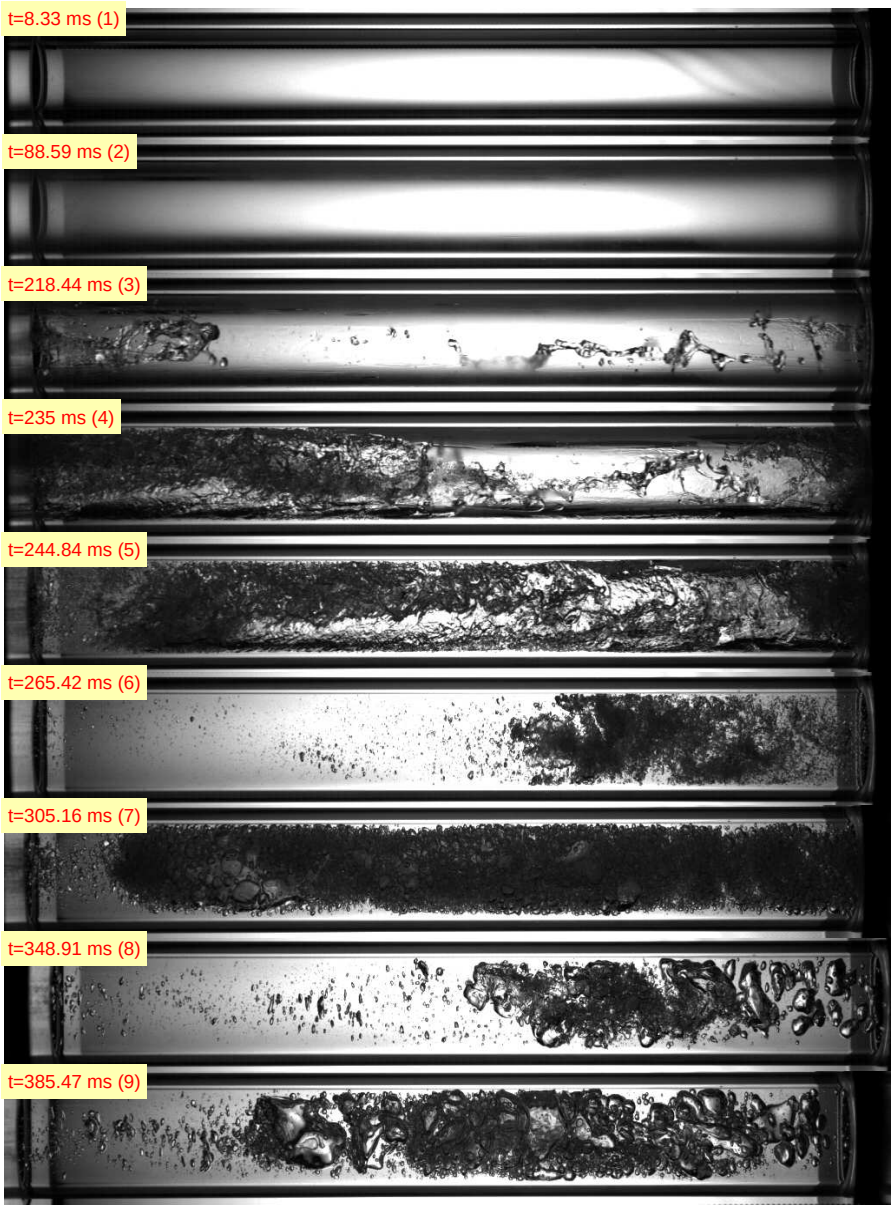

Figure 4.17: Video frames of the filling at the dead-end for the L configuration. Flow from left to right, fluid is deareated water; $P_{tank} = 7$ bar; $P_{line} = 10$ mbar

not visible anymore). This indicates that vapor arrives at the dead-end after 88 ms and it condenses on the colder wall. The vapor front travels well ahead of the liquid and is remarkably fast considering that the first liquid droplets arrive after 218 ms (3). As known by the classic fluid dynamics, a pipe elbow creates a swirling secondary flow, which can be identified in frame (4): unlike the case of straight pipe where the flow is stratified in top/bottom direction (e.g. Fig. 4.9, snapshot 2), now the liquid wets the front side of the pipe. At 244 ms (5) the main liquid front enters the optical segment and causes a sudden increase in the pressure, visible in the pressure curve of the sensors at the elbow (PD-409). The pressure profile at the elbow recalls the double spike characteristics observed previously at the dead-end. At 20 bar driving pressure, the secondary flow will impact at higher velocity and also with higher mass flow, generating the first pressure spike that is not visible with the present 7 bar tank pressure. Frames (6) and (8) captures the flow pattern at the two first pressure peaks: the minor pressure at time (8) makes the gas bubble considerably bigger than in time (6). It is also interesting to note the remarkable displacement of the pipe itself during this fast transient. Comparing frames (8) and (9), the branch moves about 4 mm; in fact the elbow configuration is known to induce the strongest FSI during water hammer [88].

4.4.2 Tee (T)

In the case of the T geometry and deareated fluid, the pressure peaks in the two branches dead-ends are identical (<1 bar difference) and their impact time is practically the same: the maximum time delay between the peaks in the two branches is 0.2 ms (Fig. 4.18, left). That can not be observed in case of saturated fluid (Fig. 4.18, right), where the two pressure profiles appear as a sort of complementary to each others: when the pressure drop in one dead-end (e.g. for PD-507 at 161 ms), it rises in the other dead-end (PD-303). This effect is due to the mutual acoustic influence of the two branches. The compression wave upon the pressure peak at one dead-end reflects in the other branch adding up to the existing wave. This mechanism is more visible in T2 geometry.

The general profile is also rougher than the deareated water profile and reproducibility is worse than the other configurations. The reason lies in the desorption of the dissolved gas which does not occur neither homogeneously nor uniformly, and it is somewhat made more random-like by the tee junction.

4.4.3 Tee with asymmetrical branches (T2)

The effect of the pressure wave reflection is visible in the case of asymmetrical branches (T2). Figure 4.19 depicts the pressure evolution at both dead-ends and at the tee junction for the T2 geometry in case of deareated water. The profile of

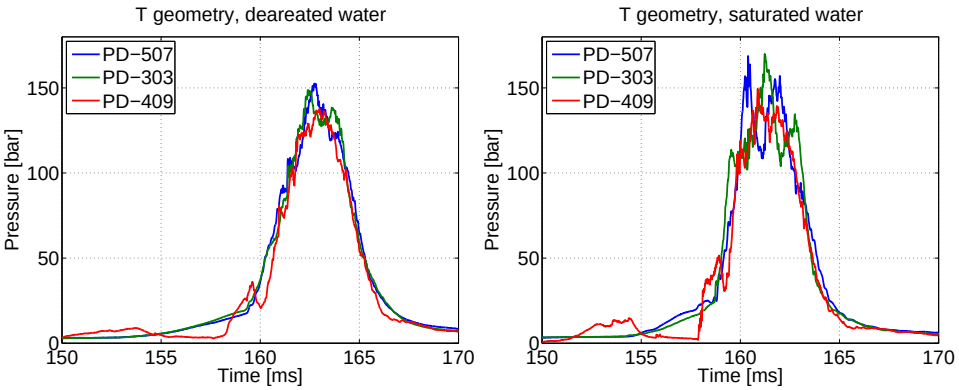

Figure 4.18: Pressure signals in the T geometry: sensors PD-507/303 are at the dead-end of the branches, while PD-409 is at the tee junction (see Fig. 3.8)

the pressure peak at both ends is the result of multiple reflections of the pressure wave traveling from one end to the other. First, the filling of the branch generates a first pressure peak, occurring sooner for the shorter branch. The higher pressure peak (225 bar, PD-303) takes place in the longer branch because it is the last cavity to be filled with the liquid. This causes a compression wave that propagates to the shorter branch inducing a second spike (210 bar, PD-507) which in turn causes a spike on the longer branch. The time delay between the two peaks is 1.3 ms. Considering the distance between the two sensors (1500 mm), this gives a speed of sound of 1154 m/s. This value is 15% smaller than the theoretical value of 1361 m/s for water: this is due to the amount of residual gas in the line that reduces the speed of sound. The main wave moves subsequently upstream towards the tank and the pressure in the test-element ends drops to about 5 bar. When the main pressure wave moves again downstream, the mutual interference of the reflections is still present in the second pressure peak (at about 240 ms). Now the shorter branch has a slightly higher pressure of 86 bar compared to 82 bar of the longer branch. From the forth peak on (t $>$ 290 ms). the effect of the acoustic reflections is no longer detectable in the pressure profile.

4.4.4 Cavitation in the elbow configuration

In the elbow geometry, cavitation occurs in both deareated and saturated water. It has also been observed in ethanol saturated at 1 bar GN2, but not in deareated ethanol nor in 20 bar GN2 saturated. This confirm the previous remark that there is an intimate connection between the pressurizing condition of the fluid and the

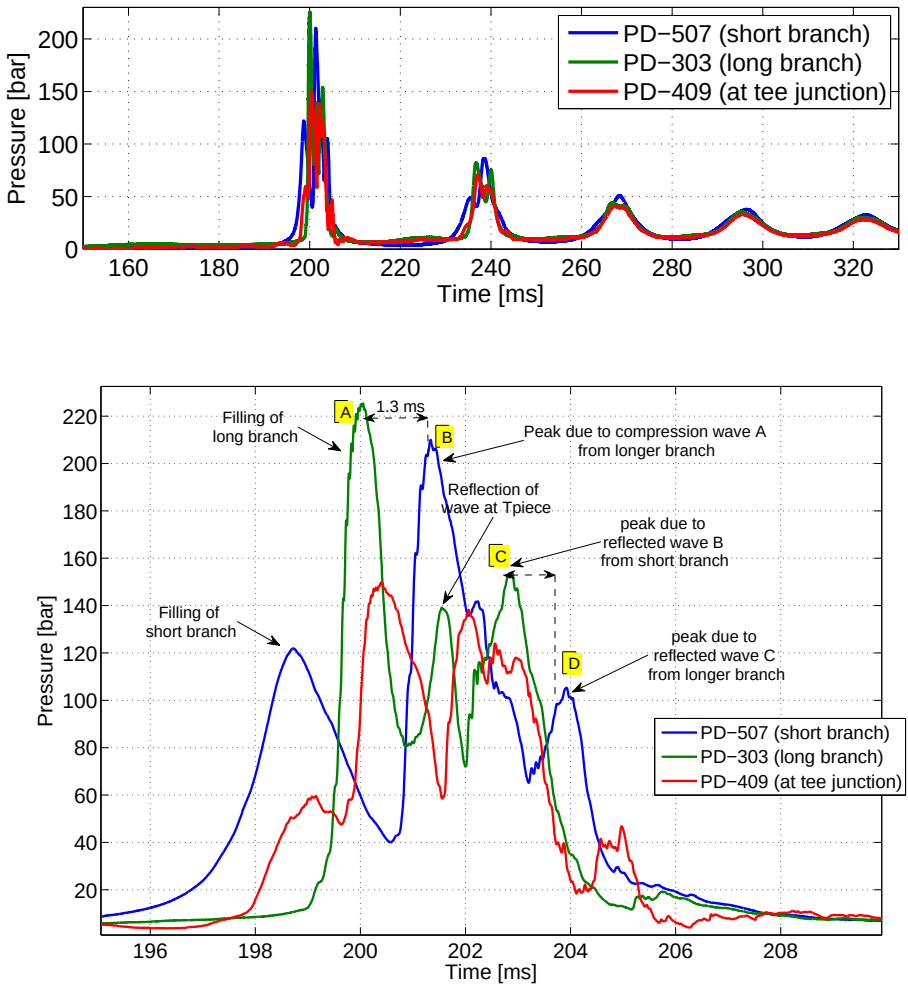

Figure 4.19: Pressure signals in the T2 geometry with asymmetrical branches

inception of cavitation. The presence of a junction such as an elbow or tee enhances the cavitation because of the additional pressure loss. This phenomenon alters the normal evolution of the pressure during the priming and introduces high frequency oscillations, related to bubble dynamic effects. Cavitation in saturated water is somewhat more violent, with stronger pressure gradient and higher pressure peaks. Figure 4.20 shows the pressure signals in three significant positions during the cav-

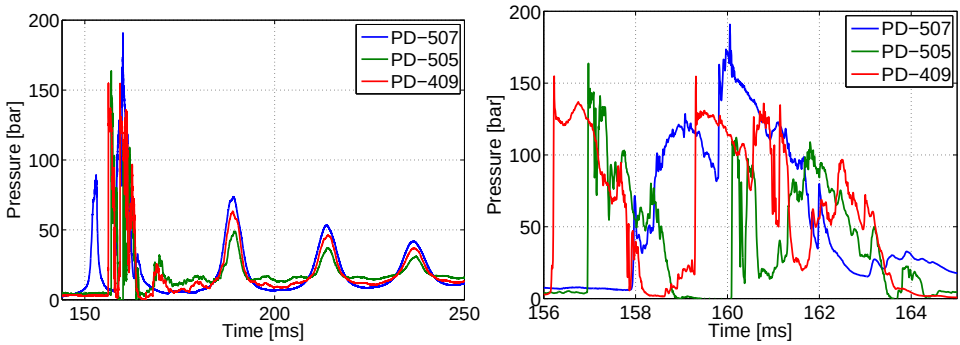

Figure 4.20: The pressure evolution upon a cavitation event in the elbow. The position of the sensors is: at the dead-end (PD-507), at the elbow (PD-409), at the valve (PD-505).

itation in the elbow set-up. The first pressure peak (magnified in Fig. 4.20, right) shows very strong gradients: the pressure rise at the elbow is 150 bar in 0.03 ms, which corresponds to a pressure gradient of 5000 bar/ms. This value is abnormally high for a usual water hammer-generated compression wave, and it rather indicates a shock wave induced by cavitation. The pressure profile of the first peak is highly irregular, only from the second peak on the three signals are in phase again and assume their usual smoother profiles.

The path of such a strong perturbation wave can be better analyzed with the additional support of the strain gauge signals. Figure 4.21 displays the simultaneous signals of all the transducers along the test section: it might look quite challenging to interpret, but only the sharp rises (almost vertical) in the signals are of interest for the purpose of this analysis. The same data can be evaluated in Fig. 4.22, where the signals are plotted in the time-space diagram, so that the path of the perturbation wave can be better tracked. The positions of all the sensors have been described in Chapter 3. To allow comparison, the signals are made dimensionless with respect to their maximum value, in this way the y-axis ranges between 0 and 1. Measuring the time delay between the sensors allows a rough estimation of the wave speed. This is particular helpful to distinguish the region filled with only liquid from the regions where gas is present. Table 4.1 lists these calculated wave speeds in the different segments along the pipe.

The strong perturbation caused by the bubble collapse occurs at the elbow (C1/PD-409 in Fig. 4.21) and propagates in both direction upstream and downstream arriving at the same time in the strain gauges U1/SG-02 and D1/SG-03. It

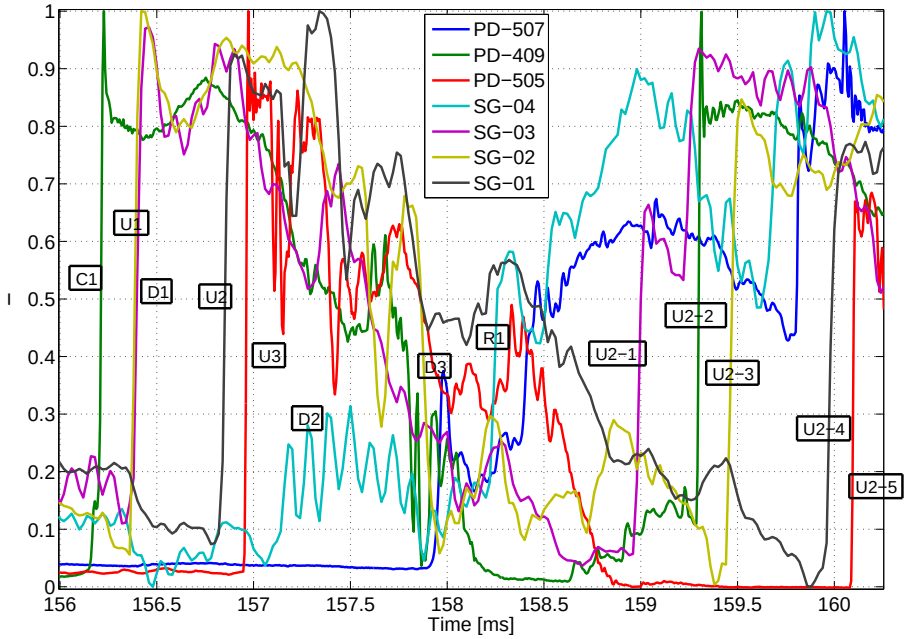

Figure 4.21: The pressure and strain gauge signals in the elbow test section during the first pressure rise

sensors	distance	label	traveling time [ms]	wave speed [m/s]	label	traveling time (backwards upstream) [ms]	wave speed [m/s]
PD-505/SG-01	101 mm	U3	0.082	1232	U2-5	0.080	1263
SG-01/-SG-02	607 mm	U2	0.46	1319	U2-4	0.48	1265
SG-02/PD-409	264 mm	U1	0.20	1320	U2-3	0.19	1390
PD-409/SG-03	306 mm	D1	0.22	1391	U2-2	0.28	1093
SG-03/-SG-04	586 mm	D2	1.74	337	U2-1	0.71	825
SG-04/PD-507	92 mm	D3	0.79	116	R1	0.32	288

Table 4.1: Position of the sensor along the test section in L geometry and the calculated wave speed. The accuracy on the time difference is ±0.01 ms.

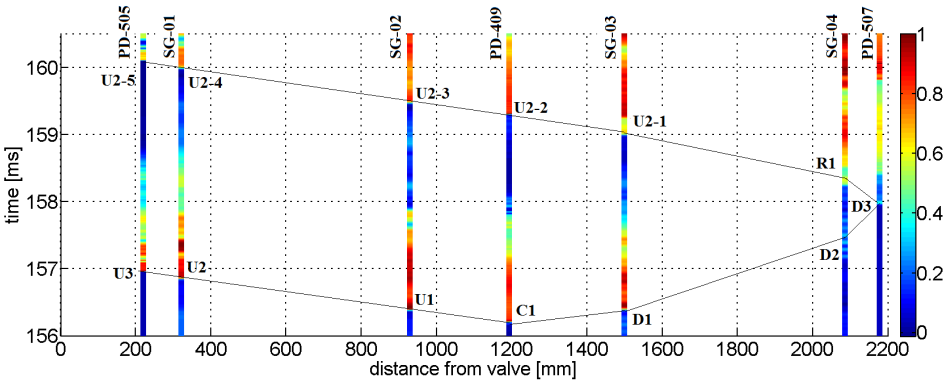

Figure 4.22: The evolution of the pressure and strain gauge signals in time-space diagram. The sharp change in color denotes the passing of the shock wave: the steepness of the line connecting these discontinuities is the wave speed (more precisely its reciprocal). The signals are dimensionless.

travels faster upstream passing over U2/SG-01 and U3/PD-505: this indicates that in this segment the pipe is filled with only water. The calculated velocity of the perturbation moving upstream is in fact between 1320 m/s and 1232 m/s (Table 4.1). The velocity towards to the dead-end is considerably slower, in fact when reaching D2/SG-04 and D3/PD-507 its value drop to 337 m/s and 116 m/s, a clear sign of the presence of gas, as expected. The wave gets then reflected (R1) and moves upstream, as detected by the sensors in U2-1/SG-03, U2-2/PD-409, U2-3/SG-02, U2-4/SG-01 and finally at the valve in U2-5/PD-505.

As listed in Table 4.1 the values of the wave speed in the upstream branch of the elbow are fairly close to the theoretical values of the speed of sound in water (1350-1390 m/s, depending on pressure and also pipe elasticity). This is in line with the fact that the upstream branch should be filled with water only, since the residual gas has been "pushed" toward the dead-end by the liquid front. However a caveat must be mentioned. The calculated wave speed is the velocity at which the perturbations propagate, which is not necessary the speed of sound of the liquid. In fact, a shock wave is generated upon bubble collapse, and its propagation speed is supersonic by definition. This might seem in contradiction with the calculated values of the wave speed. However, the above described case refers to saturated water, so the gas desorption takes place making the flow two-phase in nature. The liquid-gas mixture persists along the whole test section, at least during the initial filling, and its speed of sound is always lower than the one of pure water. Therefore

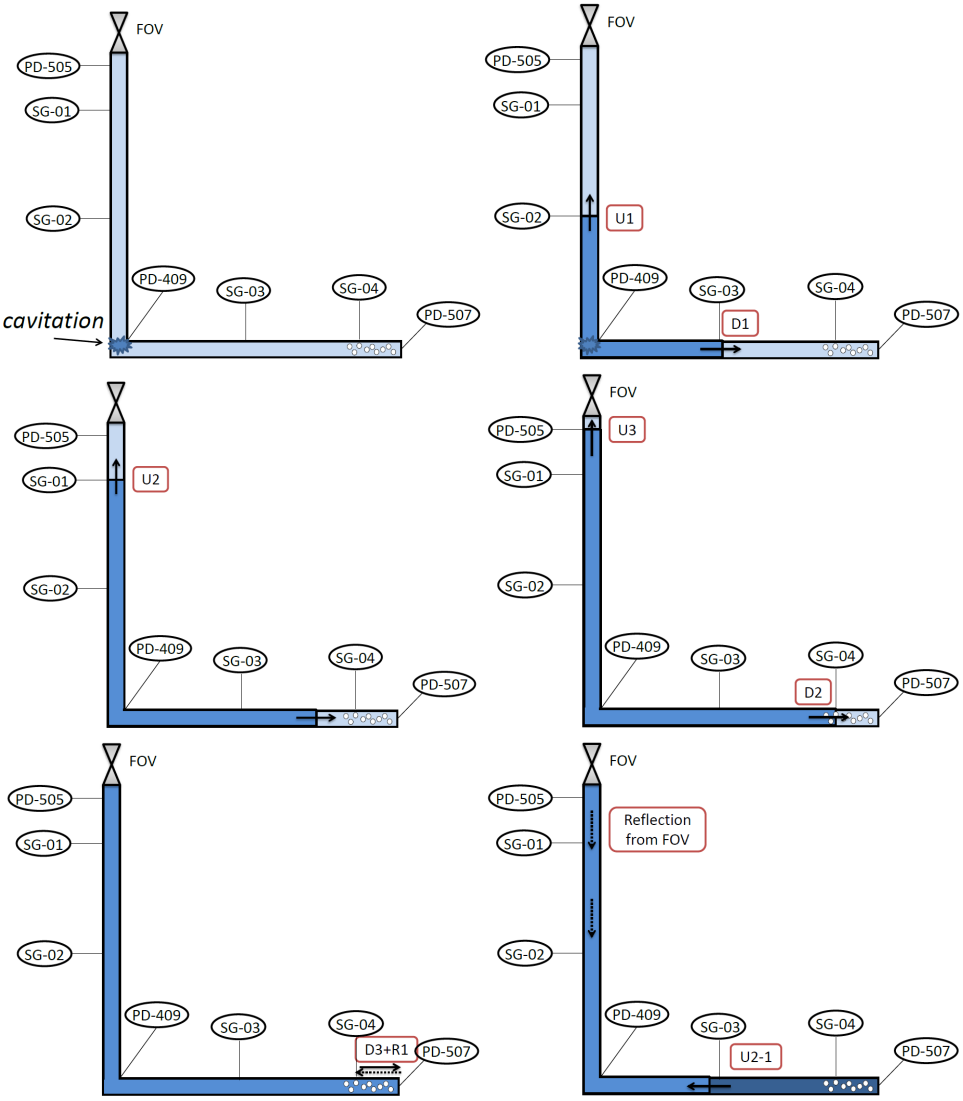

Figure 4.23: Representation of the path of the perturbation shock wave induced by the cavitation at the elbow. The label in the red boxes refer to the pressure rise as noted in Fig. 4.21. After the perturbation gets reflected at the dead-end, it moves upstream, passing over the sensors in the positions labeled U2-2, U2-3, U2-4, U2-5 in the previous figure.

the calculated wave speeds are the supersonic velocities of the shock wave as it travels in the two-phase flow. The multi-phase nature of the flow is qualitatively investigated in Chapter 7, where thanks to the support of HSI a spectacular shock wave is indeed observed and described.

The main point of this analysis is to stress out that the assessment of the speed of sound in two-phase flow might be tricky, with the further complication added by the cavitation phenomenon.

The same analysis can be performed for the T and T2 geometries. It can be shown that typical wave effects such as reflection, diffraction and interference must be taken into account in order to describe the evolution of the pressure when the wave travels across geometrical change such as the tee junction.

4.5 Fluid-structure interaction

The three mechanisms of interaction between liquid and pipe have been introduced in Section 2.3.6. The investigation on fluid-structure interaction (FSI) will here focus on the Poisson coupling and the junction coupling, while the friction coupling will be considered in Chapter 6.

The pipe elasticity affects the rigidity of the system fluid-structure by lowering the propagation speed of the pressure wave as according to Eq. (4.2):

$$c_{eff}^2 = \frac{c_f^2}{1 + \frac{K_f}{E}\frac{D}{e}\psi} \tag{4.2}$$

where the coefficient ψ depends on the support conditions (see Section 2.3.6).

4.5.1 Influence of the material elasticity

As it can be seen in Eq. (4.2), the only pipe material characteristic that plays a role is the modulus of elasticity, or Young's modulus. To assess the influence of this parameter, three different material are tested, keeping the geometric size of the pipe the same. Some relevant properties of the different materials are listed in Table 4.2.

	steel	titanium alloy	aluminum 6061
E [GPa]	180	107	68.9
Poisson ratio ν	0.305	0.320	0.334
c_{mat} [m/s]	4804	4887	5052

Table 4.2: Material properties

The values of the effective wave speed c_{eff} in different materials as according to

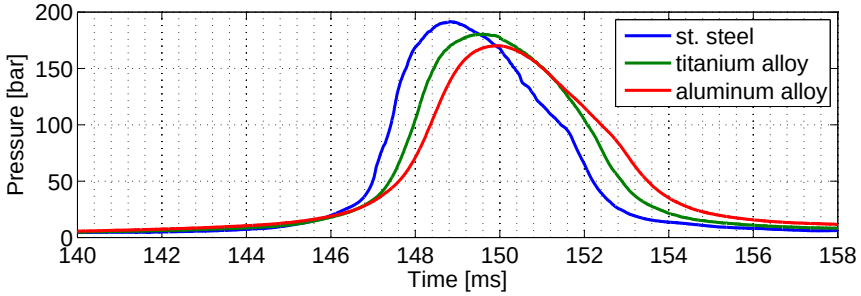

Figure 4.24: Pressure profiles in the different materials, fluid is deareated water

Eq. (4.2) are calculated in Table 4.3. As expected, the wave speed is the lowest for aluminum alloy, due to its lowest elasticity modulus, which results in 84.4% of the unconfined value for water. Since it is not possible to test with an infinitely rigid pipe, the use of the ratio with the case of stainless steel is more practical for a direct assessment of the material influence.

The experimental pressure peak profiles obtained with the three materials are depicted in Fig. 4.24. Deareated water is used to avoid the disturbances generated by the gas desorption. The influence of the material is evident not only on the pressure peak value, but also on its timing: the less rigid the pipe is, the less steep the pressure rise is, due to the displacement of the pipe which smooths the fluid pressure gradient. The measured time delay between the stainless steel and aluminum alloy is however quite small, only 1.6 ms.

The experimental values of the pressure peaks are reported in Table 4.4, as well as their ratio with respect to stainless steel. These ratio are in good agreement with

Fluid		st. steel	titanium alloy	aluminum 6061
water, $c_f = 1465$ m/s	c_{eff} [m/s] (upstr anch.)	1362	1304	1236
	c_{eff}/c_f	0.930	0.891	0.844
	$c_{eff}/c_{st.steel}$	1	0.958	0.908
ethanol, $c_f = 1229$ m/s	c_{eff} [m/s] (upstr anch.)	1171	1135	-
	c_{eff}/c_f	0.952	0.924	-
	$c_{eff}/c_{st.steel}$	1	0.970	-

Table 4.3: Effective wave speed in different material for water and ethanol. It is calculated assuming upstream anchored pipe as a boundary condition.

Fluid		st. steel	titanium alloy	aluminum 6061
water	P [bar]	191.6 ± 2.2	180.6 ± 2.6	170.2 ± 3.1
(deareated)	ratio wrt st.steel	1	0.943	0.887
ethanol	P [bar]	132.8 ± 1.8	124.8 ± 1.7	-
(deareated)	ratio wrt st.steel	1	0.940	-

Table 4.4: Experimental values of the pressure peaks obtained with the different materials (at least 3 tests for each material)

the analytic ones reported in Table 4.3, with a difference of only 2% in case of water and 3% in case of ethanol. The results are also consistent in the sense that they are all under-estimated compared to the prediction.

4.5.2 Poisson Coupling

The Poisson coupling relates the change in the fluid pressure to the radial contraction (or expansion) of the pipe wall as a consequence of axial stresses in the pipe. These stress-wave-induced disturbances travel at the speed of sound of the material, which is faster than the speed of sound of the liquid, and therefore will appear ahead of liquid pressure wave. These are known as precursor waves [88].

In order to detect the waves traveling in the pipe and in the liquid and their mutual interaction, a useful representation is by means of the distance-time diagram, as presented by Vardy et al [100] or by Wiggert and Tijsseling [106]. The boundary conditions necessary to determine the wave path are the tank, the dead-end and any position where there is a change in the internal geometry, such as valves and junctions. Limiting this analysis to the straight configuration, the liquid pressure waves will be reflected at the tank, at the dead-end and also at the valve, because of the pressure loss caused and the change in the internal diameter; the wave in the solid will travel between the dead-end and the valve, but it will not travel through it towards the tank. The much higher mass of the valve compared to the pipe and the mechanical connections with the pipe (flanges) will contribute to stop the structural axial wave. With such boundary conditions, the wave path can be drawn for both liquid and solid, as shown in Fig. 4.25. The y-axis refers to the distance, where y=0 is the valve position, the tank is at y=-1023 mm and the dead-end is at y=2045 mm. The time axis has been shifted to zero in correspondence of the initial pressure rise; the pressure signal of the sensors at the dead-end (PD-507) and at the valve (PD-505) are plotted atop.

Upon the impact at the dead-end (t=0), the main water hammer wave (thick red line) is generated and travels towards the tank as a compression wave, as detected by the sensor PD-505 at t=1.3 ms. After reaching the tank (t=2.24 ms), it then

gets reflected and travels back as an expansion wave, causing the pressure to drop at the valve (t=3.2 ms) and finally at the dead-end (t=4.48 ms). This pattern is in line with the classical water hammer theory. More interesting, it is the effect of the valve. Since the coaxial valve introduces quite a high pressure loss, it is reasonable to assume that the pressure wave gets reflected towards the dead-end. This additional wave is plotted in magenta. It can be observed that the passing of this reflection wave causes a spike in pressure rise in the sensors PD-505 (t=1.64 ms) and it is responsible for the small bump at the dead-end (t=2.78), just before the violent cavitation-induced drop. After reaching the dead-end, it bounces back and again causes a small pressure rise at the valve (t=4.24 ms), and so does its

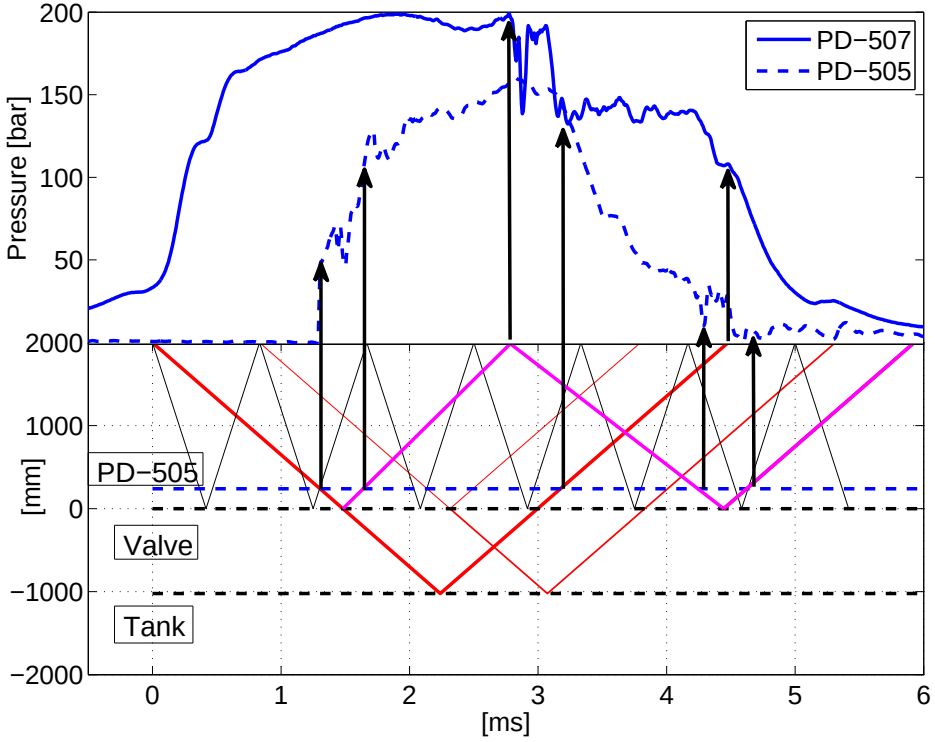

Figure 4.25: The distance-time representation of the wave paths, including both the fluid wave paths (plotted in red and magenta) and structural wave paths (plotted in black thinner lines). The corresponding pressure evolution is plotted atop to allow the potential causes for any fluid pressure perturbation.

second reflection (t=4.62 ms). When the second reflection reaches the dead-end, its intensity has damped out and no perturbation can be detected.

The interesting thing is that this additional pressure wave generated at the valve acts as a compression wave, indicating that the condition at the valve shall be considered as a (partially) closed end. This effect might be the cause for the pressure bump observed in similar experiments described in literature. In the aforementioned work of Lecourt and Steelant [54] (see Fig. 2.11), an unexplained pressure rise (labeled as "bump" in their own description) is observed at the top of the main pressure plateau, at about the middle position (i.e. when the compression wave reaches the tank). In their set-up, the overall distance tank to dead-end is 3900 mm, while the test section (valve to dead-end) is 2000 mm. That means that any (potential) reflected pressure wave from the valve would reach the dead-end after a 2000/3900 of the wave half period, which is indeed in line with the observation.

The same reasoning might justify an identical bump observed by Lema [55, page 139] in the straight pipe. In fact, considering the geometry of his experimental set-up, the timing of the wave from the valve perfectly matches the position of the bump in the pressure plateau.

Concerning now the structural waves, the timing of their path does not seems to be responsible for any pressure perturbation in the fluid. However, it is not easy to clearly detect such Poisson coupling, as the pressure signal is often disturbed by others two-phase flow phenomena, as proved. The pressure change due to the radial stresses is usually small and could be mistaken as related to bubble dynamics. In addition, the analysis of the path based on the sole time-distance diagrams as plotted in Fig. 4.25 might be trivial, since a given structural wave path could just randomly match a pressure perturbation, given the higher frequency of the structural waves. To detect the precursor wave and their potential Poisson coupling, the pressure signal must be analyzed together with the data of the strain gauges.

Analysis of strain gauges data Figure 4.26 plots the signals of the pressure sensors and strain gauges (SG) along the 2045 mm straight pipe (their exact positions is described in Chapter 3) in case of deareated water. To allow comparison, the signals are made dimensionless with respect to their maximum value, in this way the y-axis ranges between 0-1. It is possible to detect the passing of the main water hammer wave starting from the dead-end, however no evidence of the precursor wave can be observed. This in fact shall appear as a small perturbation in the strain gauge signals well ahead of the main water hammer pressure wave. More precisely, considering the speed of sound in the material (4804 m/s for stainless steel), any precursor wave should be detected at the test section inlet (SG-01, near the valve) after only 0.43 ms of the pressure rise. Despite an intensive data analysis, it was not possible to identify any Poisson coupling effect in the pressure sensor signals.

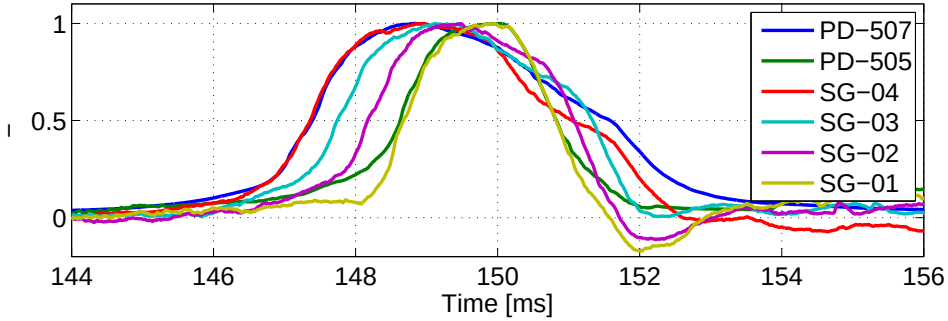

Figure 4.26: Dimensionless signals of the pressure sensors and strain gages along the pipe. Fluid is deareated water, $P_{tank} = 20$ bar; pipe material is stainless steel.

A possible explanation is based on the time scale of the excitation. Tijsseling and Vardy [89] suggested that FSI is important when the time-scale of the structural behaviour is larger than the time-scale of the excitation. The time scale of the structure is the traveling time of the wave in the solid, thus $t_s = 2L/c_s = 0.86$ ms. As a time scale of the excitation, Uffer [94] proposed the rise time of the pressure, which is about 2 ms in the actual configuration. This latter is larger than the structural time, and therefore FSI can be neglected. In fact, from the point of view of the structure, the force generated by the water hammer is not seen as a step, but rather as a ramp. Since the relaxation time of pipe is shorter in comparison with the pressure-induced excitation, the structure has enough time to adapt to the new stress condition and therefore any potential Poisson coupling effect would be smoothed. Indeed, many FSI investigations in water hammer experiments are not performed in the classical way of valve closing but instead by hitting a suspended pipe with a rod [88, 100] to properly generate a pulse and not a ramp as an excitation input for the structure.

Another possible explanation for not having detected the Poisson coupling lies in the low speed of sound of the liquid-gas mixture. The radial deformation of the pipe induces a noticeable pressure change in the fluid as long as the fluid bulk modulus K_L is high enough, as stated by the relationship $dP = -K_L dV/V$. The bulk modulus is directly linked to the speed of sound, $K_L = c^2\rho$. The amount of residual gas in the line is high enough to lower the speed of sound of the pure liquid down to ten times; that in turn dramatically lowers the liquid (or more correctly the liquid-gas mixture) compressibility so that a change in volume will correspond to a negligible or not measurable change in fluid pressure.

This condition exactly occurs during the first pressure rise at the inlet of the test section. Due to the pressure peak caused by the water hammer, the pipe undergoes an axial stress which correspond to a remarkable axial elongation, as measured by the sensor SG-01 (Fig. 4.27, left). This axial strain induces a radial contraction which however does not affect the pressure measured at PD-505. In fact, at this point the pipe is not fully filled yet with water and two-phase flow is still present at the valve. The same event occurs at the pressure rise of the second peak (Fig. 4.27, right) but now a small change in the fluid pressure can be observed since the volume is now filled with water. This small pressure rise at the valve (PD-505, marked by the black circle) takes place well ahead of the main compression wave and it is certainly due to the radial contraction of the pipe, since SG-01 shows a decreasing value[4]. It appears as a gradual increase rather than a pulse for the reasons explained before concerning the time scales. Although this effect does not correspond to a precursor wave, it might yet be referred to as Poisson coupling, since the internal fluid pressure is related to pipe wall axial strain. That does not mean that precursor waves do not occur, but the priming configuration is not the optimal setup for detecting such FSI effects.

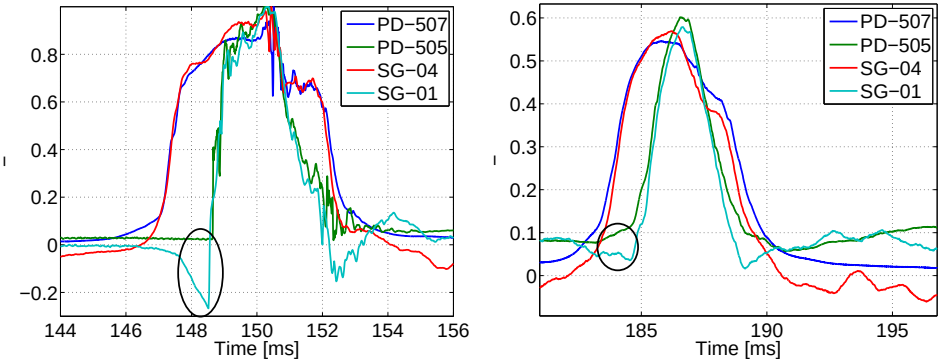

Figure 4.27: Dimensionless signals of the pressure sensors and strain gauges during the first pressure peak (left) and the second pressure peak rise (right)

[4]When a positive/negative change in the pressure is accompanied by a negative/positive change in the strain, it means that the structure acts on the fluid and not vice-versa. In fact, in static conditions, when the internal fluid pressure increases/decreases, the corresponding strain will also increases/decrease: in these cases the strain gauge acts as a pressure measurement.

4.5.3 Numerical simulations

The software EcosimPro does not include pipe motion and Poisson-coupling mechanism, so the precursor wave can not be simulated. The effect of the pipe elasticity is however taken into account by the implementation of Eq. (4.2). A parametric study run with different materials has confirmed the effect of the material elasticity on the pressure peak as experimentally found in Section 4.5.1.

A more interesting effect can be observed in the pressure plateau, where a pressure spike of about 0.5 ms duration is present at very begin (Fig. 4.28). The intensity of this spike, with respect to the value of the plateau, depends clearly on the material elasticity, being more pronounced for more deformable pipes. Since the software does not include any equation for the pipe movement, the origin of this initial over-pressure is unclear. In the source term of the mass conservation equation [31, page 95-96], the wall compressibility is multiplied by the pressure gradient $\partial P/\partial t$ to account for the volume change. This couples the geometry with the dynamics of the pressure and might then introduce a time delay. The source term would give rise to an additional volume only after a finite time, causing the pressure to decrease with the same delay. This coupling however does not seem to be correct, as any time the pressure is constant or has local maxima/minima, i.e. $\partial P/\partial t = 0$, the source term cancels out as well as the material elasticity. The implementation of equations for the longitudinal pipe wall motion are beyond the scope of this work. It has to be underlined that such over-pressure spikes have not been observed in the experiments. A second bump is present at the end of the main pressure plateau (Fig. 4.28, right), when the pressure starts decreasing due to the expansion wave

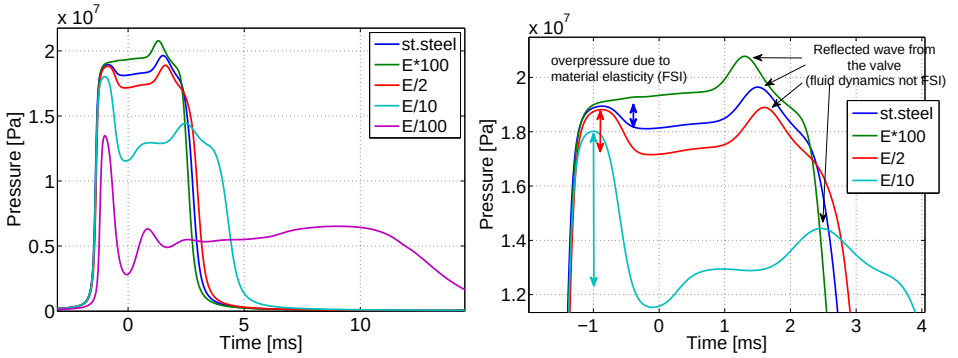

Figure 4.28: Numerical simulations of the pressure peak with different material elasticity. The reference value E in the legened corresponds to the elasticity of stainless steel. Fluid is deareated water.

coming from the tank. It is constant and independent on the material elasticity. This is indeed due to the reflected wave from the valve, as experimentally observed and already commented (Fig. 4.25).

4.5.4 Geometrical constrains

Effect of the support conditions In classical water hammer theory, the influence of the support conditions is expressed solely by the correction coefficient ψ in the speed of sound equation (Eq. 4.2). That is also the equation implemented in the numerical code of EcosimPro. The actual experimental setup corresponds to the condition of upstream anchored pipe ($\psi = 1 - \nu/2$). Due to the presence of the pressure sensor at the dead-end and the necessity of purging after each test, it was not possible to set-up a fully anchored pipe to prevent axial movement. In order to assess any effect of the support conditions, the clamps along the pipe (described in Chapter 3) have been removed so that the whole test section "hangs" from the valve and it is free to vibrate. However, comparing the test results in this condition with the standard geometry, no difference has been observed in the pressure peak. Some minor differences have been found in the frequency (see Chapter 5) and in the damping behavior (see Chapter 6).

Junction coupling When the support conditions allow for pipe motion, the most important FSI mechanism is junction coupling [88]. When a junction such as an elbow, a bend, a tee or also a valve is able to move in the axial pipe direction, mutual forces between the fluid and the pipe system may cause a dynamic interaction. Testing with the elbow and the tee geometry has not however underlined such (potential) interactions. The movement of the whole test section in the case of the elbow geometry is clearly observed in the signals of strain gauges and accelerometers, but no correspondence is detected in the pressure signals. The reason is believed to be the high compressibility of the mixture caused by the initial residual gas in the line, which uncouples the pipe dynamics from the fluid dynamics, as explained before in Section 4.5.2.

4.6 Summary

In this chapter the effects of different test and boundary conditions on the pressure peak were discussed. The most important outcome is the remarkable influence of the pressurizing conditions: when the liquid is saturated with GN2 the desorption has a dramatic effect on the pressure peak due to the amount of released gas which act as a cushion. With the support of HSI it was possible to provide an explanation of the pressure profile relating the multiple steps/plateaux to the effect of gas desorption

which creates a train of liquid slugs and gas pockets impacting on each others. Numerical simulations including the gas desorption effect also confirmed this influence, with an excellent matching between experiment and numerical simulation in case of saturated ethanol. The desorption sub-model included in EcosimPro requires to set a desorption time constant. This was done by a trial and error procedure, however the best fit value does not seem consistent if the boundary conditions are changed.

The pressurizing conditions have also shown to be intimately connected with the inception of cavitation. The occurrence of cavitation and its subsequently bubble collapse introduces high frequency oscillations and strong pressure gradients in the fluid which affect the pressure profile and change the wave pattern. The analysis of the pressure evolution in the elbow set-up showed that the strong perturbations introduced by the cavitation propagate in the fluid in both direction and get reflected at dead-end and reflected/diffracted at junction, superimposing with the main water hammer pressure wave. This is an important effect as it could lead to pressure peaks higher than the Joukowsky pressure.

The combined analysis of the pressure and strain signals offer a valuable method for the investigation of potential FSI effects. No precursor waves were detected and a possible explanation was provided. However, in particular conditions, the radial contraction of the pipe was observed to induce a pressure increase, in a similar way to the Poisson coupling mechanism.

Chapter 5

Frequency Analysis

5.1 Introduction

In this chapter the frequency content of the pressure oscillations will be analyzed with respect to the effect of different boundary conditions. As in the previous chapter, the effect of the tank and line pressures, the pressurizing conditions, the geometry and the material are investigated. The fluid speed of sound is the fundamental property for the calculation of the frequency, and the presence of a non dissolved gas dramatically affects its value. By knowing the speed of sound from the analysis of the test data, the gas content could be estimated, but its assessment is not easy due to the fact that different flow patterns lead to different formulation of the speed of sound as described in Section 2.3.5.

Calculations of the frequencies is performed with both the Fast Fourier Transform (FFT) and the Half Width at Half Max technique (HWHM, explained in Fig. 5.1). The HWHM is used to calculated the main frequency of the oscillation, namely the peak to peak timing, while the FFT is used for the analysis of higher frequency content and the detection of structural frequencies for FSI considerations. To analyze and compare the frequencies in different conditions, the peak-to-peak time is made

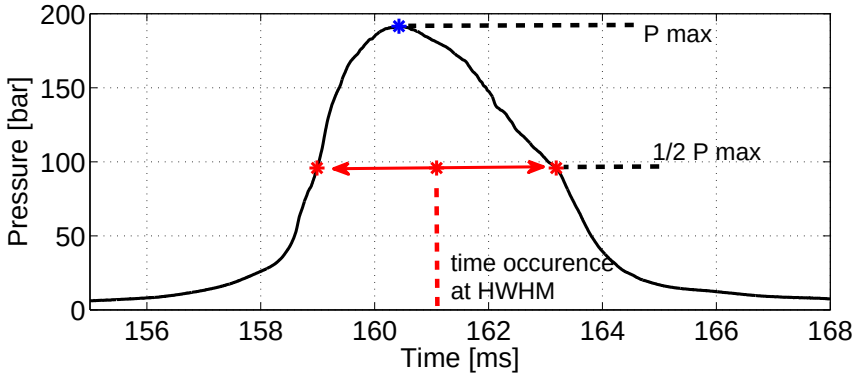

Figure 5.1: Graphical representation of the HWHM.

dimensionless with respect to the period between the first and second peak, named Δt_1. To help the comparison of the frequencies in different test conditions, the first pressure peak is shifted to t=0 in the presented diagrams.

For the sake of precision, it would be more correct to speak in terms of time period between the peaks instead of frequency. Due to column separation in fact, the time delay between the first and second peak is not related to the water hammer wave. As the pressure recovers at values higher than the vapor pressure of the fluid, the oscillations of following pressure waves can be properly referred to as water hammer frequencies.

5.1.1 General analysis of the pressure wave

First some general considerations are here highlighted to introduce the main characteristics of the wave frequency. The actual priming geometry can be sketched as in Fig. 5.2. Three different lengths play a role in the dynamic of the wave propagation. The fundamental water hammer frequency ($f = \frac{c}{4L}$) is dictated by the overall length L that the disturbance has to travel, namely from the dead-end to the tank. These positions represent in fact the physical boundary conditions in terms of pressure and velocity. In addition, when the main wave reaches the valve, it is partially reflected due to the geometry of the valve itself. The coaxial valve acts in fact like an obstacle for the fluid and thus generates a reflected wave that causes a pressure disturbance in the pressure signal as explained in Chapter 4 (see Fig. 4.24). This effect is numerically investigated in a parametric study and is illustrated in Fig. 5.3 : while the main length L is kept constant (in the numerical simulations a length L = 6 m is set in order to have higher peak duration and hence better time resolution), the test section length L_2 is increased. The "bump" in the signal can thus be clearly attributed to the reflected wave at the valve.

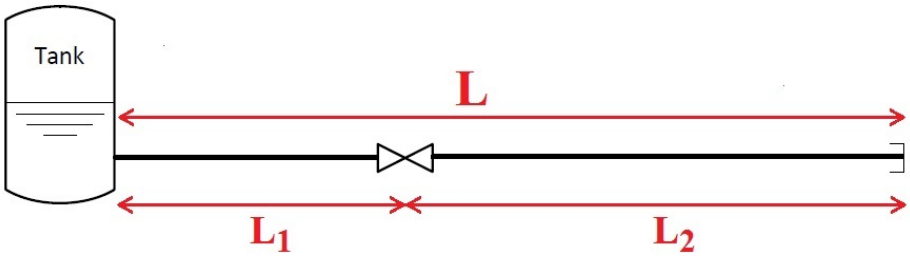

Figure 5.2: Representative lengths for the frequency assessment

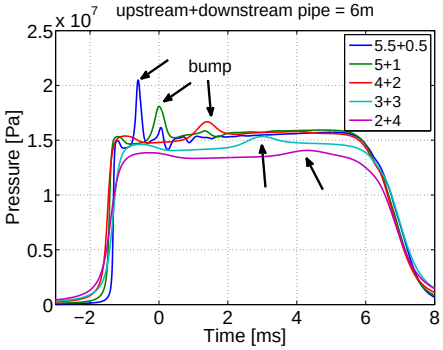

Figure 5.3: Numerical simulations remarking the "bump" caused by the wave reflection from the valve.

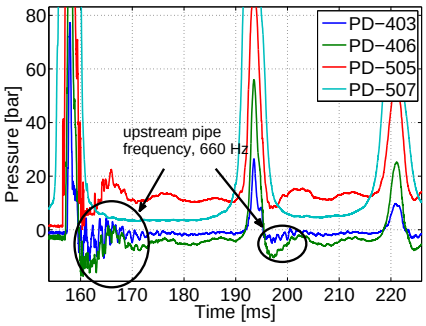

Figure 5.4: The 660 Hz oscillation visible in the upstream pipe

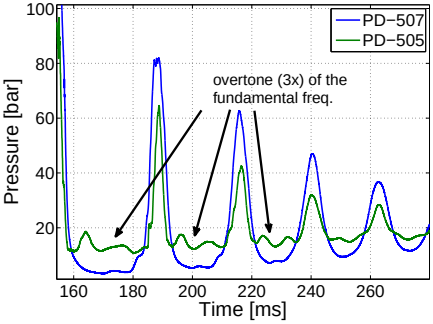

Figure 5.5: First overtone of the fundamental frequency

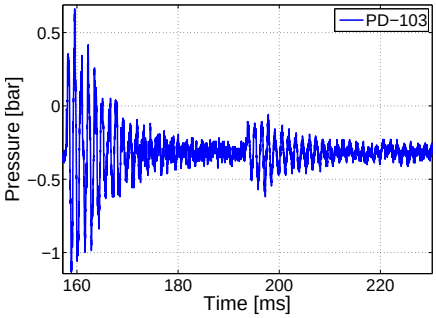

Figure 5.6: Pressure oscillations in the tank

The upstream pipe L_1 is an open-open pipe and its eigenfrequency is given by:

$$f_{L_1} = \frac{c}{2L_1} = \frac{1400\,m/s}{2 \cdot 1.023\,m} = 670\,Hz \tag{5.1}$$

When the main water hammer pressure wave arrives, it acts as an excitation and thus the fluid in the upstream pipe start oscillating at this very frequency. This can be clearly observed in Fig. 5.4 where the signals of the upstream sensors PD-403/406 are plotted. A frequency of 660 Hz is measured, which is in good agreement

with the theoretical value. This frequency is also detectable in the signal of PD-505, just downstream the valve, but not at the dead-end (PD-507) as it is damped by the high gas content.

In addition, a couple of interesting aspects can be underlined from the analysis of the experimental results. The theory of the water hammer explains that the all the odd multiple (3,5,7...) of the fundamental frequency f_0 are solutions of the problem as well. Indeed, the first overtone ($3f_0$) can be detected in the pressure signals (Fig. 5.5). A second fact observed in the experiments is the small oscillations of the pressure at the tank. Theoretically a constant pressure in the tank is assumed as a boundary condition, because the mass of water is much larger than the one in the pipe. Although this assumption is practically always valid, when the liquid level in the tank is low enough, it is possible to measure small pressure oscillations of up to 1 bar, as depicted in Fig. 5.6.

5.1.2 Numerical simulations

Numerical simulations will be here discussed only for the deareated and saturated conditions in the straight pipe geometry.

It is important to remind that in the case of two-phase flow, the grid discretization greatly affects the numerical results, therefore an educated choice must be made. The test-element is modeled with an increasing number of nodes, respectively 50, 100 and 200 nodes. While the first pressure peak is identical in each case, the frequency and the attenuation of the wave strongly depend on the number of nodes, as it can be seen in Fig. 5.7. Increasing the number of nodes, the frequency

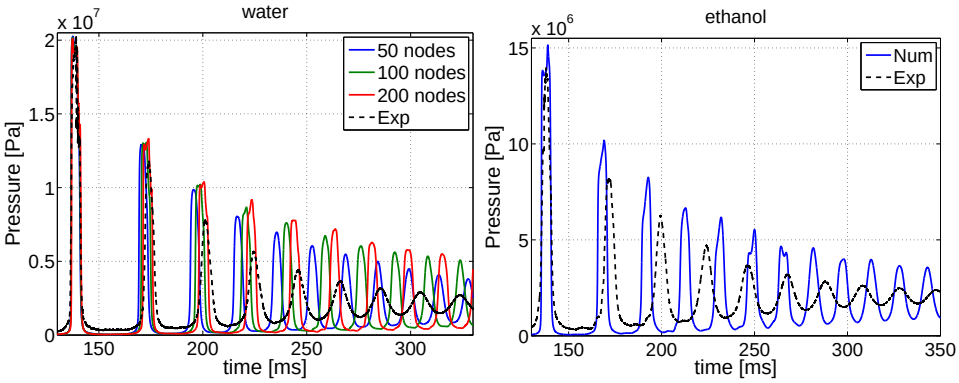

Figure 5.7: Numerical simulations for water (left) and ethanol (right). The case with ethanol has been simulated with 200 nodes

decreases and converges towards to experimental frequency. A choice of 100 nodes is an acceptable compromise between agreement with the test data and computational time. For ethanol, even with 200 nodes the mismatching is quite remarkable. The reason behind this disagreement is the known difficulty of calculating the speed of sound in a two-phase flow. Estimating the right amount of non dissolved gas is a key aspect and the desorption of gas from the liquid is a fundamental physical process to be taken into account. This will be addressed in detail in Section 5.3.

5.1.3 Speed of sound and gas content assessment

The mean speed of sound c can be indirectly calculated from the measured frequency: $c = 4L \cdot f$. Since c depends on the gas content and therefore also on the pressure (see Section 2.3.5, Eq. (5.2)), which changes rapidly both in time and in space, the 8^{th} oscillation is considered as the asymptotic steady frequency. From the 8^{th} oscillations on, the mean value of the pressure (peak to valley) is more or less equal to the tank value and the desorption process should be mostly completed. By reversing Eq. (5.2) it is then possible to assess the amount of gas present in the liquid, which includes the residual gas in the line and the released one from the desorption.

$$c = x\rho_L \left(\frac{G}{P}\right)^{1/\gamma} + \frac{\exp(\frac{P-P_0}{K_L})}{\left[(1+x)\,\rho_L \left(\frac{x\rho_L G^{1/\gamma}}{\gamma P^{(\frac{\gamma+1}{\gamma})}} + \frac{1}{E}\exp(\frac{P-P_0}{K_L})\right)\right]^{1/2}} \tag{5.2}$$

5.2 Effect of tank and line pressures

5.2.1 Tank pressure

Increasing the tank pressure leads to an increase of the main wave frequency as depicted in Fig. 5.8. This is in line with Eq. (5.2): the higher the pressure, the stiffer the gas bubbles and hence the compressibility of the liquid-gas mixture decreases.

Gas content assessment Since the line pressure is kept the same for every pressure, the gas content is the same. In the 2083 mm straight pipe test section with 10 mbar of GN2, the amount of residual gas is about 0.0065 g, assuming a perfect gas law. The mass of water in the overall line (3106 mm, since the upstream pipe is included) is 655 g, therefore the gas content mass ratio is $1 \cdot 10^{-5}$. Table 5.1 shows the experimental value of the frequencies, speed of sound and the corresponding gas content ratio calculated by Eq. (5.2). The reversed-calculated

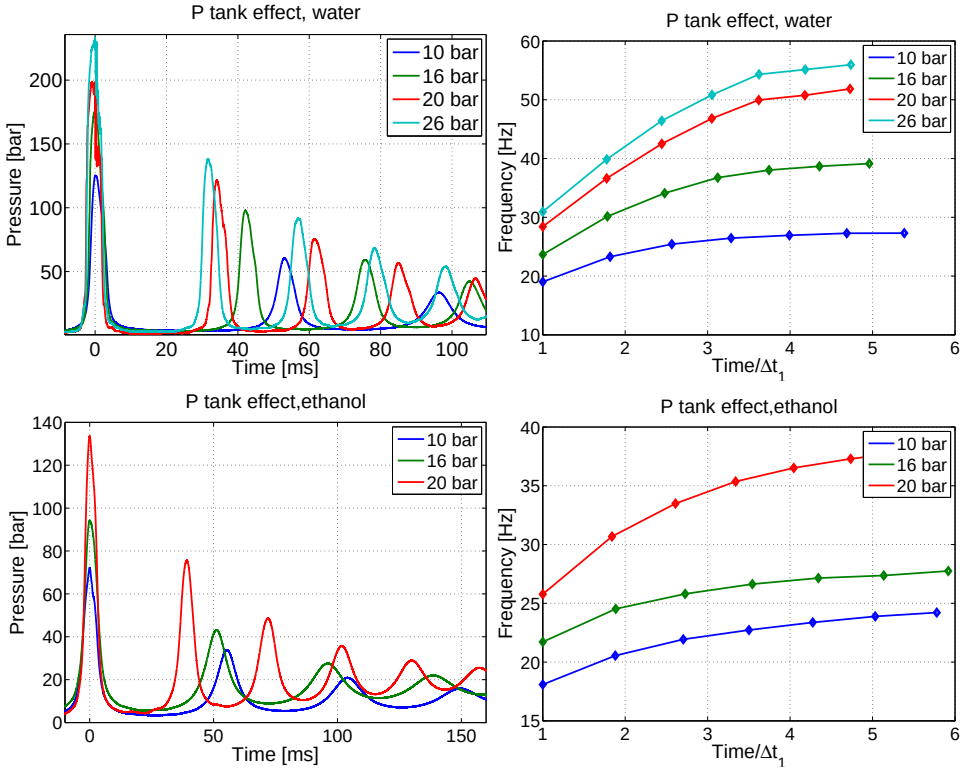

Figure 5.8: Effect of tank pressure for water (top) and ethanol (bottom).

P tank [bar]	8^{th} freq. [Hz]	c [m/s]	gas mass ratio [-]
10	27.3	339	$0.96 \cdot 10^{-4}$
16	39.1	484	$1.12 \cdot 10^{-4}$
20	52	645	$0.87 \cdot 10^{-4}$
26	55.6	707	$1.15 \cdot 10^{-4}$

Table 5.1: Experimental values of the speed of sound and its corresponding (theoretical) gas content. Fluid is water saturated at 1 bar

amount of non-dissolved gas is 10 times higher than the supposed one. For the sake of precision, in all the conditions the liquid is saturated at 1 bar for test procedure reasons. The amount of dissolved gas in water is then 0.02 g/kg × 0.655 kg = 0.013 g. Assuming the desorption process to be completed before the 8th time period, the total amount of initial residual gas + desorpted gas is then about 0.02 g in the test section. This makes a gas mass ratio of $3.6 \cdot 10^{-5}$, still three times smaller than the experimental one. The reasons for such a mismatching are not clear, probably the guessed amount of initial residual gas in the line based on the perfect gas law is under-estimated. It is however significant that the calculated amount of gas mass ratio is more or less constant for every different tank pressure. This can be better seen in Fig. 5.9 where Eq. (5.2) is plotted for the different tank pressures; the assessed gas amount is marked by diamonds.

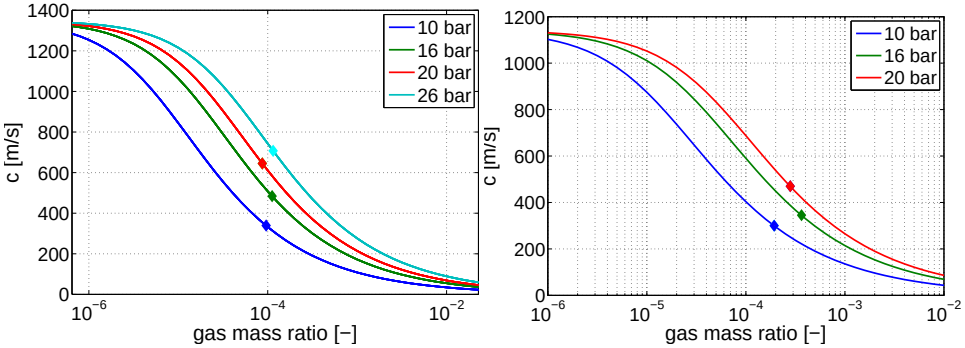

Figure 5.9: Speed of sound (left: water, right: ethanol) vs gas content with the experimental values (diamonds) for the different tank pressures

In the case of ethanol, the desorpted gas amount is about ten times higher than the water one: 0.2 g/kg × 0.524 kg = 0.105 g. Including the residual gas in the line, the total amount of GN2 is 0.105 g + 0.013 g = 0.118 g, which corresponds to a gas

P tank [bar]	8^{th} freq. [Hz]	c [m/s]	gas mass ratio [-]
10	24.2	300	$1.93 \cdot 10^{-4}$
16	27.8	345	$3.65 \cdot 10^{-4}$
20	37.9	470	$2.81 \cdot 10^{-4}$

Table 5.2: Experimental values of speed of sound and its corresponding (theoretical) gas content. Fluid is ethanol saturated at 1 bar

mass ratio of $2.25 \cdot 10^{-4}$. Making the same calculations as previously, the agreement for ethanol is much better, although the values are slightly more dispersed than the ones of water.

5.2.2 Line pressure

The effect of the initial line pressure is depicted in Fig. 5.10 for water and ethanol. As expected, the frequency increases with decreasing the line pressure due to the lower amount of residual gas in the line. However, with less gas in the line, the pressure peaks are higher and since the frequency is strongly dependent on the pressure, it is rather difficult to extrapolate a correlation among the different curves. It could be observed that for an initial high line pressure (for instance 300 and 100 mbar) the slopes are less steep than the curve of vacuum. In this case the amount of residual gas outcomes the released gas from desorption, at least for water. For ethanol in fact the slopes have not such a remarkable difference due again to its higher amount of released gas.

Gas content assessment The residual gas content is directly proportional to initial line pressure, assuming a perfect gas law. That is, the ratio among the different gas contents should correspond to the same ratio of the line pressures, subtracting the value of the dissolved gas ($0.2 \cdot 10^{-4}$). However from the data in Table 5.3 no linear relationship can be drawn. One possible explanation is that, given the significant amount of gas, the cushion effect is the predominant effect in the pressure oscillation as assumed in the rigid column model (see Section 2.4.2). Moreover, with a higher initial line pressure, the flow velocity is reduced and in this condition the flow pattern tends more to an horizontal stratification as the HSI have shown. In this configuration the speed of sound is based on a different equation. The same conclusions can be drawn for ethanol.

P line [mbar]	8^{th} freq. [Hz]	c [m/s]	gas mass ratio [-]	gas mass ratio net (no released gas) [-]
300	22.3	277	$5.87 \cdot 10^{-4}$	$5.67 \cdot 10^{-4}$
100	32.7	405	$2.64 \cdot 10^{-4}$	$2.44 \cdot 10^{-4}$
40	45.2	561	$1.27 \cdot 10^{-4}$	$1.07 \cdot 10^{-4}$
10	52	645	$0.89 \cdot 10^{-4}$	$0.69 \cdot 10^{-4}$

Table 5.3: Speed of sound and corresponding mass content for water tests

5.3 Effect of pressurizing conditions

When the saturated liquid is primed in the evacuated line, the dissolved gas desorbs increasing the amount of gas content in the line and thus reducing the speed of sound, which leads to a lower frequency. Figure 5.11 shows this effect for water and ethanol at a tank pressure of 10 bar. The reduction in frequency is more remarked for saturated ethanol as the amount of dissolved gas is higher than for water.

At 20 bar tank pressure, the occurrence of cavitation has the effect to induce strong pressure spikes in the fluid which increase the pressure level and condense some amount of vapor. Both these aspects contribute to increase the speed of sound and thus to shift the frequency towards higher values. A unbiased comparison of the frequency between deareated and saturated condition can not then be made in this case.

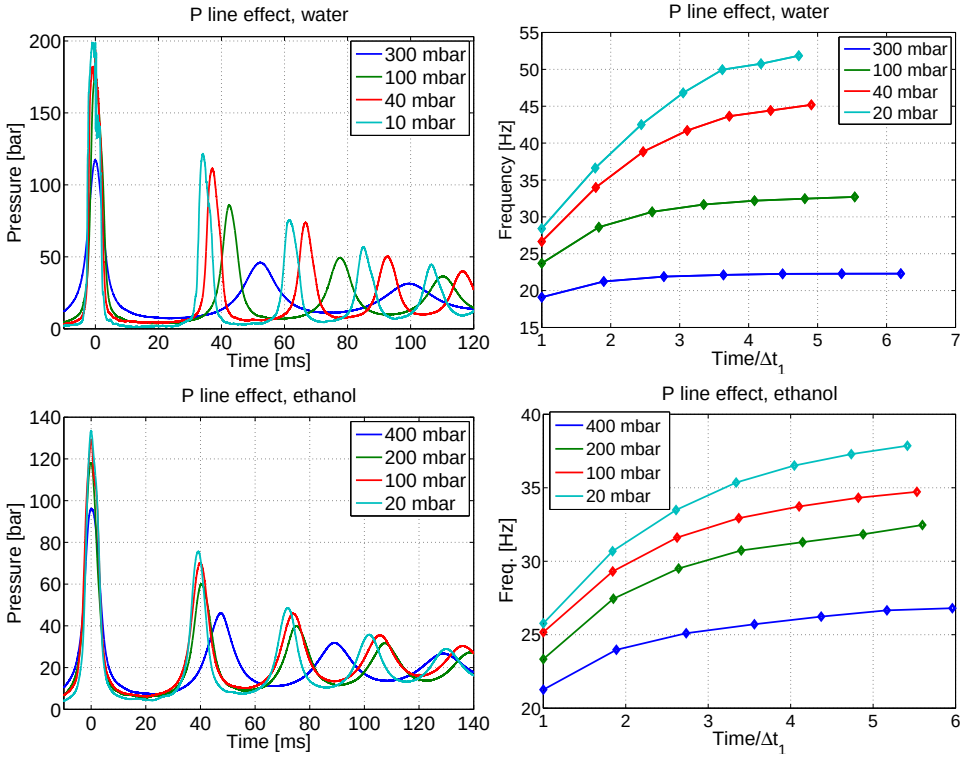

Figure 5.10: Effect of line pressure for water and ethanol.

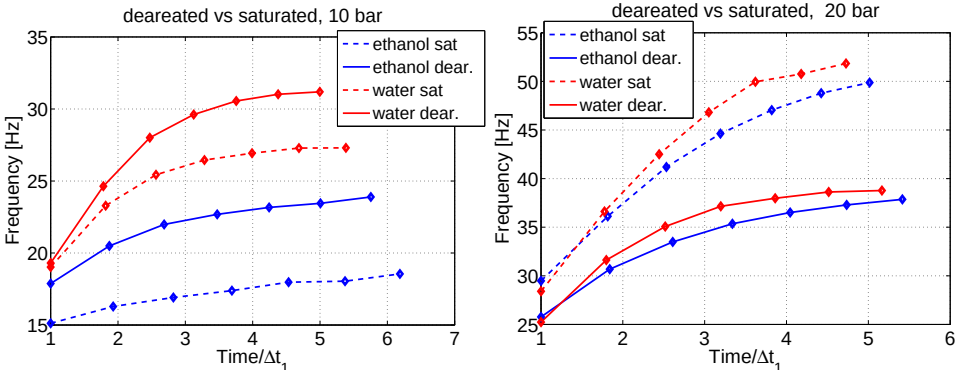

Figure 5.11: Comparison between deareated and saturated fluid at a tank pressure of 10 bar (left) and 20 bar (right)

Fluid	8^{th} freq. [Hz]	c [m/s]	gas mass ratio	GN2 by weight
water dear.	31.2	388	$0.72 \cdot 10^{-4}$	0.047 g
water sat.	27.3	339	$0.95 \cdot 10^{-4}$	0.062 g
ethanol dear.	24.2	300	$1.91 \cdot 10^{-4}$	0.101 g
ethanol sat.	18.4	228	$3.46 \cdot 10^{-4}$	0.182 g

Table 5.4: Comparison of the frequencies in case of saturated and deareated fluid for water and ethanol, $P_{tank} = 10$ bar

Gas content assessment At 10 bar the saturated liquid has an amount of dissolved GN2 of 200 mg/kg ($2 \cdot 10^{-4}$) for water and 2200 mg/kg ($22 \cdot 10^{-4}$) for ethanol. The experimental results with the assessed gas content are summarized in Table 5.4. Unlike the previous cases, the gas contents are now over-estimated with respect to the experimental data: two times higher for water (2 vs 0.95) and six times higher for ethanol (22 vs 3.46). Again, this discrepancy is likely due to the use of an homogeneous model for the calculation of the liquid-gas mixture speed of sound. When desorption takes place, gas release leads to formation of gas pockets which coalesce with each others and might result in a non uniform axial distribution. A second explanation is that not all the dissolved gas is released from the liquid. This means that the desorption process is not completed yet after 220-250 ms, the time at which the 8th frequency has been calculated. The influence of the desorption time constant is numerically investigated in the next paragraph.

Numerical simulations Numerical simulations are performed for the case of ethanol (Fig. 5.12). As in the previous chapter, the desorption time constant is varied to fit the experimental data. However, while trying to match the pressure peak by decreasing the time constant down to 150 ms, the calculated frequency deviates remarkably from the test results. This indicates again that the equation of the speed of sound is based on a non realistic flow pattern and/or the desorption rate sub-model is inadequate. For a saturated fluid, the formation of gas bubbles can be considered as randomly distributed, since the nucleation spots are triggered by small particles present in the liquid, wall roughness, welding spot, pipe imperfections or any local low pressure regions. Therefore the flow pattern might considerable be far from being homogeneous. Secondly, it can be noted that the numerical frequency does not significantly change in time being more or less constant, unlike the trend of the experiments where a progressive increase of the frequency in time can be observed.

Although the event of cavitation and bubble collapse and its related pressure spikes can not be numerically reproduced, numerical simulations at 20 bar tank pressure are run and displayed in Fig. 5.13. In the case of water, a relative slow desorption rate (time constant of 500 and 300 ms) does not affect the trend of increasing wave frequency, as observed in the experiment. Instead, for a fast desorption rate (50 ms), the frequency is almost constant. In the case of ethanol, the frequency is even decreasing with time, for every desorption time constant. This indicates that the higher amount of dissolved gas dominates the dynamics of the flow evolution.

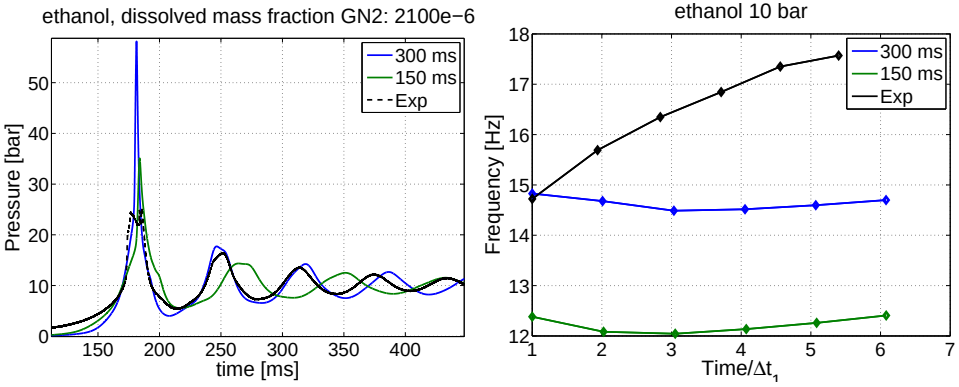

Figure 5.12: Numerical simulation for saturated ethanol with different desorption time constants, $P_{tank} = 10$ bar

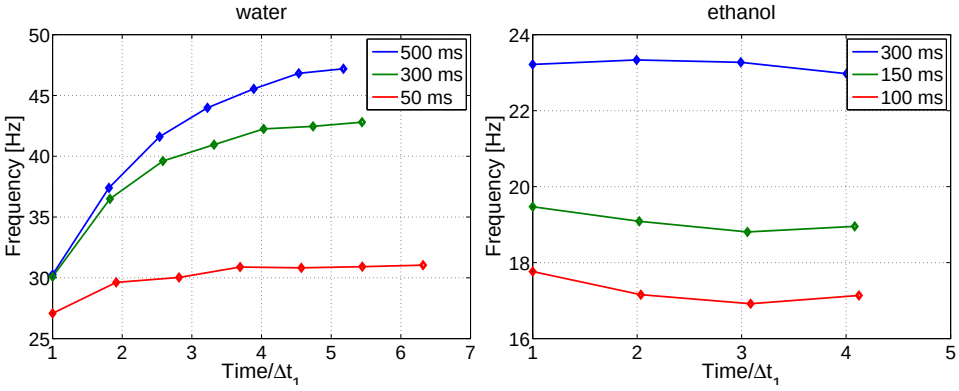

Figure 5.13: Frequency trend for different desorption rate time constant

5.3.1 Cavitation at the valve

A detailed study of the cavitation effects would require an analysis of the bubble dynamics which is beyond the scope of this present work. Some qualitatively considerations arising from the experiments are nevertheless underlined. Cavitation takes place at the valve and this process is characterized by strong pressure spikes and high frequency oscillations. This is clearly visible in the corresponding pressure sensors located upstream of the valve (PD-403/406) as shown in Fig. 5.14.

As explained in Section 2.3.3, when bubbles are disturbed, they pulsate at their natural frequency. Large bubbles (negligible surface tension and thermal conductivity) undergo adiabatic pulsations, which means that no heat is transferred either from the liquid to the gas or vice versa. The natural frequency of such bubbles is determined by the following equation [16, page 198]:

$$f = \frac{1}{2\pi r_0}\sqrt{\frac{3kP_0}{\rho}} \tag{5.3}$$

Although the radius of the cavitating bubbles is not known, a qualitative comparison between the natural bubble frequency of the two fluids can be made, which results in:

$$\frac{f_{ethanol}}{f_{water}} = \sqrt{\frac{\rho_{water}}{\rho_{ethanol}}} = \sqrt{\frac{1000^{\mathrm{kg}/\mathrm{m}^3}}{789^{\mathrm{kg}/\mathrm{m}^3}}} = 1.13 \tag{5.4}$$

This theoretical value matches perfectly the calculated one from the experiment based on the frequency ratio: $7150/6340 = 1.13$.

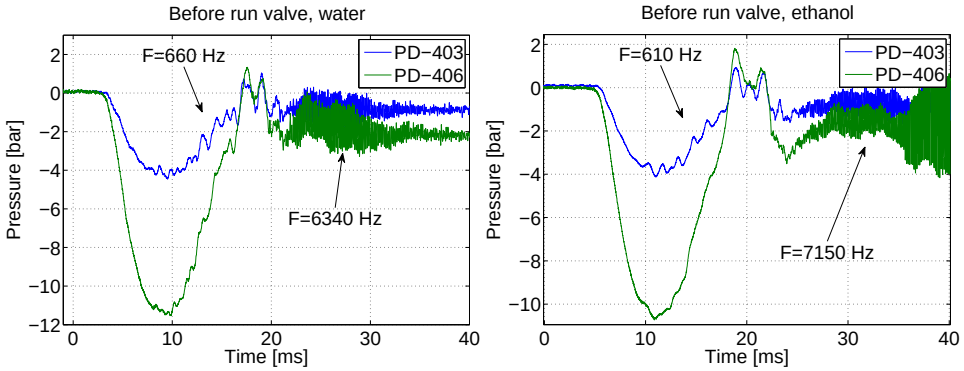

Figure 5.14: Pressure signal at the valve: the high frequency pressure oscillation is a clear sign of cavitation

Another interesting consideration visible in Fig. 5.14 is the 660 Hz (water) and 610 Hz (ethanol) oscillations occurring immediately after the valve opening. In this condition the pipe segment between the tank and the valve is excited by the sudden pressure drop which acts like a step function. As already mentioned, for an open-open pipe such as the actual segment the first natural frequency is given by Eq. (5.1). This can be reversed to estimate the actual speed of sound. This results in 1320 m/s for water and 1220 m/s for ethanol: these values are very close to the ones calculated in Chapter 2, with a difference of 2.6% for water (1355 m/s) and 1.7% for ethanol (1174 m/s).

5.4 Effect of geometry

The straight, L and T geometries have the same volumes, so that the amount of liquid filling the pipe and the amount of initial residual gas are the same. Results of

		Straight	S dear	L	L dear.	T	T dear.	T2 dear.
water	10 bar	27.3	31.3	19.7	27.6	20.4	23.5	22.5
water	20 bar	51.6	38.8	48.8	37.9	48.3	39.7	38.8
ethanol	10 bar	18.6	24.2	-	21.9	-	20.6	-
ethanol	20 bar	49.8	37.8	49.3	38.6	43.7	40.4	-

Table 5.5: The measured 8^{th} frequency of the different geometries

the different configurations are summarized in Table 5.5 for two tank pressures of 10 and 20 bar. Although the reproducibility of the pressure peak is good in case of L and T, it has to be mentioned that the frequencies show some dispersion (±10%) among the different tests. In addition, the frequency depends on the pressure level, which varies among the different setups due to the losses at the junction (elbow and tee have different losses).

However some observations can be made:

- at 10 bar without the occurence of cavitation the effect of the dissolved gas is clear, resulting in lower frequency as expected, for all the geometries (for ethanol, test with L and T only with deareated fluid).
- in the case of L geometry for water, there is no difference between deareated and saturated conditions: as proposed in Chap. 4, the elbow enhances the flow separation inducing cavitation, making the effect of gas desorption less determinant in the evolution of the flow
- in the case of T geometry, higher frequencies are expected as the branches are shorter. However the frequencies are almost the same as in the case of straight pipe. That is not understood. The pressure waves in the two branches oscillate at the same frequency and without appreciable delayed between each other as shown in Fig. 5.15.

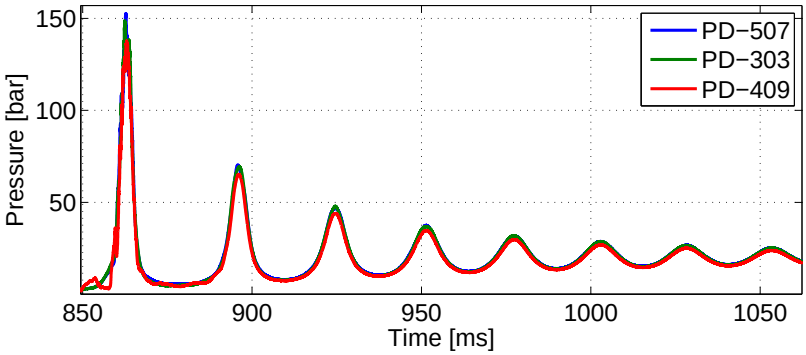

Figure 5.15: Pressures measured in the branches of T setup, deareated water

- in the case of T2 geometry, the pressure wave oscillates at the same frequency of 38.8 Hz in both branches (Fig. 5.16). This frequency is the same as for the straight pipe (deareated) and in fact the length of the test section from the valve to the dead-end of the longer branch of the tee is the same. Therefore

the longer branch is dictating the main frequency of the oscillations, whereas the shorter branch acts as a disturbance whose effect is damped off after two oscillations.

- at 10 bar, ethanol has always lower frequencies than water, as expected due to its lower speed of sound. At 20 bar instead, the frequencies of ethanol and water are very similar, due to the occurrence of cavitation that again dramatically changes the dynamic of the flow.

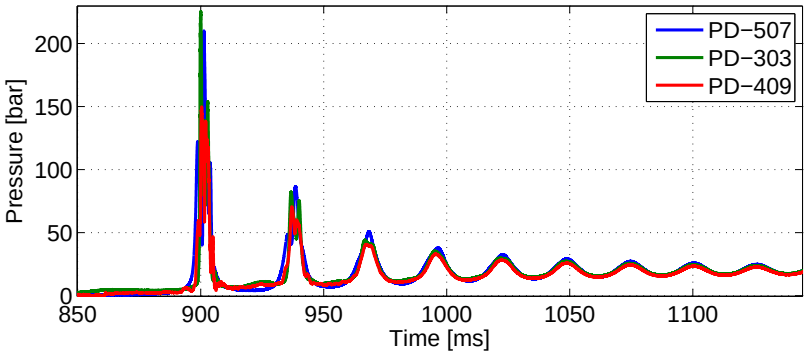

Figure 5.16: Pressures measured in the branches of T2, deareated water

5.5 Fluid-structure interaction

5.5.1 Influence of the material

Only the deareared case is investigated to avoid the effect of cavitation. Basically, the same considerations as in Chapter 4 for the pressure peak can be drawn, as the frequency and pressure peak are both depending on the speed of sound, which is affected by the material elasticity as according to Eq. (5.5):

$$c^2 = \frac{c_f^2}{1 + \frac{K_f}{E}\frac{D}{e}\psi} \tag{5.5}$$

A difference in the wave frequency among the investigated materials is observed, as illustrated in Fig. 5.17. The higher the Young modulus E, the higher the frequency, as in accordance to Eq. (5.5). A quantitative analysis of the variation of speed of sound and the comparison with the experimental values are summarized in Table

5.6. To avoid taking the gas effect into account, a relative comparison with the values of stainless steel is performed for titanium and aluminum alloys. The measured relative frequencies (or relative speed of sound) for titanium and aluminum are both lower than the predicted ones. For aluminum the discrepancy is quite high, being 0.786 instead of 0.903 (-12%). Including the presence of the gas the discrepancy increases. The reason for this is unclear. In the case of ethanol and titanium alloy, the deviation between the experimental value (0.948) and the theoretical one (0.97) is less remarked.

	stainless steel	titanium alloy TA3V	aluminum T6061
	water		
c/c_f (Eq. 5.5)	0.925	0.885	0.835
$c/c_{st.steel}$, no gas	1	0.957	0.903
$c/c_{st.steel}$, with 10^{-4} gas fraction	1	0.991	0.978
Exp. frequency ratio wrt to st.steel	1	0.918	0.786
	ethanol		
c/c_f (Eq. 5.5)	0.952	0.923	-
$c/c_{st.steel}$, no gas	1	0.970	-
Exp. frequency ratio wrt to st.steel	1	0.948	-

Table 5.6: Ratio of the speed of sound for the different materials and fluids

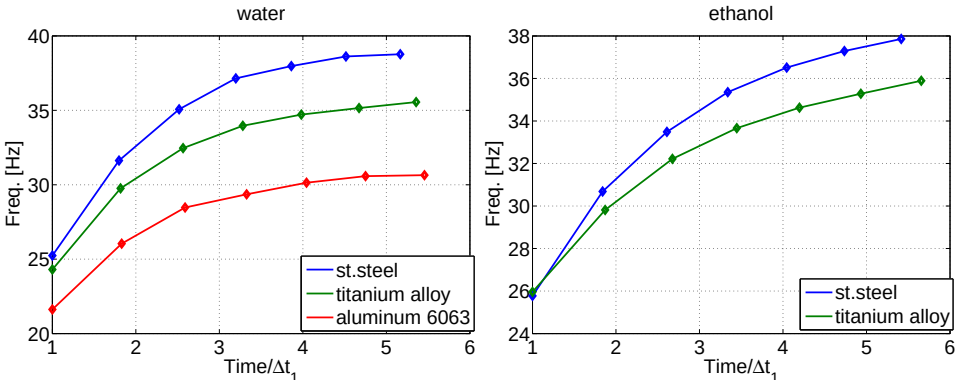

Figure 5.17: Effect of the different material on the wave frequency

5.5.2 Poisson Coupling

By comparing the FFT of the pressure signals against the FFT of the strain gages, it is theoretically possible to detect from which source the frequencies originate. Figure 5.18 shows an example of the frequency content of the pressure signals and the strain gage signals. The precursor wave due to the Poisson coupling will theoretically cause a (very small) pressure perturbation in the liquid that travels at the speed of sound of the material. For example, in case of the stainless steel test section ($c = 4800$ m/s) the expected frequency in the test section would be around 1200 Hz. However, although an extensive analysis of all the test data, it was not possible to detect this frequency in the FFT of the pressure signals. The reason is the presence of a relative high gas content, which lowers the speed of sound in the fluid. The precursor wave will shrink the pipe causing a volume reduction dV. This causes in turn an increase in pressure $dP = -K_L dV/V$, proportional to the liquid compressibility modulus. Since the change in volume dV correspond also to a change in density $-d\rho$, the pressure perturbation is:

$$dP = \frac{K_L}{\rho} d\rho = c^2 d\rho \tag{5.6}$$

Because of the high gas content, the speed of sound is dramatically reduced and hence the pressure increase would be very small and difficult to measure.

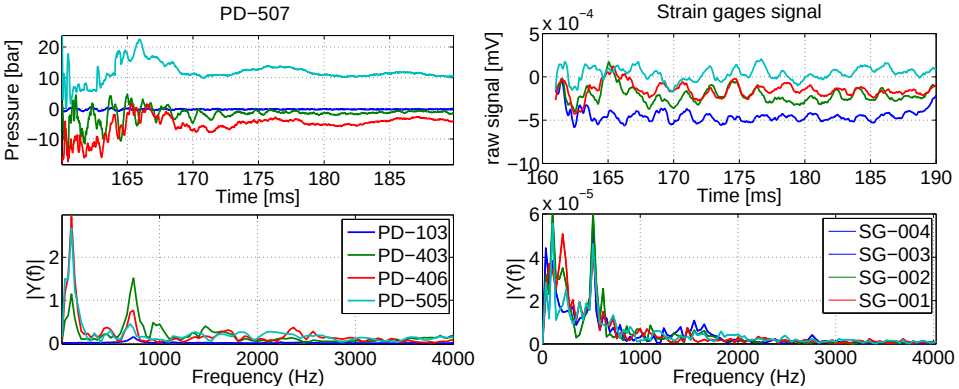

Figure 5.18: Comparison between the FFT of pressure signals (left) and strain gage signals (right)

5.5.3 Support condition

According to Eq. (5.5), a structure that is free to move (upstream anchored, $\psi = 1 - \nu/2$) has a slightly higher speed of sound and thus a higher frequency. The difference with the fully anchored case ($\psi = 1$) is however quite small, around 0.8% for water and stainless steel as a pipe material. Figure 5.19 depicts the pressure and strain gages signals in the two cases where the test section is fully anchored (left) or only upstream anchored, thus free to move (right). The signals are dimensionless. Although the strain gauges show a remarkable difference, both in frequency and damping, no difference could be detected in the pressure signals. In the unconstrained test section, the superposition of the fluid wave frequency with the structural vibration in SG-004 is clearly visible. Near the support, where the strain is higher, the structural vibration is predominant, as shown in the signal of SG-001.

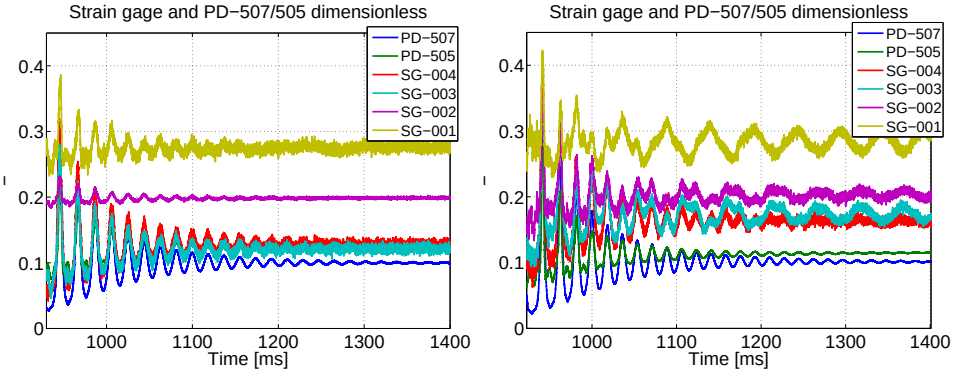

Figure 5.19: Comparison between the fully anchored test section (left, $\psi = 1$) and the upstream anchored case (right, $\psi = 1 - \nu/2$). Material is stainless steel

In all the performed tests, the structural frequencies can not be detected in the FFT of the pressure reading. Cavitation, bubble dynamics, noise, etc..., all contribute to disturb the signal. In some conditions however it is possible to observe these structural frequencies also on the pressure signals, in the special case when the pipe is not anchored and the pipe material is aluminum.

Figure 5.20 shows the dimensionless pressure and strain signals in the case of aluminum pipe upstream anchored only. The time interval between the two first peaks is magnified on the right side of Fig.5.20, showing that the pressure oscillation has clearly the same frequency of the structural vibration, e.g. SG-004. This frequency is 480 Hz, exactly the structural eigenfrequency measured in the hammer impact test. However their amplitude is so low (less than 0.5%) that is not possible

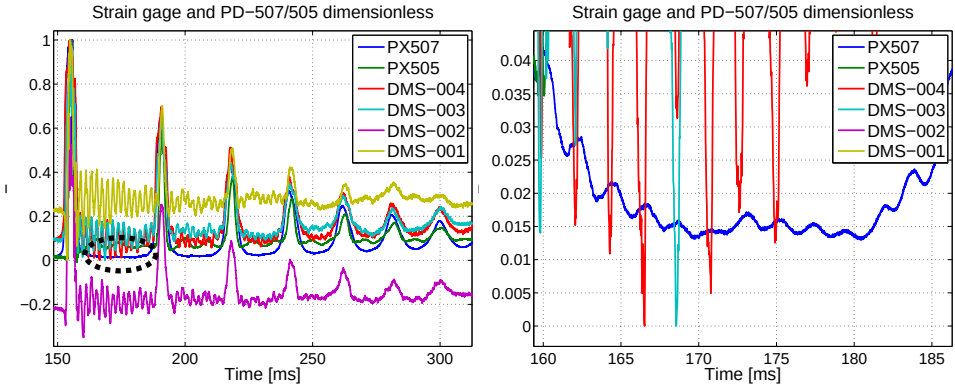

Figure 5.20: Pressure and strain gage signals in a test with no support. The frequency of the SG003-004 coincide with the oscillations of PD-507. Pipe material is stainless steell

to identify this effect somewhere else in the signal.

Figure 5.21 compare the dimensionless pressure (left) and strain (right) signals in the case of upstream anchored only and pinned test section for aluminum and steel as pipe materials. When the pipe is not pinned, the free transverse movement induces pressure oscillations in the fluid, although, as already mentioned, these oscillations have very low amplitude.

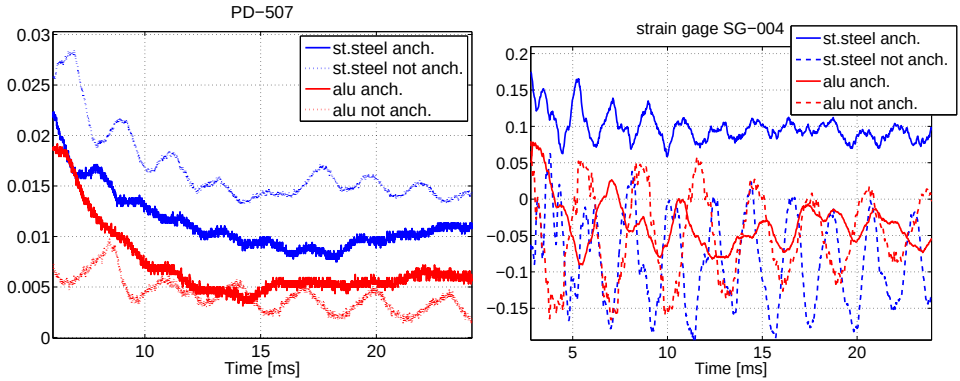

Figure 5.21: Structural vibrations in the pressure signal in case of pipe upstream anchored only (free vibrations). Signals are dimensionless.

5.6 Summary

The frequency of the pressure wave was analyzed for different configurations and conditions. The origin of the various oscillations present in the pressure signal was explained and related to physical characteristics, such as the lengths of different pipes, overtones and cavitation effects.

Based on the main frequency of the pressure wave, the speed of sound was derived and by this, the amount of gas mass fraction was assessed. This estimated gas content has been compared with the calculated residual gas in the line and the released gas from the desorption. A remarkable discrepancy between the two values was found, being the assessed gas content three times smaller than expected. Various reasons might be responsible for this mismatching. First, the speed of sound is strongly dependent on the pressure, which varies rapidly not only in time but in space as well, so an unique value for the speed of sound might be too a simplified assumption. A second source of uncertainty is the desorption rate, which is unknown (and again, not constant in time nor space). The numerical simulations have shown that it is not possible to calibrate a unique desorption time constant to fit both the pressure peak and the frequency. But probably the main reason of the discrepancy is the formulation of the speed of sound for two-phase flow which might not hold for the actual flow pattern. In fact Eq. (5.2) is valid as long as the flow is 1D homogeneous, that means no change in the radial and tangential direction. But the flow pattern at the dead-end tends to an horizontal stratification as the HSI has shown, and in this configuration a different equation for the speed of sound must be used. In addition, the bubble dynamics significantly modifies the flow pattern introducing non-homogeneous region and flow perturbations as in the case of cavitation, where severe pressure spikes change the flow evolution and cause the vapor to condense, modifying the void fraction.

Qualitatively, the most important outcome of this frequency analysis is the effect of the gas desorption which decreases the speed of sound. That is experimentally proved by comparing the deareated and saturated liquid for both water and ethanol, observing a clear difference between the frequencies.

Concerning FSI effects, a comparison of the frequency content between the pressure sensor signals and the strain gage signals was performed, but no Poisson-related frequencies were detected in the pressure signals nor in the SG signals. This is due to the high gas content that dramatically lowers the speed of sound, and thus the compressibility of the fluid. In some particular conditions, e.g. when the pipe is not anchored and the material has a low elasticity modulus, the structural vibrations of the pipe (its eigenfrequency) induced by the pressure peak, could leave track on the pressure signal, although very small.

Chapter 6

Wave Attenuation Analysis

6.1 Introduction

The attenuation of the pressure wave will be described with respect to the effects of different conditions, as in the previous chapters. To analyze the wave attenuation, the pressure is made dimensionless with respect to the first overpressure peak:

$$P^*(t) = \frac{P(t) - P_{tank}}{P_{max} - P_{tank}} \tag{6.1}$$

where the value of tank pressure is subtracted to the pressure signal to allow comparison among different conditions. In this way the dimensionless pressure will converge to zero, making it suitable for an exponential decay law. The peaks are identified by the HWHM technique and the time is made dimensionless with respect to the period between the first and second peak, named Δt_1, as explained in the previous chapter. Particular attention is paid to the numerical simulations, as the attenuation is the wave characteristic that more than others mismatches when compared to experimental data. A known reason for this disagreement between numerical predictions and test results is the use of steady friction models despite the strong transient conditions. While in some water hammer commercial codes the

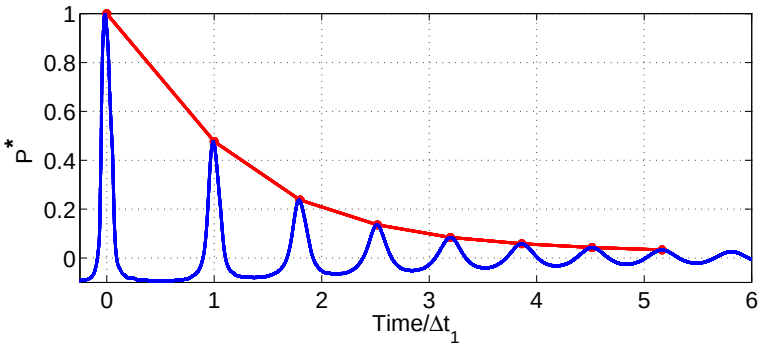

Figure 6.1: Graphical representation of the dimensionless wave attenuation

unsteady friction models are included [35], they are not implemented yet in the numerical codes of space propulsion design tool. An objective of the present work is to implement and validate an unsteady friction model (UFM) in EcosimPro/ESPSS.

A commonly used engineering approximation to analyze the attenuation of the wave is the exponential decay: the envelope of the pressure, indicated as $[\![P^*]\!]$, can be approximated by an exponential curve of the form:

$$[\![P^*(t)]\!] = \exp(-\frac{t}{\tau}) \tag{6.2}$$

where τ is the damping time constant.

Applying a logarithm to Eq. (6.2) leads to a linear expression where a linear regression allows to calculated the best fit value of τ. However, the exponential decay is a valid approximation only for systems with a linear dissipation dynamics. This assumption does not hold in water hammer cases, even for single phase, since the energy dissipation is a quadratic form of the velocity and the friction factor is highly non-linearly dependent on the velocity.To increase the accuracy of the fitting, different models other than the linear regression can be considered. To this purpose, the following functions are chosen to fit $f(t)$:

$$ln\left([\![P^*(t)]\!]\right) = f(t) = \begin{cases} -\frac{t}{\tau} & linear,\ f_1 \\ \begin{cases} -\frac{t}{\tau_1} & if\ t < t_{P3} \\ -\frac{t}{\tau_2} & if\ t \geq t_{P3} \end{cases} & piecewise,\ f_2 \\ -\frac{t^2}{\tau_A^2} - \frac{t}{\tau_B} & quadratic,\ f_3 \\ \frac{-t}{\tau_h + C \cdot t} & hyperbola,\ f_4 \end{cases}$$

1. the classical model linear in time (constant τ): although it might give higher error than others, its simplicity makes it practical for the analysis;

2. a piecewise linear function over two segments: usually the first two/three peaks appear over-damped with respect to the general wave envelope; this might be due to the column separation which interfere with the normal attenuation of the wave due to the friction. This piecewise interpolation aims to take the column separation into account: a first segment with a time constant τ_1 and the final segment with a time constant τ_2;

3. a quadratic form in time: fitting a polynomial of second order improves the curve fitting. As for the piecewise interpolation, the polynomial coefficient τ_A, τ_B shall model the physical effect of column separation which has an impact on the first part of the wave attenuation;

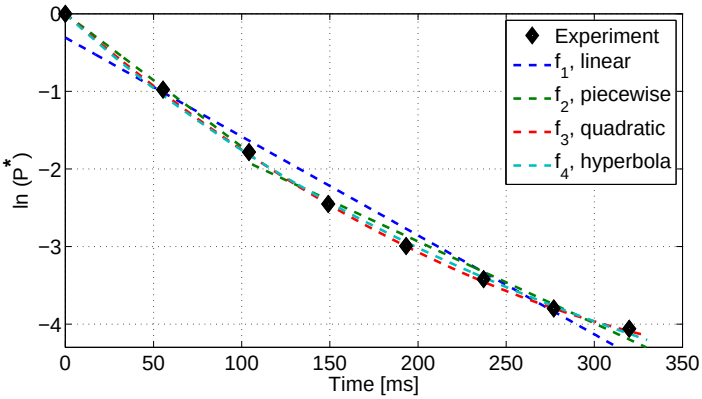

Figure 6.2: Logarithm of the pressure peaks and of their interpolation functions

4. an hyperbola function: that corresponds to a damping time "constant" τ variable in time, $\tau = \tau_h + C \cdot time$. From a physical point of view, the change of τ in time shall model the desorption of the dissolved gas, which increases the gas content and thus the wave attenuation.

A comparison of these different decay models is shown in Fig. 6.2 for a standard case. The values of τ in the models could then be correlated to the different conditions, e.g. the tank and line pressures, the amount of desorpted gas, the fluid, etc.

6.2 Parameters affecting the wave attenuation

The attenuation of the wave depends on flow parameters as well as on fluid properties. The most important is the liquid viscosity, but in case of a two-phase flow the evaluation of the friction losses is rather complex. In a two-phase flow the frictional pressure loss is even higher than that for a single-phase flow at the same mass flow rate. The presence of a gas or vapor increases the energy dissipation and many empirical or semi-empirical models have been proposed to take this fact into account. All of these models are based on a friction multiplier Φ for the liquid or vapor phase, so that the overall liquid-gas mixture pressure drop is expressed as $\Delta P_{2-ph} = \Delta P_L \Phi^2$. The method of Lockhart and Martinelli [58] was the first method that predicted the two-phase frictional pressure drop. To date, the most accurate method is probably the Friedel correlation [33], which is also the model implemented in ESPSS (see Section 3.2.1.3). In the Friedel model the friction multiplier Φ is an empirical correlations depending on many parameters:

$$\Phi = \Phi(Fr,\, We,\, \mu_g, \mu_L,\, \rho_g, \rho_L, x)$$

where Fr and We are respectively the Froude and Weber number based on the homogeneous mixture density, and x is the gas or vapor quality. It is important to underline again that the presence of gas and/or vapor is not constant nor uniform in priming, due to cavitation, condensation, gas desorption and absorption.

Among other parameters affecting the wave attenuation, also the speed of sound must be considered. Han et al. [38] performed a dimensional analysis of the water hammer attenuation. They considered the classic water hammer upon valve closing and without cavitation, so single-phase was analyzed. They analytically derived the water hammer envelope curve, showing that it is a highly non-linear function of some dimensionless parameters, which include the speed of sound. In fact, the friction is frequency-dependent, and the frequency depends on the speed of sound.

Not only the classical friction is responsible for the pressure losses, but also other energy dissipation mechanisms are connected to the attenuation of the wave. Heat losses, structure movements and phase changes all contribute to subtract energy to the fluid.

6.3 Effect of tank and line pressures

Tank pressure The dimensionless pressure attenuation for different tank pressures is shown in Fig. 6.3. The wave is more damped at lower tank pressure, although the amount of residual gas in the line is the same. The damping effect is to be attributed to the pressure itself: the higher the tank pressure, the higher the pressure peaks, so more "rigid" are the gas bubbles in the fluid. In this condition, the flow behaves more like a single-phase rather than two-phase and thus the friction is reduced at higher pressure. For the same amount of gas, the void fraction is smaller at higher pressure. Table 6.1 summarizes the values of the best fit damping time constant for water and ethanol. No remarkable difference can be noted between the two fluids, despite the higher viscosity of ethanol (1.4 vs 1.14 mPa·s).

Line pressure In this case the attenuation of the wave can be qualitatively related to the presence of gas. As shown in Fig. 6.3, the higher the residual gas in the line, the higher the attenuation of the pressure wave. The effect is remarkable on the second peak: in case of 300 mbar, for example, the peak is reduced of 50% compared to the vacuum case (dimensionless from 0.58 to 0.28 respectively for vacuum and 300 mbar, in the case of water). Table 6.2 summarizes the values of the damping time constant for water and ethanol.

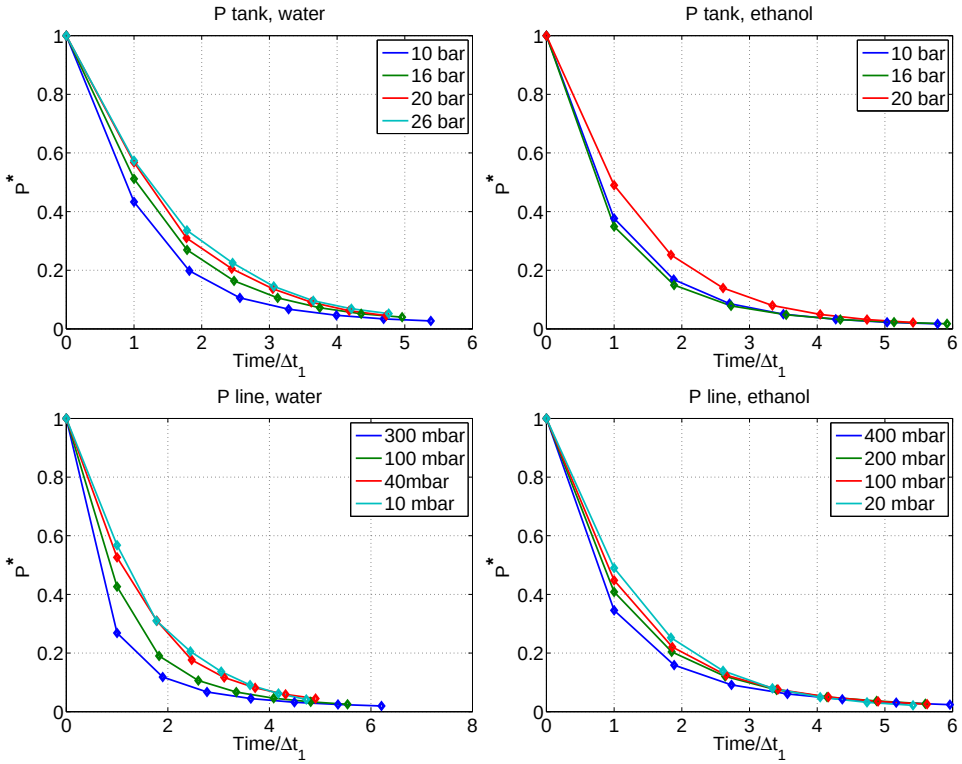

Figure 6.3: Wave attenuation for different tank and line pressures: water (left) and ethanol (right)

P_{tank}	10 bar	16 bar	20 bar	26 bar
water	68.8	59.7	54.1	50.0
ethanol	58.5	50.9	52.7	-

Table 6.1: Best fit values of damping time constant τ, ms

P_{line} [mbar]	1000	300/400	100/200	40/100	10/20
water	77.1	43.4	49.5	55.8	54.1
ethanol	-	48.5	48.3	50.5	52.7

Table 6.2: Best fit values of the damping time constant τ, in ms

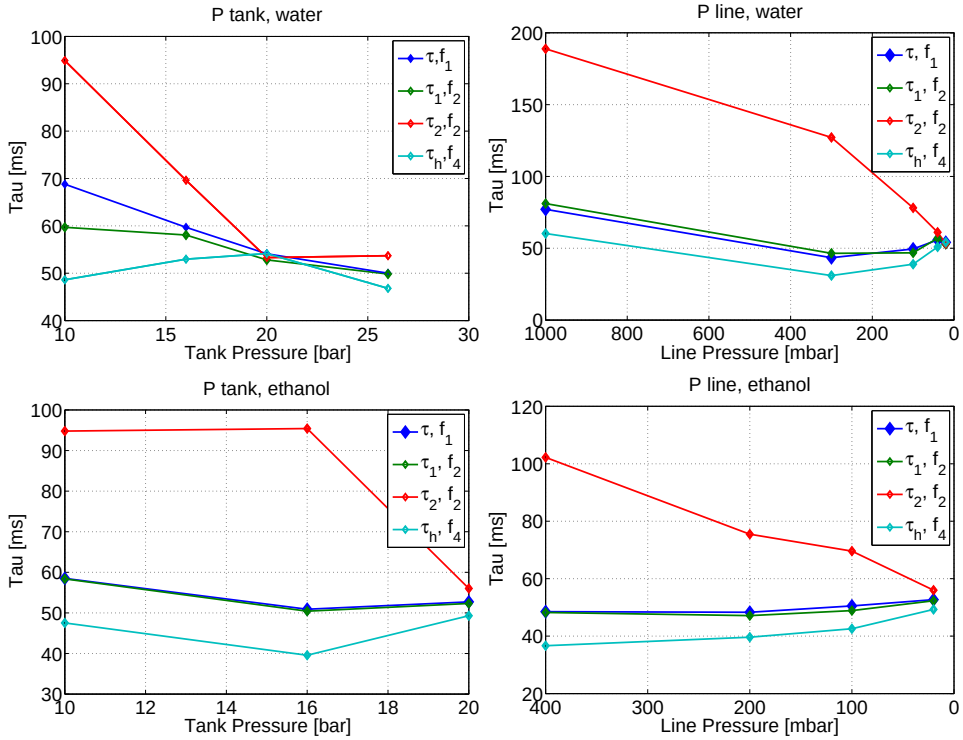

Figure 6.4: Trend of τ for the different models

As shown in Tables 6.1-6.2, in both the cases of tank and line pressures, the values of τ for water and ethanol are quite similar. This indicates that the wave attenuation is mainly depending on the gas content rather than on the fluid viscosity.

Exponential decay fitting The trend of the time constants τ used in the different models is depicted in Fig 6.4. In the case of water, the values of τ seem to converge towards the same value at $P_{tank} = 20$ bar and $P_{line} =$ vacuum. The reason for this convergence is not clear, it might be just a numerical coincidence without a physical explanation since the models are based on different laws. The same convergence toward the values at 20 bar and vacuum is observed for ethanol. In general, the trends of the models are difficult to assess and might indicate that the exponential decay fitting is too simple an approximation, unable to take into account the strong non-linear effects of the tank and line pressure on the attenuation.

6.4 Effect of pressurizing conditions

In the case of saturated liquid, the released gas from the desorption process contributes to increasing the wave attenuation, as shown in Fig. 6.5 for the case of 10 bar tank pressure. In the case of water, the second and third peaks are clearly more damped, while the difference becomes less for the following peaks. For ethanol, on the contrary, the two curves have a more remarkable difference. That indicates that the amount of GN2 released is higher for ethanol than water, as already known. To be more precise, it may also indicate that the desorption rate is faster for ethanol, as it is not so easy to clearly separate the two effects.

At 20 bar, the cavitation again interferes and causes less attenuation for the same reason described in the previous chapters. It has to be noted that in the deareated case, the curves of water and ethanol have almost identical damping behaviour. That indicates again that the fluid viscosity does not play a predominant role in the pressure losses, the damping is mainly driven by gas content as found in the previous section.

The effect of the different amount of dissolved gas on the wave attenuation can be appreciated by comparing different saturation pressure in the case of ethanol, which can dissolve more GN2 than water. Figure 6.6 shows the wave attenuation for different saturation levels of GN2 in ethanol. It is again stressed out the importance of assuring a complete saturation of the liquid, which is achieved in at least 48 hours, based on the experimental results.

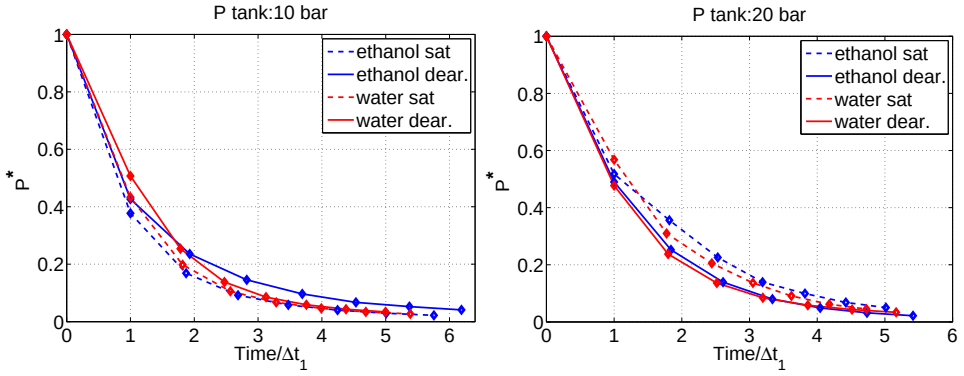

Figure 6.5: Comparison of the wave attenuation: deareated vs saturated conditions for water and ethanol

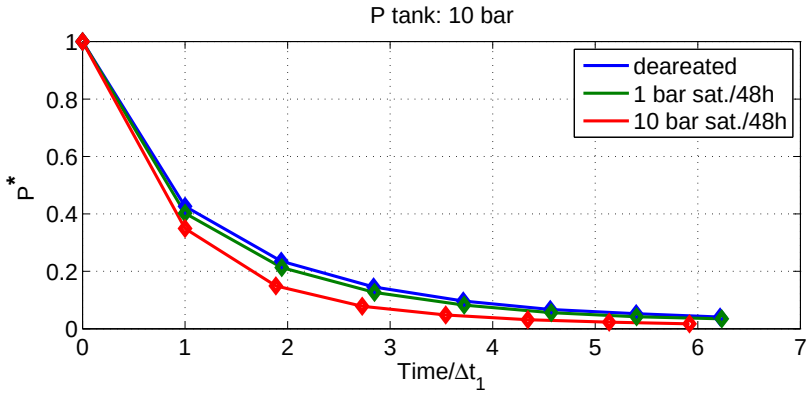

Figure 6.6: Comparison of the wave attenuation for different saturation pressure level in case of ethanol

Exponential decay fitting The values of τ for the different fitting functions are reported in Table 6.3 for water and in Table 6.4 for ethanol. The fitting errors of the models are also reported for a better evaluation of their goodness. The error of the fitting is the standard error of the linear regression, which is reported in bar for a more intuitive comprehension. In this respect, the simplest model f_1 with a constant τ, despite its simplicity, proves to be an acceptable approximation for both fluids and both fluid conditions. The quadratic model f_3 is obviously giving a better fitting than f_1, since an additional parameter for the fitting was used. The reduction in the error however is quite small, so that the added complexity does not seem justified. The piecewise function f_2 also provides a good fitting for both saturated and deareated conditions, being slightly better for ethanol. This indicates that splitting the influence of the column separation effect might be a good approach in modeling the wave attenuation. The hyperbola model f_4 shows the highest error

τ [ms] ($\pm$error)	water	
	10 bar dear.	10 bar sat.
τ constant	68.8 (1.8 bar)	62.2 (1.3 bar)
piecewise,τ_1; τ_2	68.2; 83.2 (2.2 bar)	59.7; 95 (1.6 bar)
quadratic, τ_A; τ_B	308; 75.6 (1.5 bar)	201; 62.2 (1.2 bar)
hyperbola,τ_h; C	58.9; 0.06 (3.5 bar)	48.6; 0.10 (2.1 bar)

Table 6.3: Values of τ of the different fitting functions with their interpolation error

τ [ms] ($\pm$error)	ethanol	
	10 bar dear.	10 bar sat.
τ constant	58.5 (0.6 bar)	81.5 (0.4 bar)
piecewise,$\tau_1; \tau_2$	58.4; 94.8 (0.6 bar)	88.3; 167 (0.3 bar)
quadratic, $\tau_A; \tau_B$	175; 58.8 (0.5 bar)	191; 82.8 (0.3 bar)
hyperbola,τ_h ; C	47.5; 0.09 (0.6 bar)	69.0; 0.15 (0.06 bar)

Table 6.4: Values of τ of the different fitting functions with their interpolation error

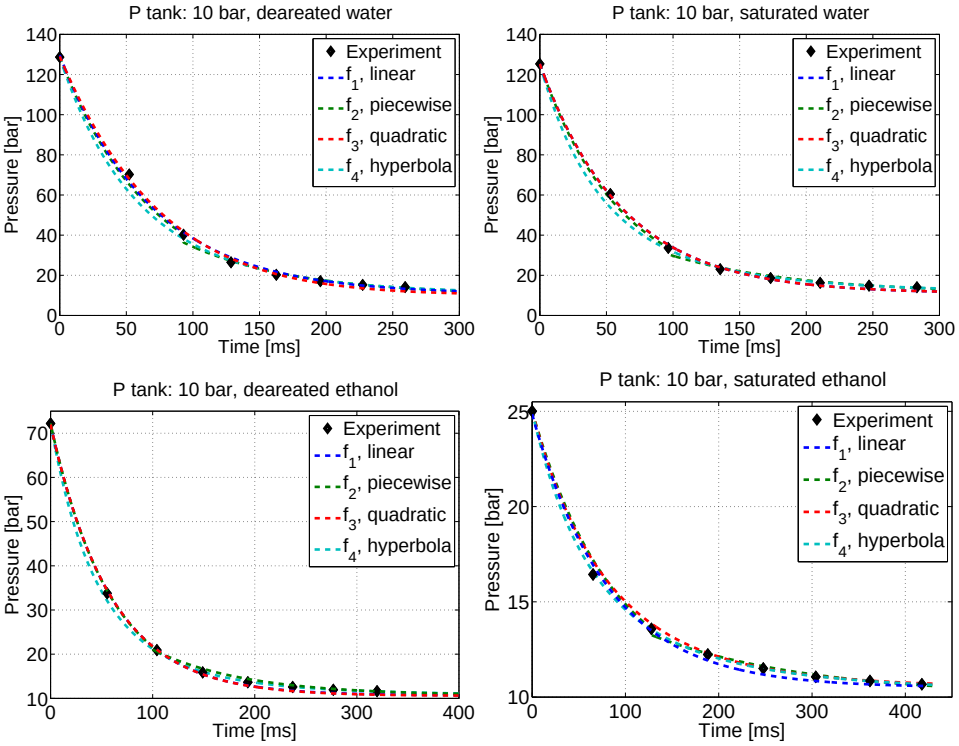

Figure 6.7: Comparison among the different wave attenuation models with the experimental data: deareated vs saturated conditions for water and ethanol. In some plots the linear model f_1 is not visible as it overlaps with f_3.

in case of saturated water, while it is the best fitting function in case of saturated ethanol. This result is obviously contradicting, although the fitting error compared to the other models is not so large in case of water. Note that in Table 6.3 and Table 6.4 the values of the hyperbola function for deareated fluid are merely indicative and should not be considered, since the hyperbola function aims to model the gas desorption. Since the effects of gas desorption are more remarkable in case of ethanol due to its faster desorption rate and its higher amount of dissolved gas, the model f_4 can still be considered a valid approximation. However with only two benchmarks it is not possible to definitely assess a model better than others. The fitting curves in the real time are shown in Fig. 6.7 for a more physical comparison.

6.5 Effect of geometry

The effect of different geometries on the wave attenuation is depicted in Fig. 6.8. The saturated and deareated curves are also plotted to better show the influence of both effects, as they are inter-dependent as described in Chapter 4. The presence of a junction, tee or elbow, introduces an additional pressure loss that contributes to increase the damping. This can be clearly seen in all the diagrams of Fig. 6.8, especially in the second peak (at Time=1), where the L and T configurations are always more damped compared to the straight pipe. Comparing the L and T set-ups, no remarkable difference can be measured in the attenuation, both in the deareated and in the saturated case. The gas desorption has the effect to increase the damping as described previously, although its effect is slightly smaller for the L and T geometry than the straight pipe case (for water at 10 bar tank pressure). This is consistent with the conclusions drawn in the analysis of the pressure peak: the presence of the junction makes the effect of the gas release process less dominant in the evolution of the flow.

6.6 Effect of material and support

Theoretically, a more deformable material, which has a lower elasticity modulus, will dissipate more energy. Comparing stainless steel and titanium, for both water and ethanol (Fig. 6.9) the curves are practically the same, being the differences within the experimental uncertainty, so it is fair to conclude that no difference can be clearly measured. In the case of aluminum and not-anchored pipe (red curve) the attenuation is more remarked. The oscillations of the test-section subtract energy to the fluid, thus increasing the damping of the pressure wave.

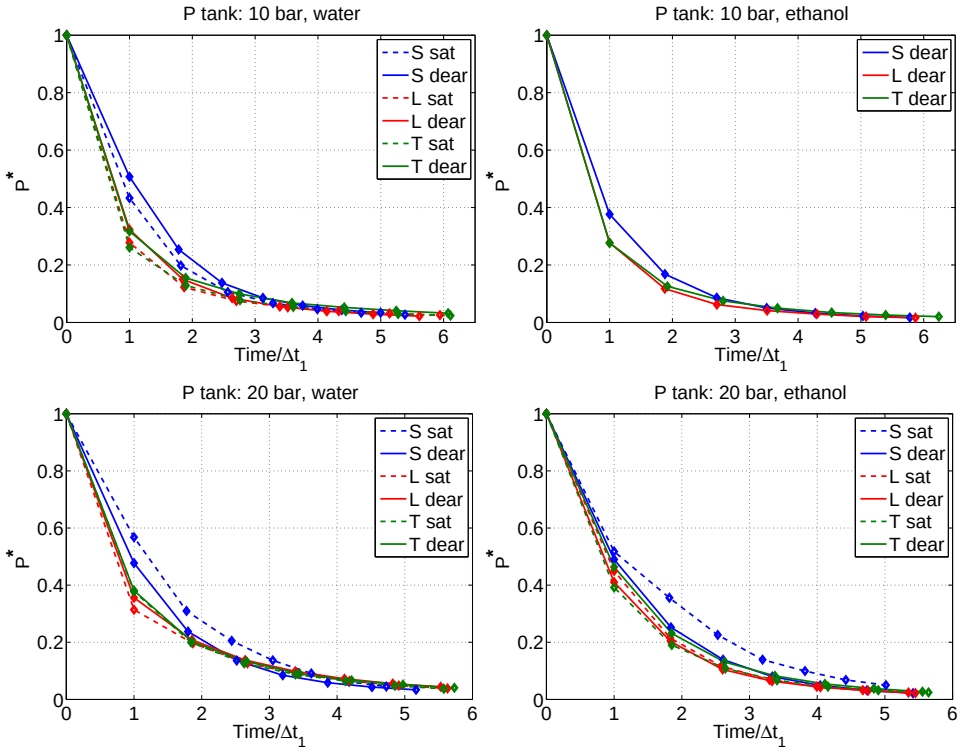

Figure 6.8: Wave attenuation for the different geometries at 10 bar and 20 bar

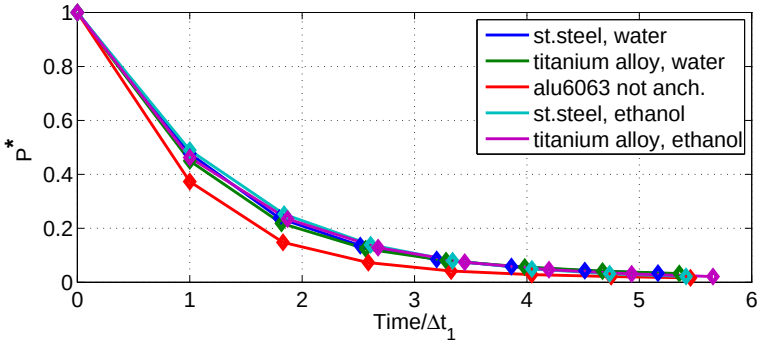

Figure 6.9: Comparison of the wave attenuation in case of different materials.

6.7 Numerical simulations with unsteady friction model

While comparing the numerical simulation with the test results, the wave attenuation is the characteristic that mismatches the experiment the most due to the use of the steady friction model. To achieve a better prediction of the wave attenuation, Brunone's UFM is implemented with the sign corrections proposed by Vitkovsky (Eq. (2.27), explained in Section 2.3.7). As a common approach, the unsteady term is added to the static friction coefficient f_s so that the total friction is $f = f_s + f_u$. The steady state friction f_s is calculated by means of Churchill's correlation valid for laminar and turbulent flow [24] (also implemented in the code of ESPSS as described in Section 3.2.1.3). Pressure losses are then evaluated according to Darcy–Weisbach's definition: $\Delta P = \frac{1}{2}\rho V^2 \frac{L}{D} f$.

Since the trial and error procedure to fit the parameter k_3 has proven to be time consuming due to the presence of two-phase flow which greatly increases the computational time, the analytically-deduced shear stress coefficient $C*$ proposed by Vardy and Brown [97] is used to evaluate k_3 (Eq. (2.26)). The shear stress coefficient $C*$ was analytically derived for single phase flows and no validation case exists for two-phase flows. The friction factor of a two-phase flow depends on the gas content and is generally higher than that of a single phase flow, as it can be seen by evaluating the Lockhart-Martinelli equations [58]. Although the gas content can be assessed from the knowledge of the speed of sound as done in the previous chapter, the two-phase friction factor itself is rather useless in the actual transient flow conditions. Its value can give a hint of how much the friction is increased with respect to the single phase flow in steady conditions, but quantitatively the unsteady friction term has a stronger influence. To take the presence of gas into account, an additional parameter k_4 is introduced as a correction to fit the experimental data, since Eq. (2.25) has been deduced for a single phase flow. The actual formulation implemented in the code of ESPSS is then given by Eq. (6.3):

$$f_u = \frac{2D}{V|V|} k_4 2\sqrt{C*} \left(\frac{\partial V}{\partial t} - c\frac{V}{|V|} \left| \frac{\partial V}{\partial x} \right| \right) \tag{6.3}$$

When $k_4 = 1$, Eq. (6.3) will be referred to as Brunone-Vardy model in the legend of the following plots. To avoid the effect of gas desorption, the numerical simulations will be compared against tests performed in deareated conditions only.

Figure 6.10 compares the results of the numerical simulations performed with the standard steady friction model and the one with the implementation of the Brunone-Vardy UFM. In the steady friction model, the friction multiplier is set to three in order to match to first pressure peak, as explained in Chapter 4. Compared to the experimental data, the prediction of the wave attenuation is improved with

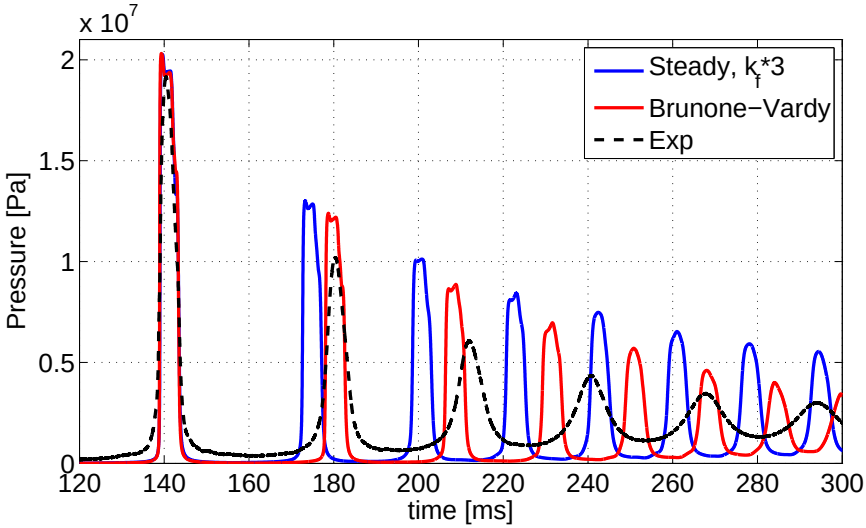

Figure 6.10: Comparison between the steady friction model and Brunone-Vardy's UFM against the experimental data, referred to the standard case of $P_{tank} = 20$ bar and vacuum. Fluid is deareated water.

the adoption of the UFM, although is still under-estimated. It is also interesting to observe that the UFM affects the frequency. The reason is the mathematical modification of the speed of sound which is coupled with the velocity gradient. Whether the influence of the unsteady friction term on the speed of sound is also physically motivated and not only a mathematical artifact is still subject of discussion [99, 7]. The shift of the frequency can be also appreciated in Fig. 6.11 where a parametric study with different values of k_4, namely 0.5, 1, 2, is plotted for comparison.

To reach a better agreement with the experimental data, a trial and error procedure for k_4 is carried out. For clarity reasons only the envelopes of the pressure are plotted in Fig. 6.12. A fairly good agreement[1] can be reached with $2.5 < k_4 < 3$. However the goodness of the fit is not easy to assess, since the first part of the pressure curve (e.g. until the 5^{th} peak, at around 270 ms, Fig. 6.12) is slightly under-damped with respect to the experimental value, while in the following final part the opposite occurs, i.e. the attenuation is over-estimated. This might be due to the effect of column separation in the first peaks, which is actually not occurring in the experiments, since the value of the pressure at the dead-end is always higher

[1]CPU time of simulation is in the order of 3 days, therefore only limited amount of trials has been carried out

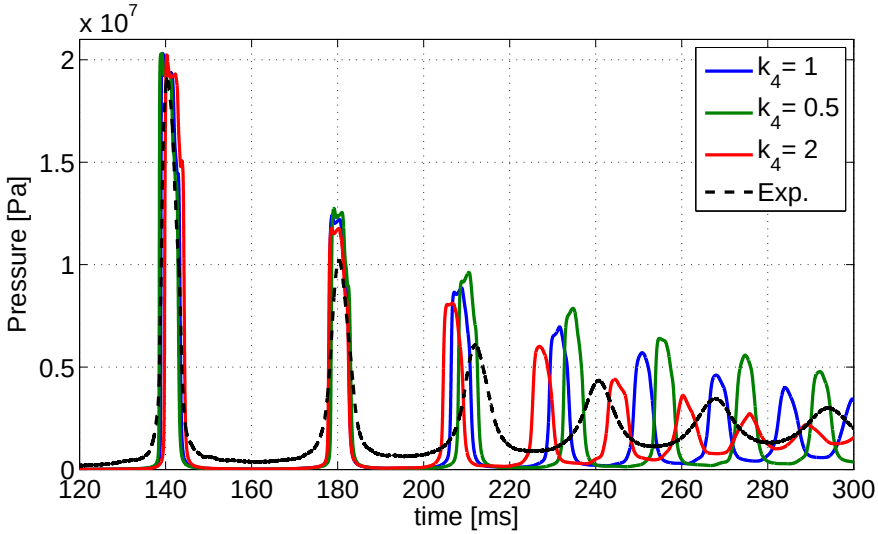

Figure 6.11: Numerical simulations with different values of k_4 vs experimental data (standard case): a slight increase in frequency with increasing k_4 can be observed.

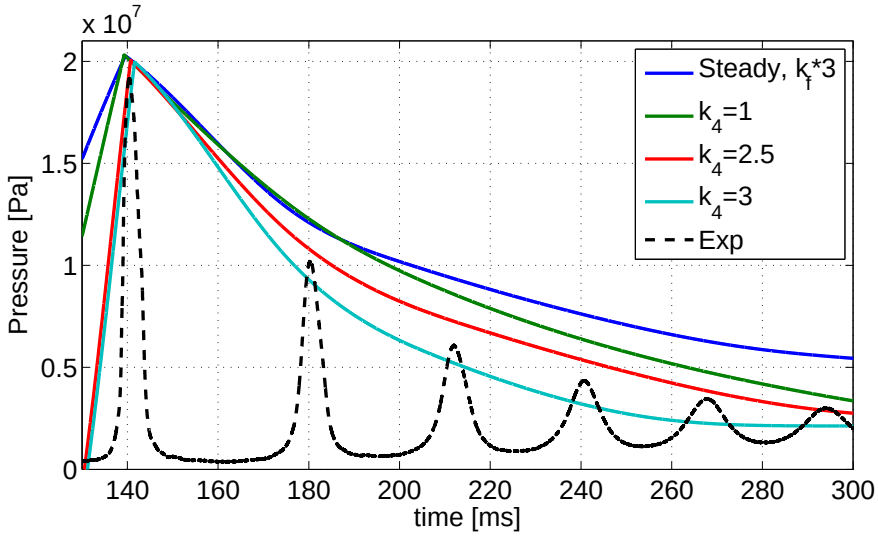

Figure 6.12: Pressure envelopes for different values of k_4 in order to find the best fit value to the experimental data

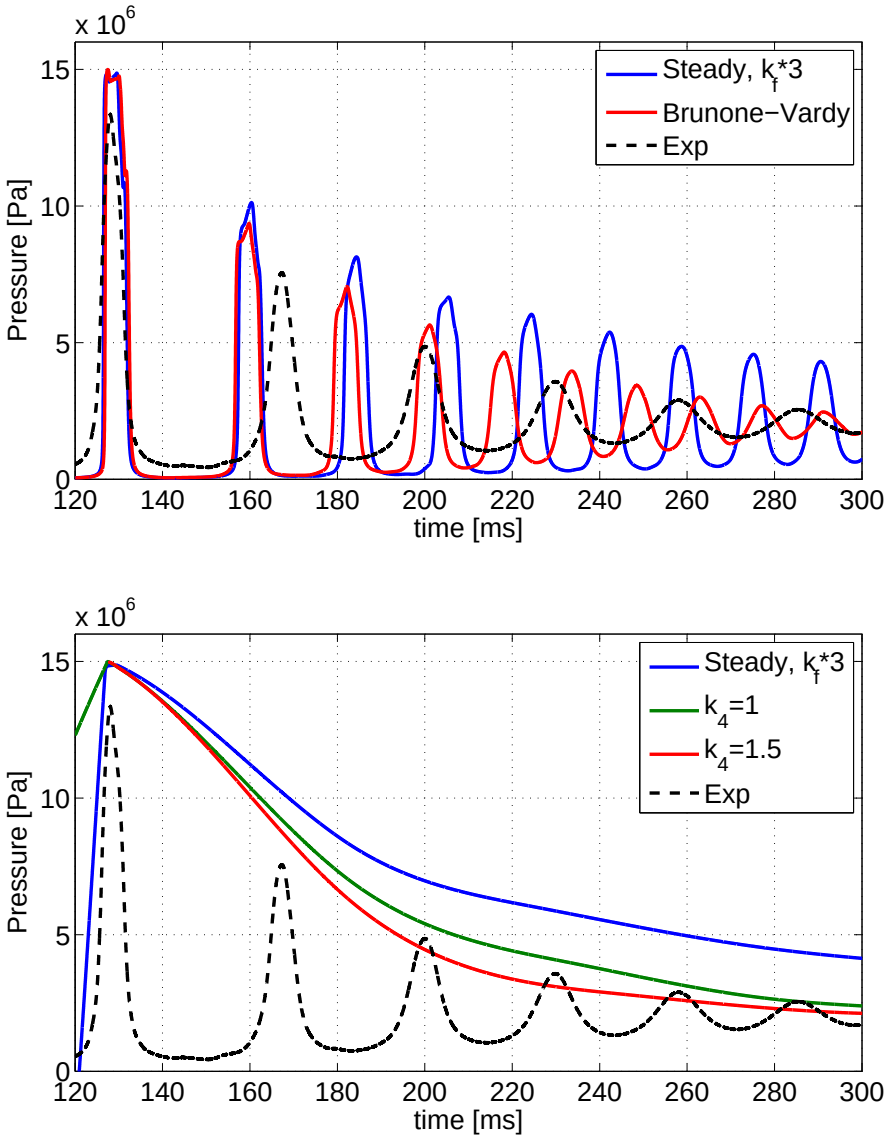

Figure 6.13: Top: comparison between the steady friction model and Brunone-Vardy's UFM vs experimental data of ethanol (standard case). Bottom: pressure envelopes for different values of k_4 in order to find the best fit value to the experimental data of ethanol (standard case).

than the vapor pressure. It is to be reminded that the code is 1D, whereas the real flow pattern is 3D and highly non homogeneous.

The results for ethanol are plotted in Fig. 6.13. As for water, the UFM improves the prediction of the wave attenuation, although still under-estimated. The frequency shift is slightly more remarked than in the case of water. This is expected since the minor density of ethanol leads to a higher velocity and thus higher velocity gradient. Figure 6.13, bottom, shows the envelopes of the pressure curves for different values of k_4. A good agreement can be reached with $1.25 < k_4 < 1.5$. The fitting parameter k_4 is lower than the one for water, so it might depend on fluid properties such the viscosity. It might also depend on the residual gas mass fraction, since the vacuum level are different for water and ethanol, being respectively 20 and 10 mbar. Given the prohibitive CPU time of the simulations, it was not feasible to extend the investigations to others boundary conditions, so the dependency of k_4 on the gas content is not assessed in this work.

6.8 Summary

The wave attenuation has been analyzed for the different tested conditions. The gas content is mainly responsible for the damping of the wave, rather than the viscosity of the fluid, since minor differences are noticed between water and ethanol for different amounts of initial gas in the line or tank pressure. An empirical analysis of the damping was performed by comparing several models, assuming an exponential decay of the pressure wave. The piecewise model and the hyperbola function of τ seem to well match the experimental results. These model attempt to take the effect of column separation and gas desorption into account for a more correct physical evaluation of the wave attenuation. The gas desorption has a clear effect on the wave attenuation: the release gas remarkably increases the damping. The effect is stronger for saturated ethanol, due to its higher amount of dissolved gas.

Similarly, the additional pressure losses induced by the elbow or tee contribute to increase the attenuation. The material proves to have no effect, except for the special case of upstream anchored pipe, where the additional strain of the pipe subtracts energy to the fluid and thus (slightly) increases the damping of the wave.

From a numerical point of view, the implementation in EcosimPro/EPSS of the UFM definitely improves the prediction of the wave attenuation. Brunone's UFM with the Vardy analitically-deduced shear decay coefficient gives fairly good predictions in terms of damping. However, given the high gas content and the non-homogeneous 3D flow pattern, the adoption of a empirical coefficient k_4 might be necessary to achieve a better prediction, as proved for the present cases.

Chapter 7

Analysis of the multiphase flow evolution

7.1 Introduction

The two main characteristics of the pressure wave such as its pressure peak and its frequency are dependent on the speed of sound. As underlined in the previous chapters, the evaluation of the speed of sound in two-phase, two-components flow is a difficult task. Different flow conditions lead to different formulations and in addition, the gas distribution is neither uniform nor constant in time, due to phenomena such as vaporization/condensation and gas desorption/absorption. One powerful mean to gain further insight is the flow visualization through the quartz segment, as already done to support the description of the pressure peak evolution. However HSI only provides qualitative information on the flow pattern, as the 2D images are not fully resolving the 3D pattern. A second approach is the numerical simulation. Although the prediction ability of 1D numerical codes for such problems is generally limited, they still provide valuable support in understanding the evolution of the flow pattern, having the advantage of providing certain quantities which are difficult or impossible to measure, such as void fraction, non condensable gas (NCG) mass fraction, vapor mass fraction, speed of sound and many others.

In this chapter, numerical results of different variables will be presented in time-space diagrams and with the support of HSI, the flow pattern evolution will be described, with particular attention to the gas/vapor content. A dedicated section is devoted to the evaluation of the speed of sound in these conditions. Additionally, the spectacular phenomena of the shock wave formation in two-phase flow is presented.

7.2 Numerical analysis of the flow evolution

7.2.1 Flow regions

In characterizing a two-phase flow one parameter used commonly is the void fraction. It is a key value to calculate other important parameters, such as mixture density, pressure drop, heat transfer, and to predict flow pattern transition. In the case of a saturated fluid, the flow is not only two-phase but also two-components due to desorption of the dissolved gas. In order to describe the flow pattern evolution it is then helpful to include as variables one parameter describing the NCG content

and one for the vapor content. In the following analysis these three variables are then chosen:

1. the void fraction α, which represents the volume fraction of the gaseous phase (vapor and NCG) in a node $\alpha = \frac{V_{gas}+V_{vap}}{V_{node}}$
2. the NCG mass fraction, which represents the mass fraction of the NCG in a node, $x_{ncg} = \frac{m_{ncg}}{m_l+m_{vap}+m_{ncg}}$
3. the vapor mass fraction, which represents the mass fraction of vapor in a node, $x_{vap} = \frac{m_{vap}}{m_l+m_{vap}+m_{ncg}}$

Based on the values of these three parameters in a given node, different flow regions[1] can be defined as listed in Table 7.1.

region	α	x_{ncg}	x_{vap}
gas (NCG)	1	1	0
gas-vapor	1	>0	>0
vapor	1	0	1
liquid-vapor	<1	0	>0
liquid-gas	<1	>0	0
liquid-gas-vapor	<1	>0	>0
liquid	0	0	0

Table 7.1: Definition of the possible multi-phase flow regions based on the values of void fraction and mass fractions

The NCG refers not only to the residual GN2 initially presents in the line, but it includes also the desorbed gas in case of saturated fluid.

Figure 7.1 shows the result of an ESPSS simulation for the evolution of these variable in space at a given time and the evolution in time at a given node (middle point of the test section, node 50) during priming. Only the vacuum case in the straight test section is here considered; the fluid is deareated water at $P_{tank} = 20$ bar and $P_{line} = 10$ mbar. The physical evolution of the flow in the pipe upon the valve opening could be described as follows. Initially, only the residual NCG is present, so $\alpha = x_{ncg} = 1$. Then the vapor generated by the flash boiling arrives at the node, forming a mixture of NCG+vapor ($\alpha = 1$, $x_{ncg} < 1$). The liquid then enters the node ($\alpha < 1$) creating a foam region ($\alpha < 1$, $x_{ncg} < 1$). One should expect that for

[1]Theoretically the liquid-gas region can not exist, since the liquid must always be in equilibrium with its own vapor. However since the vapor partial pressure is very low compared to the NCG partial pressure, it might be canceled by the truncation error. If the liquid-gas region is excluded, only α and x_{ncg} are necessary to define all the regions, being x_{vap} evaluated indirectly.

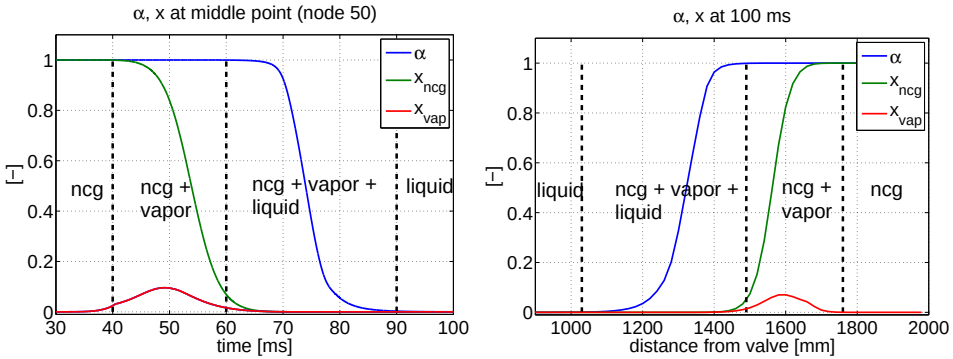

Figure 7.1: Numerical results of the evolution of void fraction and mass fractions with respect to time (left) at middle point and with respect to space (right) after 100 ms of the valve opening. The different fluid regions can be identified by the values of α, x_{ncg}, x_{vap}. Fluid is deareated water at $P_{tank} = 20$ bar and $P_{line} = 10$ mbar.

an instant only the vapor is present in the whole node ($\alpha = 1$, $x_{ncg} = 0$), but this region does not not appear, at least numerically. This is probably due to the mesh size: the node volume is too large (1 node = 20 mm) to get completely filled with only vapor, or similarly, the generated vapor due to the vacuum conditions is not sufficient. The maximum value of x_{vap} is 0.097, occurring at 1100 mm downstream the valve and at 58 ms. Later, the node gets more and more filled with liquid until $\alpha = 0$. The value of x_{ncg} is always slightly higher than x_{vap}, so also the liquid-vapor region alone ($\alpha < 1$, $x_{ncg} = 0$) does not exist numerically during the priming of the line. It does exist during cavitation, when the expansion wave causes the pressure to fall below the saturation pressure in some position along the test section. This can be clearly seen in Fig. 7.2, where the logarithm[2] of the void and mass fractions are plotted in order to gain resolution. The passage of the expansion wave generates vapor pockets, which disappear (condensation) as the pressure rises.

Saturated liquid

In the case of saturated liquid, due to the gas desorption the two-phase pattern ($\alpha > 0$) persists in all the nodes and for the whole time evolution, as it can be seen in Fig. 7.3. During the filling of the line, the development of α, x_{ncg}, x_{vap} in time at the middle of the test section (Fig. 7.3, left) is similar to the deareated case.

[2]Since $\log_{10}0$ = -Inf , the curves appear discontinuous

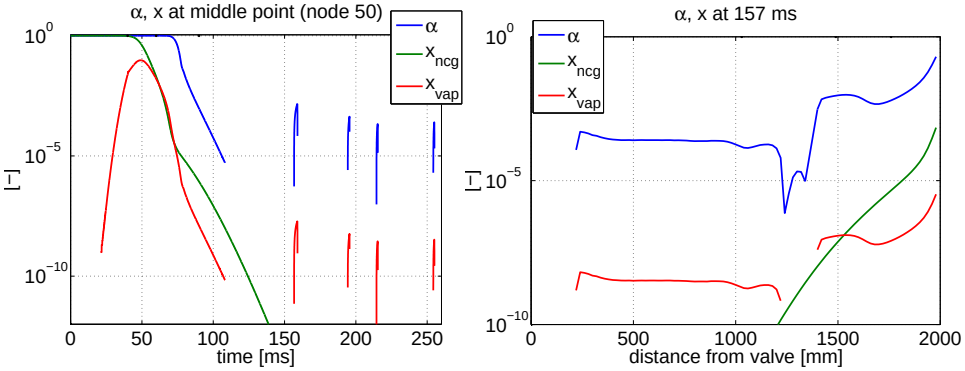

Figure 7.2: Evolution of void fraction and mass fractions in logarithmic scale with respect to time (left) at middle point and with respect to space (right) when the expansion wave passes (at 157 ms). Fluid is deareated water.

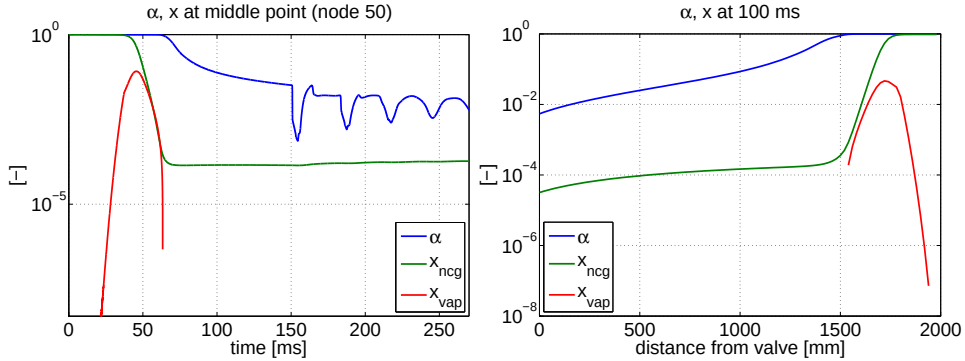

Figure 7.3: Evolution of void fraction and mass fractions with respect to time (left) and space (right). Fluid is saturated water

After the liquid front arrives at the node (at about 70 ms) , the NCG amount is almost constant and gradually increased to reach the value of the corresponding initial dissolved mass fraction ($380 \cdot 10^{-6}$). The released gas has also the effect to suppress the cavitation: the liquid-vapor regions ($x_{vap} > 0$, $x_{ncg} = 0$) occurring during the passage of the expansion wave are not generated anymore, due to the presence of NCG which prevent the pressure from dropping below the saturation level.

A comparison between deareated and saturated conditions is given in Fig. 7.4, where the values of pressure, α, x_{ncg}, x_{vap} at the dead-end are plotted. For completeness, also the case of water with non-dissolved gas is presented. In this way it is possible to appreciate the differences between the desorption process which takes a finite time (desorption time constant is 150 ms) and the liquid-gas mixture with a homogeneous and constant non-dissolved GN2 content (NCG mass fraction is 10^{-4}). In this regard, the first pressure peak is slightly higher for the saturated liquid compared to the non-dissolved NCG case. However, as the desorption process takes place, the released gas causes a more remarkable frequency shift. The increase in the wave attenuation can be also observed.

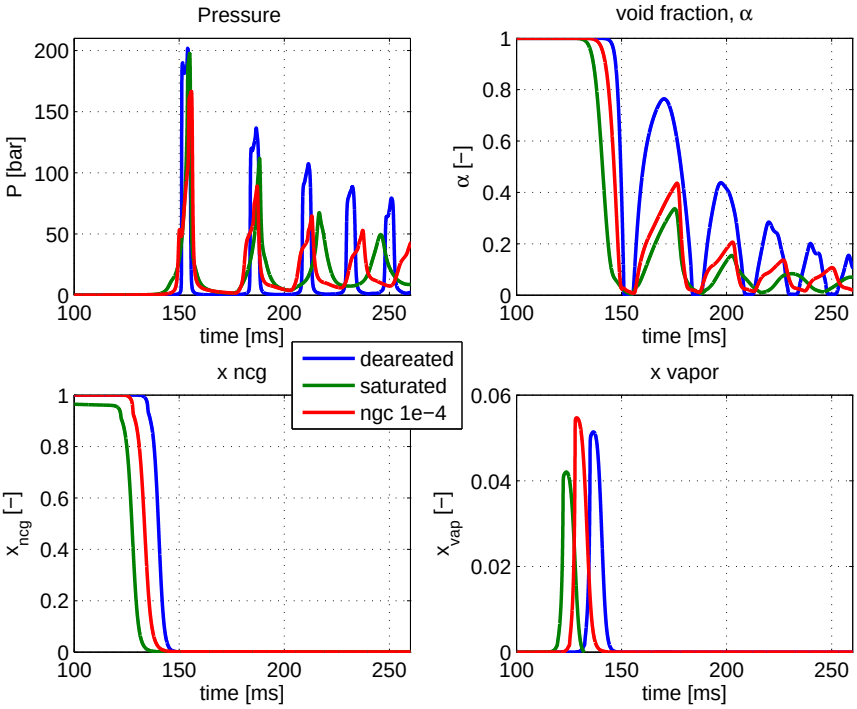

Figure 7.4: Pressure, void fraction and mass fractions at the dead-end (node 100) for three different fluid conditions

7.2.2 Space-time evolution (*x-t* diagrams)

The evolution of the flow pattern can be more effectively analyzed by plotting the space-time *(x-t)* diagrams. In this way the x-axis represents the pipe axial position while moving along the y-axis gives the temporal evolution. The color is then associated with the amplitude of the dependent variable. The test section is modeled with 100 nodes; the temporal resolution is 0.01 ms.

Figure 7.5 shows the *x-t* diagrams of α, x_{ncg}, x_{vap} for deareated and saturated water. Thanks to the colormap, it is possible to detect the position of the liquid front as the water flows towards the dead-end. This is more clear in the plot of the void fraction (Fig. 7.5, top) where the interface between liquid ($\alpha = 0$, blue) and gas ($\alpha = 1$, red) is sharper, whereas the plot of the vapor mass fraction (Fig. 7.5, bottom) shows a thick layer of vapor traveling ahead of the liquid front. Quite interesting, the vapor layer has its maximum thickness when the liquid is at the middle of the pipe and then it decreases gradually as the liquid reaches the dead-end. In fact, when the liquid is at the middle position, the initial residual gas has been compressed so that its pressure doubled from 10 mbar to 20 mbar, assuming a isothermal compression. The latter value corresponds to the saturation pressure of water, and therefore the evaporation process ceases from this position on. Because the gas and vapor mass content can range from 1 to as low as 10^{-12}, a logarithm scale allows a better resolution (Fig. 7.6). The logarithm scale has also the advantage to better underline the differences between deareated and saturated fluid.

In the case of deareated water (Fig. 7.6, top), after the first pressure peak the initial residual gas in the line is not confined in the final few nodes space at the dead-end, but it spans over a considerable length, namely from 1350 mm to the dead-end. This has important implications for the correct evaluation of the speed of sound, as it will be better explained in Section 7.4. In the saturated case (Fig. 7.6, right, top), the axial distribution of the NCG after 150 ms is monotonically increasing from the FOV to the dead-end, since the released dissolved gas (initial dissolved value is $380 \cdot 10^{-6}$ by mass) is added to the residual one in the line.

The x-t diagram of x_{vap} (Fig. 7.6, left bottom) allows to detect the formation of vapor regions as described previously, but now it is possible to appreciate both the axial distribution and the whole time evolution. This can be better seen in Fig. 7.8, where the pressure at middle point has been plotted as well to better correlate the low pressure cavitation regions with the liquid-vapor formation and their axial extension. It can be noted that the first cavitation region occurring after the pressure drop and starting just after the valve does not extend completely along the pipe until the dead-end, but it is interrupted at about 1250 mm. In an attempt to better understand why this discontinuity occurs, the distribution of the pressure at this location is analyzed. Figure 7.9 shows the $x - t$ diagram of the pressure (left) and the pressure axial profile at three different times. A sharp discontinuity

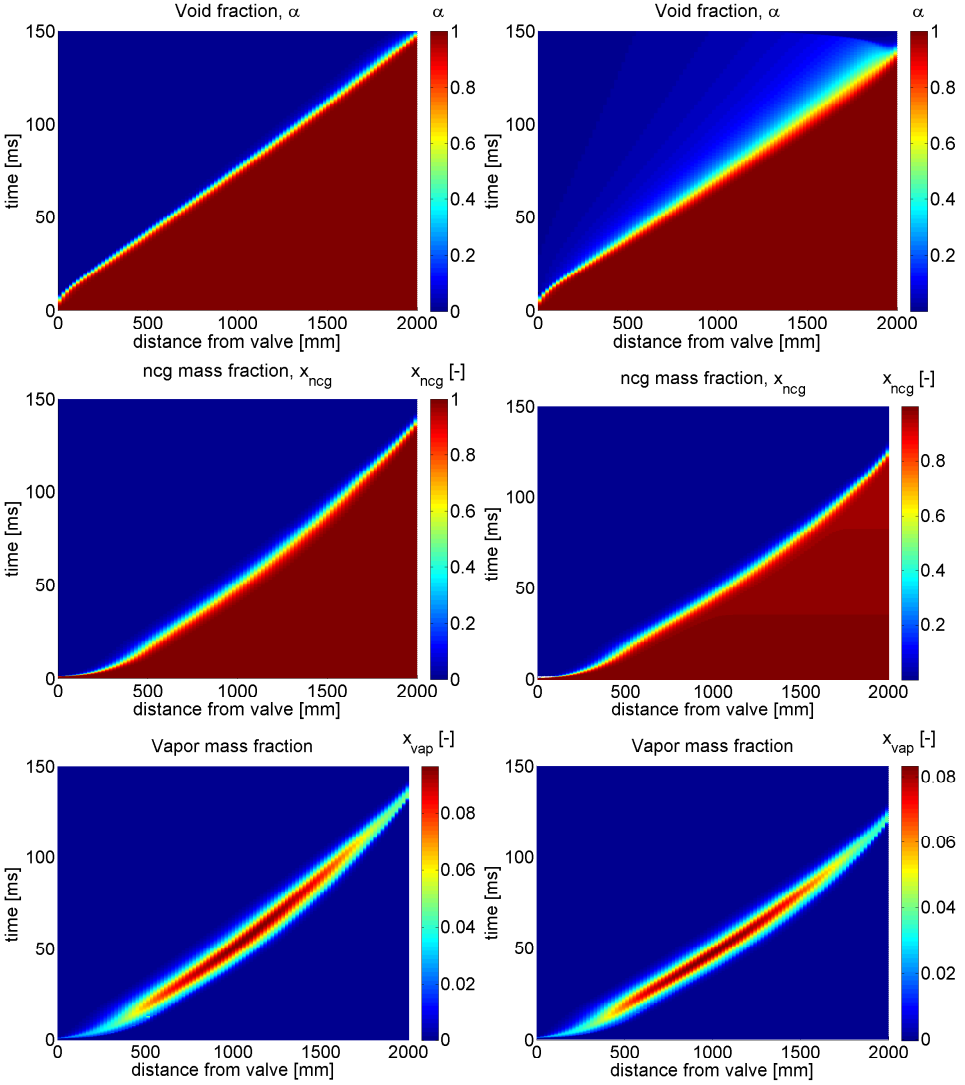

Figure 7.5: $X - t$ diagrams of void fraction, NCG mass fraction and vapor mass fraction for deareated (left) and saturated (right) water

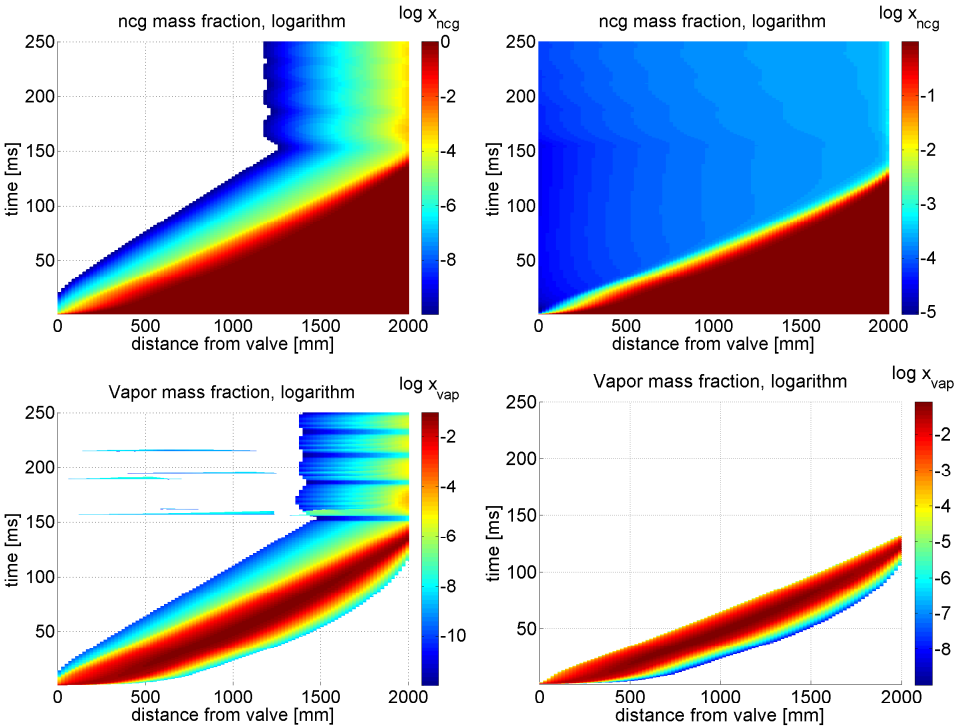

Figure 7.6: Colormap of NCG and vapor mass fractions in logarithmic scale for deareated (left) and saturated water (right). The white regions mean that the considered variable is zero, since $log_{10}0 = -\infty$, which is considered as "Not a Number" by the software.

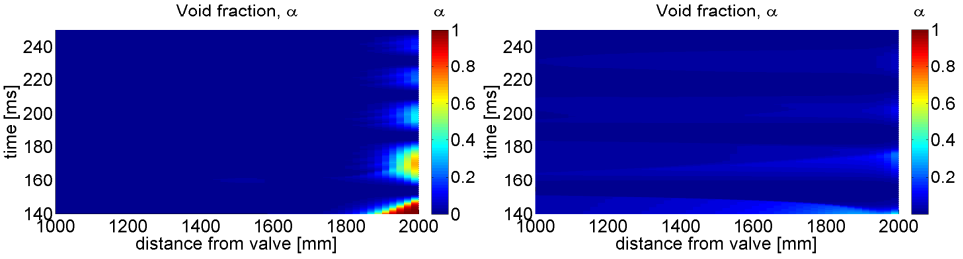

Figure 7.7: Colormap of void fraction distribution after the first pressure peak for deareated (left) and saturated (right) water

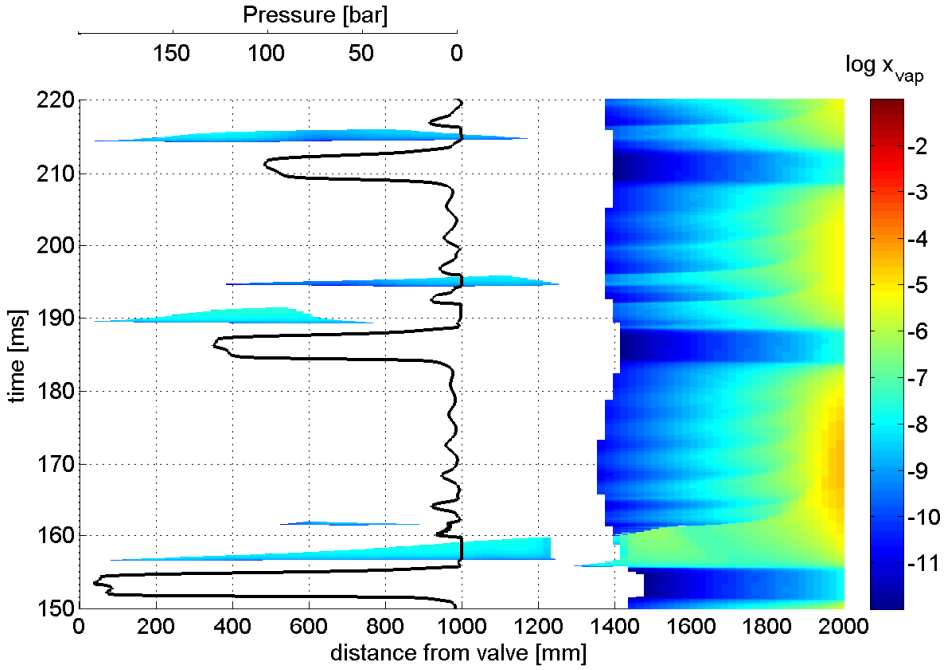

Figure 7.8: Zoom of vapor mass fraction distribution with the pressure evolution at middle point. It is possible to observe different cavitation regions along the pipe as well as the extended pocket at the dead-end

can be noted at 156.78 ms, ranging from 1300 to 1400 mm. This isolated pressure spike is very likely due to numerical instability[3] since it does not propagate along the pipe and it is quite rapidly suppressed. The same occurs at 159 ms/1400 mm, where a sudden pressure spike appears.

From a physical point of view, a possible explanation to suppress (or create) cavitation regions is the minor pressure oscillations due to the overtones. Along the pipe the pressure is not monotonically increasing nor decreasing, but local minima or maxima do exist. These are caused by the multiple odd frequencies of the fundamental pressure wave. However in such cases, the pressure gradients would not be

[3]Finite difference methods produce numerical oscillations when applied to problem with jump discontinuity (Gibbs phenomenon). To smooth such perturbations, artificial viscosity is usually introduced in the equations.

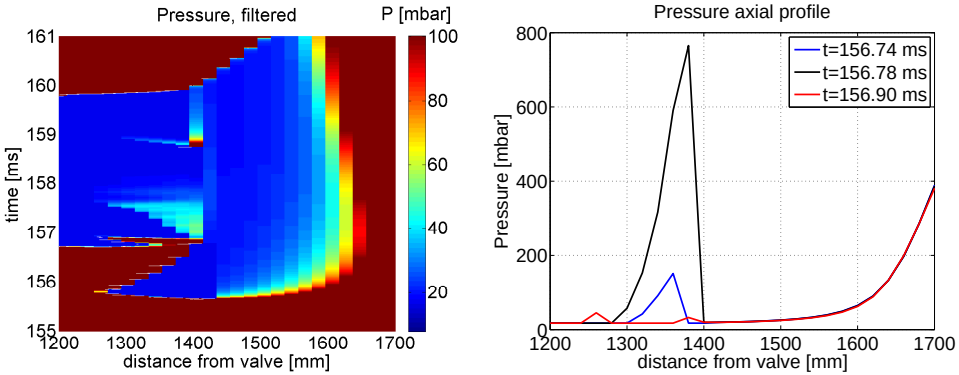

Figure 7.9: Magnified region across the cavitation discontinuity (left). The pressure has been filtered to gain resolution by limiting the values at 100 mbar. Right: the axial pressure profile at three different times.

so sharp as in the case of numerical instabilities. It is also to be reminded that the values of mass fraction can be as slow as 10^{-12}, so the numerical truncation errors are also a possible cause for local discontinuities.

In the saturated case (Fig. 7.6, right), the NCG prevents the cavitation from occurring, so there are no vapor regions after the first pressure peak. This inhibiting effect can also be seen in the following pressure peaks (Fig. 7.7) where the void fraction at the dead-end is clearly lower for the saturated case. In the deareated case (Fig. 7.7, left) the high value of void fraction at the dead-end indicates that the column separation has occurred. The case of water with an initial presence of non-dissolved NCG is presented in Appendix C.2.

Ethanol

The same analysis of the flow evolution is performed for deareated and saturated ethanol. The x-t diagrams of α, x_{ncg}, x_{vap}, pressure and speed of sound for ethanol are shown in Fig.7.10. Qualitatively, the same considerations as for water can be drawn. Quantitatively, two major differences can be underlined:

- because of the higher saturation pressure, the ethanol vapor mass fraction has greater value than the water one, reaching a maximum value of 0.16.
- in the case of saturated ethanol, the higher amount of desorbed gas leads to a considerable presence of x_{ncg} along the test section which persists for all the duration and causes a dramatic decrease of the speed of sound.

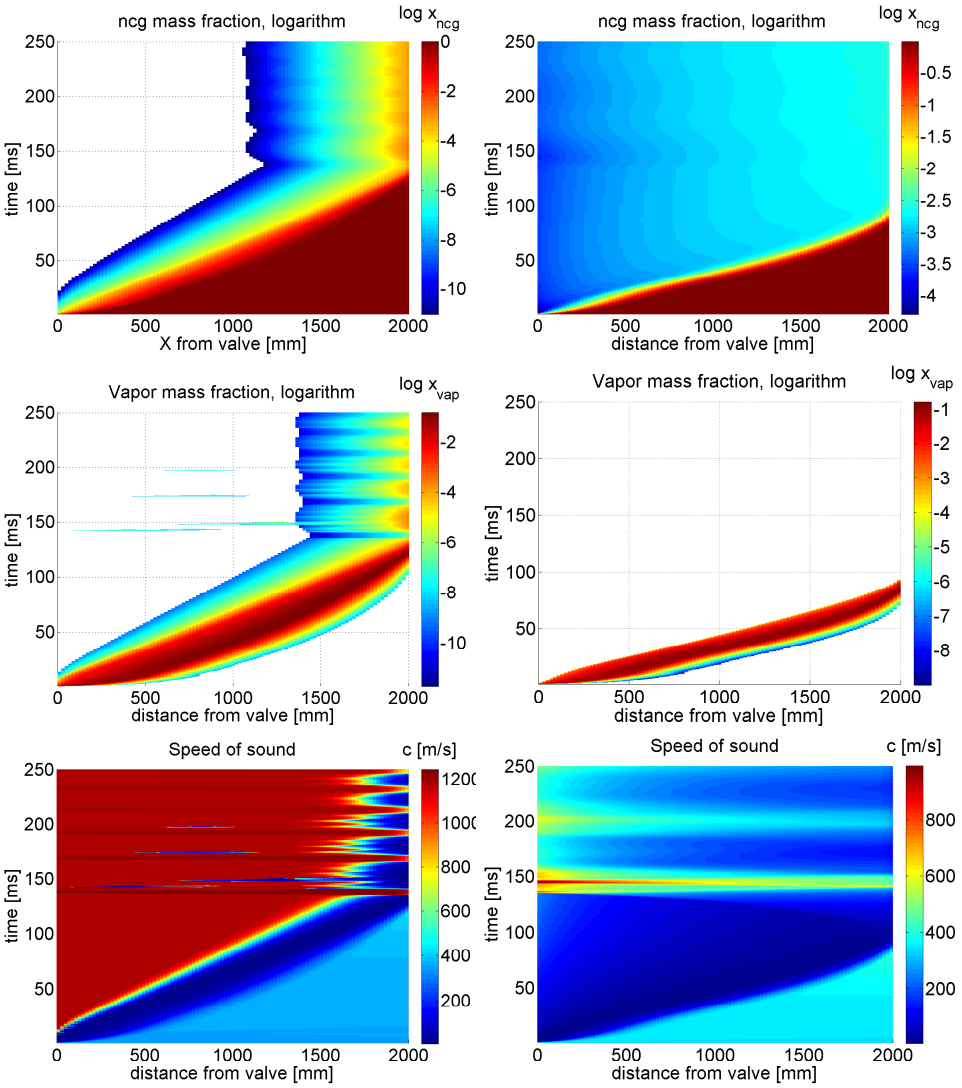

Figure 7.10: $X - t$ diagrams of NCG mass fraction, vapor mass fraction and speed of sound for deareated (left) and saturated (right) ethanol

7.3 High speed imaging of the flow evolution

The evolution of the liquid front can also be qualitatively described with the support of HSI. Figure 7.11 shows some selected video frames for deareated (left, L) and saturated (right, R) water. The first frame (1) is depicted just to allow a comparison with (2), where a tiny mist is flowing in the pipe: it is the vapor generating by the liquid front undergoing flash boiling. The images are not so sharp, but in the video it is possible to clearly see such a fog entering the dead-end. It is slightly more dispersed for deareated (2L) than saturated (2R). It is also possible to notice a small condensation of the vapor on the wall because the images get less sharp (2-3 L) . The pressure reading of the sensors at (2) is slightly negative[4] (-180 mbar): this is due to a small thermal shock induced by a weak shock wave[5] which alters the reading.

Successively some small drops of water appear (4L, 5R) and impact at the dead-end. These droplets increasing gradually in size (6) and eventually coalesce in small slug of liquid, until finally the liquid front comes (7). The flow is stratified due to the gravity. At the maximum pressure (9), the saturated flow (9R) shows more dispersed bubbles which occupy more volume, while at the first pressure valley (10), the deareated water seems to be more bubbly, although the difference is difficult to tell. No column separation occurs due to the low driving tank pressure and the presence of the initial residual gas.

Although it is not possible to extract quantitative information from the HSI in order to assess the void fraction, a qualitative comparison can be performed with the results of the numerical simulations. Figures 7.12 and 7.13 show the evolution of the void ans mass fraction profiles located in the last 200 mm of the pipe, which is the length of the quartz segment. The first change in the profile occurs at frame (6), where the vapor enters the last 200 mm ($x_{vap} > 0$, $x_{ncg} < 1$) but there is no liquid yet ($\alpha = 1$). In contrast, the HSI shows that some droplets have already impinged at the end. The first appearance of liquid in the numerical results occurs at (7), where $\alpha < 1$. The main flow stream arrives at 184 ms (8), and the related void fraction profile seems fairly representative of the real distribution. However by this frame it is possible to underline the limits of the 1D model: the real flow is stratified and after impacting at the dead-end a secondary stream bounces back

[4]Negative values of pressure are usual for dynamic pressure sensors, since the initial value is always zero at any steady pressure. However in this case the initial pressure is almost zero being vacuum at 10 mbar

[5]As the valve opens, the configuration is exactly the same as in the Riemann shock tube, where a membrane separates two different pressure regions. This gives rise to a weak shock wave in the low pressure gas side which in turns induces temperature changes: even if the pressure perturbation is of few mbar, what matters is the pressure ratio which can be considerable given the very low initial pressure of 10 mbar. These shock wave-induced pressure perturbations have been observed and described in previous work of the author [14].

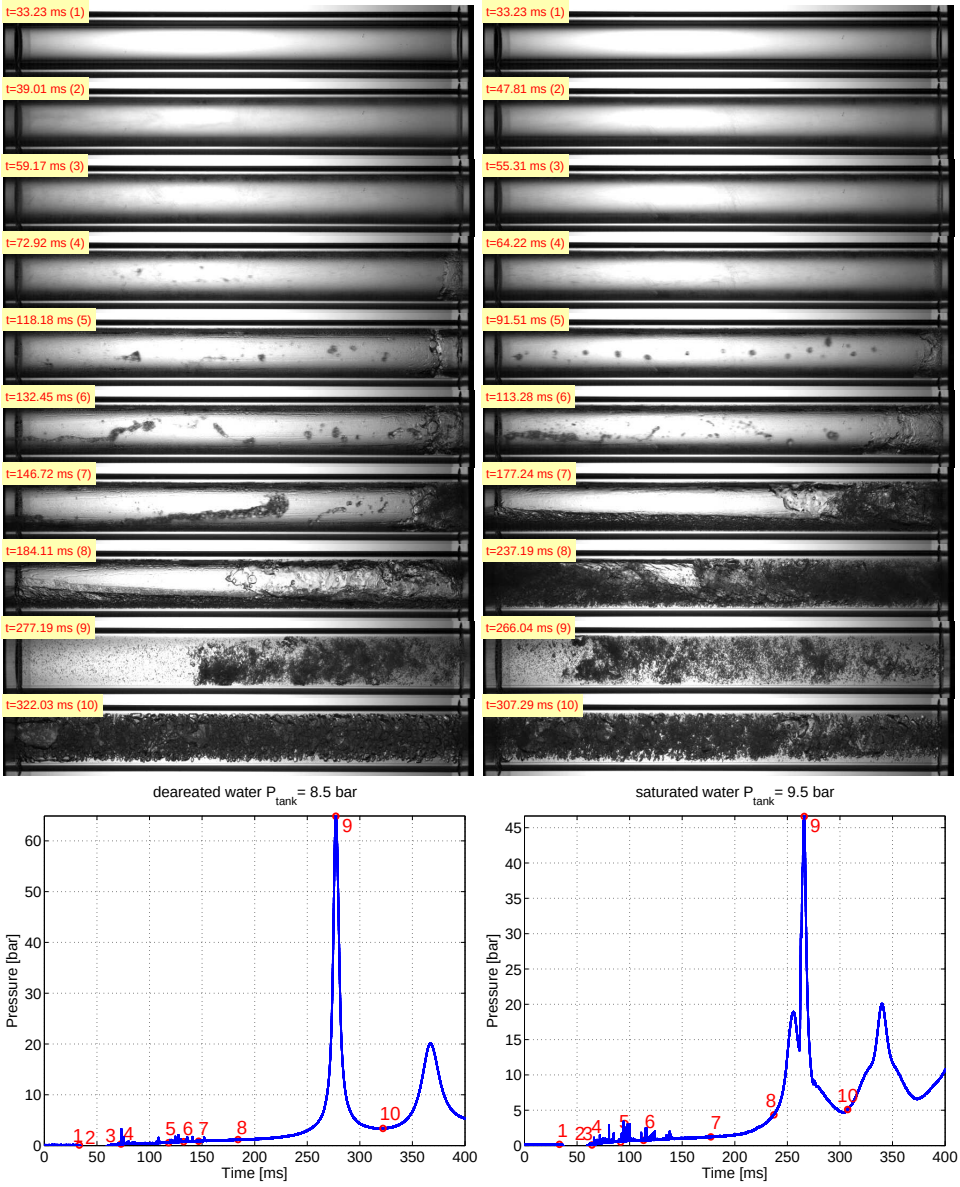

Figure 7.11: Flow visualizations for deareated (left) and saturated (right) water, downstream position, with the corresponding pressure profiles

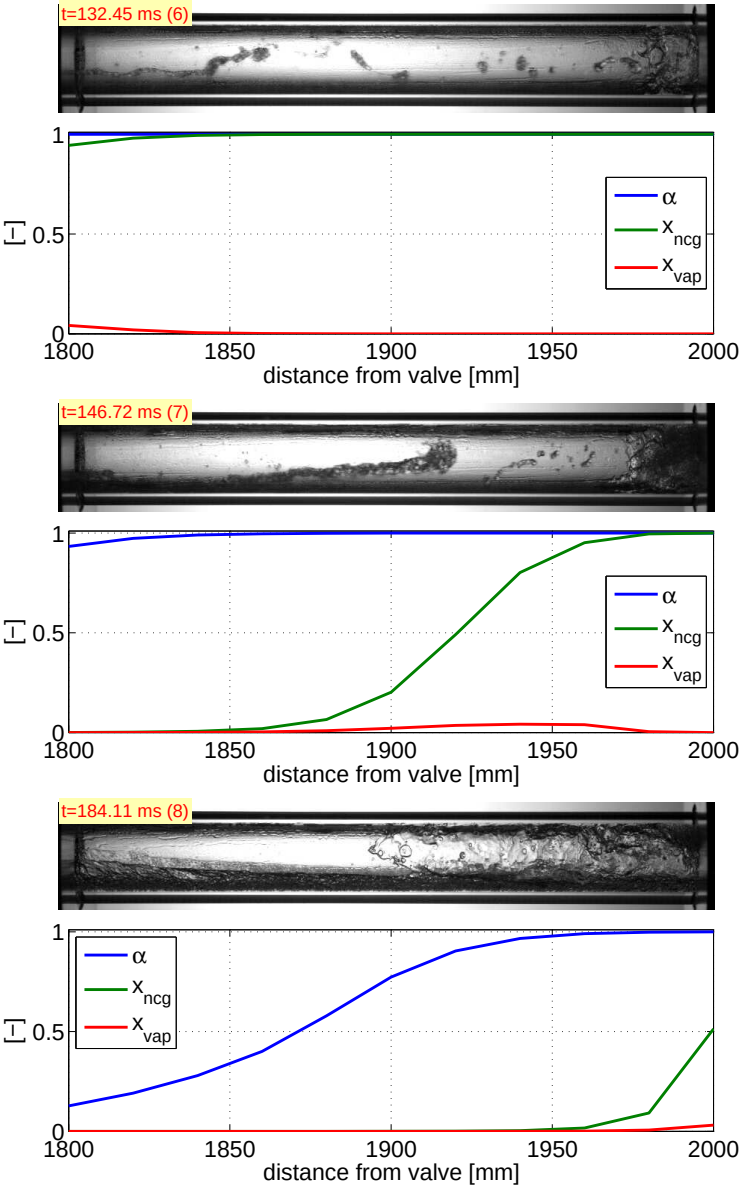

Figure 7.12: Comparison between the flow visualization and the numerical void fraction for selected frames. Deareated water

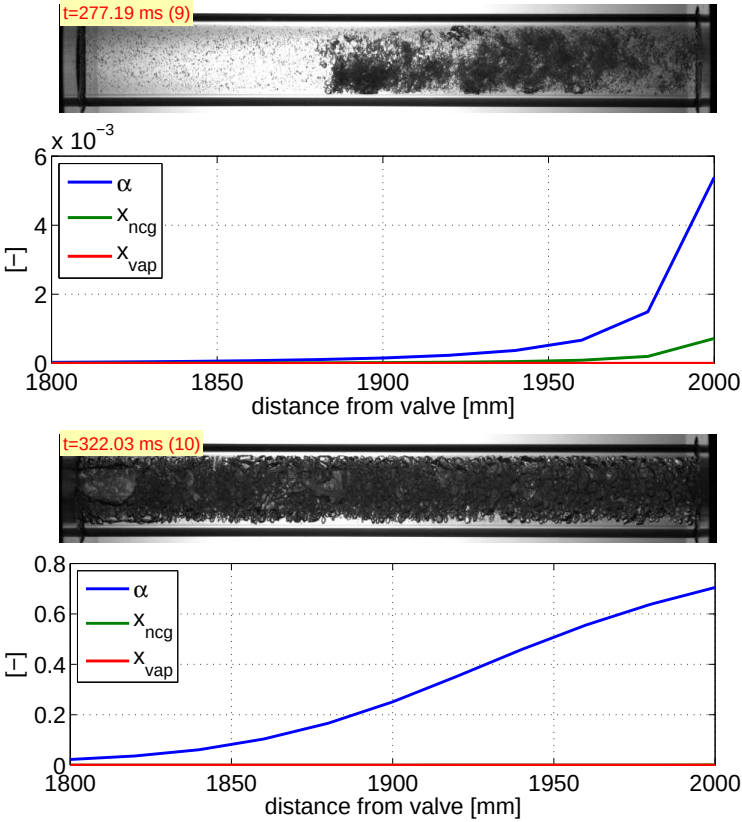

Figure 7.13: Comparison between the flow visualization and the numerical void fraction for selected frames. Deareated water

wetting the top of the pipe. By this, a sort of pocket was created, trapping the residual gas in the last 120 mm, as it can be seen in (9). This dynamic can not be reproduced by a 1D model, resulting in a unrealistic void fraction profile. For such a case, 3D transient model appears as the proper tool to simulate this complex dynamic. The void fraction at the time of minimum pressure after the first pressure peak (i.e. the valley between the two first peaks) is shown in (10), where again the calculated distribution does not match the real pattern, which appears to have a rather uniform bubble distribution. The main consequence of a miscalculated void fraction profile is a wrong estimation of the speed of sound, that in turn leads to a mismatching wave frequency.

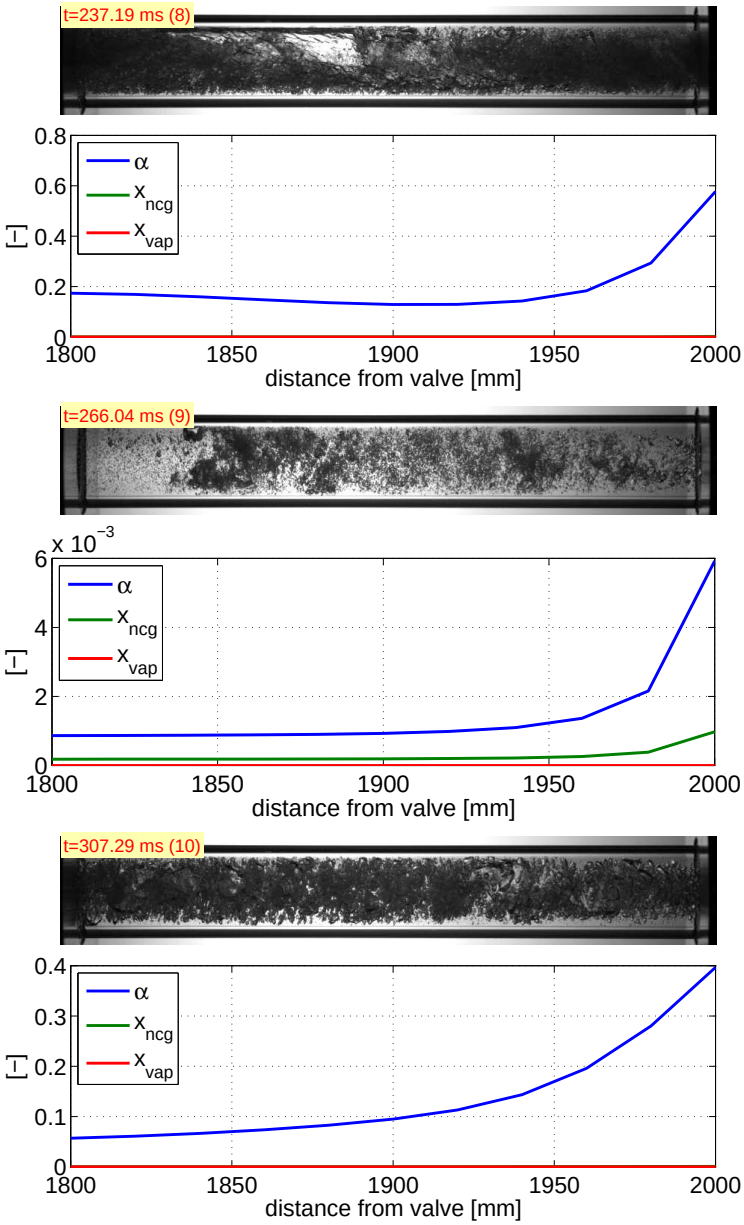

Figure 7.14: Comparison between the flow visualization and the numerical void fraction for selected frames, saturated water

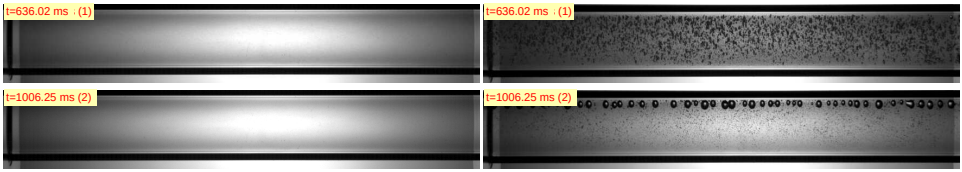

Figure 7.15: Flow visualizations for deareated (left) and saturated (right) water, upstream position, at the end of the transient

For completeness, the void and mass fraction profiles and their corresponding HSI frames in the case of saturated water are reported in Fig. 7.14. It can be remarked that the distribution of the void fraction is not monotonically increasing toward the dead-end like previously, but now a local minimum can be detected at around 1900 in (8). This is due to the desorption process, which increases the gas content in the liquid front where the pressure is lesser.

Figure 7.15 shows the fluid conditions at the end of the transient (at t=636 ms and t >1000 ms) at the upstream location. The HSI imaging confirms the high amount of gas released in case of saturated water (Fig. 7.15 , right) where the bubbles of the dissolved gas come out of the liquid and persist in the fluid.

7.3.1 Shock wave in two-phase flow

In some test conditions, a very steep pressure rise has been observed in the pressure signal of the upstream sensor PD-505 (Fig 7.16, top). The gradient of this rise is quite remarkable, about 32 bar in 0.02 ms, or 1600 bar/ms, far greater than the usual water hammer pressure surge gradient. Thanks to HSI it was possible to gain an insight of the flow pattern evolution during such an event. Figure 7.16, bottom, displays some selected video frames for the case of saturated water, with the quartz pipe mounted upstream (inlet of the test section).

Initially, the flow image (first frame at t=0) is quite dark, indicating a large gas content in form of very tiny dispersed bubble. Then suddenly the flow image becomes brighter, with a foamy appearance. The change in the flow pattern is abrupt and violent. This is indeed a shock wave generated by the collapse of vapor bubbles. As explained in Section 2.3.3, shock waves occur upon the collapse of a bubble cloud, which is the flow pattern observed here. The measured mean velocity of this shock wave is 155 m/s ±4%. This value might seem small, but one has to remember that in two-phase flow the speed of sound can be as low as few meter per second (see e.g. Fig. 2.9).

According to Brenner [16, page 149], the shock wave velocity u_1 in a bubbly flow can be estimated by Eq. (7.1):

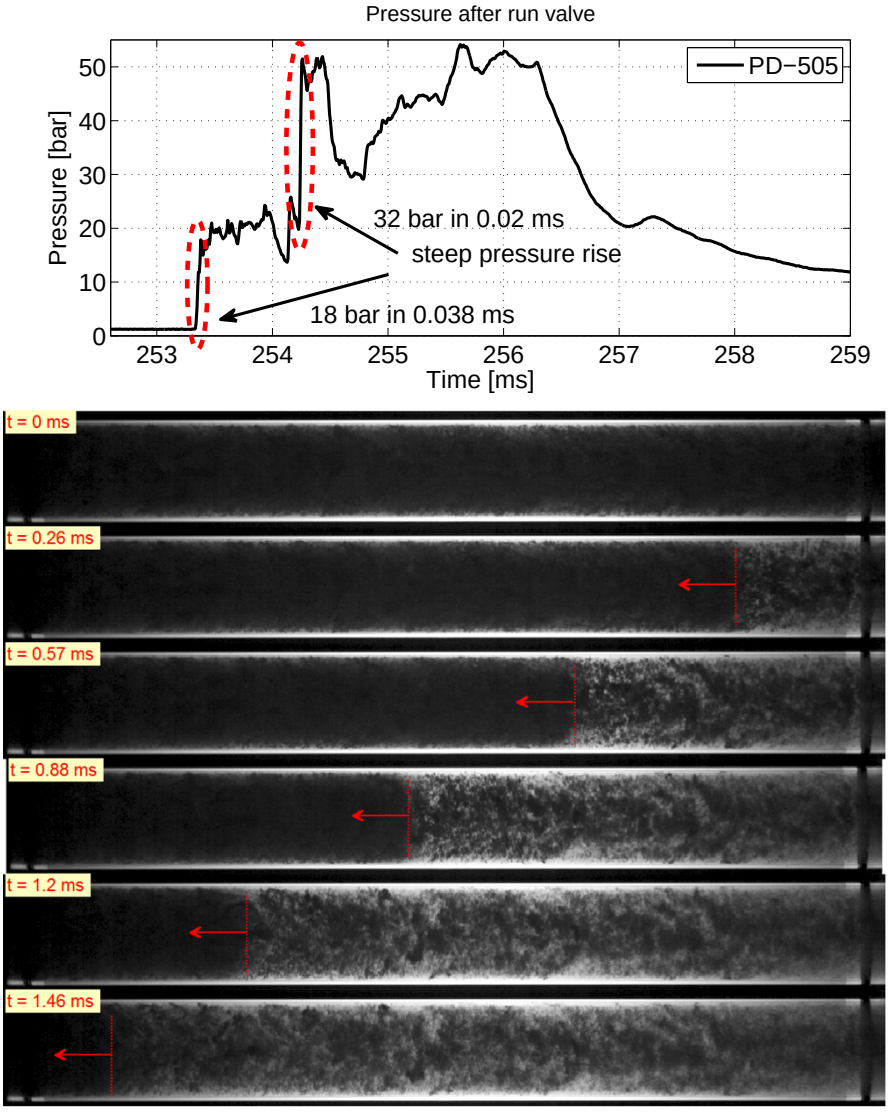

Figure 7.16: Pressure signal PD-505 and related video frames during the passage of the shock wave. The first frame corresponds to 251.9 ms. The fluid flows from left to the right, the quartz pipe is mounted 200 mm downstream the FOV. Fluid is saturated water.

$$u_1^2 = \frac{(1-\alpha_2)}{(1-\alpha_1)(\alpha_1-\alpha_2)} \left\{ \frac{(P_1 - P_{vap})}{\rho_L} \left[\left(\frac{r_1}{r_2} \right)^{3k} - 1 \right] + \frac{2\sigma}{\rho_L r_1} \left[\left(\frac{r_1}{r_2} \right)^{3k} - \frac{r_1}{r_2} \right] \right\} \tag{7.1}$$

where α is the void fraction, P is the pressure, ρ_L is the liquid density, r is the bubble radius, k is the polytropic index and σ is the surface tension; the index 1 and 2 indicate the conditions before and after the shock. Since the bubble size ratio can be related to the void fraction by mean of Eq. (7.2):

$$\left(\frac{r_2}{r_1} \right)^3 = \frac{\alpha_2(1-\alpha_1)}{\alpha_1(1-\alpha_2)} \tag{7.2}$$

the only unknown values are the void fraction before and after the shock, which were not possible to measure. However with some educated guesses based on the saturated conditions of the flow and the results of numerical simulations, Eq. (7.1) gives a Mach number $Ma = 3 \div 4$. This value is in line with other values available in literature [16, 104].

A detailed analysis of this phenomenon requires the bubble dynamics to be taken into account, which is beyond the scope of this research work. A good description of the shock wave phenomena in liquid-gas mixture is given by the aforementioned book of Brenner [16]. Such phenomena are of importance in the cavitating flow for the marine propellers. It is worthy to underline the potential hazard of such a shock wave in case of monopropellant, with the related risk of adiabatic compression detonation.

7.4 Speed of sound in a non-homogeneous mixture

In Chapter 5 it has been shown that the evaluation of the speed of sound based on the gas content does not give satisfactory predictions when compared with the experimental results. The reason is the use of a homogeneous liquid-gas mixture model, which assumes a homogeneous distribution of the gas/vapor bubbles in the liquid along the whole test section. But as shown by the HSI, the actual flow pattern during the priming is far from such an ideal conditions: the flow pattern includes tiny dispersed bubble regions, relative large gas pockets (slug flow), stratified flow regions and generally liquid-gas regions with highly non-homogeneous bubble distribution. The problem is then how to best evaluate the speed of sound in a non-homogeneous liquid-gas mixture, still assuming a 1D flow.

The easiest model which one can consider is a binary distribution of the liquid-gas: when the FOV opens, the liquid front advance in the pipe and compresses the gas towards the dead-end. The two phases are separated, so that the void fraction

is either 1 or 0 (mixing is neglected). Such a binary distribution of the liquid-gas is sketched in Fig. 7.17.

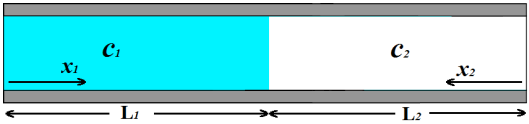

Figure 7.17: Binary distribution liquid-gas

To calculate the acoustic properties of such a pipe (eigenfrequencies and eigenmodes) the wave equation (or d'Alambert's equation for the 1D case) must be solved:

$$\frac{\partial^2 P}{\partial t^2} = c^2 \frac{\partial^2 P}{\partial x^2} \tag{7.3}$$

With the coordinate system showed in Fig. 7.17 , the boundary conditions are as follows:

1. $P_1(0) = P_{tank}$
2. $\frac{\partial P_2}{\partial x}(0) = 0$
3. $P_1(L_1) = P_2(L_2)$
4. $\frac{1}{c_1}\frac{\partial P_1}{\partial x}(L_1) = \frac{1}{c_2}\frac{\partial P_2}{\partial x}(L_2)$

where 3) and 4) account respectively for the pressure continuity and mass flow continuity at the interface.

The same calculation can be applied to a step-wise distribution of the speed of sound with the same boundary conditions at the discontinuity. Such analysis are quite common for the study of the acoustics of pipe/duct and this method is called the fluid network acoustic analysis[6] [42, 71]. The problem is to know the distribution of the speed of sound in the test section for an actual priming test, which is based on the distribution of the gas content. This value can not be measured, so an educated guess can be made only based on the numerical results. The numerical analysis of the priming process has showed that, in case of deareated fluid, the NCG content is confined in the final 650 mm of the test section, being the upstream fluid only liquid ($\alpha = 0$). This given NCG axial distribution $x_{ncg}(x)$ will then correspond to a certain profile of the speed of sound $c(x)$, as depicted in Fig. 7.18.

[6]The acoustic properties of a duct with a spatial variable speed of sound is a well-known problem in the combustion chamber of liquid rocket engine in order to study combustion instabilities

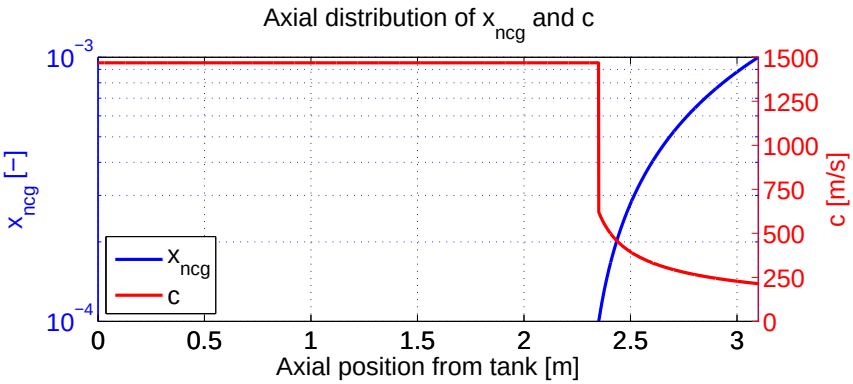

Figure 7.18: The axial distribution of x_{ncg} and its corresponding speed of sound distribution

Finally, using $c(x)$ as an input for the fluid network acoustic tool, the obtained solution is a frequency of 65 Hz, which corresponds to average speed of sound c_{avg}= 749 m/s. The experimental values are 52 Hz and 559 m/s. These predicted values are a much better estimation than the ones calculated with the homogeneous model presented in Chapter 5. However, the obvious disadvantage of such a method is that the NCG distribution must be known a priori.

The important point of this analysis is that the speed of sound based on a homogeneous liquid-gas mixture, with a uniformly distributed gas content estimated from the residual gas and/or from the desorption process, is not a valid approach since it does not represent the actual flow pattern in a priming test.

The numerically computed $x - t$ diagrams of the speed of sound for three different liquid conditions, namely deareated, saturated and with non-dissolved gas, are depicted in Fig. 7.19. In the deareated case, the sudden drops in the speed of sound located upstream (blue pockets spanning from 100 mm to 1200 mm) are due to cavitation. The formation of vapor dramatically decreased the speed of sound. The saturated case and the liquid with a non-dissolved NCG show a similar 2D map of the speed of sound. It is however possible to notice small differences in the first 200 ms evolution, due to the desorption process taking place and not completed yet.

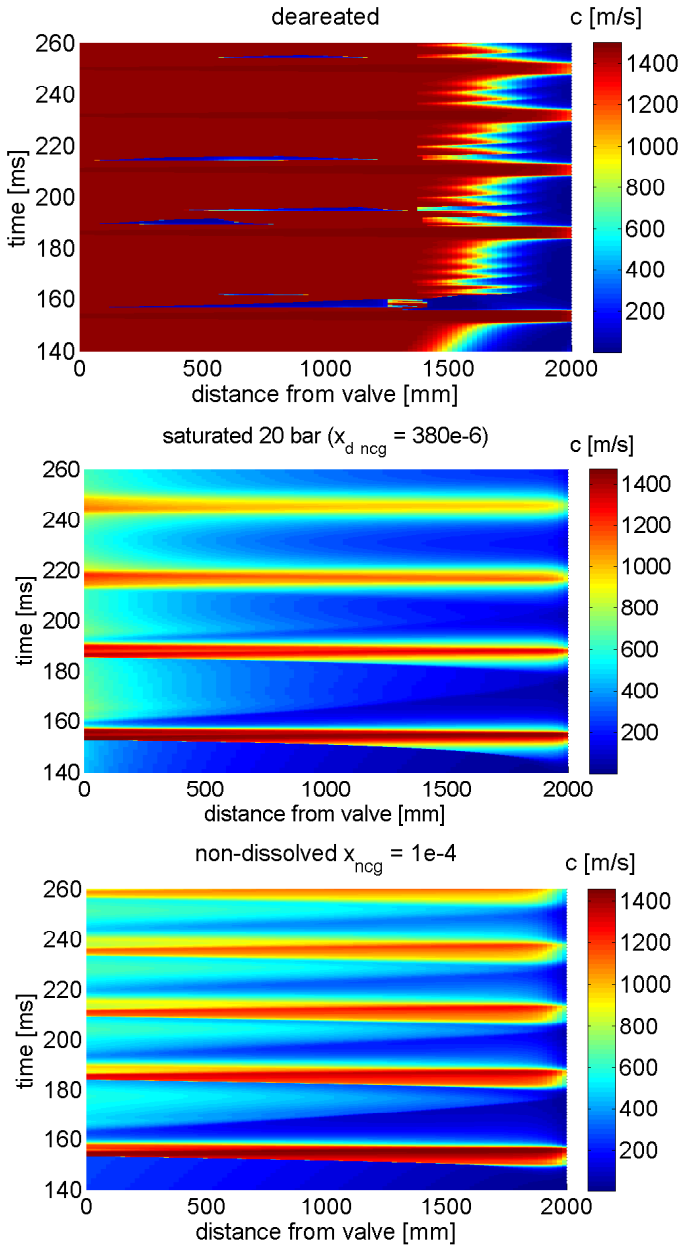

Figure 7.19: Colormap of the speed of sound for three different fluid conditions

Chapter 8

Considerations for spacecraft feedline system design

In this chapter the results discussed previously are analyzed from a different point of view, focusing more on some practical engineering considerations that might be of help to the designer of the feedline subsystem. Issues concerning the relevance of particular fluid properties or the importance of some parameters/boundary conditions are addressed. Some guidelines for the planning of an experimental investigation are also provided.

8.1 Assessment of the test replacement fluid

For various reasons, testing is often performed with a replacement fluid. Real propellants are in fact too toxic (MMH), too corrosive (NTO), too dangerous (monopropellant like hydrazine or hydrogen peroxide may undergo adiabatic detonation), too expensive or simply too unpractical to be handled in a laboratory system. In selecting the substitute fluid two questions are to be addressed:

1. what physical properties are to be considered for a representative replacement fluid ?

2. how well can the behavior of the real fluid on the basis of the test data obtained with the replacement fluid be deduced?

The answer to the first question is however related to the accuracy required. If the designer is concerned with the maximum pressure peak occurring during the priming, then the speed of sound c and the fluid density ρ are the two key parameters. If the frequency must be also estimated, then flash boiling and eventually gas desorption must be taken into account as the gas content deeply affects the speed of sound; therefore the vapor pressure P_{vap} , the surface tension σ and the solubility characteristic are the physical properties of importance. Finally, for a complete simulation of the pressure wave, the fluid viscosity μ must be included to properly simulate the wave attenuation.

8.1.1 Pressure peak comparison: water vs ethanol

Although no real propellant has been used in this research work, it is possible to draw some considerations on the assessment of the replacement fluid by comparing the test data obtained with water and ethanol. For the standard case of an evacuated line, and neglecting the cushion effect of the residual gas, the pressure peak can be estimated using Joukowsky's equation:

$$\Delta P = P = \rho c V_f \tag{8.1}$$

where the impact velocity V_f can be expressed in terms of pressure difference and density according to Bernoulli's equation and neglecting the friction:

$$V \propto \sqrt{\frac{2(P_{tank} - P_{line})}{\rho}} \tag{8.2}$$

Therefore, for the same fluid, the water hammer pressure peak can be related to the tank pressure as follows:

$$\frac{P_1}{P_{ref}} = \frac{\sqrt{P_{tank,1}}}{\sqrt{P_{tank,ref}}} \tag{8.3}$$

Similarly, at the same pressure conditions, the water hammer pressure peak of two different fluids can be related as follows:

$$\frac{P_1}{P_2} = \frac{\sqrt{\rho_1} c_1}{\sqrt{\rho_2} c_2} \tag{8.4}$$

Evaluating Eq. (8.4) for ethanol (c = 1124 m/s, ρ = 796 kg/m^3) and water (c = 1361 m/s, ρ = 1000 kg/m^3), gives a theoretical water hammer pressure ratio $P_{eth}/P_w = 0.74$. The speed of sound is calculated taking the elasticity of the pipe material into account according to Eq. (2.24).

Table 8.1 summarizes the pressure peaks obtained with the 2000 mm straight pipe and gives the theoretical values for the pressure peak ratio according to Eq. (8.3-8.4). At 20 bar tank pressure the maximum pressure peak is 198.9 bar and 133.5 bar for water and ethanol respectively. The pressure ratio ethanol/water is therefore 0.67, close to the theoretical value of 0.74. The same analysis has been performed by Anthoine and Lestrade [4] with MMH and NTO. When comparing the pressure peaks with respect to the ones obtained with water, the ratio is also lower than the expected, being 0.93 vs 0.99 for MMH and 0.66 vs 0.81 for NTO.

At lower tank pressures this ratio decreases further, due mainly to a lower pressure peak for ethanol rather than a higher peak for water, as it can be seen by the results for the ratio of the tank pressure. In fact in this case, the values for water

P_{tank}	experimental pressure peak [bar] (ratio with the value at 20 bar)		pressure peak ratio wrt to 20 bar as acc. to Eq. (8.3)	ethanol/water (0.74 acc. to Equ. 8.4)
	water	ethanol		
10 bar	125.2 (0.63)	72.2 (0.54)	0.71	0.58
16 bar	175.7 (0.88)	94.2 (0.71)	0.89	0.54
20 bar	198.9 (1)	133.5 (1)	1	0.67
22 bar	210.4 (1.06)	-	1.05	-
26 bar	233.5 (1.17)	-	1.14	-

Table 8.1: Comparison of the pressure peaks and their ratio for water and ethanol at different tank pressures

are in good agreement with the ratio predicted by Eq. (8.3). In the case of ethanol, the experimental pressure peaks are however lower than the estimated ones. One should also consider that the viscosities of the two fluids are different (1.4 mPa·s for ethanol and 1.14 mPa·s for water at 15 °C), which affects the final impact velocity. In addition, given the lower density of ethanol, its acceleration is greater causing higher friction gradients, which play a major role in unsteady friction, hence in the attenuation, more important than the viscosity value as described in Chapter 6.

Frequency

Concerning the trend of the wave frequency, it is not possible to extrapolate a simple correlation based on the tank pressure. This is due to the non linear effect of the pressure in the speed of sound equation. At the same tank pressure, water always shows a higher frequency than ethanol, in line with its higher speed of sound. Moreover the presence of gas, either the residual initial gas, the vapor or the desorbed gas, makes the equation highly non-linear, such that the assessment of

P_{tank} [bar]	water 8^{th} freq. [Hz]	ethanol 8^{th} freq. [Hz]
10	27.3	24.2
16	39.1[a]	27.8
20	38.8	37.9

Table 8.2: Comparison of the frequencies for water and ethanol at different tank pressures. [a]At 16 bar, water is 1 bar GN2 saturated, unlike the other cases where is deareated (no test performed at 16 bar with deareated water).

the frequency for a given fluid based on the experimental results of a replacement fluid might not be possible. It is thus recommended to test at the same pressure as in the operating system. The substitute fluid shall have the similar speed of sound, saturation pressure and solubility characteristic (the latter only in case of saturated conditions) as the real propellant.

8.1.2 Line pressure and vapor pressure of the liquid

The physical property vapor pressure (P_{vap}) of the liquid must be considered together with the boundary condition of the initial line pressure, P_{line}. As long as P_{line} is higher than P_{vap}, flashing is prevented[1], and the value of P_{vap} will not play a role. In upper stages using storable propellants, for safety reasons, the line is initially evacuated below the typical values of P_{vap}. In these cases the replacement test fluid should therefore have a similar P_{vap} as the real propellant in order to properly reproduce the flashing behavior. However, according to Lecourt and Steelant "the vapor pressure value is not important for the pressure rise tendency" [54]. They based their statement on several test data of ethanol and acetaldehyde under different line pressure conditions. Similar conclusion was drawn by Lema, who performed tests with water, ethanol and acetaldehyde: "there is no clear influence of the vapor pressure on the water hammer phenomenon" [55].

From a physical point of view, the boil-off mass flow rate, or evaporation rate, during the flashing process is proportional to the difference between P_{vap} and P_{line}. Therefore with a higher value of P_{vap} flash boiling is more violent and the amount of generated gas should play a more important role. Based on the experimental results obtained in this work with water and ethanol, which have both a low P_{vap}, it is not possible to draw conclusions on the effect of the vapor pressure. In Section 2.3.1 flash evaporation has been described and the main differences with cavitation have been underlined. Lamanna et al. [52] proposed the use of the dimensionless parameter R_p to describe the flashing behavior of propellants during injection:

$$R_p = \frac{P_{vap}}{P_\infty} \tag{8.5}$$

where P_∞ is the ambient pressure in which the fluid is injected, which in case of priming corresponds to P_{line}. The spray characteristics are strongly dependent on R_p, therefore it is reasonable to suppose that also in priming the vapor pressure does play a role, at least for a fluid with a high value of P_{vap}. To support this statement, the work of Anthoine and Lestrade [4] might come to help. At the laboratory of ONERA, they performed priming tests with real propellants, NTO and MMH. This is an interesting case, as NTO has a high vapor pressure, namely 958 mbar.

[1] If the valve orifice is small, cavitation might occur though

Although the authors do not make any explicit comments on the possible influence of the vapor pressure, their data show that NTO pressure hammer is remarkably lower than expected: while the theoretical pressure peak ratio with respect to water is 0.81, the experimental value is only 0.66. This might indeed be the consequence of the high amount of generated vapor during the flash evaporation, which slow down the liquid front and contributes to the cushion effect.

In order to make a more educated assessment on the effect of P_{vap}, numerical simulations are run with NTO. In addition, thanks to the fact that the fluid properties database allows to create a user-defined fluid, an artificial NTO (NTO-b) with a modified P_{vap} is used to further underline its (potential) influence. For this fictitious NTO-b, P_{vap} is set to 10 bar, whereas for NTO $P_{vap} = 0.98$ bar.

Results of the simulations are shown in Fig. 8.1. The pressure peak is remarkably different: the higher amount of vapor generated by NTO-b not only decreases the pressure peak by almost 50% but also induces a significant delay. For the same

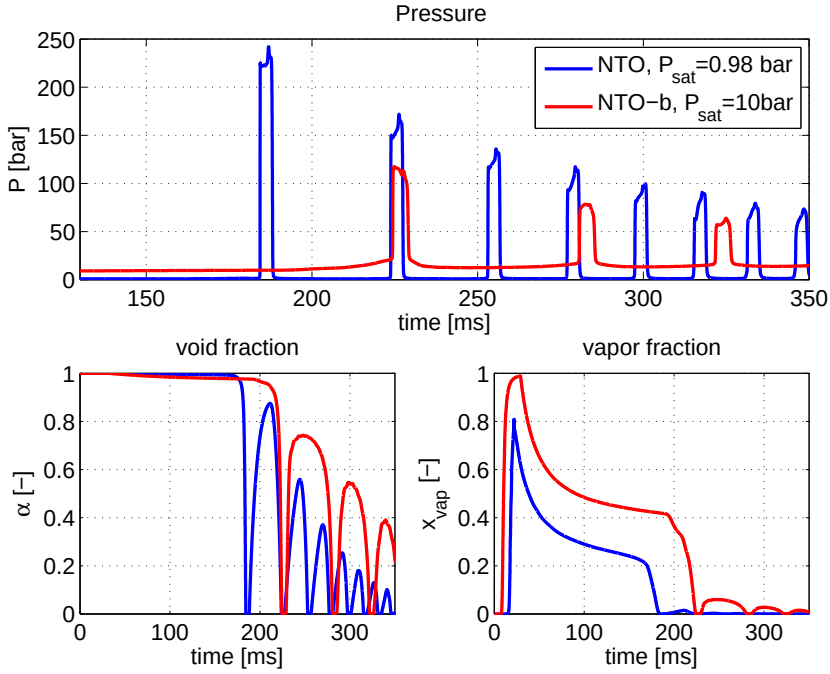

Figure 8.1: Pressure, void fraction and mass fractions at the dead-end (node 100) for NTO and NTO-b with a higher saturation pressure

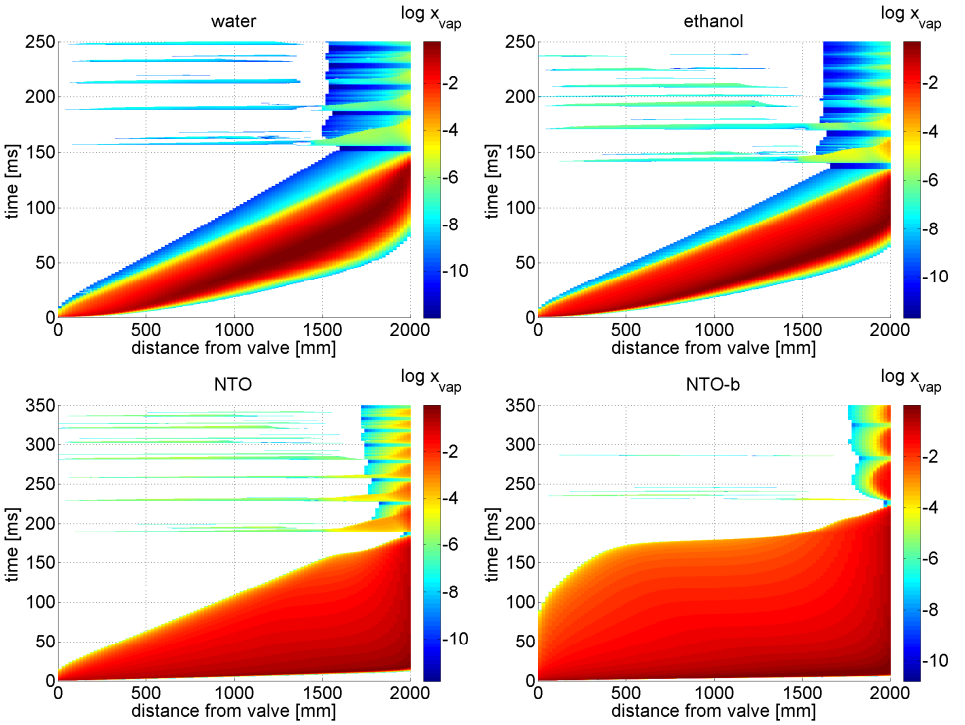

Figure 8.2: $X - t$ diagrams of the vapor mass fraction in logarithmic scale for different fluids, at $P_{tank} = 20$ bar and $P_{line} = 1$ mbar

reason, the frequency is considerably lower.

The effect of a higher value of P_{vap} is more evident in the $x - t$ diagram of the vapor mass fraction. Figure 8.2 depicts the x_{vap} colormap for different fluids. In comparison with water and ethanol, the higher P_{vap} of NTO generates a large amount of vapor, so that the whole pipe is now filled with vapor after only 13 ms, far sooner than the liquid front arrives at the dead-end. The vapor layer region, which was possible to detect in the case of water and ethanol, is replaced by an extended cloud as consequence of a more violent flash boiling. During the evolution of the liquid front, the vapor mass fraction of NTO has a maximum value of 0.91 at 14 ms and 1640 mm downstream of the FOV. For NTO-b the maximum x_{vap} is 100%, persisting over 13-15 ms and it spans from 1750 to 1900 mm downstream.

As shown, the property P_{vap} of a liquid does have an effect. The question is now shifted to how high P_{vap} shall be in order to be of importance. For the case of water

and ethanol, their values of the saturation pressure can be considered low and thus not considerably affecting the dynamic of the flow evolution. For fluids with a high value of P_{vap} such as NTO, the flash boiling does influence the process of priming, modifying the pressure peak and wave frequency. Therefore, the replacement fluid must have a similar vapor pressure as the real propellant.

Among rocket propellants with an high vapor pressure, in addition to NTO (N_2O_4) it is worthy mentioning the nitrous oxide (N_2O), with a vapor pressure of 50 bar, widely used in hybrid rockets.

For sake of completeness, the flash evaporation is also governed by two other fluid properties. According to Saury et al. [78], the evaporating mass flow rate during flashing is proportional to the value ($C_P/\Delta H_{vap}$), which includes the liquid heat capacity C_P and latent heat of vaporization ΔH_{vap}. This two fluid properties are indeed present in the Jakob number (Eq. (2.6)), an important dimensionless parameter in phase change heat transfer calculations.

8.1.3 Dimensional analysis of priming

Rather than focusing on the values of the different physical properties of the fluid, the dimensionless numbers might be more meaningful in describing the flow. A fruitful way to tackle a difficult physical modeling is by means of the dimensional analysis. By applying the Buckingkam's Pi theorem, it is possible to reduce the number of physical variables involved in the system. These groups are usually referred to as Π groups. The final relation obtained is in the form of: $\Pi_1 = f(\Pi_2, \Pi_{3,}..., \Pi_{n-m})$, where the subscript n refers to the number of physical variables involved and m is the number physical dimensions (e.g. length, mass, time) . The Buckingkam's theorem does not require the knowledge of the relationship $f(\pi_i)$, neither it allows to calculate it. For an effective use of the Pi theorem, it is essential to include all the variables involved in the phenomenon [36]. Therefore in the priming case all the fluid properties must be considered. If the water hammer pressure peak P_{wh} is assumed as final unknown, the following relationship among the dimensionless group is obtained (the derivation is shown in Appendix D):

$$\left(\frac{P_{wh}}{P_0}\right) = f\left[\left(\frac{\mu C_P}{\lambda}\right), \left(\frac{C_P \Delta T}{\Delta H_{vap}}\right), \left(\frac{\mu}{\sqrt{\rho \sigma D}}\right), \left(\frac{c}{\sqrt{\frac{\sigma}{\rho D}}}\right), \left(\frac{P_{vap} D}{\sigma}\right), \left(\frac{P_{vap}}{P_0}\right)\right] \tag{8.6}$$

where some classic dimensionless numbers used in fluid dynamics can be recognized:

- the Prandtl number $Pr = \frac{\mu C_p}{\lambda}$
- the Jakob number $Ja = \frac{C_P \Delta T}{\Delta H_{vap}}$

- the Ohnesorge number $Oh = \frac{\mu}{\sqrt{\rho \sigma D}}$
- the Weber number We and the Mach number Ma by reforming the group : $\frac{c^2 \rho D}{\sigma} \cdot \frac{V^2}{V^2} = We/Ma^2$

The presence of the most known dimensional numbers is to be expected, being priming a fluid dynamic problem. The Prandtl number is an important dimensionless parameter in heat exchange; the Jacob number is involved in all the boiling processes; the Ohnesorge number is commonly found in free surface fluid dynamics such as dispersion of liquids in gases and in spray injection (that is in fact the case of priming into a evacuated pipeline); the Weber number is used in analyzing fluid flows where there is an interface between two different fluids and the formation of droplets and bubbles; the Mach number allows to assess compressibility effects of the fluid. Not all the variables might affect the physical phenomenon: in fact experimental data or detailed numerical CFD are necessary in order to neglect the ones irrelevant that do not play a role [36].

In addition, from this analysis a new dimensionless parameter ($P_{vap} D/\sigma$) is identified. The physical meaning of this parameter is difficult to assess, however it includes two key fluid properties: the value of the vapor pressure, which indicates the tendency of the fluid to boil, and the surface tension, which represents the cohesive forces among liquid molecules. The dimensionless parameter ($P_{vap} D/\sigma$) can be seen as the ratio between the force acting to make the liquid boil to the force acting to keep the fluid in the liquid state.

Equation (8.6) can be finally written as:

$$\left(\frac{P_{wh}}{P_0}\right) = f\left[Pr,\, Ja,\, Oh,\, \frac{We}{Ma^2}, \left(\frac{P_{vap} D}{\sigma}\right), \left(\frac{P_0}{P_{vap}}\right)\right] \tag{8.7}$$

Although the dimensional analysis does not allow to calculate the exact equation behind the physics, it reduces the number of variables involved and underlines what parameters are of importance. Table 8.3 lists the values of some of these parameters for the used test fluids and for propellants NTO and MMH. The calculation of the values of these dimensionless numbers alone is of no use if not correlated to some maps or flow regimes. However such maps does not exist for priming and the values can only give general indications of the flow behavior. Some hypothesis can however be formulated. While the range of the Ohnesorge number and the range of the group ($\mathrm{We}^{0.5}/\mathrm{Ma}$) do not vary considerably (say not more than about one order of magnitude), the parameter ($P_{vap} D/\sigma$) for NTO is more than 10 times higher than ethanol and 100 times higher than water. This might indicate that the flow pattern differs significantly and could provide an additional evidence to explain the unusual results of NTO. If that be the case, it would confirm the importance of the vapor pressure as a key-property of the fluid.

dimensionless number	water	ethanol	NTO	MMH
$Oh = \frac{\mu}{\sqrt{\rho\sigma D}}$	$1.06 \cdot 10^{-3}$	$2.52 \cdot 10^{-3}$	$0.61 \cdot 10^{-3}$	$1.49 \cdot 10^{-3}$
$P_{vap}D/\sigma$	444	3144	44600	1589
$\frac{We^{0.5}}{Ma} = c\sqrt{\frac{\rho D}{\sigma}}$	21615	28122	30350	32390
$Ja = \frac{c_P\left(T_L - T_{vap}\right)}{\Delta H_{vap}}$	$1.36 \cdot 10^{-2}$	$5.21 \cdot 10^{-2}$	$10.1 \cdot 10^{-2}$	$5.45 \cdot 10^{-2}$

Table 8.3: Values of the dimensionless numbers for the different fluids. The reference length is the diameter D = 16.5 mm, reference temperature is 288 K.

8.2 Effect of pressurizing conditions

As already commented, the pressurizing conditions deeply affects the pressure wave in all its characteristics. When the fluid is deareated, speed of sound and density seems to be enough to characterize the behavior, at least in terms of pressure peak and frequency. In saturated conditions however the released gas plays a crucial role and the desorption process must be included in the analysis. This is extremely important in case of a liquid with a high mass of dissolved gas like ethanol. To be more precise, rather than the amount of dissolved gas, the desorption rate is the crucial parameter, as underlined by the discussions in Chapter 4 and 5.

Table 8.4 summarizes the pressure peaks measured for water and ethanol at different pressurizing conditions, namely a) deareated , b) saturated with GN2 at 1 bar, c) saturated with GN2 at 20 bar. When the fluid is saturated at 1 bar, which is for practical reasons the most common case in a laboratory[2], the pressure peak is slightly higher than the deareated case. This is due to cavitation occurring, which can then be seen as a collateral effect of the pressuring conditions. When the GN2 is dissolved at 20 bar, the effect of the desorption rate is more evident for ethanol than for water. Although one may question that the noticeable decrease of the pressure peak is due to the superior amount of dissolved/desorbed gas in ethanol ($4200 \cdot 10^{-6}$), it is quite surprising that it does not significantly affect the peak for water, despite the amount of dissolved gas is not negligible ($380 \cdot 10^{-6}$). On the contrary the pressure peak is even slightly higher. This fact is an evidence that the desorption rate is more important than the gas solubility itself. A saturated fluid with a very low desorption rate will behave as a deareated one, as long as the desorption time constant is high enough. There is however a lack of information

[2]to achieve deareated conditions a vacuum pump with a LN2 cold trap is used, that requires longer test preparation and limiting the amount of tests. At 20 bar saturation conditions, 3 days are required to ensure complete dissolution

P tank 20 bar	P peak water [bar]	P peak ethanol [bar]
deareated	191.6	133.5
saturated 1 bar GN2	198.9	139.4
saturated 20 bar GN2	204.5	72.2

Table 8.4: Comparison of the pressure peak for water and ethanol at different tank pressurizing conditions

on the desorption rate in literature, not only concerning rocket propellants but for common fluids as well. If the fluid is in saturation conditions, the pressure peak, as well as frequency, can not be deduced from another fluid.

Another consideration related to the desorption process concerns its interaction with the flash boiling process. The desorption rate $\dot{m}_{gas}$ is expressed as linearly proportional to the pressure difference between the gas saturation pressure $P_{g,sat}$ and the liquid instantaneous pressure P_L (Section 2.3.2, Eq. (2.8)) :

$$\dot{m}_{gas} = c_k(P_{g,sat} - P_L) \tag{8.8}$$

This expression is widely used in numerical codes for fluid transient problems in various hydraulic applications; nevertheless no modifications or comments have been found in literature in the case the liquid pressure drops below the vapor pressure, that is the initial condition of priming, where in fact $P_{line} < P_{vap}$. Kranenburg [50] modeled the difference between two cavitation patterns (column separation or dispersed bubbles) by adopting two different constant c_k. He motivated this correction on the basis of a different gas diffusion process. However in his model the pressure in the gas/vapor region was not allowed to drop below P_{vap}, as it occurs in priming. Flashing further modifies the gas diffusion process. When vapor bubbles form in the liquid, they should theoretically act as spots to further intensify the gas desorption. Furthermore, when the liquid boils, no gas is allowed to be dissolved as stated by Henry's law, so one should expect the gas release process to be faster in this condition. Although no concrete measurements were performed in this sense, the hypothesis is that the desorption rate is enhanced in case of flashing. From a modeling point of view, this would mean that Eq. (8.8) must be modified either by a change in the constant c_k or by assuming a power law dependency, e.g. $\dot{m}_{gas} \propto (P_{g,sat} - P_L)^k$, with $k > 1$. Rather than fluid dynamics, nucleation theory and molecular chemistry seem the backgrounds more suitable to tackle this problem.

The pressurizing conditions are also responsible for the non perfect reproducibil-

ity of some tests. In saturated conditions in fact, the pressure profiles are slightly different from each other, although the general shape is still the same, as it can be observed in Fig. 8.3. Among the tests, the pressure peak occurrences are within 1.5 ms and the frequency difference is 2 Hz. This not perfect reproducibility is likely to be due to the random distribution of the gas bubbles desorbing as the pressure drops below the dissolution equilibrium pressure.

8.3 Cavitation

As mentioned in the previous Section, it appears to be an intimate connection between the fluid pressurizing conditions and the occurrence of cavitation. In Chapter 4 it has been proposed that the dissolved gas, once desorbed, might act as inception spots for bubble cavitation. The experimental evidence supports this hypothesis: a small pressure drops followed by a steep rise appears in the pressure peak profile when the fluid is saturated at 1 bar. This effect is still present in case of water saturated at 20 bar, but not for ethanol, since the amount of desorbed gas is so high to damp any pressure spike induced by bubble collapse.

Cavitation has been observed also in deareated conditions when the tank pressure exceeds a specific value: beyond a given threshold pressure, the velocity at the valve increases so that the local pressure at the valve drops below the saturation value and cavitation takes place. In these occasions, it was accompanied by the typical metallic loud bang. The valve inner geometry has therefore an influence on the

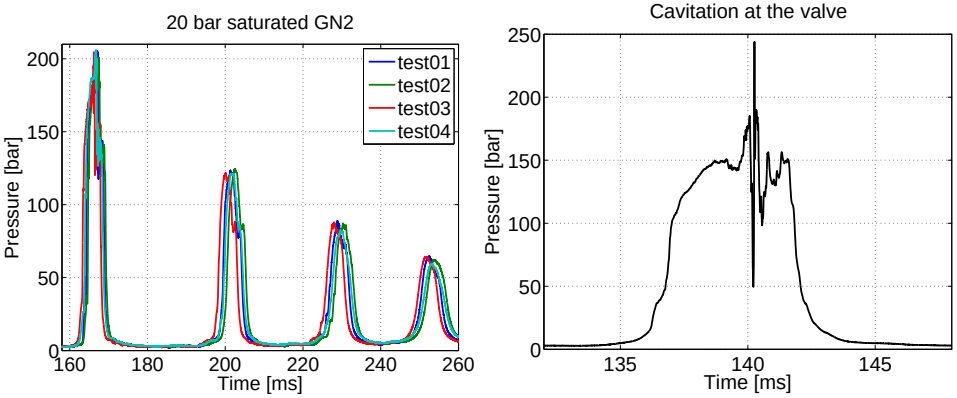

Figure 8.3: Left: the not perfect reproducibility of the pressure wave in case of saturated water, $P_{tank} = 20$ bar. Right: the highest recorded pressure peak, 244 bar: the spike in the pressure signal at 140 ms is due to bubble collapse.

occurrence of cavitation, since the valve seat acts as a flow restriction causing a local pressure minimum. Figure 8.3 depicts the highest pressure peak recorded during the test campaign, namely 244 bar. The steepness of the pressure rise after cavitation is 195 bar/35 μs = 5570 bar/ms.

Another observed event involving cavitation is the formation of a shock wave in a bubbly flow pattern. Shock waves only occurred when testing in complete saturation conditions.

8.4 Geometry

Given the same length of test section, the straight pipe configuration shows always the maximum pressure peak in all the tested cases. The presence of elbow, tee, or junctions in general contributes to increase the pressure losses and as a consequence the pressure peak decreases. This was also found by other researchers [54, 55]. The straight configuration can be assumed as the most conservative case in testing. The frequency however can not be scaled from the results obtained with the straight pipe to the others configurations. Wave reflections alter the pressure profile, affecting also the attenuation time. In case of geometry with multiple branches, the highest pressure peak occurs in the last part to be filled, usually the longest branch or the one further away from the valve. It is thus recommended to test with the same geometry as the real operating hardware.

The T and T2 geometries have shown to have low reproducibility in the case of

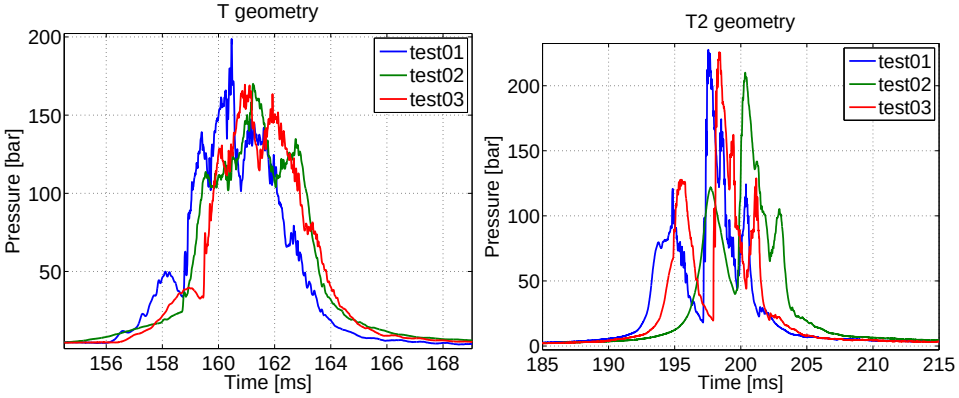

Figure 8.4: Reproducibility in case of T geometry (left) and T2 with asymmetrical branches (right). Fluid is saturated water

saturated water (Fig. 8.4). A low repeatability has been also observed by Gibek in priming experiments with a bent pipe and MMH as a fluid [37].

The influence of gravity is an open question. With a horizontal set-up, the flow becomes stratified, as shown by the HSI. The liquid wetting bottom part creates a secondary back-flow after impacting the dead-end. This causes a vapor/gas pocket to be trapped as explained in Chapter 7. Whether this effect is of importance or not, can be only evaluated by comparing the same tests in a vertical configuration. The answer may however be more complex. The ratio L/D is also of importance, not only for the friction effects. A smaller diameter should hinder the stratification effect, since capillary forces become important. A shorter test section should also have the same effect, since the flow tangential (azimuth) profile will not fully develop before reaching the dead-end. On the other hand, a vertical configuration will pose other questions. If the direction is upwards, the residual gas (and the desorbed one if any) will be compressed and confined at the dead-end. This flow pattern will have a different speed of sound of the mixture. If the direction is downwards, the residual gas will move back towards the tank, in opposite direction of the main liquid flow. The dynamic of the priming will be again different.

To make the issue more interesting, it has to be recalled that the real configuration in a spacecraft is a zero-g environment.

8.5 Numerical simulations: prediction confidence

Throughout this work, the numerical results obtained with EcosimPro/ESPSS have been validated against the experimental results in different configurations and at different boundary conditions. Some conclusive remarks are here summarized.

Prediction of the pressure peak If no correction of the friction value is implemented, the prediction of the pressure peak is always largely over-estimated, with values up to 100% greater than the experimental ones. Neglecting the unsteady friction gradients, which instead plays a fundamental role in these transient conditions, will lead to higher velocity of the liquid front. A simple increase of the static friction coefficient might be sufficient for a preliminary estimation of the pressure peak, although not representative of the physics. The friction factor multiplier ranges between 2.4 and 3 and it includes also the valve pressure loss coefficient. The latter values have been empirical found for vacuum condition (10 mbar) in the line and a reference tank pressure of 20 bar; however they will be different in case of pre-pressurized line or different tank pressure.

The prediction of the time occurrence of the peak is anticipated by about 10 ms, even with the adoption of UFM, both for water and ethanol. This might seem in contrast with the matching of the pressure peak, which would require to have the

same impact velocity. However the final impact velocity can be the same for two different acceleration profiles and therefore the impact time can differ.

Prediction of the frequency For a deareated fluid, the frequency can be estimated within 20% accuracy and it is generally over-estimated, being the actual frequency lower than the predicted one. This margin can be considered sufficient by the designer. If the calculated frequency is in the range of one of the structural eigenfrequencies or might induce acoustic coupling with the injector system, the designer would need more refined tools. For a saturated fluid, the desorption model improves the predictions, although the need of a desorption time constant makes necessary the use of experimental data to calibrate the model. The main difficulty is to correctly model the two-phase flow pattern, in particular the gas content distribution on which the speed of sound depends. As the HSI analysis has shown, the highly non-homogeneous flow pattern which develops during the priming can not be reliably reproduced by a 1D model. To this purpose 2D or even 3D models appear necessary to capture the complex dynamic of the priming. A 2D numerical simulation of priming with water was perfomed by Pinho et al. [69] by means of a commercial CFD software. Since the software implements a homogeneous flow model, the authors compared two different fluid compressibility models, remarking that the speed of sound is strongly depending on the model selected. Gauffre et al. [34] used a in-house developed CFD tool to perform 3D two-phase flow simulations of the filling of a LOx dome mock-up with water. However no mass nor energy transfer were considered, therefore cavitation could not be simulated.

Prediction of the wave attenuation Generally, the attenuation of the pressure wave is not an important engineering parameter in the design, and this is also the reason why UFMs have not been included in numerical tools for space propulsion system design so far. The pressure wave is generally attenuated in about 500-700 ms, depending on the boundary conditions. This time is fairly rapid for all the applications in main stage engines and upper stage engines. A reliable prediction of the wave attenuation might be necessary in case of a pulsating engine with an almost continuous opening/closing of the valve. This is the case for example of attitude control engines in satellites, where typical frequencies of the pulses are in the order of 2-8 Hz. To achieve a better prediction of the wave attenuation, the adoption of an UFM is necessary. As demonstrated in Chapter 6, the use of UFM definitely improves the damping characteristics, although the presence of gas in the line requires a corrective factor (k_4) to further increase the accuracy of the simulations. Indeed, UFMs have been developed and validated in single phase transient flows, and a more solid analytic/theoretical model is still missing for two-phase flows.

Chapter 9

Conclusions and future work

The filling process occurring during the start-up of a satellite or spacecraft feedline system was experimentally investigated. A dedicated test facility was built which allows to perform tests in the same conditions as the operating space system. This work aims to improve the fundamental understanding of the different physical processes taking place during priming. Phenomena such as cavitation, flash boiling, gas desorption, fluid-structure interaction occur simultaneously and can lead to a very complex pressure evolution. Among them, the gas desorption was found to play a major role. The pressurizing gas dissolved in the liquid will desorb as the fluid enters the evacuated line, strongly affecting the pressure wave characteristics such as peak, frequency and attenuation. A comparison between deareated and saturated fluid allowed in fact to assess the influence of the released gas, which be can briefly summarized as follows:

1. the pressure peak is decreased since the released gas acts as a cushion. In case of saturated ethanol, the peak is almost half the value of the deareated case, because of the large amount of dissolved GN2;

2. the frequency is lowered since the released gas decreases the speed of sound;

3. the attenuation is increased since the released gas adds extra damping and thus dissipation is higher.

It was also proved that the gas desorption is responsible for the particular profile of the first pressure peak, characterized by the presence of very fast steps/plateaux (Fig. 9.1). In the case of deareated fluid this peculiarity is not present and by means of high speed imaging a possible explanation for such behavior was provided. The desorption creates gas pockets in the fluid which leads to form separated liquid slugs. When the flow arrives at the dead-end, these liquid slugs impinge on each others resulting in the fast steps observed in the experiments.

The dissolved gas has also a more hidden effect, potentially dangerous. When a gas is dissolved in a liquid, the surface tension is lowered and the fluid is more prone to cavitate. This intimate connection with the onset of cavitation can lead under certain conditions to severe pressure spikes in the liquid which completely alter the pressure evolution. These conditions were experimentally assessed: results demonstrated a mutual dependency between the flow velocity (i.e. the tank

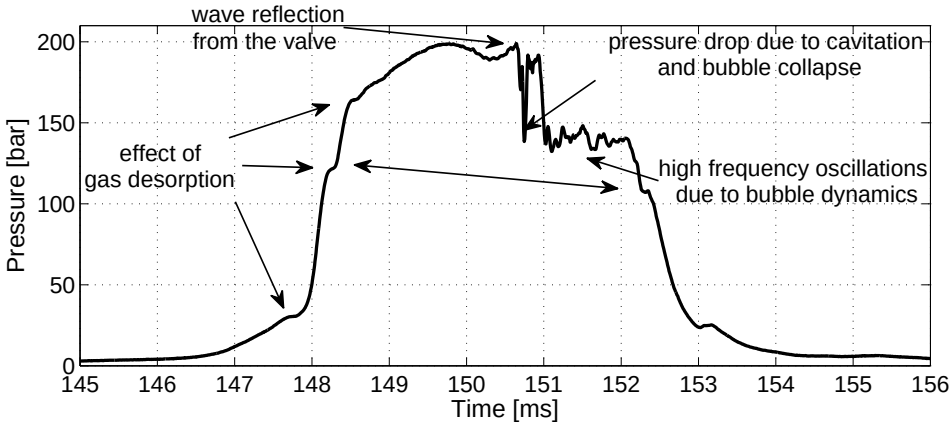

Figure 9.1: The evolution of the first pressure peak during priming: the experimental investigation helped to provide an explanation for the complex profile

pressure) at the valve and the level of saturation. In the case of fully saturated water, shock waves were observed, an event to be avoided with real propellants. The mechanism of cavitation, bubble formation and its interaction with the dissolved gas have been briefly explained in this work. A more detailed experimental and numerical investigations of the bubble dynamics effects is required. In this regard, flow visualizations are an indispensable tool, while numerically the inclusion of a dedicated sub-model such as the Rayleight-Plesset equation will allow to capture the high frequency oscillations typical of the bubble dynamics.

Flow visualizations proved to be a valuable support in the interpretation of the experimental data, allowing to describe the flow evolution and how it is affected by the different boundary conditions. To extend the database, high speed imaging at junctions such as elbow and tee will provide necessary information to better describe the flow dynamics in these configurations. In particular, flow visualizations will be essential to assess the flow pattern and the void fraction distribution. These are necessary data to evaluate the speed of sound, a fundamental parameter which, as shown, does not depend on the gas content only.

The effect of the operating conditions and the influence of different parameters was also evaluated in detailed . The initial residual gas in the line acts as a cushion slowing down the liquid front and thus it diminishes the pressure peak. The lesser the initial gas pressure, the higher the pressure peak. However when the initial line pressure is below the liquid vapor pressure, this effect is negligible, since the amount

of vapor generated by the flash boiling outcomes the initial residual gas amount.

Different geometries were tested, including straight pipe, elbow pipe, tee pipe, tee pipe with asymmetrical branches . The most important effect is that junctions such as tees or elbows cause wave reflection, which can lead to pressure peak higher than the first peak measured at the dead-end (the Joukowsky pressure). A secondary effect is that the flow pattern changes, making the effect of the gas desorption less decisive in the evolution of the pressure, as observed for water. That could not be observed for ethanol, and it was suggested that fluid properties such as viscosity, density, surface tension and/or dimensionless numbers such as Reynolds, Ohnsorge or the new proposed number $P_{vap}D/\sigma$ are key parameters to characterize the flow dynamics during priming. Further experiments with different fluids will be of great help in this regard. In addition, the effect of the diameter should be addressed in future work. In a 1D approximation, it would be more appropriate to refer to the L/D ratio as a parameter rather than the diameter alone. However the diameter is present in all the suggested dimensionless numbers and in addition for small pipe diameter capillarity effects might become of importance.

The use of strain gauges proved to be useful to detect the fluid wave propagation and to described the mechanism of wave reflection. Together with the signal of the pressure sensors, the wave speed could be assessed, which in turn allows to estimated the gas content in different region of the pipe. It was in fact shown that the initial residual gas is pushed towards the dead-and, while the upstream part of the test section can be considered as fully filled with liquid. This fact has important implications regarding the speed of sound of the mixture. The phenomenon of the precursor wave due to the fluid-structure interaction could not be observed. A refinement in the measurement technique may help to detect the precursor wave, although it was deemed that its influence would be very small and negligible with respect to the evolution of the pressure signal.

The temperature measurements must also be improved by installing fast response thermocouples. Temperature is an important quantity in case real propellants are used due to the thermal decomposition hazard.

The obtained experimental data were used to validate numerical simulations performed with Ecosim/ESPSS. In particular, the main contribution of this work to the improvement of 1D-unsteady flow modeling concerns the gas desorption model and the unsteady friction model.

Including the gas release sub-model in the equations allows to better simulate the pressure evolution, reaching a very good matching of the pressure peak. The desorption rate was found to be a sensitivity parameter but no data are available in literature, therefore it was calibrated according to the experimental results. This tuning proved to be not consistent since, while matching the pressure peak, the wave frequency showed discrepancy. This suggests that the amount of released gas

is under/over-estimated. The dynamics of gas desorption in large cavities such as occurring during column separation is different from the dynamics of gas diffusion in not cavitating liquid, where tiny dispersed gas bubbles form. Future work shall take this different dynamics into account, by adopting a gas release model depending on the flow pattern. The flow pattern can be estimated based on the void fraction value, or defined by Reynolds or Weber numbers.

The implementation of an unsteady friction model in the code showed great improvement in the prediction of the wave attenuation at the cost of an acceptable small increase in CPU time. A further improvement was achieved by adopting an empirical corrective factor k_4 to take the two-phase nature of the flow into account. In fact the implemented UFM has been developed for single phase flows, while a proper formulation for two-phase flows is still missing. Therefore future work shall include semi-empirical or analytically-derived two-phase flow friction coefficients, in order to reduce the dependency on the experimental calibration, which has the obvious disadvantage to be dependent on the actual test conditions and setup. Therefore the values of the corrective factor k_4 proposed in this work shall be considered valid only under the conditions they were obtained. The collected experimental data will also allow to explore the dependency of k_4 on the operating conditions such as pressure and gas content.

Although the full 3D-unsteady behavior of the flow can not be described by a 1D-unsteady model, the implementation of dedicated sub-models with the use of empirically derived coefficients appears to be the right course in developing a simple yet reliable numerical tool. Comparison with the results obtained by a 3D two-phase CFD code would help to indicate where modeling efforts should focus on.

Bibliography

[1] Adamkowski, A. ; Lewandowski, M.: Improved Numerical Modelling of Hydraulic Transients in Pipelines with Column Separation. In: *3rd IAHR International Meeting on Cavitation and Dynamic Problems in Hydraulic Machinery and Systems, Brno, Czech Republic*, 2009

[2] Adamkowski, A: ; Lewandowski, M.: A New Method for Numerical Prediction of Liquid Column Separation Accompanying Hydraulic Transients in Pipelines. In: *Journal of Fluids Engineering* 131 (2009)

[3] Andritsos, N. ; Williams, L. ; Hanratty, T.J.: Effect of liquid viscosity on the stratified-slug transition in horizontal pipe flow. In: *International Journal of Multiphase Flow* 15 (1989), Nr. 6, pp. 877 – 892. – ISSN 0301–9322

[4] Anthoine, J. ; Lestrade, J-Y.: Experimental database with Real Propellants to study Multiphase Fluid Hammer Phenomena. In: *Space Propulsion Conference, Cologne, Germany*, 2014

[5] Battino, Rubin ; Rettich, Timothy R. ; Tominaga, Toshihiro: The Solubility of Nitrogen and Air in Liquids. In: *Journal of Physical and Chemical Reference Data* 13 (1984), Nr. 2, pp. 563–600

[6] Bergant, A. ; Simpson, A.R.: Pipeline column separation flow regimes. In: *ASCE Journal of Hydraulic Engineering* 125 (1999), Nr. 8, pp. 835–848

[7] Bergant, A. ; Tijjsseling, A. S. ; J.P., Vitkovsky ; M.F., Lambert: Further investigation of parameters affecting water hammer wave attenuation, shape and timing Part 1: mathematical tools. In: *11th International Meeting of the Working Group on the Behaviour of Hydraulic Machinery Under Steady Oscillatory Conditions, At Stuttgart, Germany*, 2003

[8] Bergant, Anton ; Simpson, A. ; Tijjsseling, Arris S.: Water Hammer with Column Seperation: A Review of Research in the Twentieth Century / School of Civil and Environmental Engineering, University of Adelaide. 2002. – Technical Report

[9] Bergant, Anton ; Simpson, Angus ; Vitkovsky, John: Developments in unsteady pipe flow friction modelling. In: *Journal of Hydraulic Research* 39 (2001), pp. 249–257

[10] Bergant, Anton ; Tijsseeling, Arris ; Vitkovsky, John ; Covas, Didia ; Simpson, Angus ; Lambert, Martin: Parameters Affecting Water-Hammer Wave Attenuation, Shape and Timing. In: *Journal of Hydraulic Research* 46 (2008), pp. 373–391

[11] Bill, Bernhard: *Basic Theory of The Hammer Test Method*. Kistler Instrumente AG, 1998

[12] Bill, Bernhard: *Impulse Force Hammer 9722A, Instruction Manual*. Kistler Instrumente AG, 1998

[13] Boccaletto, L. ; Marchionni, M.: VEGA-AVUM-PLS model under EcosimPro Environment: Development and Validatio. In: *Space Propulsion Conference*. San Sebastian, Spain, May 2010

[14] Bombardieri, C. ; Traudt, T. ; Manfletti, C.: Experimental and Numerical Analysis of Water Hammer during the Filling Process of Pipelines. In: *Space Propulsion Conference, Cologne, Germany* (2014), May

[15] Bombardieri, C. ; Traudt, T. ; Manfletti, C.: Experimental Validation of Brunone's Unsteady Friction Model for Water Hammer in Short Pipelines in Turbulent Regime. In: *Journal of Hydraulic Research (accepted for publication)* 0 (2018)

[16] Brennen, C.E.: *Cavitation and Bubble Dynamics*. Oxford University Press, 1995

[17] Briles, O. ; Hagemann, D. ; Benz, F. ; Farkas, T.: Explosive decomposition of hydrazine due to rapid gas compression / White Sands Test Facility. 1985. – Technical Report

[18] Briles, O. ; Hollenbaugh, R.: Adiabatic compression testing of hydrazine. In: *AIAA/SAE 14th Joint Propulsion Conference*, Las Vegas, 1978

[19] Brunone, B. ; Golia, U. M. ; Greco, M.: Some Remarks on the Momentum Equations for Fast Transients. In: *International Meeting on Hydraulic Transients*, 1991

[20] Brunone, B. ; Golia, U. M. ; Greco, M.: Effects of Two-Dimensionality on Pipe Transients Modeling. In: *Journal of Hydraulic Engineering* (1995)

[21] Brusiani, F. ; Negro, S. ; Bianchi, G.M. ; Moulai, M. ; Neroorkar, K. ; Schmidt, D.: Comparison of the Homogeneous Relaxation Model and a Rayleigh Plesset Cavitation Model in Predicting the Cavitating Flow Through Various Injector Hole Shapes. In: *SAE Technical Paper*, SAE International, 04 2013

[22] Bunker, D.L. R.L.and B. R.L.and Baker ; J.H.S., Lee: Explosive Decomposition of Hydrazine by Rapid Compression of a Gas Volume. In: *Dynamics of Detonations and Explosions: Detonations. Progress in Astronautics and Aeronautics* (1991), pp. 325–341

[23] Cheng, L. ; Ribatski, G. ; Thome, J.R.: Two-Phase Flow Patterns and Flow-Pattern Maps: Fundamentals and Applications. In: *Applied Mechanics Reviews* 61 (2008), Nr. 5

[24] Churchill, S.W.: Friction factor equation spans all fluid-flow regimes. In: *Chemical engineering* 84 (1977), Nr. 24, pp. 91–92

[25] Davies, A.L.: The speed of sound in water and steam / UK Atomic Energy Authority. Winfrith, Dorchester, 1965 (AEEW-M452). – Technical Report

[26] Descartes, René: *Discours de la méthode pour bien conduire sa raison, et chercher la vérité dans les sciences.* 1637

[27] Dijk, P. J.: *Acoustics of Two-Phase Pipe Flows*, University of Twente, PhD Thesis, 2005

[28] Dressler, G. ; Joseph, G. ; Behrens, H. ; Asato, D. ; Carlson, R.: Compton Gamma Ray Observatory: Lessons Learned in Propulsion. In: *37th AIAA/ASME/SAE/ASEE Joint Propulsion Conference and Exhibit, Salt Lake City*, 2001

[29] Duan, H.F. ; ghidaoui, M.S. ; Lee, P.J. ; Tung, Y.K.: Relevance of Unsteady Friction to Pipe Size and Length in Pipe Fluid Transient. In: *Journal of Hydraulic Engineering* 138 (2012), pp. 154–166

[30] Empresarios Agrupados International: *EcosimPro 5.4 Dynamic Simulation Tool. User Manual.* Empresarios Agrupados International, 2014

[31] Empresarios Agrupados International: *ESPSS 3.0.5 Libraries User Manual.* Empresarios Agrupados International, 2014

[32] Fischer, K. ; Wilken, M.: Experimental determination of oxygen and nitrogen solubility in organic solvents up to 10 MPa at temperatures between 298 K and 398 K. In: *The Journal of Chemical Thermodynamics* 33 (2001), Nr. 10, pp. 1285 – 1308. – ISSN 0021–9614

[33] Friedel, L: Improved Friction Pressure Drop Correlations for Horizontal and Vertical Two-Phase Pipe Flow. In: *Proceedings of the European Two Phase Flow Group Meeting, Ispra, Italy, 1979* 18 (1979), pp. 485–491

[34] Gauffre, M.C. ; Neau, H. ; Simonin, O. ; Ansart, R. ; Meyers, N. ; Petitot, S.: Numerical simulation of a 3D unsteady two-phase flow in the filling cavity in oxygen of a cryogenic rocket engine. In: *48th AIAA/ASME/SAE/ASEE Joint Propulsion Conference & Exhibit, Atlanta*, 2012

[35] Ghidaoui, Mohamed S. ; Zhao, Ming ; McInnis, Duncan A. ; Axworthy, David H.: A Review of Water Hammer: Theory and Practice. In: *Applied Mechanics* 58 (2005), pp. 49–76

[36] Gibbins, J.C.: *Dimensional Analysis*. Springer, 2011

[37] Gibek, I. ; Maisonneuve, Y.: Water Hammer Tests with Real Propellants. In: *AIAA* 4081 (2005)

[38] Han, S.Y. ; Hansen, D ; Kember, G.: Multiple scales analysis of water hammer attenuation. 69 (2011), 12, pp. 677–690

[39] Hearn, Henry C.: Development and application of a priming surge analysis methodology. In: *41st AIAA/ASME/SAE/ASEE Joint Propulsion Conference & Exhibit*, 2005

[40] Hewitt, G. F. ; G., Hetsroni (Hrsg.): *Handbook of Multiphase Systems*. Hemisphere Publishing, 1982

[41] http://www.spaceref.com: *Corrective Action Defined for Delta IV Heavy Demo Early Cut-off Anomaly*. April 8, 2015

[42] Huber, A.: *Impact of fuel supply impedance and fuel staging on gas turbine combustion stability*, Technischen Universität München, PhD Thesis, 2009

[43] Hullier, V. L.: Propulsion in the ATV spacecraft system - Lessons learnt. In: *45th AIAA/ASME/SAE/ASEE Joint Propulsion Conference*, 2009

[44] Hutchinson, F. E. ; Schmitz, H. D.: Adiabatic compression phenomena in hydrazine propulsion systems. In: *20th AIAA/SAE/ASME Joint Propulsion Conference, Cincinnati, Ohio, June 11-13*, 1984

[45] Joh, Chang Y. ; Park, Kum D.: Pressure surge analysis and reduction in the KOMPSAT propellant feed system. In: *Proceedings KORUS 2000. The 4th Korea-Russia International Symposium on Science and Technology*, 2000

[46] Johnson, R.W.: *The Handbook of Fluid Dynamics*. CRC Press, 1998

[47] Kaye, G.W.C. ; Laby, T.H.: *Tables of Physical and Chemical Constants*. 15th ed. Longman, 1986

[48] Kieffer, S. W.: Sound speed in liquid-gas mixtures: Water-air and water-steam. In: *Journal of Geophysical Research* 82 (1977), Nr. 20, pp. 2895–2904. – ISSN 2156–2202

[49] Korteweg, D.J.: Über die Fortpflanzungsgeschwindigkeit des Schalles in elastischen Röhren. In: *Annalen der Physik* 241 (1878), Nr. 12, pp. 525–542

[50] Kranenburg, C.: Gas release during transient cavitation in pipes. In: *Journal of the Hydraulics Division* 100 (1974), pp. 1383–1398

[51] Kwak, H.Y. ; Oh, S.D.: Gas-vapor bubble nucleation: a unified approach. In: *Journal of Colloid and Interface Science* 278 (2004), Nr. 2, pp. 436 – 446. – ISSN 0021–9797

[52] Lamanna, Grazia ; Kamoun, H. ; Weigand, Bernhard ; Manfletti, C. ; Rees, A. ; Sender, J. ; Oschwald, M. ; Steelant, Johan: Flashing behavior of rocket engine propellants. In: *Atomization and Sprays* 25 (2015), Nr. 10, pp. 837–856. – ISSN 1044–5110

[53] Laverty, F. ; Capus, P. ; Lubrano, G. ; Le-Marchand, Y. ; Iffly, A. ; Garçon, P.: Live Propellant Transient Test Results Achieved in the ExoMars Test Campaign. In: *4th Space Propulsion Conference*. Cologne, Germany, May 2014

[54] Lecourt, Renaud ; Steelant, Johan: Experimental Investigation of Water-hammer in Simplified Feed Lines of Satellite Propulsion Systems. In: *Journal of Propulsion and Power* 23 (2007), pp. 1214–1224

[55] Lema, M.: *Multiphase Fluid Hammer: Modeling, Experiments and Simulations*, Universite' Libre de Bruxelles, PhD Thesis, 2014

[56] Lin, T.Y. ; Baker, D.: Analysis and Testing of Propellant Feed System Priming Process. In: *Journal of Propulsion and Power* 11 (1995), pp. 505–512

[57] Liu, Y.: *Acoustic properties of reservoir fluids*, Stanford University, PhD Thesis, 1998

[58] Lockhart, R. W. ; Martinelli, R. C.: Proposed correlation of data for isothermal two-phase, two-component flow in pipes. In: *Chemical Engineering Progress* 45 (1949), Nr. 1, pp. 39–48

[59] Lubetkin, S. D.: Why Is It Much Easier To Nucleate Gas Bubbles than Theory Predicts? In: *Langmuir* 19 (2003), Nr. 7, pp. 2575–2587

[60] McWilliam, D. ; Duggins, R. K.: Speed of Sound in Bubbly Liquids. In: *Proceedings of the Institution of Mechanical Engineers, Conference Proceedings* 184 (1969), Nr. 3, pp. 102–107

[61] Michaelis, M. ; Bauer, L. ; Kajon, D. ; Avila, J.R. ; Rosenko, E. ; Jäger, M. ; Kachler, T.: The Propulsion Qualification Model for the Orion ESM Propulsion Subsystem. In: *5th Space Propulsion Conference*. Rome, Italy, May 2016

[62] M.Lema ; J.Steelant: Experimental Characterization of the Priming Phase using a Propellant Line mock-up. In: *Space Propulsion Conference, Bordeaux, France* (2012), May, 8

[63] Morgan, Michael J.: Pressure transient characterization test for Star-2 propulsion system fuel manifold. In: *40th AIAA/ASME/SAE/ASEE Joint Propulsion Conference and Exhibit*, 2004

[64] Mori, Y. ; Hijikata, K. ; Nagatani, T.: Effect of dissolved gas on bubble nucleation. In: *International Journal of Heat and Mass Transfer* 19 (1976), Nr. 10, pp. 1153 – 1159. – ISSN 0017–9310

[65] NIST: *Standard Reference Data Thermophysical Properties of Fluid Systems*. http://webbook.nist.gov/chemistry/fluid/,

[66] Pasquier, A. ; Lescouzères, R. ; Tregubow, V. ; Wollenhaupt, B. ; Peukert, M.: Live Propellant Transient Test Results Achieved in the ExoMars Test Campaign. In: *4th Space Propulsion Conference*. Cologne, Germany, May 2014

[67] Perko, Hans-Dieter: *Gasausscheidung in instationärer Rohrströmung*, Universität Hannover, PhD Thesis, 1985

[68] Pezzinga, G.: Evaluation of Unsteady Flow Resistance by Quasi-2D or 1D Models. In: *Journal of Hydraulic Engineering* 126(10) (2000), pp. 778–785

[69] Pinho, J. ; Lema, M. ; Rambaud, P. ; Steelant, J.: Multiphase Investigation of Water Hammer Phenomenon Using the Full Cavitation Model. In: *Journal of Propulsion and Power* 30 (2014), pp. 105–113

[70] Plesset, M.S.: Effect of dissolved gases on cavitation in liquids / California Institute of Technology, Division of Engineeing and Applied Science. 1970. – Technical Report

[71] Polifke, W. ; Hoek, J. van d. ; Verhaar, B.: Everything you always wanted to know about f and g / Technische Universität München. 1997. – Technical Report

[72] Prickett, R.P. ; Mayer, E. ; Hermel, J.: Water Hammer in a Spacecraft Propellant Feed System. In: *Journal of Propulsion and Power* 8 (1992), pp. 592–597

[73] Ramcke, T.: *Simulation der Flash-Verdampfung bei der kryogenen Einspritzung von in-Orbit Raketentriebwerken*, Universität der Bundeswehr München, PhD Thesis, 2016

[74] Rayleigh, O.M. F.R.S. L.: On the pressure developed in a liquid during the collapse of a spherical cavity. In: *Philosophical Magazine* 34 (1917), Nr. 200, pp. 94–98

[75] Riehle, M. ; Diedrich, T. ; Perigo, D. ; Kraus, S ; Bühner, M.: Propulsion System for the European Lunar Lander - Development Status and Breadboarding Activities. In: *3th Space Propulsion Conference*. Bordeaux, France, May 2012

[76] Rooze, J.: *Cavitation in gas-saturated liquids*, Technische Universiteit Eindhoven, PhD Thesis, 2012

[77] Sadatomi, M. ; Kawahara, A. ; Matsuo, M. ; Ishimura, K.: Effects of Surface Tension on Two-Phase Gas-Liquid Flows in Horizontal Small Diameter Pipes. In: *Journal of Power and Energy Systems* 4 (2010), pp. 290–300

[78] Saury, D. ; Harmand, S. ; Siroux, M.: Flash evaporation from a water pool: Influence of the liquid height and of the depressurization rate. In: *International Journal of Thermal Sciences* 44 (2005), Nr. 10, pp. 953 – 965. – ISSN 1290–0729

[79] Scroggins, A.R.: A Streamlined Approach to Venturi Sizing. In: *48th AIAA/ASME/SAE/ASEE Joint Propulsion Conference & Exhibit* Bd. 2012-4028, 2012

[80] Silva-Araya, W. F. ; Chaudhry, M. H.: Unsteady Friction in Rough Pipes. In: *Journal of Hydraulic Engineering* 127 (2001), Nr. 7

[81] Simpson, A. R. ; Bergant, A: Numerical comparison of pipe-column-separation models. In: *Journal of Hydraulic Engineering* 120 (1994), Nr. 3, pp. 361–377

[82] Simpson, A.R.: *Large water hammer pressures due to column separation in sloping pipes*, The University of Michigan, Dept. of Civil Engineering, PhD Thesis, 1986

[83] Storli, P.-T. ; Nielsen, T. K.: Transient Friction in Pressurized Pipes. II: Two-Coefficient Instantaneous Acceleration-Based Model. In: *Journal of Hydraulic Engineering* 137 (2011), Nr. 6

[84] Sun, R. ; Hu, W. ; Duan, Z.: Prediction of Nitrogen Solubility in Pure Water and Aqueous NaCl Solutions up to High Temperature, Pressure, and Ionic Strength. In: *Journal of Solution Chemistry* 30 (2001), Nr. 6, pp. 561–573. – ISSN 1572–8927

[85] Taitel, Y. ; Dukler, A. E.: A model for predicting flow regime transitions in horizontal and near horizontal gas-liquid flow. In: *AIChE Journal* 22 (1976), Nr. 1, pp. 47–55. – ISSN 1547–5905

[86] Taylor, B. N. ; Kuyatt, C.E.: Guidelines for Evaluating and Expressing the Uncertainty of NIST Measurement Results / NIST. 1994. – Technical Report

[87] Tijsseling, A. S. ; Vardy, A. E.: What is wave speed? In: *12th International Conference on Pressure Surge, Fluid Transients and Water Hammer, Dublin, Ireland 18th-20th November*, 2015

[88] Tijsseling, A.S.: Fluid-structure interaction in liquid-filled pipe systems: a review. In: *Journal of Fluids and Structures* 10 (1996), Nr. 2, pp. 109 – 146. – ISSN 0889–9746

[89] Tijsseling, A.S. A. ; Vardy, A.E.: Time scales and FSI in unsteady liquid-filled pipe flow / Eindhoven University of Technology. 2004. – Technical Report

[90] Tokunaga, J.: Solubilities of oxygen, nitrogen, and carbon dioxide in aqueous alcohol solutions. In: *Journal of Chemical & Engineering Data* 20 (1975), Nr. 1, pp. 41–46

[91] Traudt, T. ; Bombardieri, C. ; Manfletti, C.: Influences on water-hammer wave shape: an experimental study. In: *CEAS Space Journal* 8 (2016), Nr. 3, pp. 215–228

[92] Trevena, D H.: Cavitation and the generation of tension in liquids. In: *Journal of Physics D: Applied Physics* 17 (1984), Nr. 11, pp. 2139

[93] Trikha, A. K.: An Efficient Method for Simulating Frequency-Dependent Friction in Transient Liquid Flow. In: *ASME journal Fluids Eng.* 97(1) (1975), pp. 97–105

[94] Uffer, R.A.: Water hammer conservatisms. In: *ASME-PVP* 253 (1993), pp. 179–184

[95] Valencia-Bel, F. ; Matteo, F. D. ; Meerbeeck, W. van: Assessment for Hydrazine detonability during priming system activities. In: *4th Space Propulsion Conference*. Cologne, Germany, May 2014

[96] Vardy, A. E. ; Brown, J. M. B.: On turbulent, unsteady, smooth-pipe friction. In: *7th Internation Conference on Pressure Surge and Fluid Transient in Pipelines and Open Channels, Harrogate, UK, BHR Group*, 1996, pp. 289–311

[97] Vardy, A. E. ; Brown, J. M. B.: Transient Turbulent Friction in Smooth Pipe Flows. In: *Journal of Sound and Vibration* 259 (2003), pp. 1011–1036

[98] Vardy, A. E. ; Brown, J. M. B.: Transient Turbulent Friction in Fully Rough Pipe Flows. In: *Journal of Sound and Vibration* 270 (2004), pp. 233–257

[99] Vardy, A. E. ; Tijsseling, A. S.: Method of characteristics: (why) is it so good? In: *12th International Conference on Pressure Surge, Fluid Transients and Water Hammer, Dublin, Ireland 18th-20th November*, 2015

[100] Vardy, A.E. ; Fan, D. ; Tijsseling, A.S.: Fluid-Structure Interaction in a T-piece pipe. In: *Journal of Fluids and Structures* 10 (1996), Nr. 7, pp. 763 – 786. – ISSN 0889–9746

[101] Vitkovsky, J. P. ; Bergant, A. ; Simpson, A.R. ; Lambert, M. F.: Discussion of ‘‘Systematic Evulation of One-Dimensional Unsteady Friction Models in Simple Pipelines’’. In: *Journal of Hydraulic Engineering* 132 (2006), Nr. 7

[102] Vítkovsky, J. ; A., Bergant ; Simpson, A ; M., Lambert: Systematic Evaluation of One-Dimensional Unsteady Friction Models in Simple Pipelines. In: *Journal of Hydraulic Engineering* 132 (2006), pp. 696–708

[103] Wallis, G. B.: *One-dimensional two-phase flow*. McGraw-Hill, 1969

[104] Wang, Y.C.: *Shock waves in bubbly cavitating flows*, California Institute of Technology, PhD Thesis, 1996

[105] Weisman, J. ; Duncan, D. ; Gibson, J. ; Crawford, T.: Effects of fluid properties and pipe diameter on two-phase flow patterns in horizontal lines. In: *International Journal of Multiphase Flow* 5 (1979), Nr. 6, pp. 437 – 462. – ISSN 0301–9322

[106] Wiggert, D. ; Tijsseeling, A.: Fluid transients and fluid-structure interaction in flexible liquid-filled piping. In: *ASME. Appl. Mech. Rev.* 54(5) (2001), pp. 455–481

[107] Wiggert, D. C. ; Sundquist, M. J.: The Effect of Gaseous Cavitation on Fluid Transients. In: *Journal of Fluids Engineering* 101 (1979), Nr. 1, pp. 79–86

[108] Wijngaarden, L V.: One-Dimensional Flow of Liquids Containing Small Gas Bubbles. In: *Annual Review of Fluid Mechanics* 4 (1972), Nr. 1, pp. 369–396

[109] Wijngaarden, L. van: On the collective collapse of a large number of gas bubbles in water, 1966, pp. 854–861

[110] Wylie, Benjamin ; Streeter, Victor L.: *Fluid Transients*. McGraw-Hill Book Company, Inc., 1978

[111] Yaggy, K.L.: Analysis of Propellant Flow into Evacuated and Pressurized Lines. In: *AIAA* (1984), June, 11, Nr. 1984-1346

[112] Yamamoto, H. ; Ichikawa, K. ; Tokunaga, J.: Solubility of helium in methanol + water, ethanol + water, 1-propanol + water, and 2-propanol + water solutions at 25 degree C. In: *Journal of Chemical & Engineering Data* 39 (1994), Nr. 1, pp. 155–157

[113] Zielke, Werner: *Frequency Dependent Friction in Transient Pipe Flow*, University of Michigan, PhD Thesis, 1966

Appendix A

Sensor accuracy and uncertainty analysis

The accuracy of the pressure sensors is listed in Table A.1. Only the pressure sensors are here considered, since the strain gauge and accelerometer measurements are not used as values per se, but to perform FFT or timing analysis. The uncertainty analysis based on the procedure recommended by NIST [86] is here followed.

Pressure sensors model, from Kistler	Max Range	Linear Error (FS)	Thermal zero shift (FS)	NI-Card model (bit)
4043A200	200 bar	±0.3%	±0.5%	6361 (16 bit)
4043A2 (for vacuum)	2 bar	±0.15%	±0.7%	6361 (16 bit)
601A (dynamic)	250 bar	±0.5%	-	6133 (14 bit)

Table A.1: Sensors characteristics and their accuracy. The linear error and the thermal zero shift of the sensors are taken from the manufacturer datasheet.

The linear error is due to the calibration curve, and it is given as percentage of the Full Scale (FS). The greatest source of error is due to temperature shift, i.e. the difference between the actual temperature at which the sensor performs and the temperature at which the sensor was calibrated. This includes the thermal zero shift error (effect of temperature on the zero signal) and the error due to thermal sensitivity shift, rated as 0.2% FS /10 K in the compensated operating temperature (-20 °C to 40 °C). In addition to the calibration error of the sensor itself, all the measuring chain shall be considered in evaluating the uncertainty.

The list of all the sources of uncertainty to be considered is therefore:

- linear error
- thermal zero shift
- thermal sensitivity shift
- amplifier error (<0.1% FS)
- filter error (0.1 % FS)
- A/D conversion error due to the resolution of the acquisition card ($1/2^{\text{n bit }+1}$)

The maximum deviation of the room temperature from the given calibration temperature was 5° C. Finally, the overall uncertainty U is then calculated by the root of sum of squares of each error Δ_i:

$$U = \sqrt{\sum_{i=1}^{n} \Delta_i^2}$$

The uncertainties of each sensor are summarized in Table A.2.

Pressure sensors model, from Kistler	Max Range	uncertainty
4043A200	200 bar	±1.22 bar
4043A2 (for vacuum)	2 bar	±0.015 bar
601A (dynamic)	250 bar	±1.34 bar

Table A.2: The overall uncertainty of the pressure sensors used

The uncertainty of the vacuum pressure sensor is about 15 mbar, which is more than the vacuum pressure level reached in the tests (10 mbar). To achieve higher accuracy, an adjustment of the sensor output was performed in the post-processing after each test by accounting for the thermal sensitivity shift. The actual temperature near the sensor was measured and the calibration curve was properly corrected. The uncertainty is then reduced to ±3 mbar.

Appendix B

Test-bench eigenfrequencies

In order to measure the natural frequencies of the structure, the impact hammer test is performed. The test section is hit in different points and from different directions. The response signal is measured by accelerometers and the structural natural frequencies are then detected by a frequency analysis (FFT). To excite the structure, a special hammer has to be used. It is an Impulse Force Hammer model 9722A200 from Kistler, it incorporates a quartz force sensing element to measure the pulse force. The procedure of the impact hammer test including the correct mounting of the accelerometers is performed as according to the manual of the hammer [12] and following the recommendations given by Bill [11].

An example of the results obtained in the impact hammer test are shown in Fig. B.1, while the natural frequencies of the test sections are summarized in Table B.1. It is important to remark that the mass of liquid in the test section in not negligible compared to the mass of the pipe and therefore the test section must be filled with the liquid during the impact hammer test. Consequently, a second important remark is that the internal fluid pressure causes a small shift of the natural frequency because it slightly change the stiffness of the pipe. This has been experimentally measured by comparing tests with water at 1 bar vs 20 bar and must be taken into account when analyzing the vibrations of the pipe during the actual priming, with pressure peak up to 200 bar.

Natural Frequency	st. steel (a)	st. steel (b)	st. steel (a, c)	aluminum T6061 (a, c)	aluminum T6061 (b)	titanium T3AV (b)
1st [Hz]	544	750	151	480	488	506
2nd [Hz]	468	478	65	332	535	762
3rd [Hz]	251	261	251	47	788	482
4th [Hz]	42	44	733	720	49	630
5th [Hz]	1144	1161	251	1558	1594	1383

Table B.1: Natural frequencies of the different test sections obtained from impact hammer tests. Only the straight set-up is analyzed. Legend: (a) with water at 1 bar; (b) with water at 20 bar; (c) pipe not pinned.

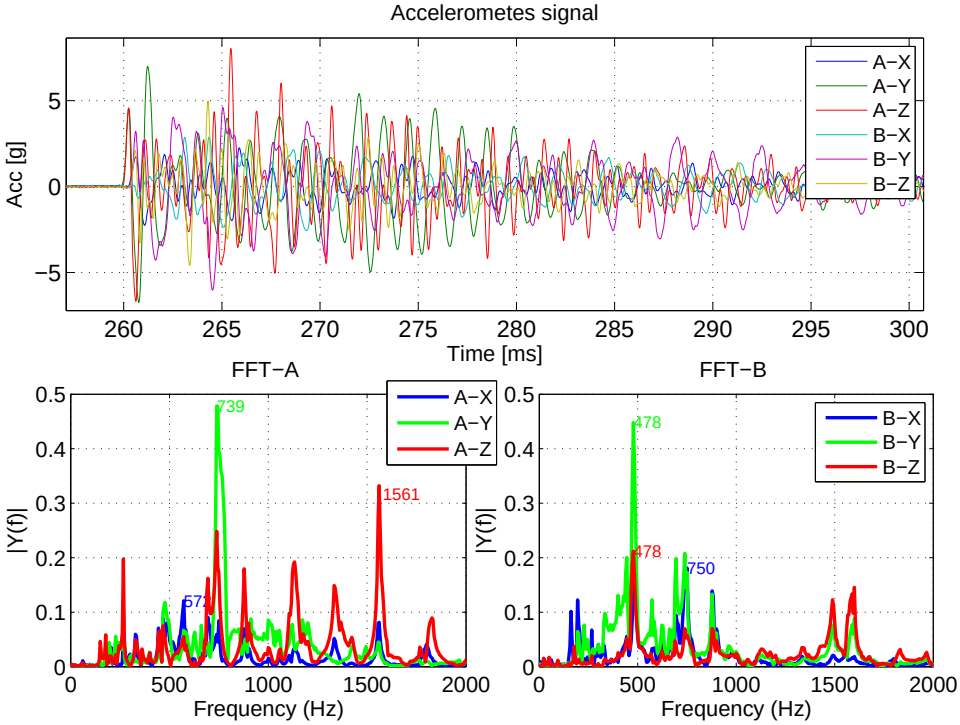

Figure B.1: Example of impact hammer test post-analysis: the FFT of the accelerometers signals are displayed at the bottom, while the raw data of the accelerometers (A and B) are plotted at the top. The three axis are labeled X, Y, Z. The data shown here refer to the stainless steel test-section.

Appendix C

Additional data

C.1 Temperature measurements

The used thermocouples with 0.5 mm tip have too slow a response and are not able to measure fast temperature transients. As it can be seen in Fig. C.1, the temperature signal at the dead-end can not follow the dynamic of the pressure evolution. The measured temperature increase is about 2.5 K in the vacuum case, which means that the real temperature increase is higher.

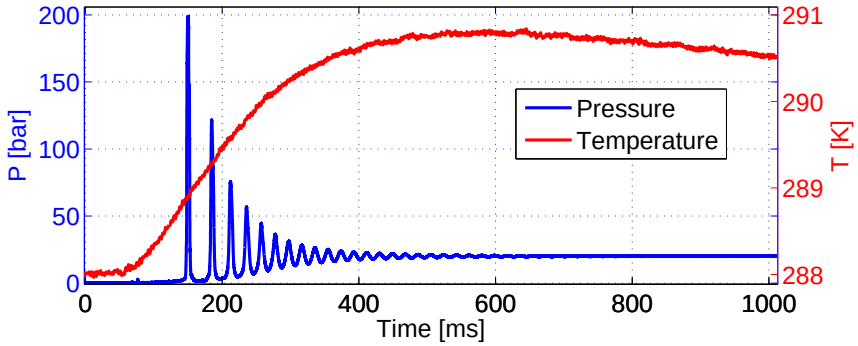

Figure C.1: Temperature measurement at the dead-end in a standard vacuum case

Although the temperature measurements are not reliable, a qualitatively consideration can be made. Slightly higher temperatures are observed for higher initial line pressures (Fig. C.2). This can be explained by the heat transfer between the gas and the liquid/wall. The liquid front traveling towards the dead-end will compress the initial residual gas, which undergoes compression. Depending on how fast the compression rate is, the compression can be assumed between the adiabatic and isothermal condition (polytropic compression of index k). In a 1D approximation, the final temperature T_2 should then be higher for lower P_{line}, since the pressure ratio is higher:

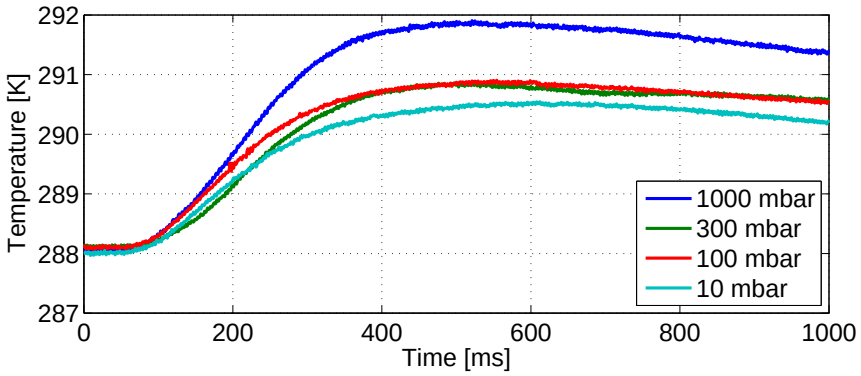

Figure C.2: Comparison of the temperature signals at different line pressures

$$\frac{P_2}{P_1} = \left(\frac{T_2}{T_1}\right)^{\frac{k}{k-1}} \tag{C.1}$$

However, the convective heat transfer between the gas and the liquid/wall can not be neglected. A higher P_{line} means a higher amount of residual gas in the line, which means more gas mass to be cooled or in other words a higher thermal inertia. Therefore the gas temperature will decrease slower for higher P_{line}, although the real final temperature might be lower for higher P_{line}. The inadequate thermocouple response can not measure the initial rapid temperature increase due to the compression.

This consideration might be of help in understanding previous temperature measurement anomalies reported in literature. Gibec and Maisonneuve [37] measured a temperature increase of 23 K in priming tests with hydrazine, speculating that it was due to hydrazine decomposition. The corresponding test condition was a line pressure of 5 bar, whereas the tests with a line pressure of 1 bar showed a temperature increase of only 6 K. Anthoine and Lestrade [4] reported a temperature increase higher than 350 K in priming tests with NTO in vacuum conditions. In this case the high temperature can not be referred to the residual gas (10 mbar line pressure), but to the high amount of vapor generated by flash boiling, as discussed in Section 8.1.2. This however poses other questions, since the compression of a vapor should cause its condensation.

C.2 Numerical simulations: additional x-t diagrams

The results of additional numerical simulations of interest are here reported.

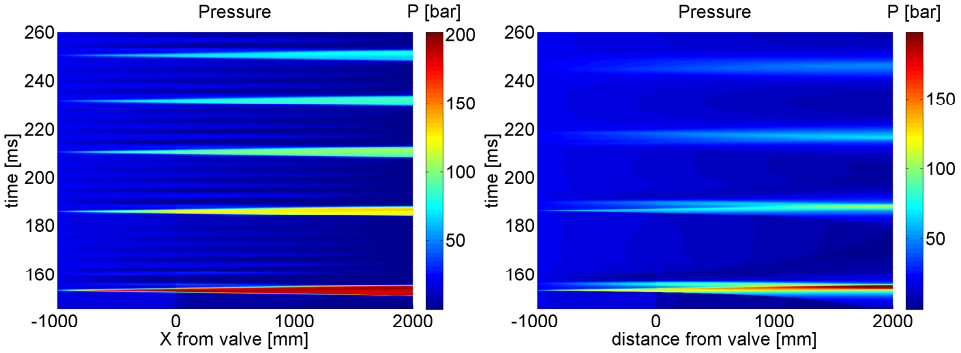

Figure C.3: $X-t$ diagrams of the pressure for deareated (left) and saturated (right) water

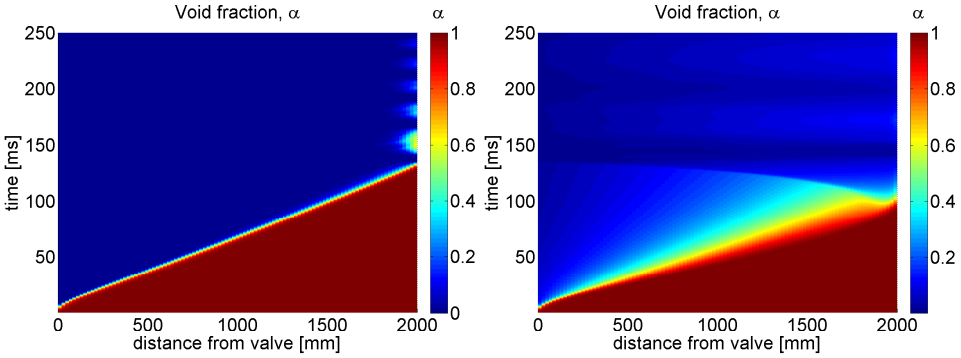

Figure C.4: $X-t$ diagrams of the void fraction for deareated (left) and saturated (right) ethanol

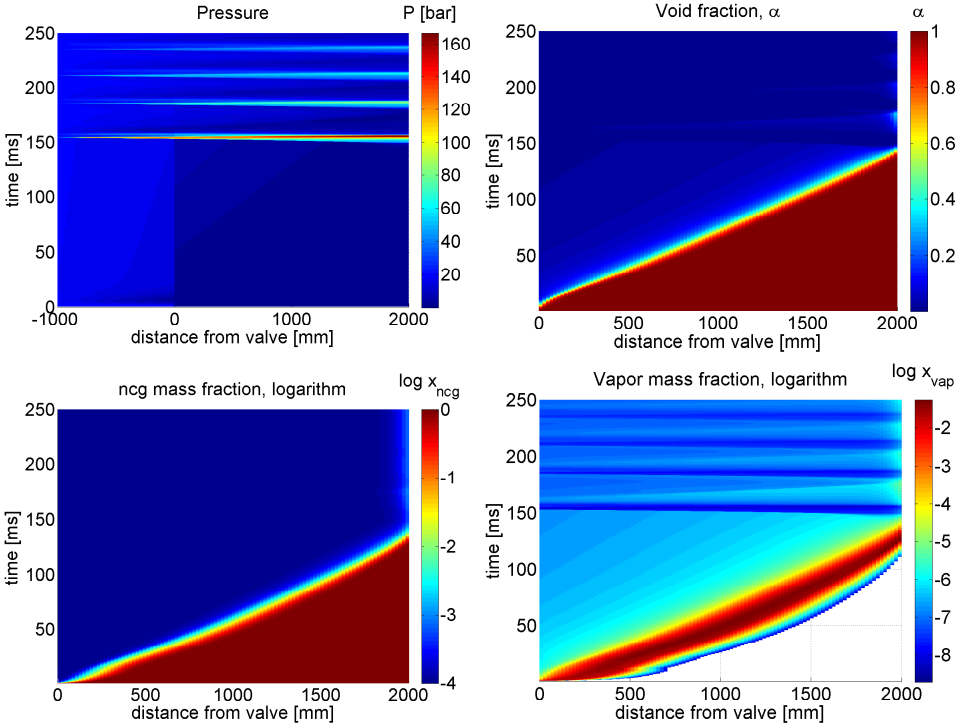

Figure C.5: $X - t$ diagrams for water with a non dissolved NCG content of 10^{-4}

Appendix D

Dimensional analysis of priming

Buckingkam's Pi theorem allows to reduce the number of physical variables involved in the system. The Pi theorem states that:

> *if there are n variable in a problem and these variable contain m primary dimensions (e.g. mass M, length L, time T), the equation relating all the variables will have (n-m) dimensionless groups*

These groups are usually referred to as Π groups. The final relation obtained is in the form of:

$$\Pi_1 = f\left(\Pi_2, \Pi_3, ..., \Pi_{n-m}\right)$$

For an effective use of the Pi theorem, it is essential to include all the variables involved in the phenomenon, based on experience and the engineering feeling. Omitting a physical variable leads to a wrong relationship, therefore it is advisable to include all the variables that might affect the phenomenon, and then later, e.g. after some experimental investigations, neglecting the ones irrelevant that do not play any role [36]. In case of a complex phenomenon like priming, in addition to physical variables such as the fluid pressure, relevant fluid properties must also be included in the analysis. These are listed in Table D.1.

For simplicity, only the case with perfect vacuum downstream is analyzed; in case a gas is present, then all the fluid properties ratio shall also be included in the relations, e.g. $\left(\frac{\mu_g}{\mu_l}, \frac{\rho_g}{\rho_l}, ...\right)$. The geometrical similarity must also be ensured[1], i.e. the ratio L/D . As listed in Table D.1, there are 11 variable and 5 primary dimensions or base units (the length L, the time T, the mass M, the temperature K and the energy[2] J), thus 6 Π groups are to be found. Assuming the water hammer pressure peak P_{wh} as the desired variable, the following expression must be balanced in terms of primary dimensions:

$$P_{wh} \propto c^a \cdot D^b \cdot P_o^c \cdot P_{vap}^d \cdot C_P^e \cdot \Delta H_{vap}^f \cdot \Delta T^g \cdot \mu^h \cdot \rho^i \cdot \sigma^l \cdot \lambda^m \tag{D.1}$$

[1] strictly speaking, also the relative roughness ϵ/D

[2] the energy unit, Joule [J], is considered as a primary dimension as no heat is converted into work

Variable	Symbol	Unit	Dimensions (base units)
speed of sound	c	m/s	$[L][T]^{-1}$
diameter (reference length)	D	m	$[L]$
initial tank pressure	P_o	N/m^2	$[M][L]^{-1}[T]^{-2}$
fluid vapor pressure	P_{vap}	N/m^2	$[M][L]^{-1}[T]^{-2}$
fluid thermal capacity	C_P	$J/kg/K$	$[J][M]^{-1}[K]^{-1}$
heat of vaporization	ΔH_{vap}	J/kg	$[J][M]^{-1}$
temperature difference	ΔT	K	$[K]$
fluid viscosity	μ	$Pa \cdot s$	$[M][L]^{-1}[T]^{-1}$
fluid density	ρ	kg/m^3	$[M][L]^{-3}$
fluid surface tension	σ	N/m	$[M][T]^{-2}$
fluid thermal conductivity	λ	$W/m/K$	$[J][T]^{-1}[L]^{-1}[K]^{-1}$

Table D.1: Variables involved in priming process

Therefore the exponents *a, b, c, ...,m* must be calculated assuring the dimensional homogeneity. For instance, the energy balance [J] leads to $e + f + m = 0$.

A system of 5 equations in 11 variables is then obtained, which leads to the following relationship:

$$\left(\frac{P_{wh}}{P_0}\right) = f\left[\left(\frac{\mu C_P}{\lambda}\right), \left(\frac{C_P \Delta T}{\Delta H_{vap}}\right), \left(\frac{\mu}{\sqrt{\rho\sigma D}}\right), \left(\frac{c}{\sqrt{\frac{\sigma}{\rho D}}}\right), \left(\frac{P_{vap} D}{\sigma}\right), \left(\frac{P_0}{P_{vap}}\right)\right] \tag{D.2}$$

where some classic dimensionless numbers used in fluid dynamics appear. The choice of P_{vap} or P_0 to get dimensionless variables makes no difference and does not affect the relationship (the reference pressure can be either P_{vap} or P_0, in fact $f(\Pi_1, \Pi_2) = f(\Pi_1 \cdot \Pi_2, \Pi_2)$ [36]).

One should expect the Reynolds number to appear as well, but no reference velocity is defined. The term $\left(\frac{c}{\sqrt{\frac{\sigma}{\rho D}}}\right)$ can be rewritten as $\frac{c^2 \rho D}{\sigma} \cdot \frac{V^2}{V^2} = We/Ma^2$, where now the Weber number We and the Mach number Ma also appear. However from a physical point of view, We and Ma hold no meaning in this context as no velocity is defined. The final expression can be then written as:

$$\left(\frac{P_{wh}}{P_0}\right) = f\left[Pr,\, Ja,\, Oh,\, \frac{We}{Ma^2}, \left(\frac{P_{vap} D}{\sigma}\right), \left(\frac{P_{vap}}{P_0}\right)\right] \tag{D.3}$$